Jet Photoproduction and Photon Structure

Eileen Anne Heaphy

University College London

Thesis submitted for the degree of

Doctor of Philosophy

Dedicated to my parents

Abstract

Events containing two and three jets have been studied in photoproduction at HERA. The data were taken with the ZEUS detector during 1996 and 1997 in a photon-proton centre-of-mass energy range 134-277 GeV. Differential cross sections are presented in limited kinematic regions including, for the first time at ZEUS, that with respect to the fraction of the incoming photon momentum participating in the production of the jets, $x_\gamma^{\rm obs}$. Two-jet events were required to contain at least two jets with transverse energy greater than 14 GeV and 11 GeV, in the pseudorapidity region $-1 < \eta^{\rm jet} < 2.4$. Their measurements are compared to next-to-leading-order QCD predictions with three different parametrisations for the photon parton densities. None of the predictions describe the data adequately, even when theoretical uncertainties are taken into account.

The three-jet cross section is defined for events with at least three jets in the region $-1 < \eta^{\rm jet} < 2$ and with an an invariant mass greater than 50 GeV. It has been measured and compared with fixed order parton shower Monte Carlo calculations and leading-order QCD predictions. Both models described the shape of the distributions adequately, despite the lack of higher orders. The scattering angle of the most energetic jet in the three-jet rest frame has been investigated and shows some sensitivity to both the photon and proton parton distributions.

Preface

HERA collides electrons (or positrons) with protons, at a centre of mass energy of about 300 GeV. The dominant type of particle interaction at HERA is photoproduction. In these events a quasi-real photon, radiated off the incoming positron, interacts with a parton from the incoming proton. The resulting quarks and gluons cannot be observed directly due to the phenomena known as 'colour confinement'. Instead a spray of hadrons, called a jet, emerges in the approximate direction of each parton. The properties of jets are described by the same theory that governs quarks and gluons, Quantum Chromodynamics (QCD). In hard photoproduction, at least two jets are produced with relatively large transverse energy, and two types of subprocesses contribute to the cross section: direct and resolved. The latter type of process concerns events where the interacting photon exhibits a structure.

The two- and three-jet photoproduction distributions presented in this thesis have been measured in order to test QCD calculations, and to provide information on the structure of photons. The two-jet cross section is defined in a region of phase space in which theoretical uncertainties are relatively small compared to previous publications, that is at higher transverse energy. Presenting the cross section with respect to the fraction of the incoming photon momentum participating in the production of the jets, $x_\gamma^{\rm obs}$, shows explicitly its relation to the photon structure. The three-jet photoproduction results build on those presented in the first and only HERA three-jet photoproduction paper [10], and take advantage of greatly increased statistics. In particular, the differential cross section measurements presented are sensitive to the dynamics of three jet events, and the structure of the photon and proton.

Pre-HERA, very little was known about hard interactions in photoproduction. The first evidence for photons having a structure more complicated than a meson was offered by the NA14 collaboration in 1986 [1]. The presence of a hard resolved component in the photon was confirmed by the AMY collaboration in 1992 [2], and later H1 [3] and ZEUS [4]. Direct processes were clearly isolated in two-jet events for the first time in 1993 [5]. In a 1996 two-jet paper [6], cross sections differential in the jet scattering angle were presented for direct- and resolved-enhanced regions separately. The two distributions differed in shape, as expected from considerations of the spin of the exchanged propagator, and were described well by QCD calculations. An effective parton distribution of the photon was extracted for the first time using inclusive two-jet data in 1998 [7].

This thesis is structured as follows. In chapter 1 basic QCD and hadron structure theory is described. The HERA accelerator is discussed in chapter 2, along with the components of the ZEUS detector that are used in the analyses presented. The reconstruction of event kinematics from raw ZEUS data is followed in chapter 3. Two- and three-jet cross sections are defined explicitly in chapter 4, and the method of selecting these types of events efficiently from other ZEUS events is detailed in chapter 5. In chapter 6, the ability of Monte Carlo predictions to describe these events is tested. Chapters 7 and 8 deal with the process of unfolding distributions and assigning appropriate errors to the results, which are themselves presented in chapter 9. In the final chapter of the thesis, chapter 10, the two-jet and three-jet results are discussed and interpreted.

Contents

List of Figures

List of Tables

Chapter 1

Hadron Physics

1.1 Historical Preface

By the beginning of the 1960's, a perplexing number of apparently fundamental particles had been discovered, but no theory explained their existence. The first real progress towards a theory was made by Gell-Mann in 1961. He proposed a scheme that arranged these mesons and baryons into geometrical patterns according to their charge and strangeness. Dubbed the Eightfold Way [11], it proved an astounding success in 1964, when the Ω^- [12] baryon it predicted was found in experiments at Brookhaven.

This successful classification of hadrons led directly to the formation of the Quark Model by Gell-Mann [13] and Zweig [14] independently in 1964. They suggested that hadrons were not fundamental particles, but consisted of three more elementary constituents, called quarks, occurring in three flavours (u, d and s) corresponding to the fundamental representation of the SU(3) group.

The existence of hadrons with three seemingly identical quarks (for example Ω^- which has three strange quarks with spins aligned) appeared to violate Pauli's exclusion principle. For the theory to hold there had to exist another quantum number. In 1965, Greenberg [15] and colleagues proposed a new quantum number with three possible states, which they called colour. In this system all naturally occurring particles are colour-less, such that baryons contain one quark in each state - red, green and blue (or anti-quarks with anti-red etc.), whilst mesons have one quark with colour and the other with the corresponding anti-colour.

This hypothesis seemed to some at the time to be a desperate attempt to save the quark model. In fact, it was exactly the breakthrough needed in order for a quantum field theory to describe the strong force to be developed. The ensuing theory, called Quantum Chromodynamics (QCD) [16] was constructed in an analogous way to QED, but with colour (not charge) as the source of the force between coloured (rather than charged) particles. Like quark flavours in the quark model, the three quark colours correspond to the fundamental representation of the SU(3) group, but unlike the quark model the symmetry of colour is an exact symmetry.

Deep inelastic scattering experiments at SLAC [17] analogous to Rutherford's famous scattering experiment suggested that the proton consisted of point-like objects. These **partons** were eventually accepted as the quarks postulated in Gell-Mann and Zweig's model.

1.2 Introduction to Quantum Chromodynamics

QCD is a non-Abelian Yang-Mills gauge theory where interactions are mediated by a massless spin-1 boson, the gluon, which couples to a conserved colour charge.

Although analogous to QED, QCD has three important properties that complicate theoretical predictions and make comparisons with experiment more difficult. Firstly, there are three kinds of colour charge, whereas there is only one type of electric charge (which can be positive or negative). Secondly, whilst in QED the mediating boson, the photon, carries no net charge of its own, the gluons of QCD are bicoloured, carrying one positive colour and one negative colour (e.g. one of the eight gluons is a blue, anti-red gluon). This means that, unlike photons, gluons can couple to other gluons.

Lastly, the strength of the coupling constant in QCD, α_s, becomes larger in the regime of large-distance or low-momentum transfer interactions. The result is that quarks and gluons are not directly observed as free particles, but are confined inside hadrons. Conversely, in high-energy or short-distance reactions they behave essentially like free particles and are said to be *asymptotically* free.

The 'constant' α_s is termed a running coupling constant and is described at lowest order by the formula:

$$\alpha_s(\mu_r^2) = \frac{1}{b_0 \ln \frac{\mu_r^2}{\Lambda_{QCD}^2}} \tag{1.1}$$

where μ_r is the renormalisation scale, usually set to the four-momentum transfer in the interaction, and Λ_{QCD} is a fundamental parameter of QCD. The value of α_s is determined experimentally to be $\alpha_s(M_z) = 0.1185 \pm 0.002$ [18]. The value of b_0 is given by $(11N_c - 2N_f)/12\pi$, where N_c is the number of colours, and N_f the number of active quark flavours at scale μ_r. Clearly b_0 has to be positive for asymptotic freedom ($\alpha_s \to 0$ as $\mu_r \to \infty$) and colour confinement ($\alpha_s \to \infty$ as $\mu_r \to \Lambda$) to emerge.

The number of colours and flavours influence the form of the running because of charge screening effects. Like vacuum polarisation in QED, quark polarisation screens effective colour charge and causes the coupling strength to increase at short range (see Figure 1.1(a) and (b)). However in QCD the self-coupling gluon introduces gluon polarisation diagrams which have an anti-screening effect (Figure 1.1(c)). The value of N_c and N_f are such that the effect of gluon polarisation wins out over quark polarisation, and b_0 is positive.

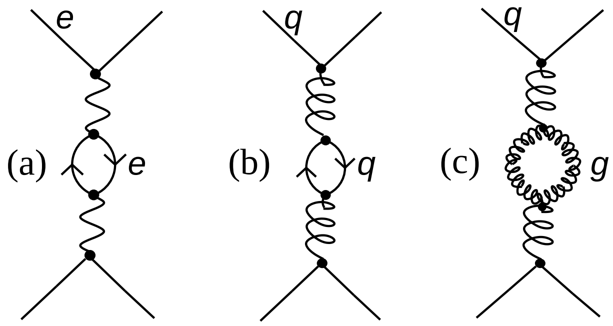

Figure 1.1: Lowest order vacuum polarisation diagrams in (a) QED and (b) QCD; and (c) gluon polarisation in QCD.

In QCD physical quantities can be expressed by a perturbation series in powers of α_s. From equation 1.1 it is clear that α_s is only small enough to allow higher orders in the series to be neglected when $\mu_r^2 >> \Lambda_{QCD}^2$. Cross sections where this condition is met are said to possess a **hard-scale**. In practice, a hard QCD scatter is always accompanied by soft non-perturbative processes. These arise in the initial and final state as the spectator quarks and gluons move away from each other. The potential energy in the colour field increases as they separate, making it favourable for new $q\bar{q}$ pairs to be created from the vacuum. The emerging spray of quarks interact with each other through gluon exchange, until the size of α_s is large enough that the partons are forced to bind together into hadrons.

To make comparisons between experimental data and perturbative QCD (pQCD) predictions, observable quantities must be chosen such that they are minimally contaminated by non-perturbative physics. Also, they should be **infrared safe**, i.e. not affected by the emission of soft or collinear partons, as such quantities are usually strongly correlated to the parton-level kinematics of the hard scatter.

1.3 Proton Structure

Having established that the proton is not a fundamental particle, it is desirable to know more about its substructure. The main physics goal of HERA has been to study this structure in deep inelastic scattering experiments. **Structure functions** are dimensionless variables that relate directly to the distribution of quarks and gluons inside hadrons. The measurement of structure functions has both vindicated the hypothesis of the quark-parton model, and influenced the development of QCD which supersedes it.

1.3.1 Deep Inelastic Scattering

In deep inelastic scattering (DIS), a proton is struck with enough energy by an incident electron, that it does not merely recoil, but breaks apart. The neutral current (NC) interaction ($eP \to eX$) occurs via the exchange of a vector boson, γ or Z^0, while in a charge current (CC) interaction ($eP \to \nu X$) a $W^{\pm}$ is exchanged. Figure 1.2 shows a schematic of the lowest order NC DIS process, where the shaded oval conceals the interaction details at the photon-proton vertex and the X represents the debris into which the proton has broken. Standard HERA notation is used to describe DIS processes and also the photoproduction processes discussed in later sections.

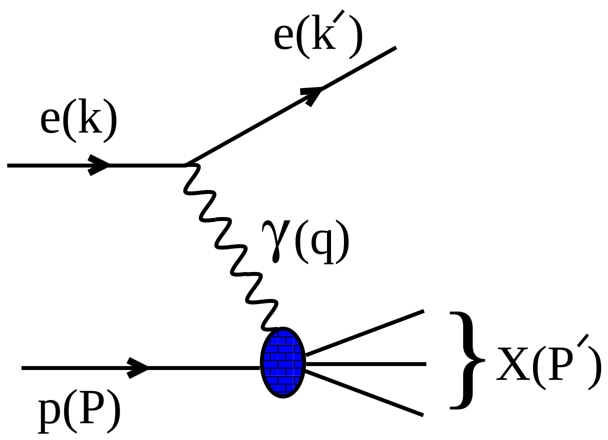

Figure 1.2: Lowest order process for NC DIS. The four-momenta are indicated in brackets.

The following are Lorentz invariant quantities used to specify the kinematics of an ep scattering event:

$$q^2 = (k - k')^2 = -Q^2 \tag{1.2}$$

$$x = \frac{Q^2}{2P \cdot q} \qquad (0 \leq x \leq 1) \tag{1.3}$$

$$y = \frac{P \cdot q}{P \cdot k} \qquad (0 \leq y \leq 1). \tag{1.4}$$

It is convenient to use the positive quantity Q^2, the negative square of the transferred momentum at the lepton vertex, rather than q^2. In the proton's rest frame y is the fraction of electron beam energy carried away by the photon; x is the Bjorken [19] variable.

In the infinite proton momentum frame, the transverse energy of the partons inside the proton is taken to be ≈ 0. Due to time dilation, interactions between partons in the proton occur on a much larger time scale than that of the parton-photon interaction. In this frame x corresponds to the fraction of the longitudinal proton momentum participating in the interaction.

The square of the total energy available in the centre of mass frame is:

$$s = (P + k)^2 \approx 2p \cdot k. \tag{1.5}$$

By substituting equations 1.3 and 1.4 into 1.5 the following is obtained:

$$Q^2 \approx sxy, \tag{1.6}$$

from which it is clear that at fixed s, only two of the variables x, y and Q^2 are independent, and the maximum Q^2 obtainable is when $x = 1$ and $y = 1$.

The Q^2 variable is of fundamental interest for several reasons. In DIS Q^2 provides the hard scale ($Q^2 >> \Lambda^2_{QCD}$) that enables perturbation theory to be used for calculations. It is also used to distinguish between the DIS regime ($Q^2 \gg 1$ GeV^2) and the photoproduction regime, where $Q^2 \approx 0$ GeV^2, and an alternative hard scale must be used to facilitate pQCD calculations. The *ep* cross section falls steeply with Q^2, as $\sim 1/Q^4$, and so low Q^2 processes dominate.

Of paramount importance is the direct relationship of Q to the resolving power of the virtual photon. The wavelength of the virtual photon is given by:

$$\lambda = \frac{h}{|q|} \tag{1.7}$$

and hence it can resolve smaller and smaller structures within the proton as the momentum transfer in the interaction increases.

1.3.2 The Quark-Parton Model

In Feynman's parton model [20], the *inelastic* scattering of the electron off the proton, such as described in DIS, is seen as *elastic* scattering of the electron off a free point-like object (dubbed a parton by Feynman) within the proton. The *ep* cross section is given by the incoherent sum of contributions from individual free quarks to the electron-quark scattering. The leptonic vertex is completely calculable from electroweak theory but the hadronic vertex is not. It contains a non-perturbative component related to the distribution of different quark flavours in the proton, which have to be measured. The probability that the struck parton i carries a fraction x of the proton's momentum P is given by the parton distribution function (PDF) f_i, as illustrated in Figure 1.3.

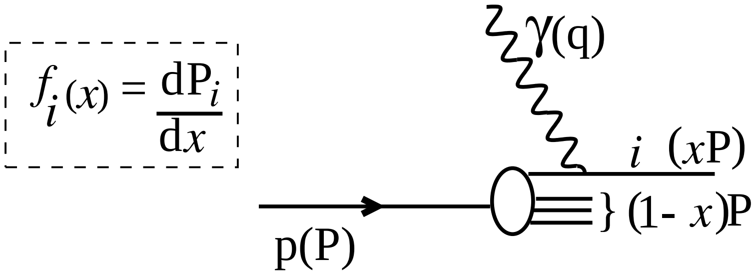

Figure 1.3: Parton distribution function.

The double differential cross section for the NC process in Figure 1.2 can be written in terms of three dimensionless structure functions $F_2(x, Q^2)$, $F_L(x, Q^2)$ and $F_3(x, Q^2)$:

$$\frac{\mathrm{d}\sigma_{NC}(e\pm)}{\mathrm{d}x\mathrm{d}Q^2} = \frac{4\pi\alpha^2}{xQ^4}\left[\left((1-y)+\frac{y^2}{2}\right)F_2(x,Q^2) - \frac{y^2}{2}F_L(x,Q^2) \mp \left(y-\frac{y^2}{2}\right)xF_3(x,Q^2)\right] \tag{1.8}$$

where $F_L = F_2 - 2xF_1$ is the longitudinal structure function and α is the fine structure constant. F_3 is the parity violating term, due to $\gamma - Z$ interference, which means it is only significant when $Q^2 >> M_Z$.

F_1 and F_2 are two independent dimensionless structure functions which contain information about the incalculable part of the hadronic vertex. Bjorken predicted that at very high energies their dependence on Q^2 would fade away, as they become functions of x alone:

$$F_1(x, Q^2) \to F_1(x) \tag{1.9}$$

$$F_2(x, Q^2) \rightarrow F_2(x) \tag{1.10}$$

This phenomena known as Bjorken Scaling was dramatically confirmed in DIS experiments at SLAC in 1969 . That same year, Callan and Gross [21] suggested that the Bjorken structure functions are related:

$$2xF_1(x) = F_2(x) \tag{1.11}$$

which is a direct consequence of:

$$F_2(x) = \sum_i e_i^2 x f_i(x) \tag{1.12}$$

where F_2 becomes the sum of the momentum fractions of each parton i, carrying charge e_i within the proton. The partons included in i are all the flavours of quarks and anti-quarks allowed by conservation laws to participate in the interaction.

The Callan-Gross relation (equation 1.11) holds if the proton *only* consists of charged spin-$\frac{1}{2}$ partons. For charged spin-0 partons it is predicted that $2xF_1/F_2 = 0$. It also implies that $F_L = 0$, i.e. the cross section for longitudinally polarised photons is zero. The experimental confirmation of scaling and the Callan-Gross relation provided the first compelling reason to identify the partons in the the parton model with the quarks in Gell-Mann's and Zweig's model, hence the name the quark-parton model.

1.3.3 Quark-Parton model and QCD

From the success of Bjorken scaling and the Callan-Gross relation, it is also to be expected that the following holds true:

$$\sum_i \int_0^1 \mathrm{d}x f_i(x) x = 1 \tag{1.13}$$

where the densities f_i are integrated over the momenta of the partons inside the proton and summed for each type of parton, i.

However, experiments found this value to be ≈ 0.5 [23], indicating that about half of the proton's momentum had to be in *neutral* partons. This prompted

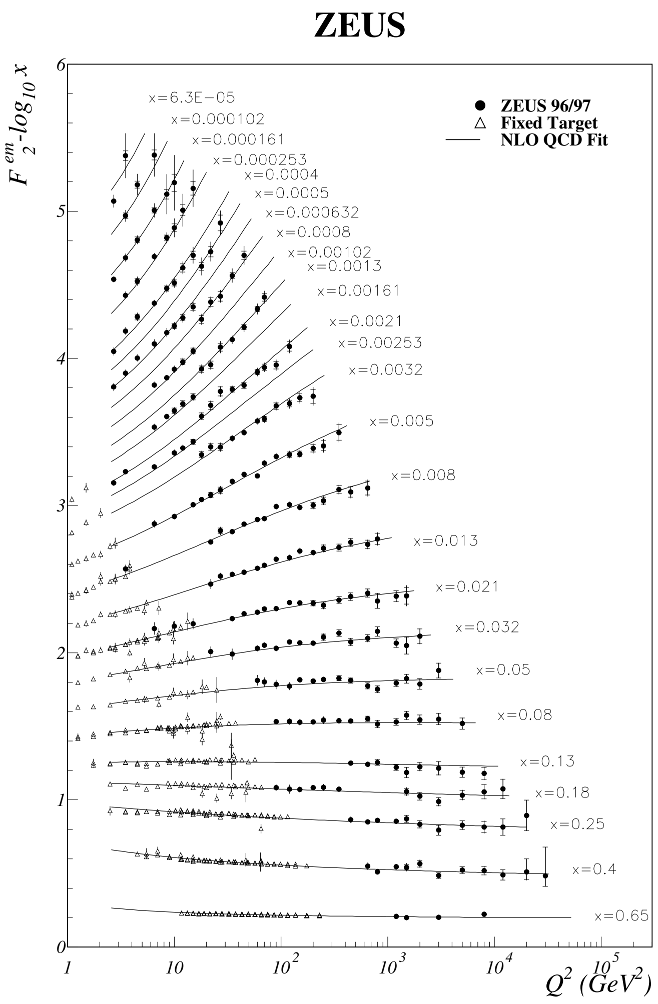

Figure 1.4: The structure function F_2^{em} as a function of Q^2 for fixed x [22].

the improved QPM, essentially QCD, which included gluons and **sea quarks** (arising from gluon splitting) to the original **valence quarks** allowed in the proton soup.

QCD immediately implied two main digressions from the QPM. The presence of sea quarks which can have some transverse momentum implies that the coupling to longitudinally polarised photons is possible. This allows a non-zero F_L and the violation of the Callan-Gross relation.

Also, exact scaling would be violated at high Q^2, in the region where the virtual photon is no longer probing the distribution of the valence quarks, but is resolving the sea quarks, or a valence quark that has radiated a gluon. This behaviour has been confirmed in HERA experiments [24]. Figure 1.4 shows that at small x, F_2 (and hence the quark densities) increases with Q^2. This is attributed to the increase in the number of sea quarks and gluons being resolved by the virtual photon.

1.4 Photon Structure

The photon is a fundamental ingredient of both QED and QCD. In QED a *bare* or structureless photon mediates the electromagnetic force between charged objects, (see Figure 1.5(a)). According to Heisenberg's uncertainty principle:

$$\Delta E \Delta t \geq \frac{h}{4\pi}, \tag{1.14}$$

i.e. the photon can borrow an amount of energy ΔE , such that it violates conservation of energy, if it does so within time Δt. During Δt the photon can likewise fluctuate into a charged fermion anti-fermion ($f\bar{f}$) system. Looking more closely at the interaction, energy and momentum are actually conserved at each vertex

A probe parton can interact *directly* with the photon when it is in the bare state, or with a parton from the $f\bar{f}$ system. In the second case, the parton content of the photon is *resolved* by the probe parton.

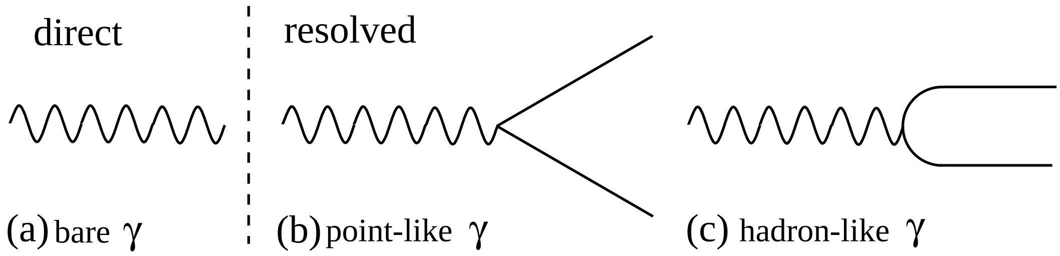

Figure 1.5: The different appearances of the photon. Shown are (a) the direct or bare photon, and (b,c) the resolved photon, which can be either point-like, (b), or hadron-like, (c).

The resolved photon can be regarded as an extended object consisting of charged fermions and gluons, and be further subdivided into two components:

point-like and **hadron-like**. The point-like or **anomalous** photon has split into an unbound $q\bar{q}$ pair (Figure 1.5(b)), and its contribution to the photon structure is in principal calculable in perturbative QCD. The hadron-like photon has fluctuated into a bound $q\bar{q}$ state with the same quantum numbers as the photon, and its structure is well described by the vector meson dominance model (VDM).

Information on the photon structure comes mainly from DIS electron-photon scattering at e^+e^- colliders, but also from hard photoproduction at HERA. In the following sections the theoretical background for photoproduction is discussed briefly, before a more detailed discussion of hard photoproduction and photon structure functions.

1.4.1 The Photoproduction Regime

Photoproduction cross sections in ep scattering at HERA can be treated as a convolution of a flux of transversely-polarised quasi-real photons from the electron and the photon-proton interactions:

$$\frac{\mathrm{d}\sigma_{ep}(z, Q^2)}{\mathrm{d}z} = \sigma_{\gamma p}(z) f_{\gamma\to e}(z, Q^2) \tag{1.15}$$

where the photon flux $f_{\gamma\to e}(z, Q^2)$ is the probability that an electron radiates a photon with given virtuality Q^2 and a particular fraction of the electron's longitudinal momentum, z. The Equivalent Photon Approximation (EPA) [25] gives the general photon flux as:

$$f_{\gamma\to e}(z, Q^2) = \frac{\alpha_{em}}{2\pi Q^2}\left[\frac{1+(1-z)^2}{z} - 2\frac{1-z}{z}\frac{Q^2_{\mathrm{min}}}{Q^2}\right], \tag{1.16}$$

where the $Q^2_{\mathrm{min}}(= (m_e z)^2/(1-z))$ is the lowest virtuality that can be obtained. The photon spectrum for photoproduction events can be obtained by integrating expression 1.16 between the minimum and maximum Q^2 value attainable, $Q^2_{min} < Q^2 < Q^2_{max} << 1$ GeV^2, which yields:

$$f_{\gamma\to e}(z) = \frac{\alpha_{em}}{2\pi}\left[\frac{1+(1-z)^2}{z}\ln\frac{Q^2_{max}}{Q^2_{min}} - 2\frac{(1-z)}{z}\left(1-\frac{Q^2_{min}}{Q^2_{max}}\right)\right] \tag{1.17}$$

This is called as the Weizsäcker-Williams approximation (WWA) [25] . The softness of the photon means that it cannot be used as the probing scale for perturbative calculations in QCD. In jet photoproduction at HERA, the hard scale is provided by the transverse energy of the jets.

Hard Photoproduction at HERA

In hard photoproduction, photon-proton scattering results in two jets with relatively high transverse energy at leading order. Two types of subprocess contribute to the cross section: **resolved** and **direct**. In a direct, leading-order (LO) event, a bare photon scatters directly off the parton from the proton; an example is the interaction in Figure 1.6(a). In a resolved event, such as in 1.6(b), the photon acts as a source of partons, one of which scatters off the parton from the proton.

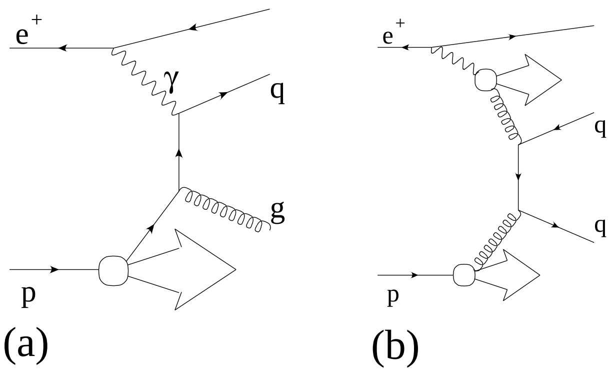

Figure 1.6: Leading order hard photoproduction processes. (a) direct, (b) resolved

In the case where the photon is resolved, only part of its momentum x_γ enters into the hard scatter, the rest goes into the formation of a photon remnant collinear with the photon (and electron beam) direction. At LO, $x_\gamma = 1$ for direct events. However, the distinction between resolved and direct events is blurred at higher orders. The observable $x_\gamma^{\rm obs}$ is defined in QCD to all orders and can be used as a means of separating the cross section into a photon structure sensitive region (low $x_\gamma^{\rm obs}$) dominated by resolved-like events, and a less sensitive region (high $x_\gamma^{\rm obs}$) dominated by direct-like events. The reconstruction of this useful variable and more description of the kinematics of two- and three-jet events is discussed in Chapter 3.

1.4.2 The Generalised Photoproduction Model

A generalised picture of LO resolved photoproduction is shown in Figure 1.7. The scales μ_p and μ_γ *factorise* the event into the perturbative hard subprocess and non-perturbative parton distribution functions. Their values are arbitrarily chosen to be the transverse energy of the jets.

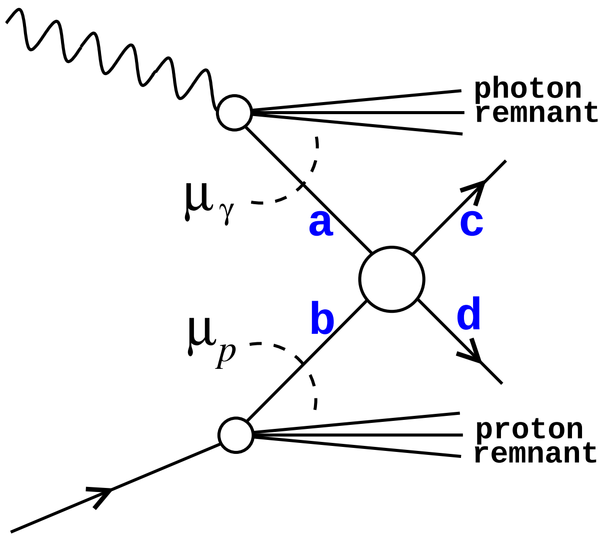

Figure 1.7: General Leading Order picture for resolved photoproduction

A general expression for the resolved cross section is given in equation 1.18

$$d\sigma^{res}_{\gamma p\to cd} = \sum_{ab} \int_{x_\gamma} dx_\gamma f_{\gamma\to a}\left(x_\gamma, \mu_\gamma^2\right) \int_{x_p} dx_p f_{p\to b}\left(x_p, \mu_p^2\right) d\hat{\sigma}_{ab\to cd} \tag{1.18}$$

where the short distance cross section $d\hat{\sigma}_{ab\to cd}$ is determined from the perturbatively calculable $2\to 2$ scattering matrix element, $\mathcal{M}_{ab\to cd}$, and two-body phase space:

$$d\hat{\sigma}_{ab\to cd} = \frac{1}{2s}\overline{|\mathcal{M}|}^2 dPS \tag{1.19}$$

The non-perturbative parts of the expression 1.18 are the parton densities in the proton, $f_{p\to b}$, and photon, $f_{\gamma\to a}$.

The proton parton densities are well constrained by experiments, such as deep-inelastic scattering at HERA as described in section 1.3.1. Uncertainty from the matrix element is decreased by including Next-to-Leading Order (NLO) diagrams in the calculations, which reduces its dependence on the factorisation scale chosen. Within this scheme, then, it is $f_{\gamma\to a}$ that provides the largest uncertainty on the cross section. It follows that the high-E_{T} two-jet photoproduction measurements presented in this thesis are sensitive to the photon structure, and are suitable for testing the currently available parametrisation of photon PDFs.

1.4.3 Photon Structure Functions

The $e\gamma$ DIS cross section can be written in terms of photon structure functions, in a fashion that is similar to the way ep DIS cross sections are parametrised in terms of proton structure functions,

$$\frac{\mathrm{d}\sigma_{e\gamma\to eX}}{\mathrm{d}x\mathrm{d}Q^2} = \frac{2\pi\alpha^2}{xQ^4}\left[\left(1+(1-y)^2\right)F_2^\gamma - y^2F_L^\gamma\right]. \tag{1.20}$$

Similarly, the F_2^γ structure function can be written in terms of the quark densities in the photon, $q_i^\gamma(x,Q^2)$,

$$F_2^\gamma(x,Q^2) = 2x\sum_i e_{q_i}^2 q_i^\gamma(x,Q^2) \tag{1.21}$$

where e_{q_i} are quark charges and the sum runs over all flavours, i.

There are also significant differences between proton and photon structure functions. Proton structure functions have to be determined completely from experiment, but their behaviour as a function of μ is calculable in QCD and governed by the DGLAP [26] parton evolution equations. The DGLAP equations, extended to the photon case, can also be used to evolve the photon structure functions. However, at scales that are large enough for the VDM component to be ignored, the photon structure functions are completely determined. Unfortunately, these calculations are only applicable at very high scales and high x, and not where direct measurements of F_2^γ are made.

The scaling behaviour also differs. The photon structure functions rise with x, above $x \approx 0.1$ as it becomes increasingly more likely that quarks are produced via $\gamma \to q\bar{q}$ splitting rather that gluon splitting. The gluon fraction of the photon is most significant at low x, due to the dominance of gluon splitting over $g \to q\bar{q}$.

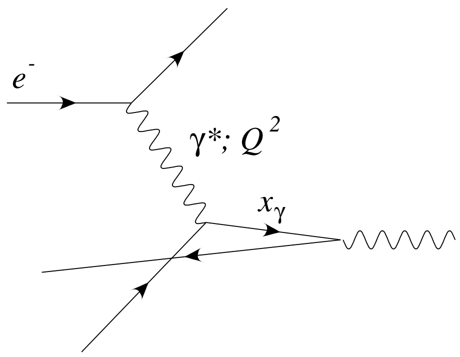

Figure 1.8: Deep inelastic electron-photon scattering

Photon Structure at e^+e^- Colliders

The photon structure function, F_2^γ, has been measured in deep inelastic electron photon scattering at e^+e^- experiments producing results such as those in Figure 1.9. From these results F_2^γ and hence photon PDFs are not well constrained at $\mu^2 \geq 100$ GeV^2 or at high x_γ, due to large experimental uncertainties in this kinematic range. The gluon density in particular is poorly constrained, since LO γ-DIS, illustrated in Figure 1.8, is only sensitive to the quark densities in the photon. From Figure 1.9 is it clear that there is a wide spread in predicted gluon densities that are consistent with F_2^γ data.

Photon Structure at HERA

The F_2^γ structure function cannot be measured directly at HERA, however high-E_T jet photoproduction cross sections are sensitive to the structure of the photon.

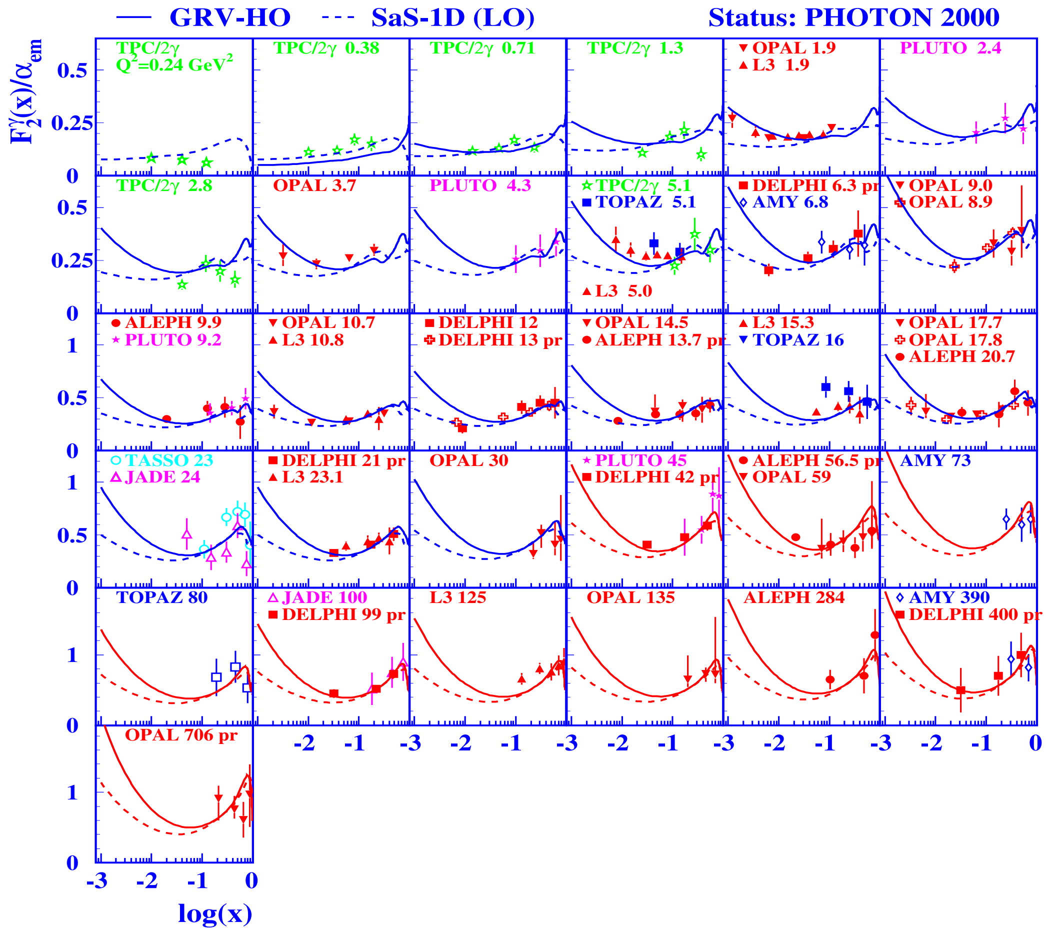

Figure 1.9: Compilation of photon structure function data [27]. The x dependence of F_2^γ in different Q^2 bins is shown compared to GRV NLO (solid line) and SaS1D LO (dashed line) PDFs. The Q^2 values are denoted in GeV^2 by the key in each box, along with the experiment from which the data are taken.

Jet photoproduction, unlike γ-DIS, is already sensitive to the gluon content of the photon at LO and cross sections can be measured accurately up to $x_\gamma^{\rm obs} = 1$. In addition to this, the scales at which the photon structure can be probed in jet photoproduction at HERA, are much higher than those achievable elsewhere, with $\mu^2 \geq$ 190 GeV for the two-jet analysis presented in this thesis, as is depicted by the shading in Figure 1.10.

1.4.4 Available Photon PDFs

There are several NLO parametrisations of the structure of real photons available. They differ mainly in the factorisation scheme chosen, the form of their input

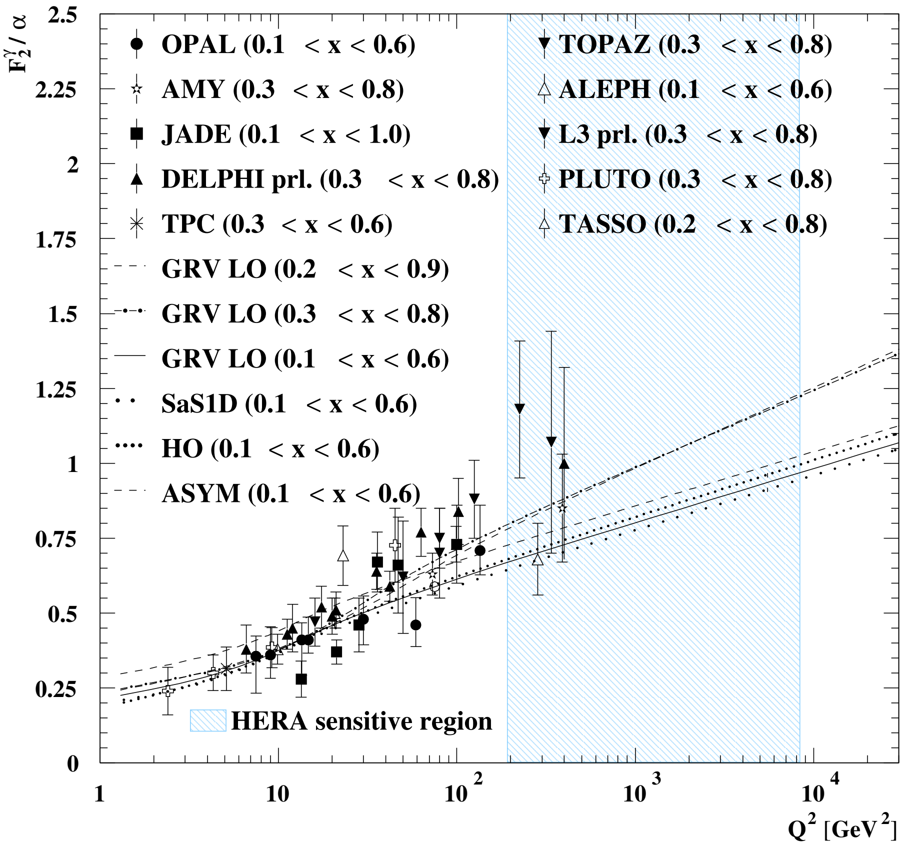

Figure 1.10: The measured Q^2 evolution of F_2^γ, taken from [28], and modified to show the region of phase space accessed by the two-jet photoproduction analysis.

distributions and input scales. The general approach however is the same: the perturbatively incalculable initial quark and gluon distributions are fixed at some scale Q_0^2, and then evolved to higher scales using the DGLAP equations.

Data are used to constrain the values of the free parameters and the overall normalisation. The F_2^γ measurements used to constrain the parton densities come from from PETRA [29–31], PEP [32], TRISTAN [33,34] and LEP [35,36]. As discussed in the previous section, only quark densities are reasonably well constrained, and only in the region $0.01 \lesssim x \lesssim 0.8$. The gluon distribution is not tightly constrained.

The NLO parametrisations used in the pQCD calculations presented in comparison with measurements in this work are shown in Figure 1.11 and are now discussed.

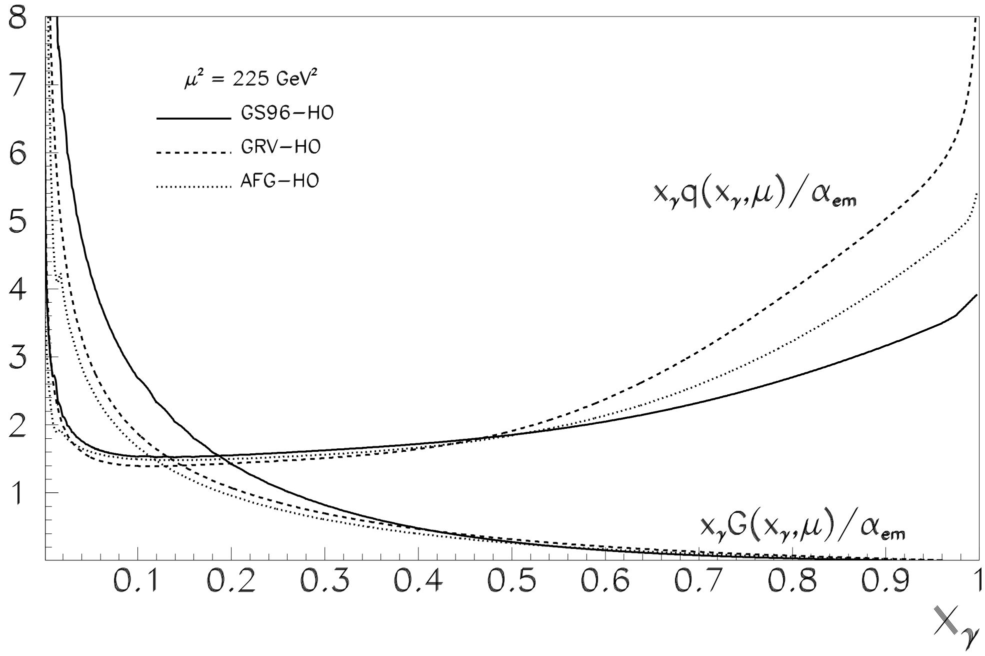

Figure 1.11: Comparison of quark and gluon density distributions in the photon for three different PDFs, at a factorisation scale $\mu^2 = 225$ GeV^2, and given in the $\overline{\text{MS}}$ factorisation scheme.

Glück, Reya & Vogt

The GRV-HO [37, 38] parametrisation is based on a valence-like VDM input model, which approximates the photon parton densities using the parton densities of the pion. It is assumed that the anomalous component of the photon vanishes at the very low input scale used, $Q_0^2 = 0.3\,\text{GeV}^2$, and can be generated dynamically by the evolution equations. There is only one free parameter, which is constrained by the data, and the DIS$_\gamma$ factorisation scheme [37] is used.

Aurenche, Fontannaz & Guillet

The AFG-HO [39] parametrisation has a similar input model to GRV-HO, but the starting scale is slightly higher, $Q_0^2 = 0.5\,\text{GeV}^2$ and the $\overline{\text{MS}}$ factorisation scheme [40] is used.

Gordon & Storrow

The GS96-HO [41] parametrisation of the photon structure has a higher input scale than those from AFG and GRV, $Q_0^2 = 3\,\mathrm{GeV}^2$, and so the input model includes both an anomalous and VDM component. The factorisation scheme used is $\overline{\mathrm{MS}}$.

1.5 Overview of Hadronic Interactions

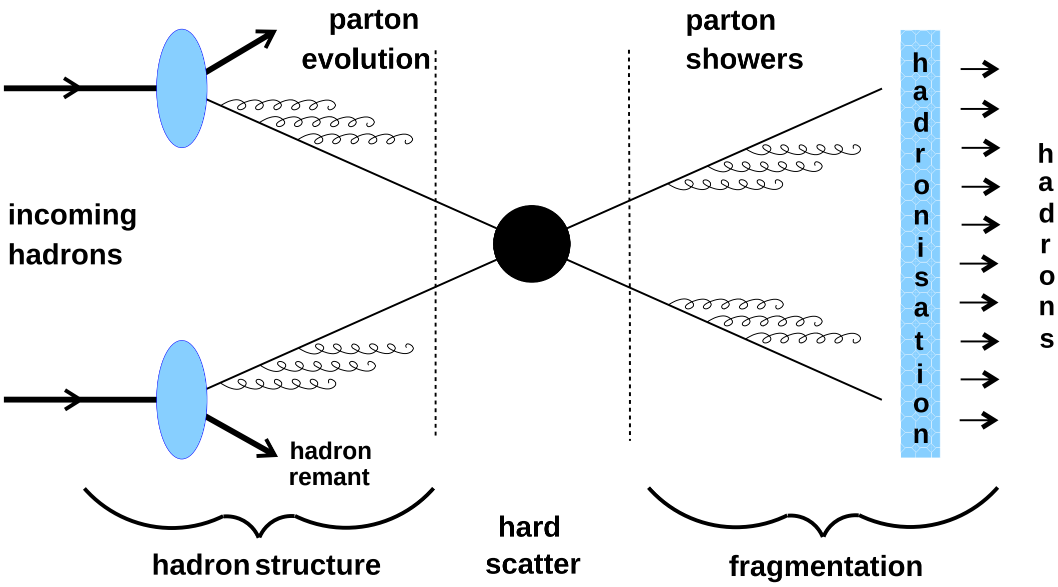

Figure 1.12: Overview of a leading order (LO) hadron-hadron interaction

A schematic overview of a generalised hadron-hadron interaction is illustrated in Figure 1.12. The interaction is entirely governed by the strong force, which concerns coloured particles, but is colour neutral in the initial and final states.

There are three main parts to the diagram, the first third concerns the structure of the interacting hadrons, the second the hard scatter between partons, and finally the fragmentation of outgoing partons from the hard scatter into hadrons.

The structural composition of each hadron is described by its parton distribution function (PDF), which is a function fixed at some scale μ_0 by parametrisations to structure function data, and then evolved to the factorisation scale μ_f using DGLAP evolution equations.

The value of μ_f is usually taken to be equal to the momentum transfer in the hard interaction, and is the cut-off point between the hadron structure and the hard scatter. The processes either side of this scale are thought to be independent of each other, so the characteristics of a hard scatter are not influenced by the source of the partons involved.

This concept, called **hadron universality**, is used to infer that the photon PDFs obtained from e^+e^- experiments also apply to the photons in ep experiments at HERA.

The hard scatter is calculable in pQCD when it involves a sufficiently hard scale. The dependence of the calculation on the renormalisation scale chosen, μ_r is reduced by incorporating NLO diagrams.

The fragmentation which follows has two stages. Firstly, outgoing partons from the hard scatter emit a spray of further partons in a manner that is similar to parton evolution. These parton showers are calculable by a resummation of dominant logarithmic terms to infinite order in α_s, when the emissions are sufficiently hard. The final stage of fragmentation and the interaction in general is hadronisation. Since no hard scale is involved it is not calculable in QCD, and so hadronisation is only well described by phenomenological models.

The hadrons evolved from an outgoing parton of the hard scatter are expected to be clustered around the direction of the original parton, and to have related energies. Hadron clusters in the final state, or *jets*, can be used to reconstruct the kinematics of the hard scatter, which is obviously of interest. Different methods of finding and defining jets are discussed in chapter 3.

The picture of hadron-hadron interactions presented here is necessarily simplified. Some of the more relevant complications and details to this picture are now discussed.

Multi-parton Interactions

It is possible that more than one parton from each hadron is involved in a hard scatter. An example is shown in Figure 1.13, where two independent hard scatters take place between the hadrons. Such multi-parton interactions (MPIs) are not included in any pQCD calculations, but are included in some LO Monte Carlo (MC) event generators. In the case where a hadron-like state evolved from a quasi-real photon, MPIs are most likely at low values of x_γ. In this region the parton densities are high (see Figure 1.11) and a large fraction of the photon's momentum is available for secondary hard scatters.

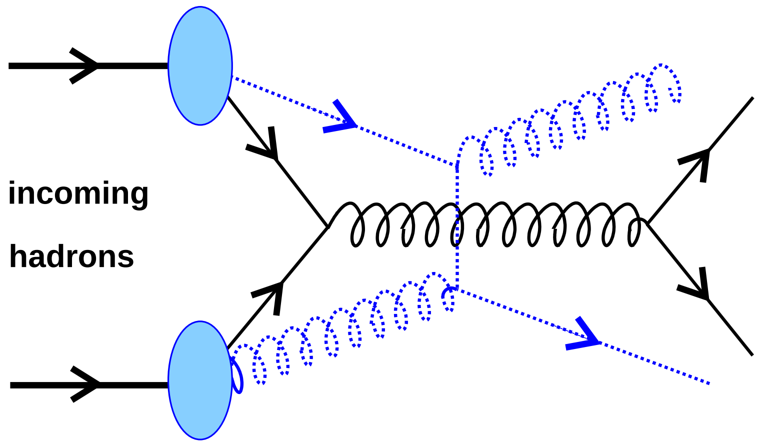

Figure 1.13: Schematic of a multi-parton interaction between two hadrons, involving two independent hard scatters.

QCD Coherence

The emission of soft gluons between colour connected partons is not well described without considering the effects of QCD colour coherence. There are two main effects termed **intrajet** and **interjet**. The intrajet coherence constrains the gluon radiation within a parton shower, requiring that sequential parton splittings have successively smaller opening angles as the evolution proceeds to lower scales.

The interjet coherence refers to the suppression of gluon emission between partons that are not connected by colour strings, which represent the colour field. The string effect has been studied extensively using events with three jets in the final state by DELPHI [42], L3 [43] and OPAL [44]. A smaller particle flow is seen in the region between quark jets in $q\bar{q}g$ than in $q\bar{q}\gamma$ events due to quantum mechanical inteference effects.

1.6 Theoretical Predictions

The jet measurements made in this thesis are compared to various theoretical predictions to test the current understanding of QCD and show up areas of weakness. Theoretical predictions are also depended upon to correct measured distributions for detector-induced effects.

The final states produced in hadronic interactions are usually extremely complicated, and related to the physics subprocess in a non-trivial manner. In practice, cross sections for jet photoproduction events are not entirely analytically calculable because of the high particle multiplicities involved, and because each event consists of both pertrubative and non-perturbative phases. Instead, subprocesses are factorised into initial state radiation, hard subprocess and final state radiation. These components, along with hadronic parton distributions and fragmentation, are treated independently and each event is generated by combining them in a probabilistic manner.

There are two types of theoretical predictions used in this thesis, called here Monte Carlo Event Generators (MC) and perturbative QCD (pQCD) predictions. MC generators use a phenomenological model to simulate the non-perturbative hadronisation stage and hence produce events with as much detail as experimentally observable ones, but currently use only leading order matrix element calculations. Perturbative QCD predictions used in this thesis incorporate matrix elements up to $\mathcal{O}(\alpha\alpha_s^2)$ but do not simulate the final state, and so are not directly comparable to uncorrected data. The development of pQCD calculations which include hadronisation is being encouraged within the physics community, but as yet none are available. The particular theoretical predictions used in this thesis are now discussed.

1.6.1 Monte Carlo Models

The generators used in this thesis are HERWIG [45] and PYTHIA [46], which both include a broad range of high-energy hadronic subprocesses, and are described in detail elsewhere. The building blocks used in the construction of complete events are now considered, with particular attention paid to the differences between the two generators.

Incoming partons The spectrum of photons in the beam electron is generated in HERWIG according to the EPA and using the WWA in PYTHIA. The flavour and energy share of partons inside the colliding photons and protons are characterised by parton distribution functions. One parton from the proton and one from the photon initiate a shower of partons while the remainder make up the beam remants or take part in secondary hard scatters.

Initial-state shower Each of the two partons undergo successive splittings such as $q \to qg$, governed by the DGLAP evolution equations. Initially, the partons have a low space-like virtuality which then increases with each successive radiation of a time-like parton. In HERWIG, the upper limit on the space-like mass is bounded by Q of the hard subprocess.

Elementary hard subprocess The matrix elements are based on LO $2 \to 2$ body scattering and are exactly calculable in pQCD. In events with three or more jets in the final state parton showers are responsible for the additional jets. The Q^2 of the hard subprocess sets the boundaries for initial and final-state radiation, and also influences the parton distributions within the beam partons.

Final-state showers The outgoing partons from the hard scatter have a virtuality Q^2_{max} controlled by the hard subprocess. The partons' virtuality decreases with successive emissions to a minimum cut-off Q_0^2. HERWIG ensures that the effects of coherent radiation and intefering gluons are treated correctly by demanding that the splitting angle between partons decreases with successive emissions. In PYTHIA the emissions are ordering in terms of virtuality of the radiated partons, and the angular ordering is implemented separately.

Hadronisation This stage, sometimes referred to as fragmentation, usually involves two stages. The first is the creation of colour-singlet composites from the particles in the parton showers, which is done using the LUND string model in PYTHIA whilst HERWIG opts for a Cluster-based model. The second stage is the decay of these composites into stable final-state observable hadrons.

In the LUND model, a string is envisioned to exist between say a q and a $\bar{q}$ which has an energy per unit length of ≈ 1 GeV/fm. As the quarks move apart from each other the potential energy in the strings increases. If the invariant mass of the string is large enough a break occurs and a new q and $\bar{q}$ come into existence at the new string ends. The process repeats until there is no longer enough energy in the strings to produce new quarks, and only on-mass-shell hadrons remain, made up of whole strings with a q and $\bar{q}$ at either end. Unstable hadrons are decayed according to their measured branching ratios and masses, and their decay products are usually distributed according to phase space.

The Cluster hadronisation model is local in colour and independent of the hard subprocess. All the gluons that exist after the end of parton showering are split into $q\bar{q}$ or diquark-antidiquark pairs. From each q (or diquark) a colour line can be drawn to a $\bar{q}$ (or antidiquark) with which a colour-singlet cluster is formed. The clusters are fragmented into lighter hadrons, or if they are too light, their mass is adjusted to the lightest same-flavoured hadron by exchanging momentum with nearby clusters. Heavy clusters with masses below the fission threshold have a randomly-flavoured $q\bar{q}$ pair added and are decayed isotropically into two hadrons.

In the actual program execution the first step is to produce the hard subprocess. The exchanged momentum Q sets the upper boundary for intial- and final-state radiation, which procedes such that the inital-state radiation is actually backwards evolved towards the incoming hadrons.

HERWIG and PYTHIA contain free parameters which are tuned to data. HERWIG has fewer and therefore a greater predictive power.

The normalisation of jet photoproduction cross sections is not well reproduced by LO MC due to the sizeable nature of NLO corrections. The cross sections are also highly dependent on the factorisation and normalisation scales. For most distributions, however, higher order corrections to their actual shape are expected to be relatively small. To describe the data, the MC cross sections are scaled by the factors in table 1.1. These are obtained by fitting direct and resolved events, which are generated separately, to the x_γ^{obs} distribution in real data (see chapter 6). The factors are applied to the MC used throughout the rest of this thesis.

Analysis	Event Generator	cross section weighting	
		Direct	Resolved
2-jet	HERWIG 5.9	1.73	1.91
	PYTHIA 6.1	1.38	1.19
3-jet	HERWIG 5.9	2.45	1.98
	PYTHIA 5.7	2.09	1.30

Table 1.1: MC normalisation factors

1.6.2 Perturbative QCD Calculations

The pQCD calculations presented in this thesis are obtained using code provided by S. Frixione and G. Ridolfi [47]. They use the subtraction method to cancel analytically the infrared divergences which arise in the calculation. The renormalisation and factorisation scales are both chosen to be half the total transverse energy of the event. The value of the strong coupling constant used is 0.116

and Λ_{QCD} is set to 202 MeV to be consistent with the proton PDF used, CTEQ 4M [48].

The calculations include $2 \rightarrow 2$ parton processes to one-loop order and tree-level $2 \rightarrow 3$ processes. As such, the pQCD predictions are up to $\mathcal{O}(\alpha\alpha_s^2)$, which is NLO for two-jet and LO for three-jet photoproduction. One advantage of NLO predictions is a reduction in their scale dependence compared with LO.

The $\mathcal{O}(\alpha\alpha_s^2)$ calculations of Klasen and Kramer [49], Harris and Owens [50] and Frixione and Ridolfi have been compared in [51] and shown to agree to within 5% for both two- and three-jet cross sections at HERA.

Chapter 2

HERA and ZEUS

2.1 HERA

HERA [52] (Hadron Elektron Ring Anlage) is the world's first and, to date, only collider designed to collide leptons (either electrons or positrons) with protons. It is run by the DESY (Deutsches Elektronen Synchrotron) laboratory in Hamburg, Germany and has been operational since 1992. The data analysed and presented in this thesis were collected during the 96/97 running period. During this time, HERA collided beams of 27.5 GeV positrons and 820 GeV protons, giving rise to a centre of mass energy of 300 GeV. This is an order of magnitude higher than previous fixed target experiments, and allows previously inacessible kinematic regions to be measured.

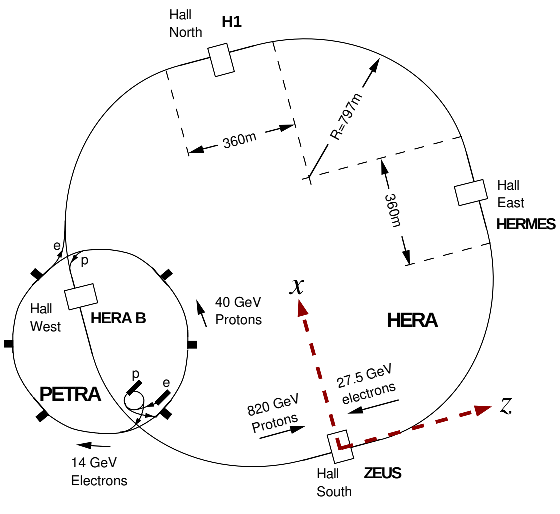

Figure 2.1: The HERA ring

HERA consists of two rings, one for the proton beam and one for the positron beam. A maximum of 210 positron and proton bunches are accelerated around the rings, each separated by about 30m. The counter-rotating beams cross at the interaction points and the bunches cross every 96ns.

There are four experiments located equidistantly on the 6.3 km HERA ring, shown in Figure 2.1. Two of these are fixed target experiments: HERMES [53] and HERA-B [54] based at the East and West Halls respectively. The HERMES detector is used to investigate nucleon spin structure functions, by colliding a polarised electron (or positron) beam with a polarised gas target. At HERA-B the proton beam halo interacts with a fixed wire target, facilitating the study of CP violation in the decay of B mesons.

The H1 [55] and ZEUS detectors are situated at the north and south interaction points respectively. They are both multipurpose detectors, such that they cover almost 4π of the solid angle, combine tracking and calorimetry and are capable of particle identification. They are therefore sensitive to a wide variety of lepton-proton (ep) interactions, and can be used to search for new physics. The ZEUS detector, used in the analyses presented in this thesis is now discussed in more detail.

2.2 ZEUS

A right handed coordinate system is used at ZEUS [56], with the z axis in the direction of the proton beam and x-axis pointing towards the centre of the HERA ring, as indicated in Figure 2.1. In cylindrical polar coordinates, r is the radial distance from the z axis, and ϕ is the azimuthal angle. Pseudorapidity, η, is a function of polar angle with respect to the z axis, and is defined as $\eta = -\ln\tan(\theta/2)$.

The ZEUS detector [58] is designed to accurately measure the position, momentum and energies of particles produced in ep interactions in the HERA collider. A longitudinal section of the detector is shown in Figure 2.2. The main

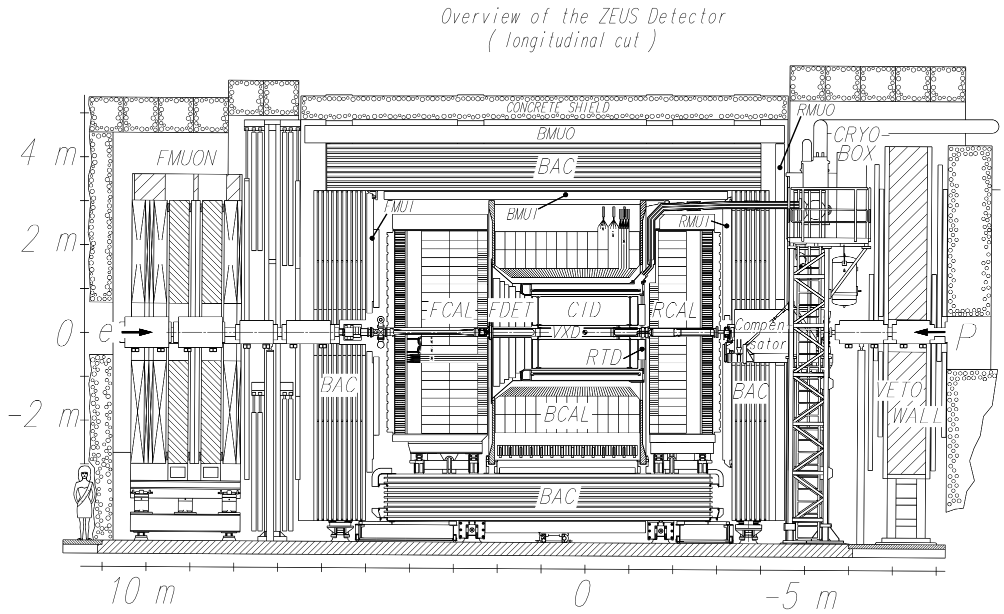

Figure 2.2: The ZEUS detector

components used in the analysis are the central tracking detector, calorimeter and luminosity monitor.

2.2.1 Central Tracking Detector

The central tracking detector (CTD) [57] is a cylindrical wire drift chamber at the centre of ZEUS, and covers the polar angle range $15° - 164°$. An octant of the chamber, in the r-ϕ plane, is shown in Figure 2.3. It consists of 72 cylindrical layers, subdivided into 9 superlayers. Wires are arranged parallel to the beam axis and at a small stereo angle to it of about $5°$, which allows the z trajectory of tracks to be determined to within $\sim$5cm.

The CTD is surrounded by a superconducting solenoid magnet with a uniform 1.4 T magnetic field, which bends the trajectories of charged particles. The measured transverse momentum, $P_{\rm T}$, resolution for full length tracks is $\sigma_{P_{\rm T}}/P_{\rm T} = 0.0058 P_{\rm T} \bigoplus 0.0065 \bigoplus 0.0014/P_{\rm T}$ [59] where $P_{\rm T}$ is in GeV.

2.2.2 Calorimeter

ZEUS has a uranium-scintillator calorimeter composed of alternate layers of 3.3mm thick depleted uranium and 2.6mm thick scintillator material. These

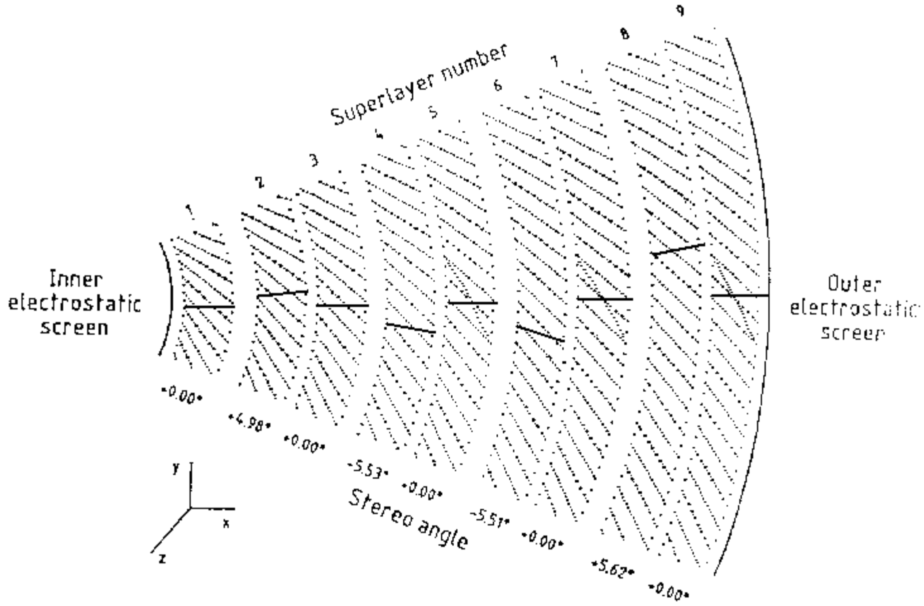

Figure 2.3: An octant of the CTD

thicknesses have been selected such that the energy response to electrons and hadrons is the same for particles of the same energy. For electrons the resolution is $18\%/\sqrt{E}$ and for hadrons it is $35\%/\sqrt{E}$, as measured under test beam conditions and where E is given in GeV.

The calorimeter is physically divided into 3 sections, the forward, rear and barrel calorimeters (FCAL, RCAL, BCAL) which together cover 99.6% of the solid angle. Each calorimeter is deep enough to ensure containment in excess of 95% for 90% of the particle jets of maximum energy. The maximum energies for the FCAL and RCAL are the proton and electron beam energy respectively, and hence the FCAL is deeper than the RCAL.

The calorimeter is longitudinally segmented into layers of electromagnetic cells (EMC) and hadronic cells (HAC). Figure 2.4 shows the RCAL, an RCAL module and the arrangement of EMC and HAC towers within a module. The EMC towers are innermost to the interaction point and have a depth of 1 nuclear interaction length (1 λ). There are 2 EMC cells to a tower in the RCAL, measuring 10×20cm, and 4 EMC cells to a tower elsewhere, measuring 5×20cm.

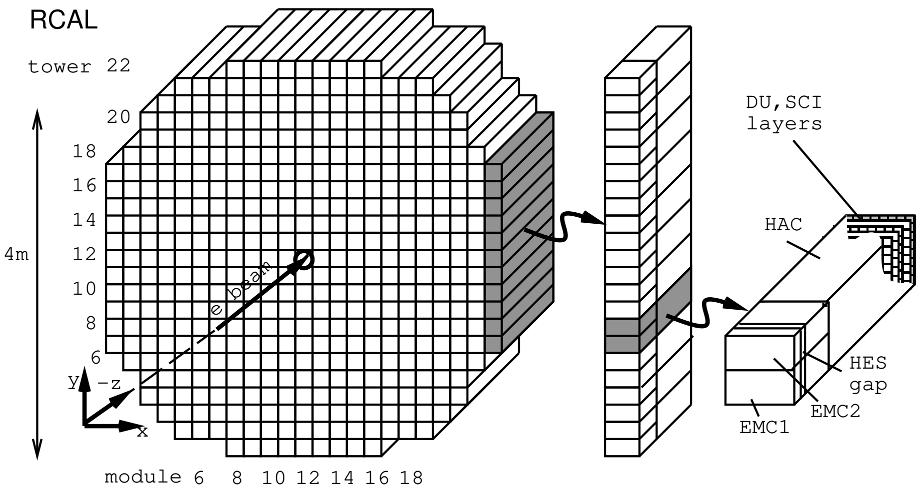

Figure 2.4: The RCAL

In the RCAL there is 1 HAC tower behind the EMC tower, with cells measuring 20×20cm. In the FCAL and BCAL there are 2 HAC towers, each with a depth of 4-6 λ.

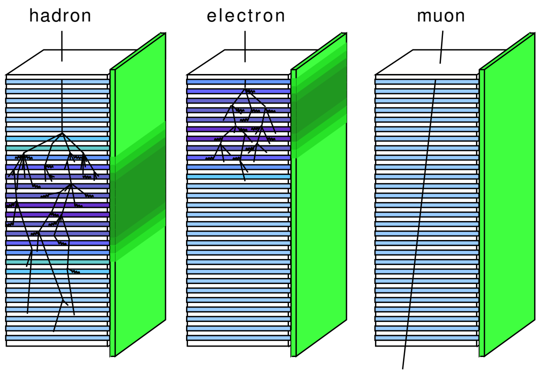

Figure 2.5: Typical particle shower profiles

The energy deposition profiles of hadrons, electrons and muons in the calorimter differ. This makes it possible to discern what type of particle has been detected. Typical shower profiles are shown in Figure 2.5. Electrons and photons begin to shower immediately upon entering the calorimeter, and are contained in a small volume both longitudinally and laterally. Hadrons typically begin showering later, and produce deeper, wider showers. Muons do not shower at all, losing most of their energy through ionisation, and so the muon energy cannot be measured in the CAL.

2.2.3 Luminosity Monitor

The Bethe-Heitler process $ep \to ep\gamma$ has a high cross section that is well known from theoretical calculations to within 0.5%. The luminosity monitoring system detects the rate of hard bremsstrahlung photons from this process to measure the ep luminosity at HERA. It consists of an electron detector and a photon detector, positioned 34m and 104m respectively from the centre of the detector in the electron beam direction (see Figure 2.6). A magnetic field deflects electrons that have lost some of their energy through bremsstrahlung into the electron detector. Scattered electrons from photoproduction events are also detected in this way. Photons radiated at very small angles to the beam axis are detected in the photon calorimeter. Both the photon and electron detectors consist of lead-scintillator calorimeters. The luminosities collected in the 1996 and 1997 data taking periods were measured with a systematic error of 1.1% [60] and 1.8% [61] respectively.

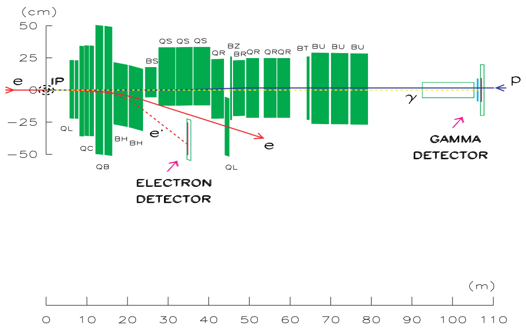

Figure 2.6: The lumi monitor with respect to the beam magnets.

2.2.4 Background Rejection

Non-ep background results from beam gas interactions and cosmic muons. The detector is 25m below ground level, and is surrounded by a 1m thick layer of concrete, which reduces cosmic muon background. An 87cm thick instrumented iron veto wall situated at z = -750cm, absorbs particles in the proton beam halo and rejects beam gas events. The C5 collimator, positioned behind the RCAL at 315 cm from the interaction point, is equipped with scintillator counters on both sides and is used to veto events which have timing inconsistent with an ep interaction. More information on how timing information is used to reject background events is given in chapter 5.

Chapter 3

Event Reconstruction

The scope of this chapter is to cover the chain of events from the moment an *ep* interaction occurs inside the ZEUS detector, to the full reconstruction of the kinematics of that event.

3.1 Data Acquisition and Reconstruction

3.1.1 The ZEUS Trigger

The ZEUS trigger is designed to efficiently select *ep* events from the tumult of detector information, whilst rejecting those from background sources, predominantly beam gas interactions. Proton and electron bunches cross each other in the detector every 96 ns, a rate of 10.4 million crossings per second. However, fewer than 200,000 of these produce a non-zero signal in the detector, and an even smaller fraction contain 'interesting' *ep* events to be written to tape. On average, less than ten events per second are kept, which is a huge reduction over the initial data rate.

A three-level trigger is employed to perform the selection process, as illustrated in Figure 3.1. The chain starts with a fast custom-designed hardware trigger, consisting of electronics mounted on or near to the detector. The result of every bunch crossing must be analysed and a quick decision made whether to discard the event or pass it on to the next level, with a minimal deadtime for the component. With each level the degree of sophistication increases, as more processing time is available and greater use is made of more flexible, but slower, software. A general description of the trigger follows. For details of the specific trigger selection for two- and three-jet events, see chapter 5.

First Level Trigger (FLT)

The information from the detector on each bunch crossing is stored in pipelines, which are 46 bunch crossings deep. Each component which participates in the

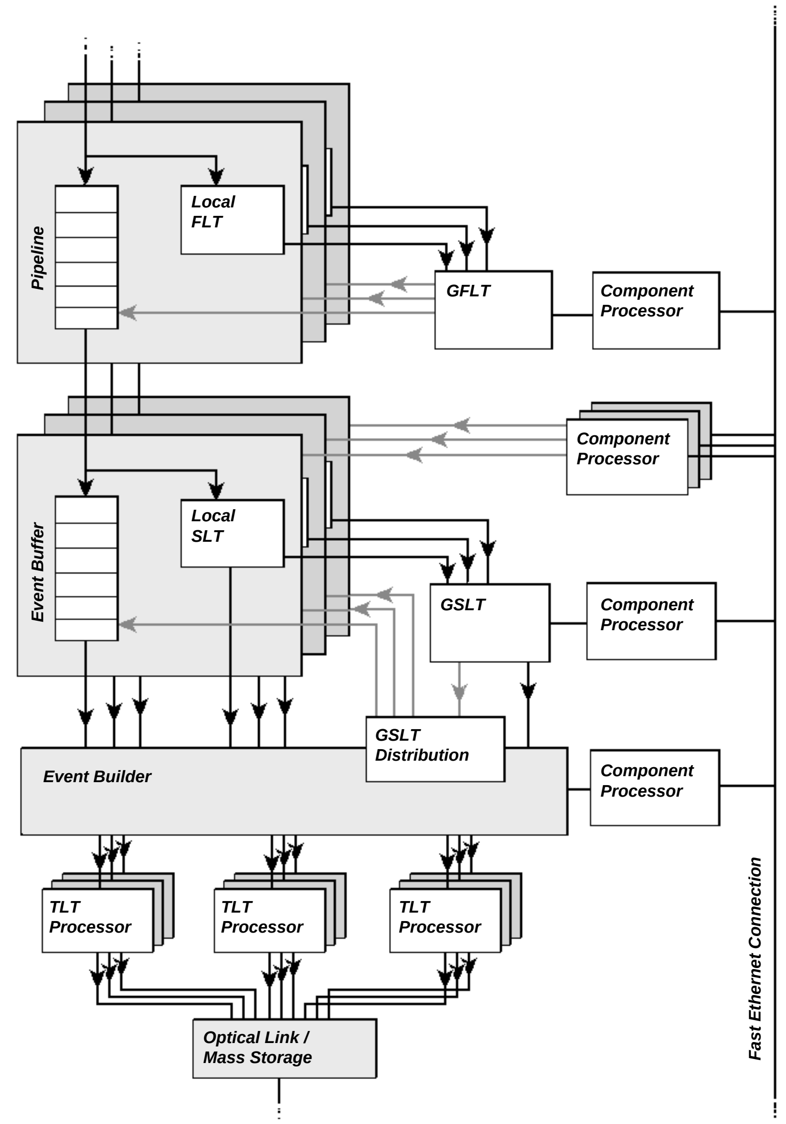

Figure 3.1: Schematic of the three-level ZEUS trigger system

FLT sends a trigger signal to the Global FLT (GFLT) after 2.5 μs, which then has less than 2 μs to make an overall decision. The FLT uses crude quantities such as local energy sums and timing information to make its decision. The most important component FLTs are the Calorimeter FLT, the CTD-FLT, and vetoes such as the Veto-wall and C5 FLTs. The FLT reduces the bunch crossing rate of 10.4 MHz to less than 1 kHz.

Second Level Trigger (SLT)

The SLT has an order of a few milliseconds to make its decision, and again a Global SLT (GSLT) collates information from all the component SLTs. The SLT rejects around 90% of the events passed to it from the FLT, and has a maximum output rate of 100 Hz.

Third Level Trigger (TLT)

Events satisfying the requirements of the SLT are first sent to the Event Builder (EVB) before being passed on to the TLT. The EVB builds the full event and puts it into standard ZEUS format. The TLT runs almost a complete version of the offline reconstruction code, allowing selection algorithms similar to those used in offline analysis to be implemented. Selected events are then written to tape for future analysis.

Events are selected at the TLT according to the interests of the various analysis groups at ZEUS by applying physics filters, taking care not to discard rare events. Interesting events that are not statistically limited are pre-scaled, i.e. a certain fraction are rejected at random, which helps keep the output rate at roughly 3-10 Hz.

3.1.2 The Offline Reconstruction

Events stored on tape are later reconstructed offline with the ZEus PHYsics Reconstruction package, ZEPHYR. It reconstructs physics events in three stages. Firstly, information from the luminosity monitor, tracking chambers, and calorimeters are fully reconstructed. Then ZEPHYR finds clusters in the calorimters and

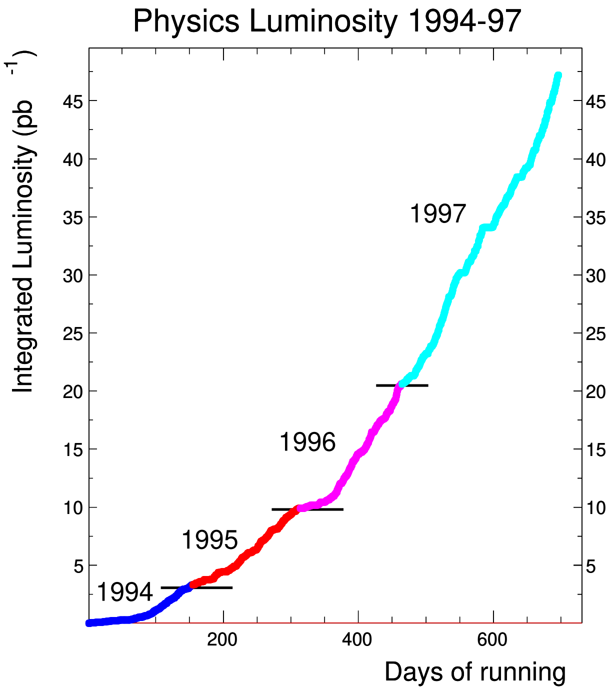

Figure 3.2: Integrate luminosity suitable for physics analysis, 1994-97.

attempts to match them to tracks. Finally, some particle identification is done by combining measurements from detector components such as the CTD and CAL.

This information is then used to apply very specific physics filters to the data, almost like a fourth level trigger. Information concerning the *type* of physics event is added to the event record, in the form of trigger bits, which is then written out to disk in a reduced format called the mini Data Summary Tape (DST).

A further selection vetoes data taking runs where one or more of the essential detector components were not running optimally. Figure 3.2 shows the integrated luminosity after this selection, including the data analysed in this thesis from the 1996 to 1997 (96/97) running period.

3.1.3 Reconstruction of Monte Carlo Events

On the right hand side of Figure 3.3 the ZEUS data acquisition chain (DAQ) is shown, which has just been discussed. In order to compare the collected data with theoretical predictions, Monte Carlo events inspired by various physics models need to be treated in an analagous fashion. These events can then be used to correct the raw data for detector effects, and to give an understanding of systematic errors in the measurements.

The ZEUS Monte Carlo software chain, shown on the left in Figure 3.3, is designed to simulate the real data taken by ZEUS. There are four programs in the chain, beginning with the event generator. A number of different generators are available, all producing a list of particles and their four-momenta, and they are collected into the AMADEUS package. The MOZART package then simulates the detector response for each event, which is then fed into the trigger simulator, CZAR. The output from CZAR is processed by exactly the same reconstruction package used in the DAQ chain, ZEPHYR.

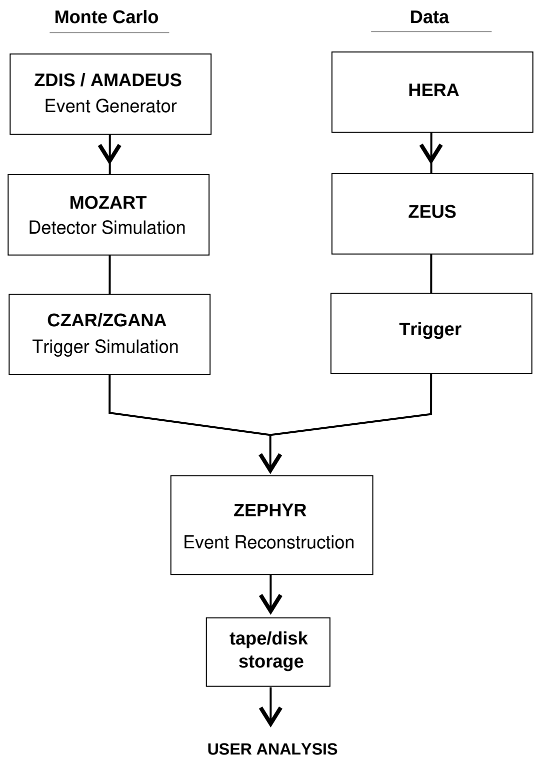

Figure 3.3: Schematic of the Monte Carlo software chain and the ZEUS DAQ.

3.2 Reconstruction of the Hadronic Final State

The reconstruction in ZEUS of energy deposited by hadrons in the final state has in the past relied only on calorimeter information [62]. However there are circumstances, such as for low momentum charged particles, when tracking information is more reliable. In this section details of the tracking and calorimeter reconstruction are given, and an algorithm for combining them to best effect is discussed.

The calorimeter response to real data differs to its simulated response, which gives rise to an energy scale uncertainty on measured cross sections. An energy correction routine has been developed [63] to reduce this uncertainty and to compensate for energy losses due to dead material in front of the CAL. The philosophy behind this correction procedure, which has been used in the analyses presented in this thesis, is explained, and plots demonstrating its efficacy are included.

3.2.1 The Tracking Reconstruction

Pattern recognition software runs over all the hits found in the CTD. Working from the outside in, it joins up hits in each superlayer to form tracks. When the pattern recognition is finished, all the tracks found are fitted to a five parameter helix, from the inside-out. The position of the primary vertex is then determined, if possible, and the tracks that are consistent with it are refitted using this vertex.

3.2.2 The Calorimeter Reconstruction

The calorimeter reconstruction package [64] unpacks the energy for every cell with an energy, E, above a noise-related threshold and the timing information from the photo-multiplier tubes (PMTs) located on either side of each cell. The absolute calibration scale is obtained from regular test runs, which monitor the uranium noise signal.

A number of steps are taken to suppress the effects of noise and various sources of energy loss in the calorimeter, which are difficult to simulate in MC. Firstly, particular cells are removed from the calorimeter data, and ignored, as follows. If the fractional difference between left and right PMTs on a cell, I_{cell}, is very large it is likely be the result of a spark in the electronics. To minimise this effect, cells with $|I_{cell}| > 0.90$ are removed. Also, isolated cells, as defined by the condensates [64] algorithm, are removed when they have relatively low energy: $E_{emc} < 100$ MeV, $E_{hac} < 150$ MeV or when $E < 700$ MeV and $|I_{cell}| > 0.70$.

Next, the energy in the remaining cells is scaled by a factor of 1.000, 1.050 or 1.025 depending on whether they are in the F, B or RCAL. The purpose of these factors is to compensate for the difference between the energy response in the real and simulated detector, and so are applied only to real data. The observed difference is partly due to the absolute energy scale in the data, and partly to inadequacies in the MC simulation of showers. The values of the scaling factors used are from NC-DIS studies [65].

In ideal test conditions the calorimeter energy resolution was measured to be $\sigma/E = 18\%/\sqrt{E}$ for electromagnetic and $\sigma/E = 35\%/\sqrt{E}$ for hadronic particles, where E is in GeV. However, particles produced in ep interactions may have to traverse several radiation lengths of dead material before they reach the surface of the CAL. The energy losses associated with this are very difficult to simulate accurately in the detector. Additionally there are energy losses in the transition regions between the F, B and RCAL which are not well simulated. Both of these effects worsen the effective calorimeter energy resolution to $\sigma/E \approx 25\%/\sqrt{E}$ for electromagnetic and $\sigma/E \approx 40\%/\sqrt{E}$ for hadronic particles.

After all these corrections are applied, the uncertainty in the absolute energy scale is deemed to be 1-3% for the scattered electron and $\sim 5\%$ for hadrons [66].

3.2.3 The Hadronic Energy Flow Algorithm

The aim of the Hadronic Energy Flow Algorithm [67] is to use tracking information, wherever possible, to improve the energy resolution of hadrons in the final state, normally determined by calorimeter information only. There are essentially three steps: finding islands of energy in the calorimeter, matching of these islands to tracks, and finally, making a decision on whether to keep track or CAL information.

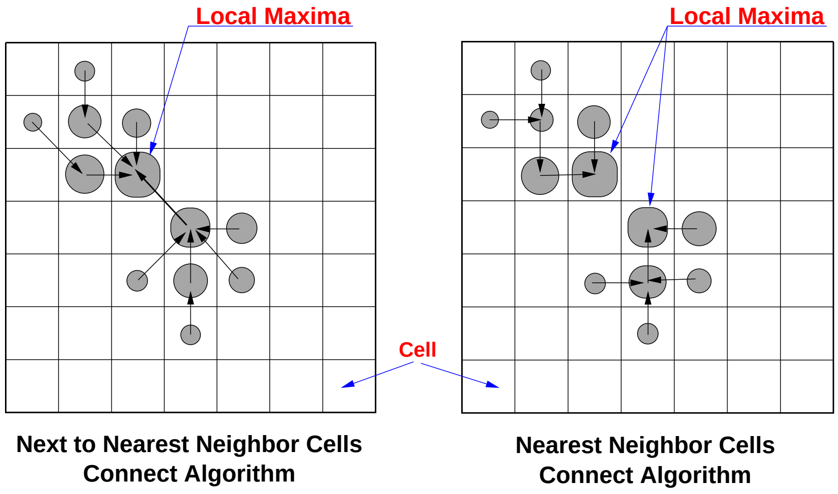

Figure 3.4: Schematic representation of the two cell island clustering modes

The calorimeter cells are first sorted into islands by combining cells with their highest energy neighbours. This is an iterative process, done in one of two ways, as shown in Figure 3.4. Islands in all layers of the calorimeter are then clustered into cone islands [68] using a probability function depending on the angular separation of the cell islands. In the matching step, only vertex fitted tracks that have traversed at least three superlayers in the tracking detectors are considered, and they are required to have a minimum transverse momentum $P_T > 0.1$ GeV. Each track is extrapolated to the surface of the calorimeter, and is deemed to match an island if the distance of closest approach to it is less than 20 cm or within the radius of the island.

After matching, there are three types of objects as illustrated in Figure 3.5. There are charged tracks with no matched islands, attributed to low energy pions, and there are trackless islands assumed to be from neutral particles. Only in the third scenario, where one or more tracks are matched to an island is there a choice between using CAL or tracking information.

The decision making process is complex and described in more detail elsewhere [67]. Basically, there are two requirements that must be met in order to replace CAL with tracking information. Firstly, the island energy must be due entirely to the associated track (or tracks), and secondly, the energy resolution of the track must be better than that of the island. The final set of **energy flow objects** are called ZUFOs (Zeus Unidentified Flow Objects), and are characterized by their energy and momenta.

There are several reasons for using ZUFOs to reconstruct the hadronic final state rather than using CAL cells alone, other than the improvement in energy resolution. The measured P_{T} of a track is less affected by dead material energy losses than cell energy measurements. Also low energy charged particles that have not reached the calorimeter are included in the total hadronic energy sum, that would otherwise be missed. Low energy particles that do reach the calorimeter may be deposited away from the main direction of the particle shower they belong to. The algorithm should account for these and associate their energy with the correct particle shower.

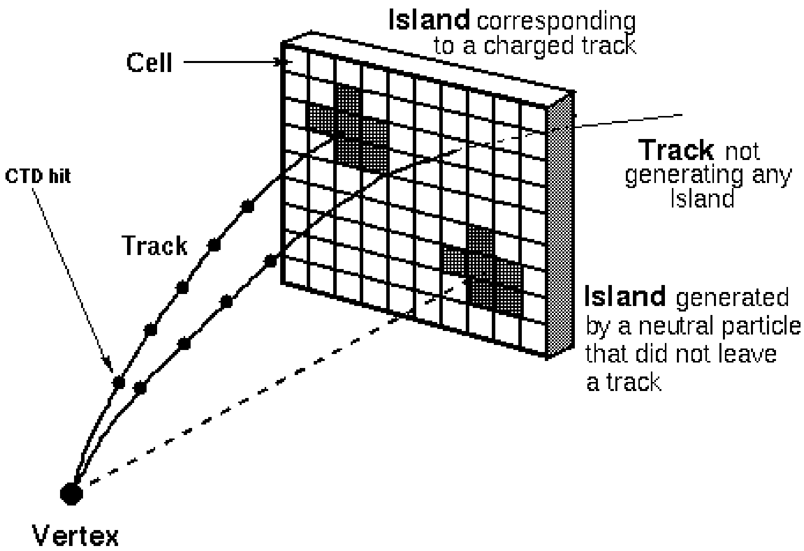

Figure 3.5: Combining tracking and calorimeter information.

3.2.4 Hadronic Energy Corrections

Using ZUFOs, the fraction of *track*-measured transverse energy flow in two-jet photoproduction events peaks at $\sim 20\%$ in the FCAL and $\sim 35\%$ in the BCAL.

This fraction drops steadily with transverse energy, and is negligible at $E_T >$ 15 GeV. The remaining ZUFOs rely on CAL information alone, and so are subject to dead material energy losses. A correction routine designed to compensate for these losses is now discussed.

Method

The method exploits energy and momentum conservation in high Q^2 NC-DIS events as follows. The transverse momentum of a well measured scattered positron is balanced by that of a collimated shower of hadronic particles. Correction factors are obtained that minimise the difference between the hadronic final state and positron four-momenta in a sample of NC-DIS events. The same correction factors can in theory be applied to the 'calorimeter' ZUFOs in other events, such as two-jet photoproduction.

The transverse momenta of the positron, $P_{\mathrm{T}}^{\mathrm{elec}}$, and of the hadrons, $P_{\mathrm{T}}^{\mathrm{had}}$, are obtained from events where most of the hadronic energy flow is in the forward direction. A subsample of high y NC-DIS events, more sensitive to hadronic energy deposited in the backward direction, was used to reconstruct y from the scattered positron, y^{elec}, and the hadrons in the final state, y^{had}.

The energy loss dependence is parametrised as:

$$f_i(E) = 1 + A_i \cdot \exp(-B_i \cdot E), \tag{3.1}$$

for a cell island with energy, E. The correction factors A_i and B_i were determined by minimising a function of the form in equation 3.2. Relative differences bigger than 20% are truncated at this value to prevent too strong an influence in the fit of poorly measured events.

$$\sum \min\left(\left(\frac{P_{\mathrm{T}}^{\mathrm{elec}} - P_{\mathrm{T}}^{\mathrm{had}}}{P_{\mathrm{T}}^{\mathrm{elec}}}\right)^2, 0.2^2\right) + \sum \min\left(\left(\frac{y^{\mathrm{elec}} - y^{\mathrm{had}}}{y_{\mathrm{elec}}}\right)^2, 0.2^2\right) \tag{3.2}$$

Independent correction factors were produced for MC and Data in order to reduce their sensitivity to the energy scale. The correction factors are parametrised as a function of the polar angle, θ, and the uncorrected island energy. The resulting functions are shown in Figure 3.6

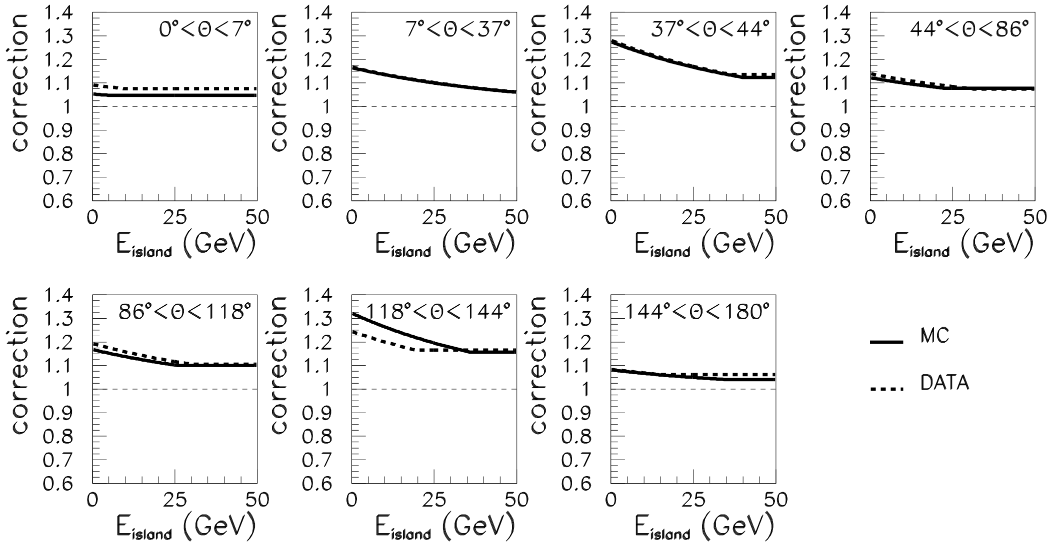

Figure 3.6: Energy correction functions for data and Monte Carlo (taken from [63])

Performance

The performance of the correction factors on photoproduction MC was tested with events generated by HERWIG 5.9. The relative difference in measured and true jet transverse energy, $E_T^{\rm jet}$ and $E_{\rm T,\,hadr}^{\rm jet}$ respectively, is shown as a function of jet pseudorapidity $\eta^{\rm jet}$ in Figure 3.7. The comparison is made for uncorrected islands, uncorrected ZUFOs and corrected ZUFOs, and the $E_T^{\rm jet}$ resolution is indicated by a shaded band. It is clear that both the bias and resolution are improved for ZUFOs jets over islands-jets, and that for jets found using energy corrected ZUFOs the improvement is greatest. The dips in the distributions at $\eta^{\rm jet} \approx -1$ and $\eta^{\rm jet} \approx 1$ (the transition regions between CALs) are also smoothed out by the correction procedure.

A reduction in the energy scale difference in data and MC is demonstrated in Figure 3.8, based on NC-DIS events. The relative difference in transverse momentum measured using the double angle method [69], $P_{\rm T\,DA}$ and the hadron energy $P_{\rm T\,had}$ is shown as a function of the hadronic angle $\gamma_{\rm had}$. This difference is much smaller for corrected ZUFOs than for uncorrected, for both data and MC. Figure 3.8 also shows that the difference between data and MC is smaller for corrected ZUFOs than for uncorrected islands, and is generally less than 2%.

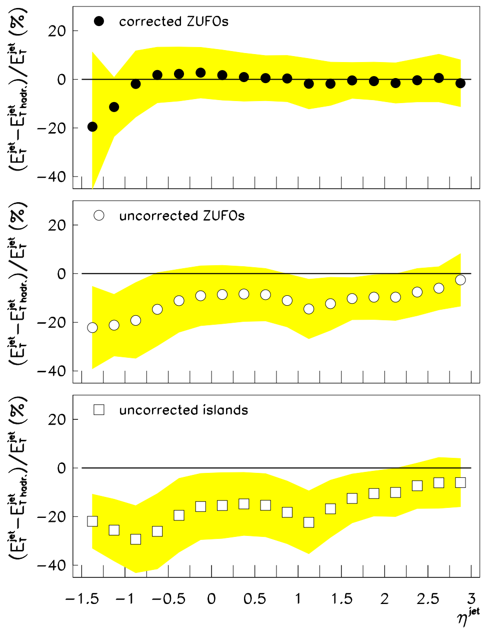

Figure 3.7: Comparison of reconstructed and true E_T^{jet} as a function of η^{jet}, with the resolution in E_T^{jet} shown as a shaded band. (Taken from [63].)

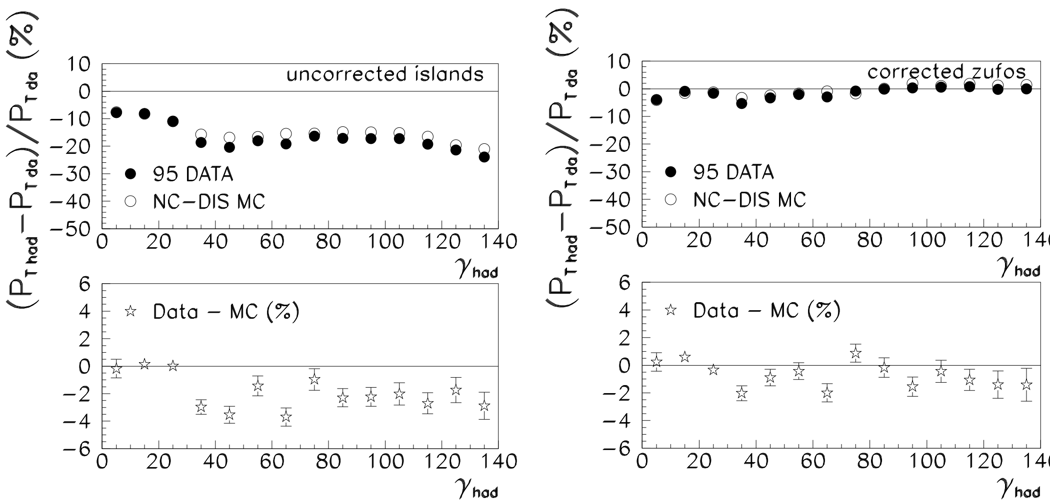

Figure 3.8: Comparison of p_T reconstructed from the hadronic final state and p_T calculated using the double angle method, as a function of hadronic scattering angle. Errors are statistical errors only. (Taken from [63].)

3.2.5 Jet Reconstruction

The outgoing partons from a hard scatter undergo parton showering and hadronisation before they interact with the detector. Therefore, as the partons cannot be detected directly, entities called jets are constructed from the final state hadrons, which approximate the energy and orientation of the original partons from which they developed. Jets are defined entirely by the algorithm used to find them. In MC, the input to the jet algorithm can come from the four-momenta of hadrons (hadron level), the outgoing partons at some stage of their evolution (parton level) or from detector information such as cell energies or ZUFOs (detector level).

A good jet algorithm should be as insensitive as possible to the level at which it is applied, and should define variables that are invariant under a boost in the beam direction. There are two types of algorithm in common use at ZEUS, the EUCELL [71] cone algorithm and the k_T [72] clustering algorithm. The cone algorithm has known problems in its treatment of overlapping jets and infrared safety beyond NLO. The cluster algorithm is not plagued by these difficulties and is therefore the preferred method of jet finding.

The k_T Clustering Algorithm

The algorithm is run in the inclusive mode [73] as follows. Firstly, for each object (which may be a parton, hadron or ZUFO, depending on the level) a distance parameter, d_i, is defined:

$$d_i = E_{T,i}^2 \tag{3.3}$$

and a parameter, d_{ij}, for each pair of objects:

$$d_{ij} = min(E_{T,i}^2, E_{T,j}^2)\frac{R_{ij}^2}{R^2} \tag{3.4}$$

where $R_{ij}^2 = \Delta\eta_{ij}^2 + \Delta\phi_{ij}^2$, and R is a parameter of order 1. The second step is to find the smallest of all the d_i and d_{ij}, and label it d_{min}. If d_{min} is a d_{ij} the objects i and j are merged into a new object, k, such that:

$$E_{T,k} = E_{T,i} + E_{T,j} \tag{3.5}$$

$$\eta_k = [E_{T,i}\,\eta_i + E_{T,j}\,\eta_j]/E_{T,k} \tag{3.6}$$

$$\phi_k = [E_{T,i}\,\phi_i + E_{T,j}\,\phi_j]/E_{T,k}\ , \tag{3.7}$$

which is similar to the Snowmass convention [74]. If d_{min} is a d_i, the object i is considered a single jet, and so is removed from the list of objects. The algorithm loops over these two steps until there are no objects left, only jets.

3.3 Reconstruction of Event Kinematics

In this section all the kinematic variables important to the analyses in this thesis are defined and the method of reconstructing them from the detector information described.

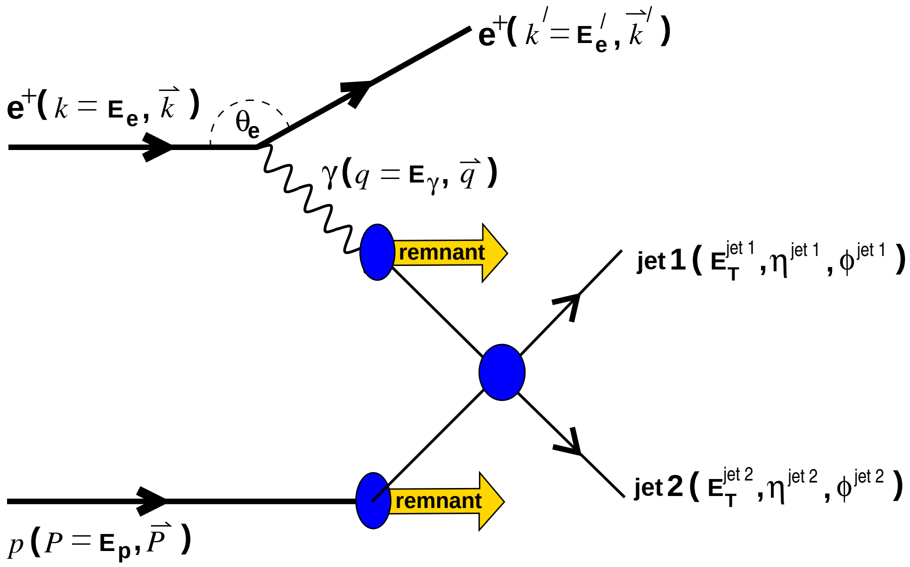

Figure 3.9: Generalised resolved diagram with particle four-momenta labelled in brackets

The y and Q^2 variables are relevant to both two-jet and three-jet studies, and are defined as follows using the particle four momenta as illustrated in Figure 3.9.

$$y = \frac{q \cdot P}{k \cdot P} = 1 - \frac{E'_e}{2E_e}(1 - \cos\theta_e) \tag{3.8}$$

$$Q^2 = -q^2 = -(k - k')^2 = 2E_e E'_e(1 + \cos\theta_e) \tag{3.9}$$

In the photoproduction limit $\theta_e \to 180^\circ$ and equation 3.8 reduces to $y \approx E_\gamma/E_e$. The scattered positron is not usually detected in photoproduction at ZEUS, and so the above equations cannot be used to reconstruct y and Q^2. Instead, the Jacquet-Blondel [75] method is used:

$$y_{jb} = \frac{\sum_i (E_i - P_{z,i})}{2E_e} \tag{3.10}$$

$$Q^2_{jb} = \frac{\left(\sum_i P_{x,i}\right)^2 + \left(\sum P_{y,i}\right)^2}{(1 - y_{jb})} \tag{3.11}$$

where the sum is over all hadronic final state objects, i, be they calorimeter cells or ZUFOs.

3.3.1 Two-jet Kinematics

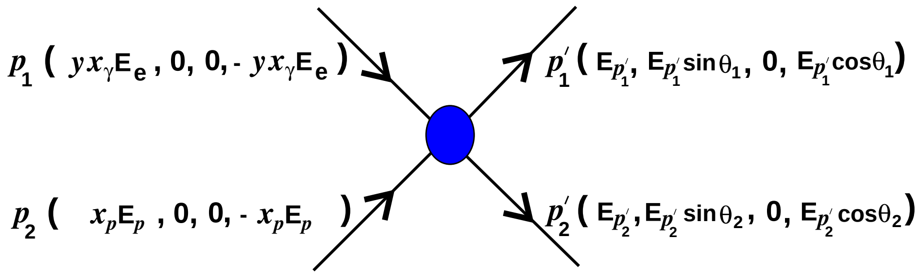

Figure 3.10: A simplified two-body elastic scattering between a parton from the proton and a parton from the photon, with the parton four-momenta indicated in brackets.

For two-to-two body scattering between partons with four-momenta as labelled in Figure 3.10, the fraction of the photon's momentum entering the hard scatter is given by:

$$x_\gamma = \frac{E_T^{p_1'} e^{-\eta^{p_1'}} + E_T^{p_2'} e^{-\eta^{p_2'}}}{2yE_e} \tag{3.12}$$

This variable provides a way of distinguishing between direct events ($x_\gamma = 1$) and resolved events ($x_\gamma < 1$) at LO. However, there are problems with defining x_γ beyond LO [76], and it is not possible to measure p_1' and p_2' directly. An analogous variable, x_γ^{obs} [76], is defined as the fraction of the photon's momentum that contributes to the production of the two highest-E_{T} jets. It can be reconstructed at the parton, hadron and detector levels, and is unambiguously defined to all orders in pQCD as:

$$x_\gamma^{\rm obs} = \frac{E_{\rm T}^{\rm jet\,1} e^{-\eta^{\rm jet\,1}} + E_{\rm T}^{\rm jet\,2} e^{-\eta^{\rm jet\,2}}}{2yE_{\rm e}} \tag{3.13}$$

Only two variables are needed to specify the two-body rest frame, the centre-of-mass scattering angle, θ^*, and the two-jet mass, M_{jj}. Explicitly, θ^* is the angle between the jet-jet axis and the proton beam direction in the two-jet rest frame, and it can be reconstructed from the pseudorapidity of the two jets:

$$\cos\theta^* = \tanh\left(\frac{\eta^{\rm jet\,1} - \eta^{\rm jet\,2}}{2}\right) \tag{3.14}$$

The two-jet invariant mass is reconstructed from the jets using equation 3.15, which assumes that the jets are massless.

$$M_{\rm 2j} = \sqrt{2E_{\rm T}^{\rm jet\,1} E_{\rm T}^{\rm jet\,2}\left[\cosh(\eta^{\rm jet\,1} - \eta^{\rm jet\,2}) - \cos(\phi^{\rm jet\,1} - \phi^{\rm jet\,2})\right]} \tag{3.15}$$

3.3.2 Three-jet Kinematics

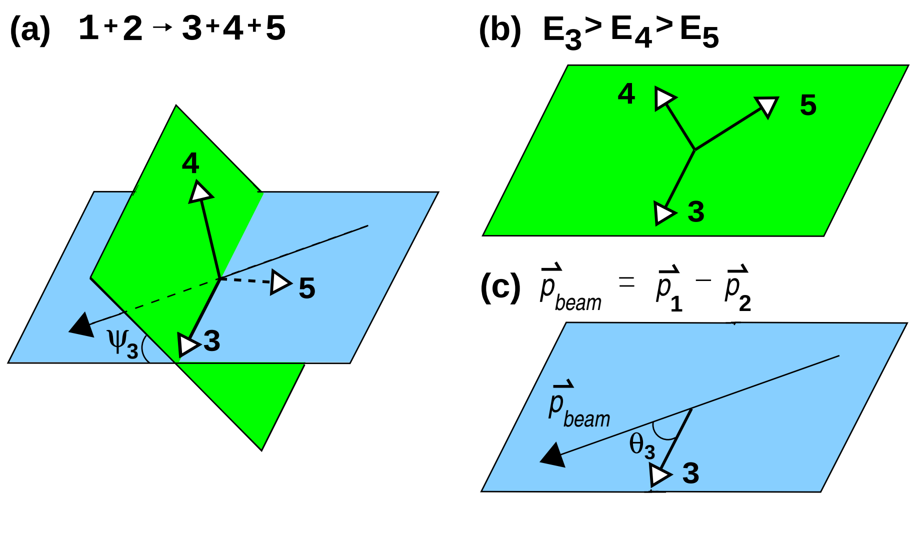

Figure 3.11: Diagram defining the angles used to describe the three-jet system in the three-jet rest-frame

The three-jet rest frame is illustrated in Figure 3.11, where 1 and 2 refer to the incoming partons and the outgoing jets are labelled 3, 4 and 5, by convention. The three jets with the highest transverse energy in the lab frame are first boosted to the three-jet rest frame, where they lie in a plane as shown in Figure 3.11(b). The jets are then reordered according to their energy such that $E_3 > E_4 > E_5$.

The rest-frame kinematics are described by the three-jet mass,

$$\begin{aligned} {M_{3\mathrm{j}}}^2 = & \, 2E_{\mathrm{T}}^{\mathrm{jet\,1}} E_{\mathrm{T}}^{\mathrm{jet\,2}} \left[\cosh(\eta^{\mathrm{jet\,1}} - \eta^{\mathrm{jet\,2}}) - \cos(\phi^{\mathrm{jet\,1}} - \phi^{\mathrm{jet\,2}})\right] \\ & + 2E_{\mathrm{T}}^{\mathrm{jet\,1}} E_{\mathrm{T}}^{\mathrm{jet\,3}} \left[\cosh(\eta^{\mathrm{jet\,1}} - \eta^{\mathrm{jet\,3}}) - \cos(\phi^{\mathrm{jet\,1}} - \phi^{\mathrm{jet\,3}})\right] \\ & + 2E_{\mathrm{T}}^{\mathrm{jet\,2}} E_{\mathrm{T}}^{\mathrm{jet\,3}} \left[\cosh(\eta^{\mathrm{jet\,2}} - \eta^{\mathrm{jet\,3}}) - \cos(\phi^{\mathrm{jet\,2}} - \phi^{\mathrm{jet\,3}})\right] \end{aligned} \tag{3.16}$$

and the angle between the leading jet and the proton beam direction ($\vec{p}_{\mathrm{beam}}$) as defined in Figure 3.11(c), and reconstructed using:

$$\cos\theta_3 \equiv \frac{\vec{p}_{\mathrm{beam}} \cdot \vec{p}_3}{|\vec{p}_{\mathrm{beam}}||\vec{p}_3|} \tag{3.17}$$

where $\vec{p_3}$ is the three momentum of the leading jet in the three-jet rest frame. These variables reduce to the two-jet system variables, as $E_5 \to 0$ ($\cos\theta_3 \to \cos\theta^*$, $M_{3\mathrm{j}} \to M_{2\mathrm{j}}$).

Jets in a two-jet rest frame are indistinguishable from each other in terms of orientation and energy. In the three-jet rest frame, however, this is not so, and to fully describe the three jets an additional three variables are required, ψ_3, X_3 and X_4.

The angle, ψ_3, between the plane containing the three jets (Figure 3.11(b)), and that containing the beam and the leading jet (Figure 3.11(c)) is calculated using the three-momenta of the rest-frame jets

$$\cos\psi_3 \equiv \frac{(\vec{p}_3 \times \vec{p}_{\mathrm{beam}}) \cdot (\vec{p}_4 \times \vec{p}_5)}{|\vec{p}_3 \times \vec{p}_{\mathrm{beam}}||\vec{p}_4 \times \vec{p}_5|} \tag{3.18}$$

The fraction of available energy carried by each jet is expressed by the Dalitz variables, X_3, X_4 and X_5, which are normalized such that $X_3 + X_4 + X_5 = 2$. Their values are restricted by momentum conservation to the ranges shown in brackets,

$$X_3 \equiv \frac{2E_3}{E_3 + E_4 + E_5} = \frac{2E_3}{M_{3\mathrm{j}}} \qquad (2/3 \leq X_3 \leq 1) \tag{3.19}$$

$$X_4 \equiv \frac{2E_4}{E_3 + E_4 + E_5} = \frac{2E_4}{M_{3\mathrm{j}}} \qquad (1/2 \leq X_4 \leq 1) \tag{3.20}$$

$$X_5 \equiv \frac{2E_5}{E_3 + E_4 + E_5} = \frac{2E_5}{M_{3\mathrm{j}}} \qquad (0 \leq X_5 \leq 2/3) \tag{3.21}$$

and only two of the above are needed to fully describe the three-jet system.

The fraction of the photon's momentum that goes into the production of the three highest-E_T jets is given by:

$$x_\gamma^{\mathrm{obs}} = \frac{E_{\mathrm{T}}^{\mathrm{jet\,1}} e^{-\eta^{\mathrm{jet\,1}}} + \ E_{\mathrm{T}}^{\mathrm{jet\,2}} e^{-\eta^{\mathrm{jet\,2}}} + \ E_{\mathrm{T}}^{\mathrm{jet\,3}} e^{-\eta^{\mathrm{jet\,3}}}}{2yE_{\mathrm{e}}} \tag{3.22}$$

Chapter 4

Definition of measured cross sections

4.1 Two-jet Measurements

The two-jet cross section is measured in a region of phase space that has been chosen such that theoretical uncertainties are expected to be relatively small, and the effects of photon structure are evident. The hard scale required to make pQCD predictions applicable is provided by the transverse energy of the jets. It has been shown that using asymmetric jet-E_{T} cuts make the calculations more stable, and that for $E_{\mathrm{T}} > 11$ GeV the influence of soft physics, such as MPIs, is greatly reduced. Therefore the energy of the jets is chosen such that $E_{\mathrm{T}}^{\mathrm{jet\,1}}> 14$ GeV and $E_{T}^{jet\,1} > 11$ GeV. The measurement is restricted to the well measured regions of η and y: $-1 < \eta < 2$ and $0.2 < y < 0.85$, and is defined in the photoproduction regime: $Q^2 < 1$ GeV.

The cross section differential in $x_{\gamma}^{\mathrm{obs}}$ is measured in four slices of $E_{\mathrm{T}}^{\mathrm{jet\,1}}$ in the range $14 <E_{\mathrm{T}}^{\mathrm{jet\,1}}< 90$ GeV. The $x_{\gamma}^{\mathrm{obs}}$ variable is interesting because it is directly sensitive to the photon structure. The distribution of two-jet events in $|\cos\theta^{*}|$ is also studied to give information on two-jet dynamics.

4.2 Three-jet Measurement

The three-jet cross section, like the two-jet, is defined in the range $Q^2 < 1$ GeV and $0.2 < y < 0.85$. Requiring three jets with $E_{T}^{\mathrm{jet\,1,2}} > 6$ GeV, $E_{T}^{\mathrm{jet\,3}} > 5$ GeV and an invariant mass $M_{3\mathrm{j}} > 50$ GeV effectively removes non-perturabive effects from the data, which are not modelled by pQCD calculations. The cross section is restricted to the η region which is well modelled for three-jet events $|\eta| < 2.4$. Also, the cross section is restricted by $|\cos\theta_3| < 0.8$ to reduce the bias introduced to this variable by the E_{T} and $M_{3\mathrm{j}}$ cuts. The fraction of available energy taken by the leading jet is limited to $X_3 < 0.95$, to increase the average fraction taken by the third jet.

The cross section is measured with respect to $M_{3\mathrm{j}}$, $\cos\theta_3$, ψ_3, X_3 and X_4 as in the previous three-jet analysis, but with the upper y range increased from 0.8 to 0.85. In addition, the cross section differential in three-jet x_γ^{obs} is presented for the first time. The angular distributions, $\cos\theta_3$ and ψ_3, are presented in bins of x_γ^{obs} so that the influence of photon structure on three-jet dynamics can be examined.

Chapter 5

Selection of Jet Photoproduction Events

The data collected with the ZEUS detector in the 96/97 running period corresponds to an integrated luminosity of 38.4 pb^{-1}. The selection of jet photoproduction events is done in two stages: a quick online selection using the ZEUS trigger, and a more refined offline selection. The cuts applied at both stages are designed to minimise the level of background contamination, whilst maximising the number of genuine jet photoproduction events in the kinematic regions as defined in chapter 4.

5.1 Online Event Selection

The function of the three-level trigger employed by ZEUS has already been described in general terms in section 3.1.1. The particular trigger chain used in both the three-jet and two-jet analyses is now described explicitly.

5.1.1 First Level Trigger

Jets deposit a large amount of energy in the calorimeter, and therefore at least one of the following energy sums is required:

- $E^{CAL} \gtrsim 15$ GeV **or** $E^{CAL}_{EMC} \gtrsim 10$ GeV **or** $E^{BCAL}_{EMC} \gtrsim 3.4$ GeV **or** $E^{RCAL}_{EMC} \gtrsim 2$ GeV **or** $E^{CAL}_{\mathrm{T}} \gtrsim 11.6$ GeV, where the calorimeter energies are calculated excluding the FCAL cells nearest the beampipe.

and

- At least one track is found with $-50 < z_{vtx} < 80$ cm in the first superlayer of the CTD. This requirement rejects non-physics background from beam gas interactions and cosmics.

  and

- The event is not vetoed by the C5, SRTD or veto wall detectors. These are upstream of the proton beam and are therefore sensitive to proton beam gas interactions.

5.1.2 Second Level Trigger

SLT quantities such as E_{T} and p_z are calculated using the nominal IP vertex, (x,y,z)=(0,0,0). The SLT selection requires:

- A vertex is found with $|z_{vtx}| < 60$ cm.

  and

- There is at least one track associated with the vertex.

  and

- $\Sigma_i(E - p_z) > 8.0$ GeV, where the sum runs over all calorimeter cells i and (p_x, p_y, p_z) is the momentum vector assigned to each cell of energy E. The cell angles are calculated from the geometric centre of the cell and the vertex position of the event. Neglecting detector resolution effects, fully contained neutral current events have $\Sigma_i(E - p_z)$ equal to $2E_e$, i.e. twice the positron beam energy. Events from beam-gas interactions, which do not have energy deposits in the RCAL, will have $\Sigma_i(E - p_z)$ close to zero. Photoproduction events, which typically have the scattered electron remaining in the rear beam pipe, also give $\Sigma_i(E - p_z)$ values significantly lower than $2E_e$. Therefore this cut reduces beam-gas contamination.

  and

- If $\Sigma_i(E - p_z) < 12$ GeV then $\Sigma_i(p_z/E) < 0.95$

  The timing of ZEUS components is calibrated in such a way that interactions occuring at the nominal interaction point are detected at $t = 0$. Events are detected in the FCAL, BCAL and RCAL at times t_{FCAL}, t_{BCAL} and t_{RCAL} respectively. Events which did not occur near the IP are rejected when:

- $t^{lower}_{BCAL} - t^{upper}_{BCAL} > 10$ ns. The times t^{lower}_{BCAL} and t^{upper}_{BCAL} are the that of the lower and upper halves of the BCAL. This rejects cosmic muons entering the detector from above.

- $t_{FCAL} - t_{RCAL} > 8$ ns. Rejects upstream proton beam gas interactions.

- $|t_{RCAL}| > 8$ ns, or $t_{FCAL} > 8$ ns.

5.1.3 Third Level Trigger

At the TLT the final online selection is made, making use of various jet algorithms and the full track record. The TLT branch used by this analysis (HPP14) triggers on low-E_{T} two-jet events and corresponds directly to DST bit 77. Events passed by this TLT branch have:

- At least two jets with $E_{\mathrm{T}} > 4$ GeV and $\eta < 2.5$

- $E - p_z < 75$ GeV.

- $p_z/E < 1.0$

- Fewer than six tracks crossing three CTD superlayers which come no closer than 75 cm to the interaction vertex.

Events are vetoed based on calorimeter timing information when:

- 7 ns $< t_{FCAL} - t_{RCAL} <$ 15 ns <u>**and**</u> 7 ns $< t_{RCAL} - t_{RCAL} <$ 15 ns, where the time is recorded in the beam pipe regions.

- $|t_{RCAL}| > 6$ ns **or** $|t_{FCAL}| > 8$ ns **or** $|t_{FCAL} - t_{RCAL}| > 8$ ns **or** $|t_{\rm cal}^{\rm total}| > 8$ ns.

The efficiency of this trigger chain is estimated using HERWIG MC events and is shown in Figure 5.1 as a function of the z vertex of the event. The number

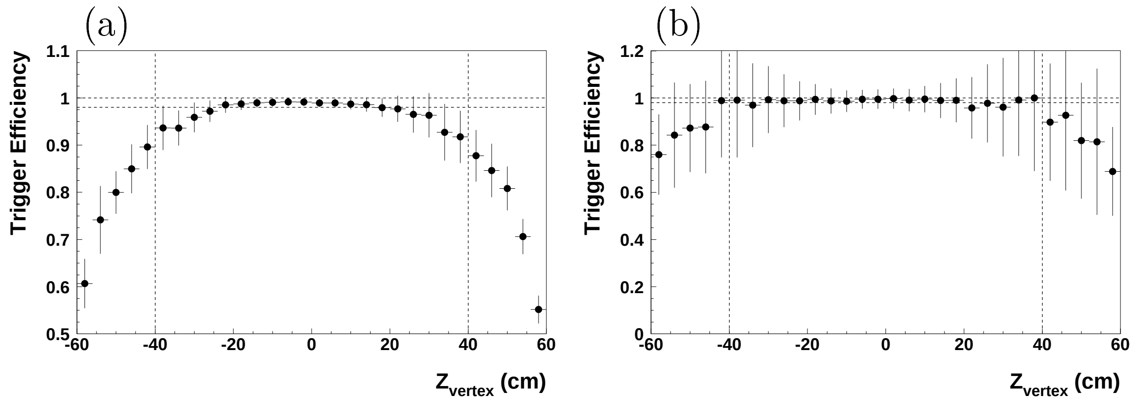

Figure 5.1: Trigger efficiency as a function of the vertex position in the z-direction for (a) two-jet events and (b) three-jet events.

of events at hadron level that satisfy the definition of the two- and three-jet cross sections are compared with those that also pass the trigger requirements at the detector level. The efficiency is better than 98% for the majority of events and decreases with distance from the nominal interaction point.

5.2 Offline Event Selection

The cuts applied by the offline event selection fall into two categories: **kinematic cuts** which restrict the phase space over which the measurement is made, and **cleaning cuts** which reduce the fraction of events in the sample originating from background processes.

The kinematic cuts may also reduce background contamination, but are mainly influenced by how well the detector can measure the desired events in the phase space available. For example the accepted η range is restricted to the region where the energy flows have been studied and understood. For two-jet events with $E_{\mathrm{T}}^{\mathrm{jet\,1,2}} > 14, 11$ GeV this range is $-1 < \eta < 2$ [9], and for three-jet events it is $|\eta| < 2.4$ [77].

The cleaning cuts used in two- and three-jet selection are very similar. Whilst they reduce the number of background events in the sample, they also throw away 'good' events. In order to correctly measure the cross section for a given kinematic region, these events must be effectively added back in later, using MC to estimate the number of events lost. The methods used to correct for this and other detector effects are discussed in chapter 7.

The particular cuts used to select two- and three-jet photoproduction events from the data sample are now discussed.

5.2.1 Two-jet Events

(A) General selection

Firstly, the hadronic energy flow algorithm described in section 3.2.3 is applied to those events which have passed the online selection. The resulting ZUFOs are then subjected to the correction functions obtained using the method in section 4.2.4, before the k_T clustering algorithm is applied. Events are selected which contain at least two jets in the pseudorapidity range $-1 < \eta^{\mathrm{jet}} < 2$, and with transverse energy $E_{\mathrm{T}}^{\mathrm{jet\,1}} > 14$ GeV, $E_{\mathrm{T}}^{\mathrm{jet\,2}} > 11$ GeV.

In Figure 5.2 the description of the data by two types of MC, HERWIG and PYTHIA, is shown. The input vertex distribution to the MC models is derived from the data. Figures 5.2(a) and (b) show the estimated contamination to the data from NC-DIS background. The DIS fraction is estimated by HERWIG in the region $1 < Q^2 < 40$ GeV^2, which is a subset of the full HERWIG sample, and by ARIADNE 4.08 [78] in the region $Q^2 > 40$ GeV^2. ARIADNE is not used for the full range because it has a very large uncertainty in the cross-section normalisation at low values of Q^2 [79]. The number of events in the MC samples are normalised to the integrated luminosity represented by the data.

NC-DIS events form a substantial fraction of those measured at high values of y_{jb}, peaking at ~ 1, as a result of an electron being misidentified as a jet. Events with $y_{\mathrm{jb}} > 0.85$ are therefore rejected. Events are also rejected with $y_{\mathrm{jb}} < 0.2$, which is a slightly tighter cut than that already applied online to remove beam gas contamination.

A small amount of DIS contamination comes from CC-DIS events, which characteristicly have a large fraction of missing transverse momentum. They are efficiently removed from the sample by requiring $P_{\mathrm{T}}/\sqrt{E_{\mathrm{T}}} < 1.5\ \sqrt{\mathrm{GeV}}$.

In photoproduction events the electron scatters at very small angles to the beam direction and is always lost down the beam pipe. However, for $\sim$15% of events an electron candidate is found in the detector. MC studies suggest that these electrons are in fact largely misidentified pions, which have decayed into photons. The y_{e} calculated from the energy and scattering angle of this electron candidate is shown in Figure 5.2(b), for events where the candidate energy $>$ 5 GeV. DIS events dominate the distribution at low y_{e}, but form a diminishing fraction of events as y_{e} increases. To reduce NC-DIS contamination events with $y_e < 0.85$ are rejected.

The cuts on y_{jb} and y_{e}, and the geometry of the beam pipe hole through which the scattered beam electron is lost, effectively restrict the virtuality of the exchanged photon to $Q^2 < 1$ GeV^2, with a median Q^2 of 10^{-3} GeV^2.

To reduce background from non-*ep* processes it is required a vertex is found within 40 cm of the nominal interaction point (Figure 5.2(c)) and that more than 10% of all tracks found in an event point to this vertex 5.2(d). The number of vertex fitted tracks in the data is well reproduced by HERWIG MC as shown in Figure 5.2(e) but is not so well described by PYTHIA.

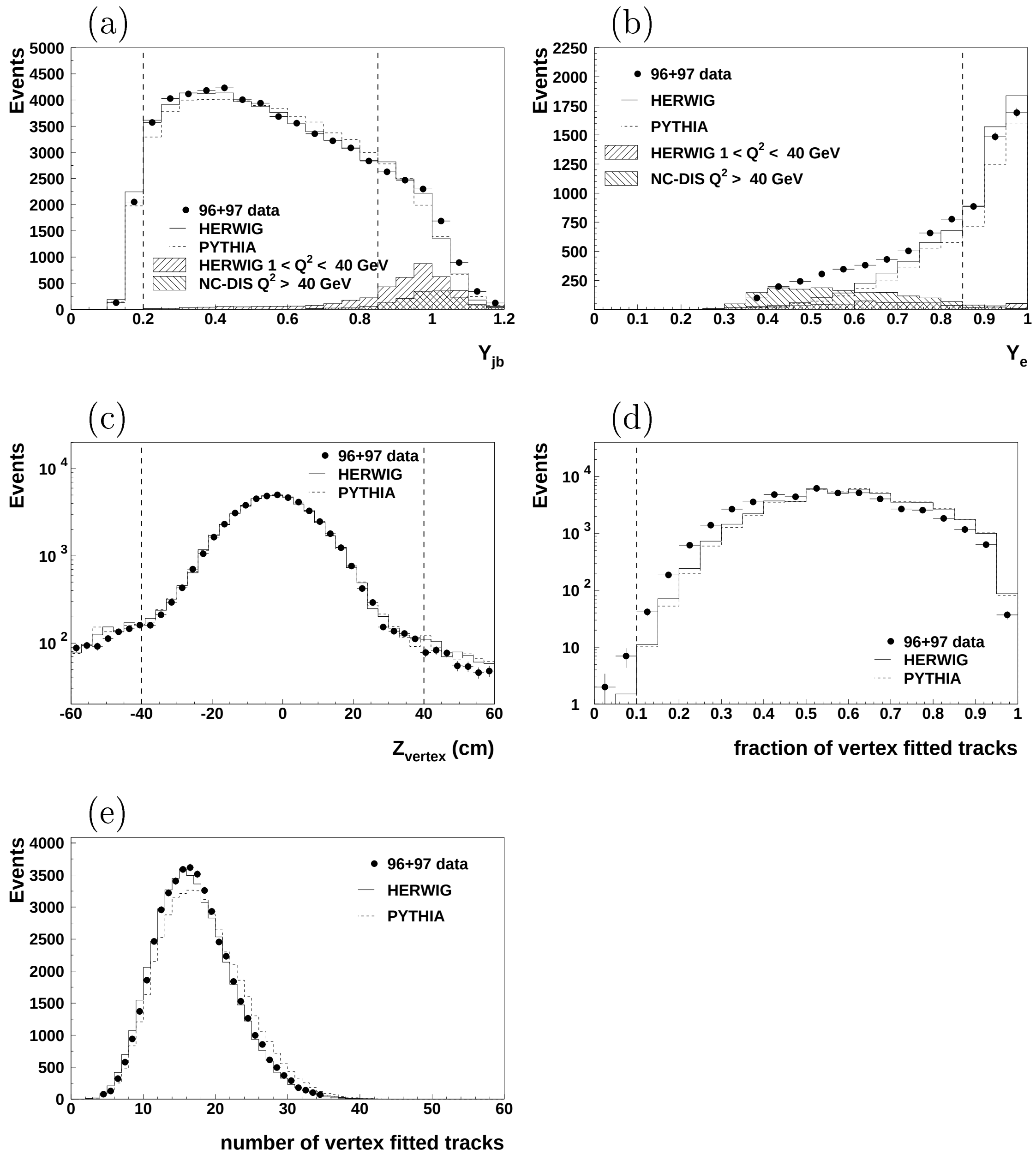

Figure 5.2: Distributions of some of the variables used in the selection of two-jet photoproduction events. For each plot all cuts described in section 5.2.1(A) are applied except those pertaining to the variable shown. The placement of cuts are denoted by dashed lines.

(B) Event Selection for $|\cos\theta^*|$ Distributions

The E_{T} selection cuts described in section 5.2.1(A) bias the $|\cos\theta^*|$ distribution as can be seen in Figure 5.3. The high $|\cos\theta^*|$, low $M_{2\mathrm{j}}$ regions are most heavily affected, indeed some parts of the distribution are completely excluded. The reason is that jets with low transverse energy tend to be produced at angles close to the beam direction, and so these events tend also to have high values of $|\cos\theta^*|$. Also, the presence of the beam pipe means that the acceptance tends to zero as $|\cos\theta^*| \to 1$. The approximate relationship between $E_{\mathrm{T}}^{\mathrm{jet}}$, $M_{2\mathrm{j}}$ and $\cos\theta^*$ is given by equation 5.1 which is derived from equation 3.15 by assuming that the two jets are produced back-to-back in ϕ and have equal $E_{\mathrm{T}}^{\mathrm{jet}}$.

$$M_{12} \approx 2E_{\mathrm{T}}^{\mathrm{jet}} / \sqrt{1 - |\cos\theta^*|^2} \tag{5.1}$$

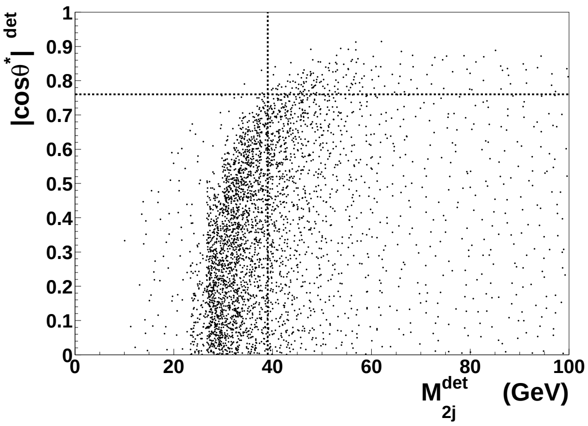

Figure 5.3: The scattering angle $|\cos\theta^*|$ as a function of two-jet invariant mass $M_{2\mathrm{j}}$ for events passing the cuts described in section 5.2.1(A).

Equation 5.1 implies that it may be possible to remove this bias by restricting the measured region of phase space in $|\cos\theta^*|$ and $M_{2\mathrm{j}}$. Values of $|\cos\theta^*| < 0.76$ and $M_{2\mathrm{j}} > 39.0$ GeV are chosen in order to maximise the $|\cos\theta^*|$ range over which the distribution is measured whilst retaining good statistics.

To test the efficacy of these cuts a direct comparison is made between the number of events passing the cuts described in section 5.2.1(A), and those passing identical cuts except with much lower $E_{\mathrm{T}}^{\mathrm{jet}}$ requirements: $E_{\mathrm{T}}^{\mathrm{jet}\,1,2} > 7.0$ GeV. The result is shown as a function of $M_{2\mathrm{j}}$ and $|\cos\theta^*|$ in Figure 5.4(a) and as a ratio in Figure 5.4(b) . The plots show that at low values of $M_{2\mathrm{j}}$ the distribution is strongly dependent on the choice of E_{T} cuts. This bias reduces with increasing $M_{2\mathrm{j}}$ and is virtually non-existent at $M_{2\mathrm{j}} > 39.0$ GeV except in the region $|\cos\theta^*| > 0.76$. The plots prove that equation 5.1 is a reasonable approximation, and that these cuts are sufficient to eliminate any bias in the measurement from the choice of E_{T} cuts.

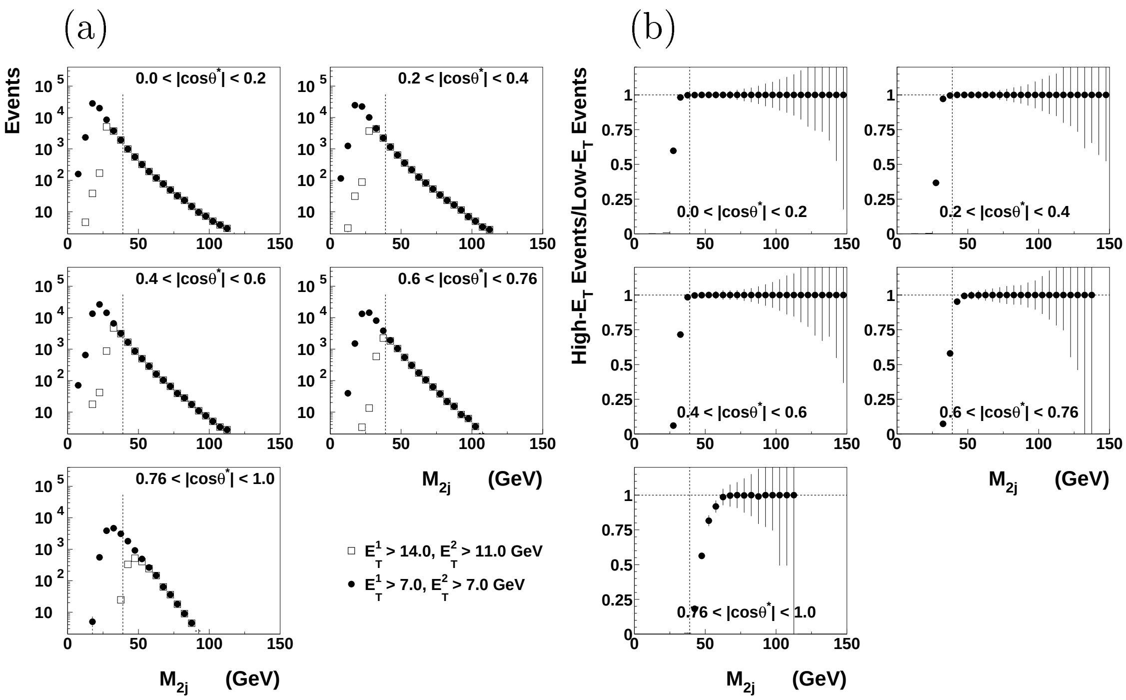

Figure 5.4: (a) Comparison of events passing high-E_{T} two-jet selection cuts ($E_{\mathrm{T}}^{\mathrm{jet}\,1} > 14$ GeV, $E_{\mathrm{T}}^{\mathrm{jet}\,2} > 11$ GeV) to those passing low-E_{T} cuts ($E_{\mathrm{T}}^{\mathrm{jet}\,1,2} > 7.0$ GeV) as a function of $M_{2\mathrm{j}}$ and in slices of $|\cos\theta^*|$. (b) Ratio of high-E_{T} to low-E_{T} events.

It is desirable that the accessible phase space is uniform as a function of $\cos\theta^*$, so that any shape seen in the measured distribution is attributable to the dynamics of the subprocess and not due, in part, to the cuts imposed. The shaded areas in Figure 5.5 show the phase space delimited by the cuts on $\eta^{\mathrm{jet}\,1,2}$ and $|\cos\theta^*|$, which is directly related to $\Delta\eta^{\mathrm{jet}}$:

$$|\cos\theta^*| = \tanh\left(\frac{|\Delta\eta^{\mathrm{jet}}|}{2}\right) \tag{5.2}$$

The phase space is clearly non-uniform, peaking at $\Delta\eta = 0 \equiv \cos\theta^* = 0$. The accessible phase space is therefore restricted to the region darkly shaded in Figure 5.5 by demanding events with $0 < \bar{\eta} < 1$. The distribution of events as a function of $|\cos\theta^*|$ and the average longitudinal boost, $\bar{\eta}$, is shown in Figure 5.6.

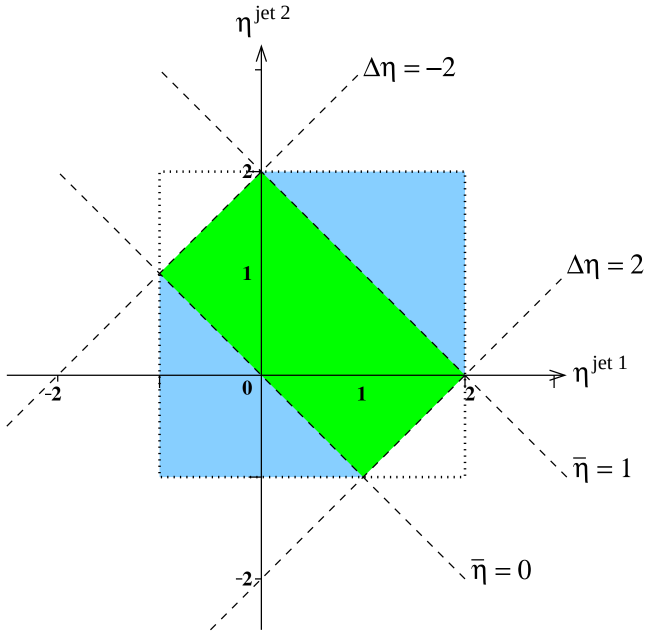

Figure 5.5: Diagram showing the range of accessible phase space in terms of the pseudorapidities of the leading and non-leading jets. The dotted box delimits the range $-1 < \eta^{\text{jet}\,1,2} < 2$. The dashed lines with equations $\Delta\eta = 2$ and $\Delta\eta = -2$ delimit the range imposed by requiring $|\cos\theta^*| < 0.76$.

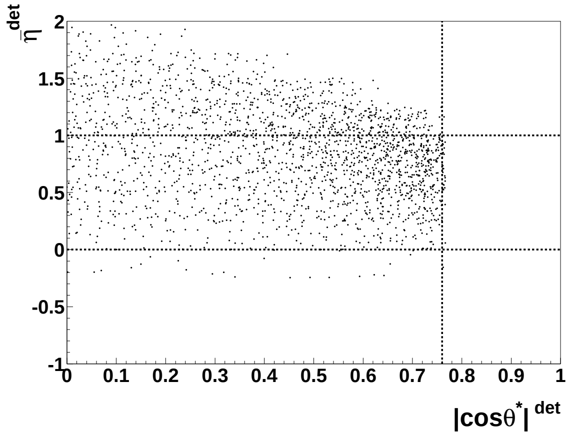

Figure 5.6: Distribution of events in $|\cos\theta^*|$ and $\bar{\eta}$ passing selection cuts in section 5.2.1(A) and with $M_{2\mathrm{j}} > 39.0$ GeV, $|\cos\theta^*| < 0.76$.

After all the cuts in section 5.2.1(A) have been applied to the data 47,824 events remain: 22672 events in the range $14 < E_{\mathrm{T}}^{\text{jet}\,1} < 17$ GeV, 20912 between $17 < E_{\mathrm{T}}^{\text{jet}\,1} < 25$ GeV, 3586 between $25 < E_{\mathrm{T}}^{\text{jet}\,1} < 35$ GeV and 654 between $35 < E_{\mathrm{T}}^{\text{jet}\,1} < 90$ GeV. After the cuts in section 5.2.1(B) are applied, 8645 events remain: 2376 with $x_\gamma^{\text{obs}} < 0.75$ and 6269 with $x_\gamma^{\text{obs}} > 0.75$. A summary of all the cuts used in the offline selection of two-jet photoproduction events is given in table 8.1.

5.2.2 Three-jet Events

The cuts used to select three-jet photoproduction events differ little in philosophy to those applied in two-jet selection, and so require only a little additional explanation.

Events are required to have at least two jets with $E_{\mathrm{T}} > 6$ GeV and a third with $E_{\mathrm{T}} > 5$ GeV, lying in the pseudorapidity region: $|\eta^{\mathrm{jet}}| < 2.4$. As in the two-jet case, enforcing a minimum E_{T} threshold biases the $\cos\theta_3$ and $M_{3\mathrm{j}}$ distributions, shown in Figure 5.7.

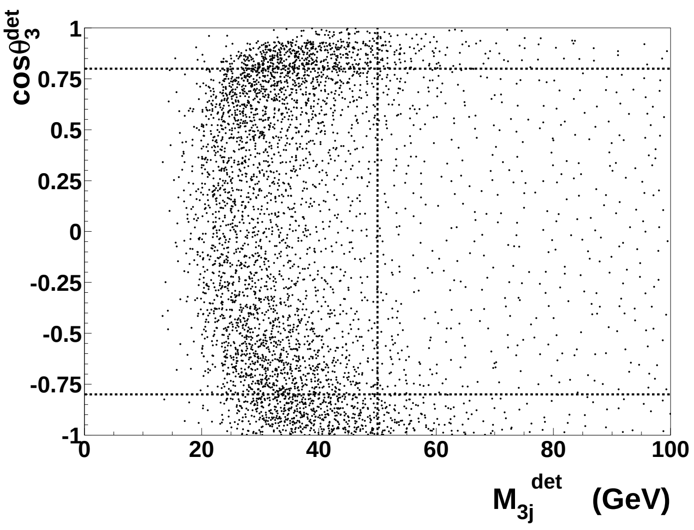

Figure 5.7: The scattering angle $\cos\theta_3$ as a function of three-jet invariant mass, $M_{3\mathrm{j}}$, for events passing all other cuts described in section 5.2.2.

This time, however, it is not so easy to calculate the approximate relationship between $M_{3\mathrm{j}}$, $\cos\theta_3$ and $E_{\mathrm{T}}^{\mathrm{jet}}$. The position of the cuts on $M_{3\mathrm{j}}$ and $\cos\theta_3$ are decided chiefly using the information in Figures 5.7 and 5.8. The bias in the distributions diminishes with increasing $M_{3\mathrm{j}}$, but is never totally removed. Requiring events with $|\cos\theta_3| < 0.8$ and $M_{3\mathrm{j}} > 50$ GeV keeps the bias under 20% whilst retaining good statistics. Figure 5.9 shows that while the normalisation of the measured angular distributions are biased by the choice of E_{T} cuts, the shape is affected little.

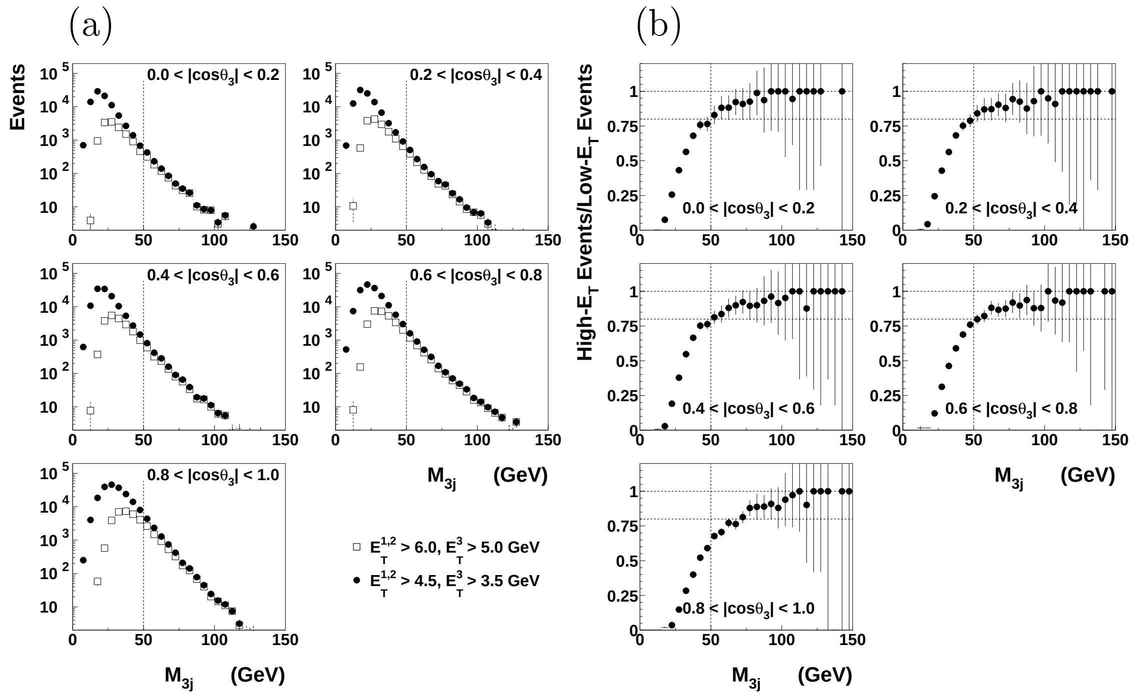

Figure 5.8: (a) Comparison of events passing high-E_{T} three-jet selection cuts ($E_{\mathrm{T}}^{\mathrm{jet}\,1,2} > 6$ GeV, $E_{\mathrm{T}}^{\mathrm{jet}\,3} > 5.0$ GeV) to those passing low-E_{T} cuts ($E_{\mathrm{T}}^{\mathrm{jet}\,1,2} > 4.5$ GeV, $E_{\mathrm{T}}^{\mathrm{jet}\,3} > 3.5$ GeV) as a function of $M_{2\mathrm{j}}$ and in slices of $|\cos\theta^{*}|$. (b) Ratio of high-E_{T} to low-E_{T} events.

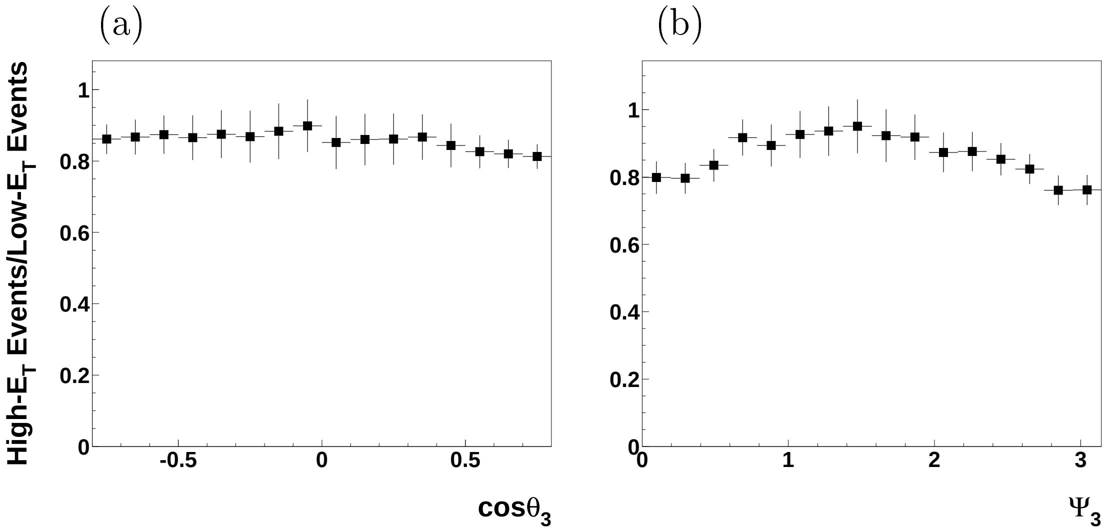

Figure 5.9: Ratio of events passing high-$\mathrm{E_T}$ three-jet selection cuts to those passing low-$\mathrm{E_T}$ cuts as a function of (a) $\cos\theta_3$ and (b) ψ_3. All other cuts described in section 5.2.2 are applied.

As in two-jet selection beam-gas and NC-DIS events are rejected by requiring:

- $0.2 < y_{\mathrm{jb}} < 0.85$
- $y_e > 0.85$
- $|z_{vtx}| < 40$ cm
- $\frac{\#\ vertex\ tracks}{\#\ all\ tracks} > 0.1$

as demonstrated in Figure 5.11.

The CC-DIS background has been studied in the previous three-jet analysis [77]. A cut on the missing transverse momentum of $P_T/\sqrt{E_{\mathrm{T}}} < 2\ \sqrt{GeV}$ is estimated to reduce the already small contamination to less than 0.02%, which can be safely neglected.

Although the E_{T} cuts are low compared to the two-jet selection, requiring a third jet and high invariant mass effectively removes non-perturbative physics events from the sample, such as multi-parton interactions. It is interesting to note that although no cut has been placed on the average boost, $\bar{\eta}$, the phase space accessed as a function of $\cos\theta_3$, shown in Figure 5.10, appears already to be roughly uniform.

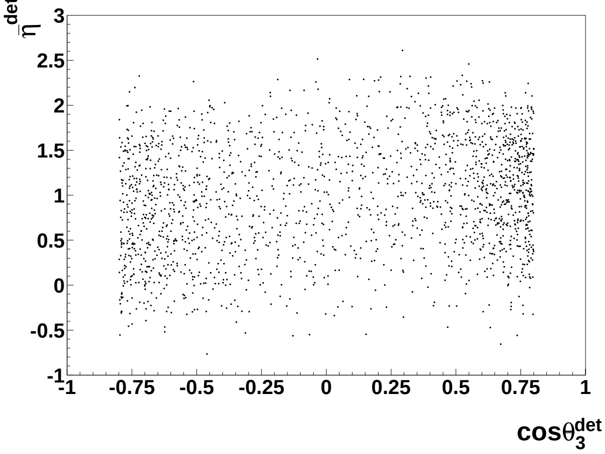

Figure 5.10: Distribution of events in $|\cos\theta^*|$ and $\bar{\eta}$ passing selection cuts in section 5.2.1(A) and with $M_{2\mathrm{j}} > 39.0$ GeV, $|\cos\theta^*| < 0.76$.

In addition to the cuts already described the energy fraction taken by the first jet is restricted by $X_3 < 0.95$, to increase the energy available for a third jet. After all cuts are applied to the data, 6316 events remain: 661 with $x_\gamma^{\rm obs} < 0.5$, 1494 with $0.5 < x_\gamma^{\rm obs} < 0.75$, 2223 with $0.75 < x_\gamma^{\rm obs} < 0.90$ and 1938 with $0.9 < x_\gamma^{\rm obs} < 1$. A summary of the cuts used in the offline selection of three-jet photoproduction events is given in table 8.2.

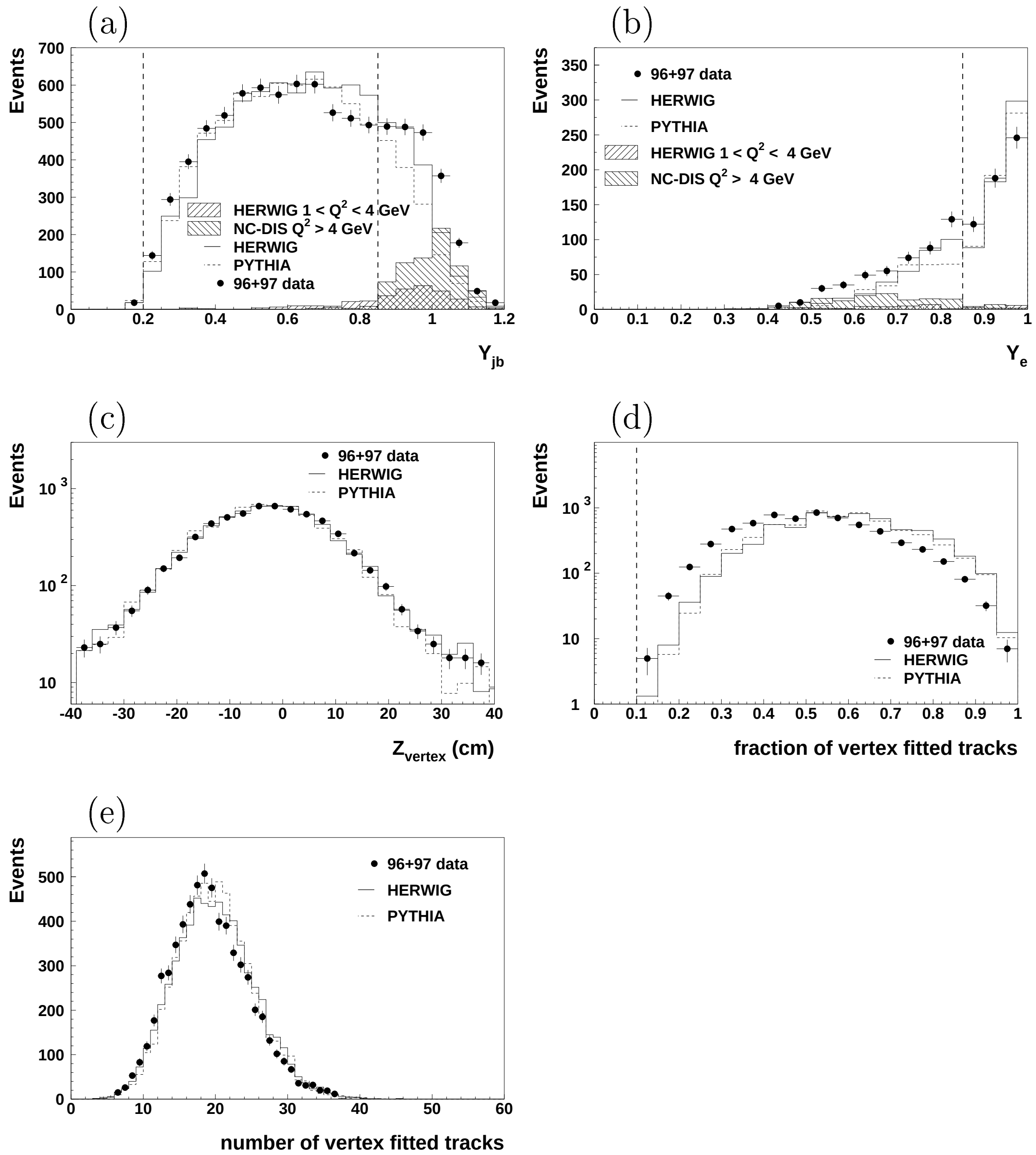

Figure 5.11: Distributions of some of the variables used in the selection of three-jet photoproduction events. For each plot all cuts described in section 5.2.2 are applied except those pertaining to the variable shown. The placement of cuts are denoted by dashed lines.

Chapter 6

Description of Data by Monte Carlo

In chapter 2 the main features of the PYTHIA and HERWIG MC event generators were described, and the reconstruction of both real and MC events were discussed in chapter 4. In this chapter, MC predictions are compared with real data distributions using **detector level** quantities, which refers to those obtained after event reconstruction. **Hadron level** is defined here as the stage in an event after hadronisation but before detection.

If a MC sample describes the data well at detector level, it is reasonable to surmise that it also describes hadron level data. If this is the case, the MC sample can be used to correct data distributions for detector-induced effects and obtain a hadron-level cross section. It is also possible, using MC, to correct the data one more step to **parton level**, the stage after the hard-scatter but before parton showering. Parton level cross sections are directly comparable to pQCD calculations, but are ill-defined and rely more heavily on the MC model used to correct them, and so the cross sections presented in this thesis are corrected only to hadron level.

The data are compared to two different event generators, HERWIG and PYTHIA. As neither describe the data at detector and therefore hadron level perfectly, the data corrections have some model dependency. The MC which best describes the data is used to correct it, whilst the other is used to check for systematic effects resulting from the model dependency.

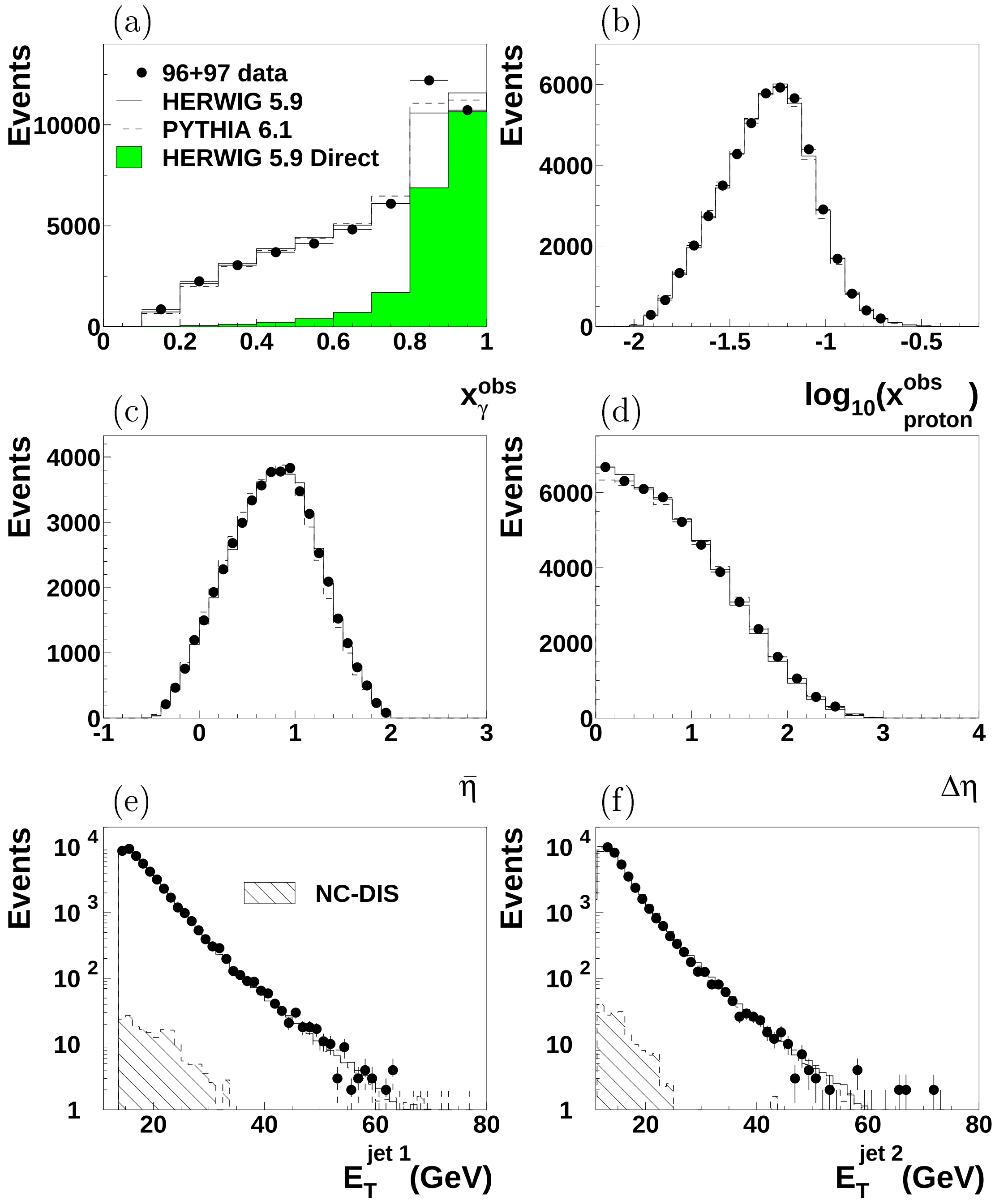

Figure 6.1: Comparison of data to HERWIG and PYTHIA predictions for two-jet quantities.

6.1 Two-jet Distributions

The 96/97 data, HERWIG 5.9 and PYTHIA 6.1 samples have been subjected to the full two-jet selection procedure described in section 5.2.1(A). The MC cross sections are multiplied by the factors in Table 1.1 and the luminosity of the data to give the number of events plotted in Figures 6.1 and 6.3. HERWIG distributions were generated using the CTEQ 3L LO [80] PDF for the proton and GRV-G LO [37, 38] for the photon, and consist of roughly five times the number of the selected events in the data. The PDFs used in the generation of PYTHIA events were GRV 94 LO [81] for the proton and SaS-G 2D LO [82] for the photon, and four times as many events as the data sample were generated.

The $x_\gamma^{\rm obs}$ distribution in Figure 6.1(a) is well described by both MC models and peaks at $x_\gamma^{\rm obs} > 0.8$. This is the region where direct events dominate, according to HERWIG MC, as is illustrated by the shaded histogram. In a previous two-jet analysis, using 1994 data which required jets with $E_{\rm T}^{\rm jet} > 6$ GeV, the $x_\gamma^{\rm obs}$ distribution was significantly better described at low values of $x_\gamma^{\rm obs}$ by MC models which included a simulation of multiple interactions (MPI). In this analysis much higher $E_{\rm T}$ cuts are applied to remove soft physics which, judging by the quality of the MC description of data at $x_\gamma^{\rm obs} < 0.5$, is effective. In particular, the data are not sensitive to MPI events, which are simulated in PYTHIA but not HERWIG, as the difference between the two models is generally small.

The fraction of the proton's momentum taking part in the hard scatter, $x_{\rm proton}^{\rm obs}$, is given by:

$$x_{\rm proton}^{\rm obs} = \frac{E_{\rm T}^{\rm jet\,1} e^{\eta^{\rm jet\,1}} + \ E_{\rm T}^{\rm jet\,2} e^{\eta^{\rm jet\,2}}}{2\,E_p}, \tag{6.1}$$

and is between 0.01 and 0.4 for two-jet events, peaking at around 0.05 as shown in Figure 6.1(b). Both MC models describe the full range well, though the HERWIG description at high $x_{\rm proton}^{\rm obs}$ is slightly better.

The distribution of $\bar{\eta}$ in Figure 6.1(c) is shifted towards the proton direction, reflecting the asymmetry in the beam momenta. The $\Delta\eta$ distribution in

Figure 6.1(c) is relatively broad and peaked at zero. HERWIG gives a slightly better description than PYTHIA of the data for these two distributions.

In Figures 6.1(e) and 6.1(f) the number of events as a function of the transverse energy of the first and second jets are shown. The distributions falls rapidly with $E_{\mathrm{T}}^{\mathrm{jet}}$ and there is good agreement between MC and data. NC-DIS MC events generated using ARIADNE 4.08 and passing the two-jet selection cuts are also shown. The ratio of NC-DIS MC events to real data events as a function of $E_{\mathrm{T}}^{\mathrm{jet\,1}}$ is shown in Figure 6.2. The MC indicates that the contamination is of the same magnitude in each measured $E_{\mathrm{T}}^{\mathrm{jet\,1}}$ range, at $\sim$0.4%.

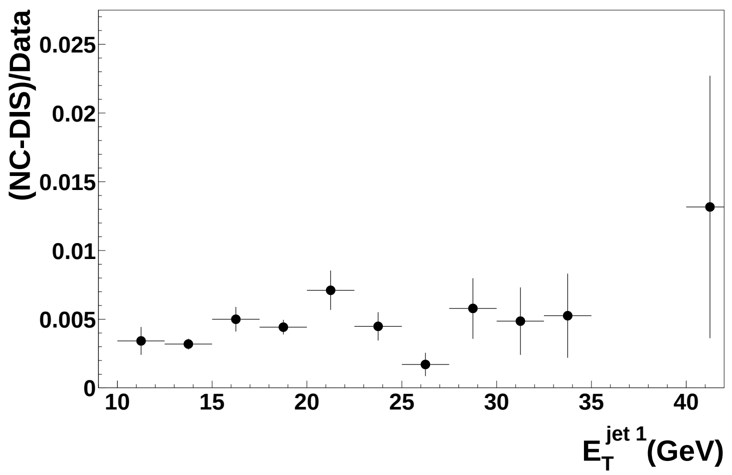

Figure 6.2: Ratio of data to NC-DIS MC events as a function of the transverse energy of the leading jet for events passing the two-jet selection criteria in section 5.2.1(A).

The $x_{\gamma}^{\mathrm{obs}}$ distributions in Figure 6.3(a)-(d) steepen as $E_{\mathrm{T}}^{\mathrm{jet\,1}}$ increases. This is partly a kinematic effect which follows from equation 5.1 and:

$$M_{2j} = \sqrt{4E_eE_pyx_{\gamma}x_p}, \tag{6.2}$$

where E_e and E_p are the positron and proton beam energies respectively. It is also the result of two-jet dynamics, whereby resolved events are more peaked at high $|\cos\theta^*|$ than direct events and therefore tend to have lower transverse energy. The

$|\cos\theta^*|$ distribution is shown separately for resolved- and direct-enhanced regions in Figures 6.3(e) and (f) respectively. Using a cut-off of $x_\gamma^{\rm obs} = 0.75$ to define these regions is justified by Figure 6.3(a), which shows the direct component of the HERWIG 5.9 sample as a shaded histogram. The MC reproduces the general shape of the distributions adequately.

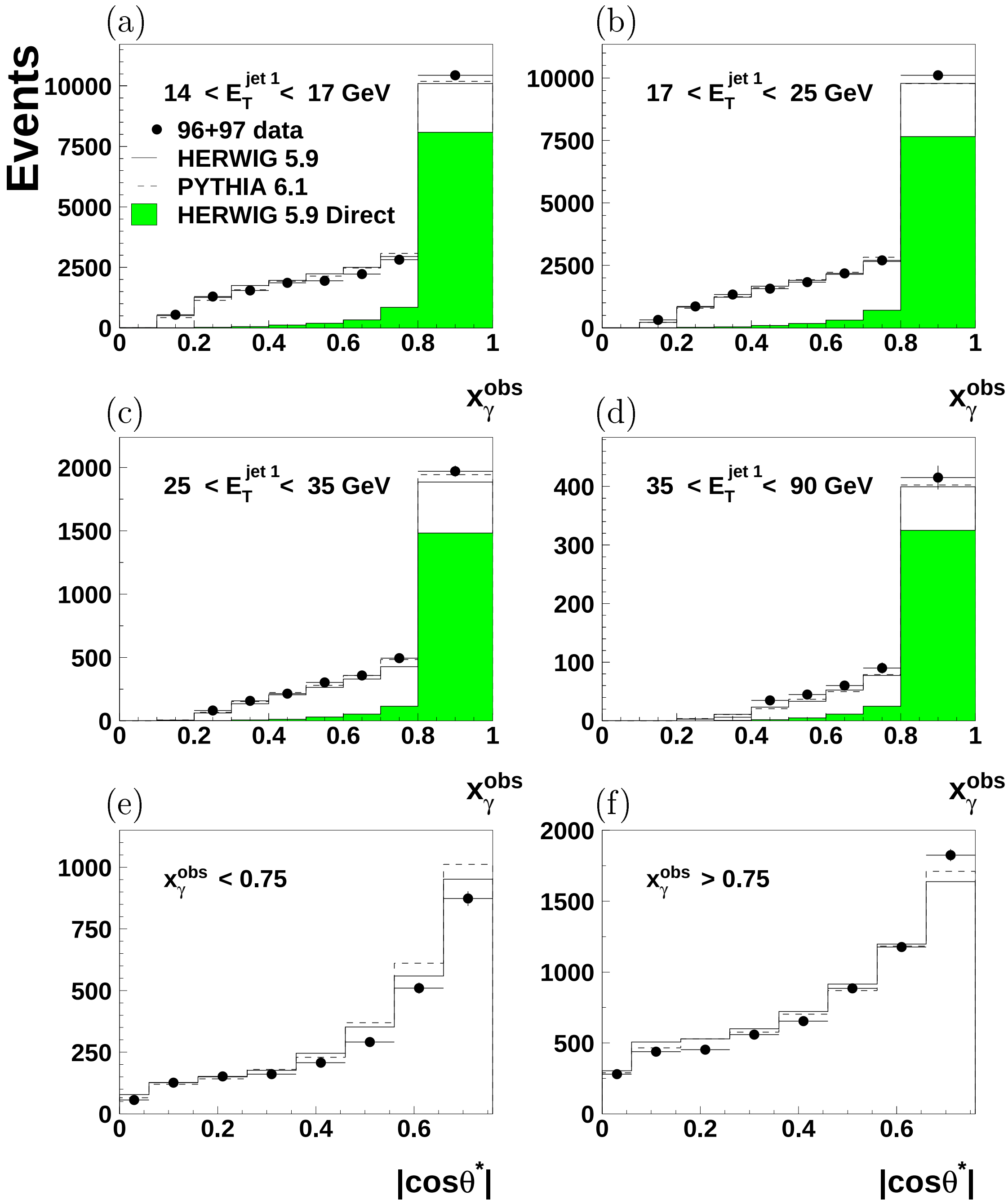

Figure 6.3: Comparison of data to HERWIG and PYTHIA predictions for two-jet quantities.

6.2 Three-jet Distributions

The distributions shown in Figures 6.4, 6.6 and 6.7 are obtained by applying the three-jet selection to both the 96/97 data sample and to two different sets of MC events. HERWIG 5.9 and PYTHIA 5.7 samples were generated with CTEQ 3L LO for the proton PDF and using GRV-G LO for the photon PDF. Multiple interactions were simulated in HERWIG only. The MC events are normalised to the luminosity of the data using the factors in Table 1.1 in a similar manner to two-jet events. HERWIG events correspond to roughly double the statistics of the data, whilst the PYTHIA sample has around one and a half times as many events. The distributions in Figures 6.6 and 6.7 are later corrected to hadron-level cross sections.

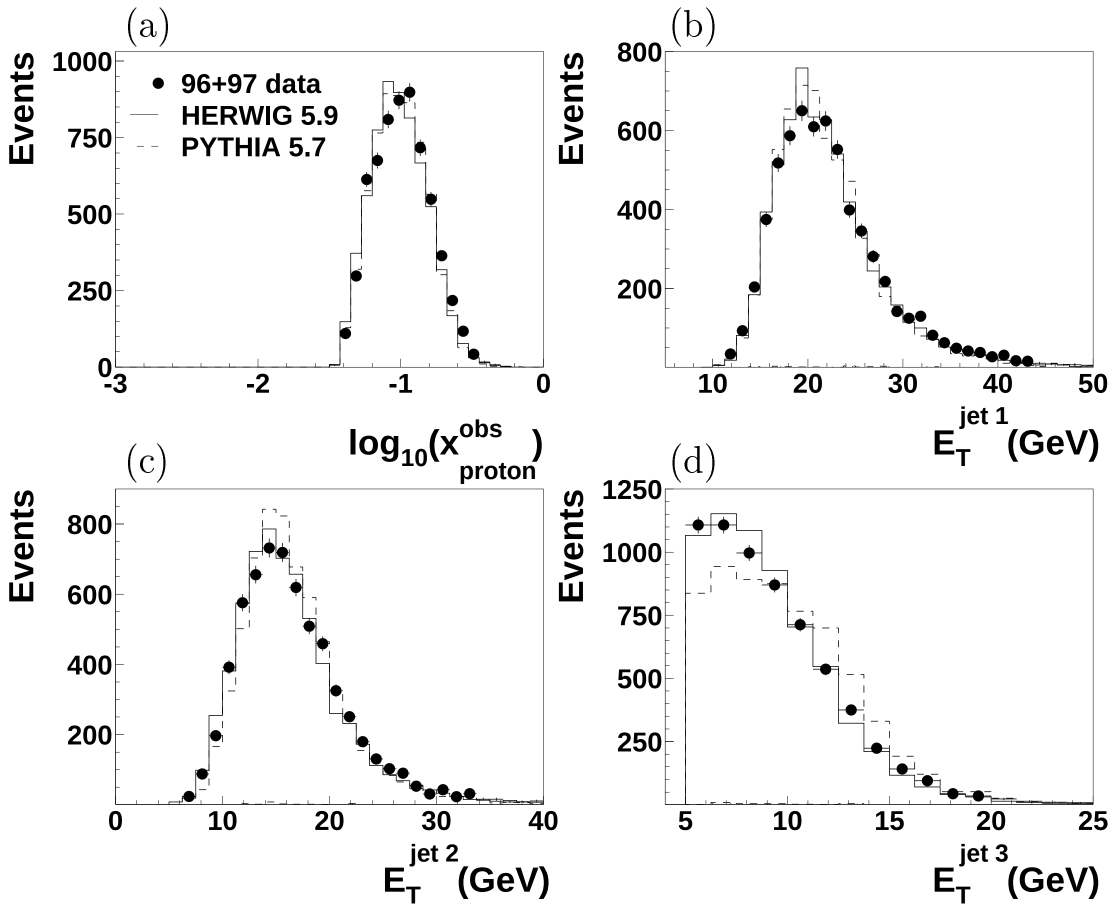

Figure 6.4: Comparison of data to HERWIG and PYTHIA predictions for three-jet quantities.

The $x^{\rm obs}_{\rm proton}$ distribution in Figure 6.4(a) is narrower than the corresponding two-jet distribution and peaks at a higher value, $x^{\rm obs}_{\rm proton} \approx 0.1$, which is partly due to the inclusion of a third jet in the definition of $x^{\rm obs}_{\rm proton}$:

$$x^{\rm obs}_{\rm proton} = \frac{E_{\rm T}^{\rm jet\,1} e^{\eta^{\rm jet\,1}} + E_{\rm T}^{\rm jet\,2} e^{\eta^{\rm jet\,2}} + E_{\rm T}^{\rm jet\,3} e^{\eta^{\rm jet\,3}}}{2\,E_p} \tag{6.3}$$

The transverse energy spectra of the first, second and third jets peak at 20 GeV, 14 GeV and 5 GeV respectively. HERWIG describes these distributions better than PYTHIA, particularly the $E_{\rm T}$ distribution of the third jet for which the PYTHIA distribution is much too broad.

The mass distribution in Figure 6.6(a) falls rapidly and is described well by both MCs, though HERWIG is better. The $x^{\rm obs}_{\gamma}$ distribution in Figure 6.6(b) peaks at high $x^{\rm obs}_{\gamma}$ and, according to HERWIG-Direct, a cut on $x^{\rm obs}_{\gamma}$ is an effective way to separate the distribution into the direct ($x^{\rm obs}_{\gamma} > 0.75$) and resolved ($x^{\rm obs}_{\gamma} < 0.75$) enhanced regions.

The $\cos\theta_3$ distribution in Figure 6.6(c) exhibits clear forward and backward peaks, indicating that low-$E_{\rm T}^{\rm jet}$, small scattering angle events are favoured as in Rutherford scattering and two-jet cross-sections. HERWIG 5.9 gives a superior description of the data, particularly at the edges of the distribution.

The ψ_3 distribution in Figure 6.6(d) peaks at ~ 0.5 and ~ 2.6 rather than at 0 and π which might be expected from colour coherence effects. Also, the phase space is greatly suppressed at the edges of the distribution by the minimum $E_{\rm T}^{\rm jet}$ requirements and the jet algorithm. Neither MC model describes the full range well, though PYTHIA is slightly better than HERWIG, which is more strongly peaked than the data.

The distributions of the energy sharing quantities X_3 and X_4 are compared to PYTHIA and HERWIG in Figure 6.6(e) and (f). The distributions are peaked at the values predicted by phase space considerations, illustrated in Figure 6.5(a) and are not very sensitive to the pQCD matrix elements, as was shown in [10]. HERWIG describes the X_3 distribution better than PYTHIA, which has a distribution that is too broad.

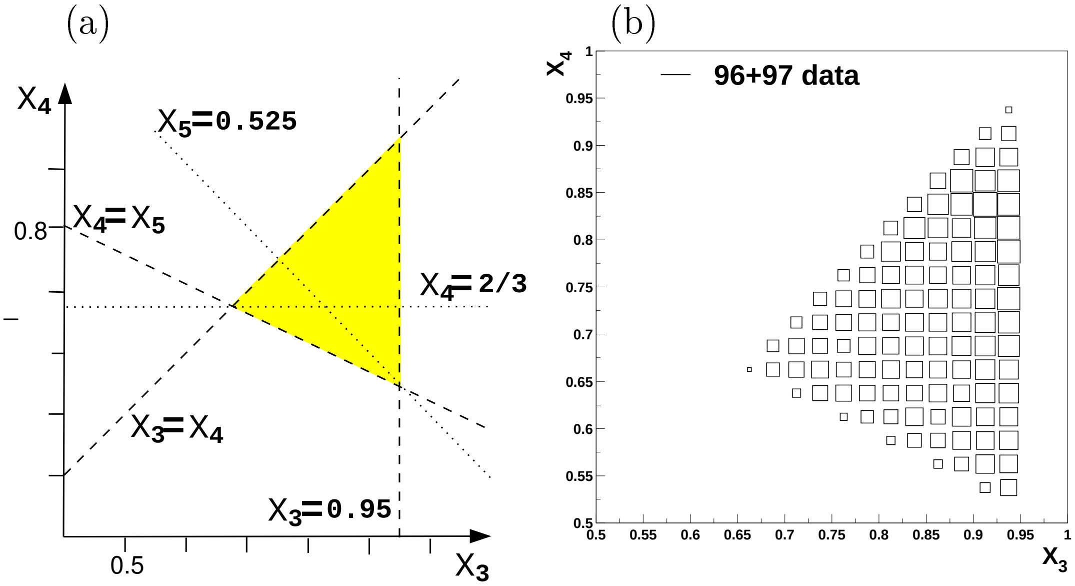

Figure 6.5: (a) Illustration of the phase space available to the energy sharing variables X_3, X_4 and hence X_5. The phase space restricted by requiring $X_3 > X_4 > X_5$ and $X_3 < 0.95$ is indicated by the shaded area. The dotted lines show the values at which the available phase space for each quantity is maximised. (b) The distribution of data in X_3 and X_4. The boxes are proportional to the number of events.

The slight asymmetry seen in the $\cos\theta_3$ distribution is shown to depend on $x_\gamma^{\rm obs}$ in Figures 6.7(a)-(d). The general shapes of the distributions are reproduced by the MC, with HERWIG giving a slightly better description than PYTHIA. The shape of the ψ_3 distribution, also different for resolved and direct enhanced regions, is shown in Figures 6.6(e) and (f).

Summary The data have been compared to two different MC models for both two-jet and three-jet distributions. The general agreement between data and MC is good, vindicating the normalisation of resolved and direct MC events used. HERWIG 5.9 is chosen in both cases as the central MC to correct the data distributions for detector effects, and to chose appropriate binning of the data, which is discussed in the next section. For both two-jet and three-jet distributions a MC including MPI simulation is compared to one without MPI. The lack of strong differences between the two MC suggests that, in the region of phase space studied, MPI are a negligible effect.

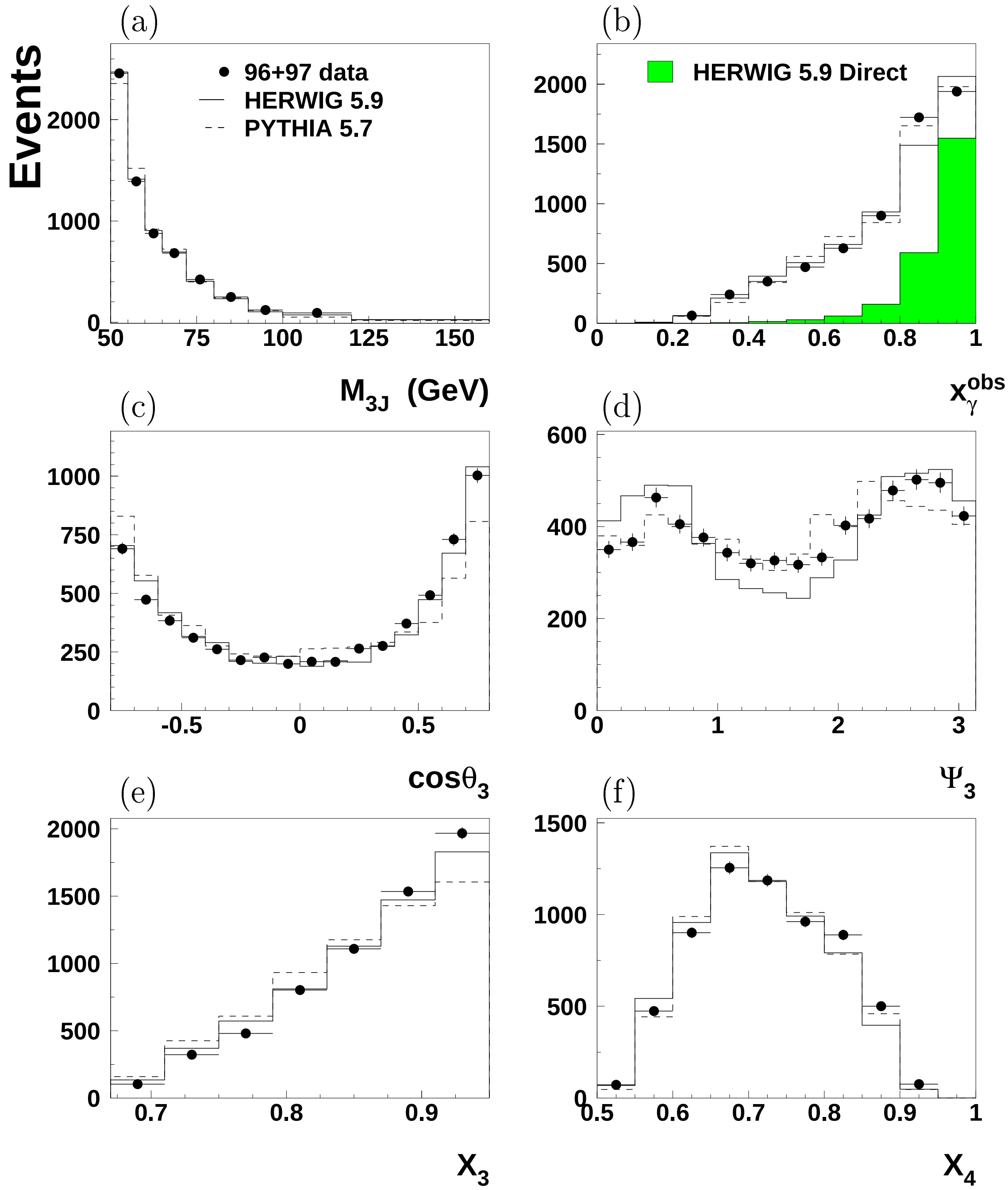

Figure 6.6: Comparison of data to HERWIG and PYTHIA predictions for three-jet quantities.

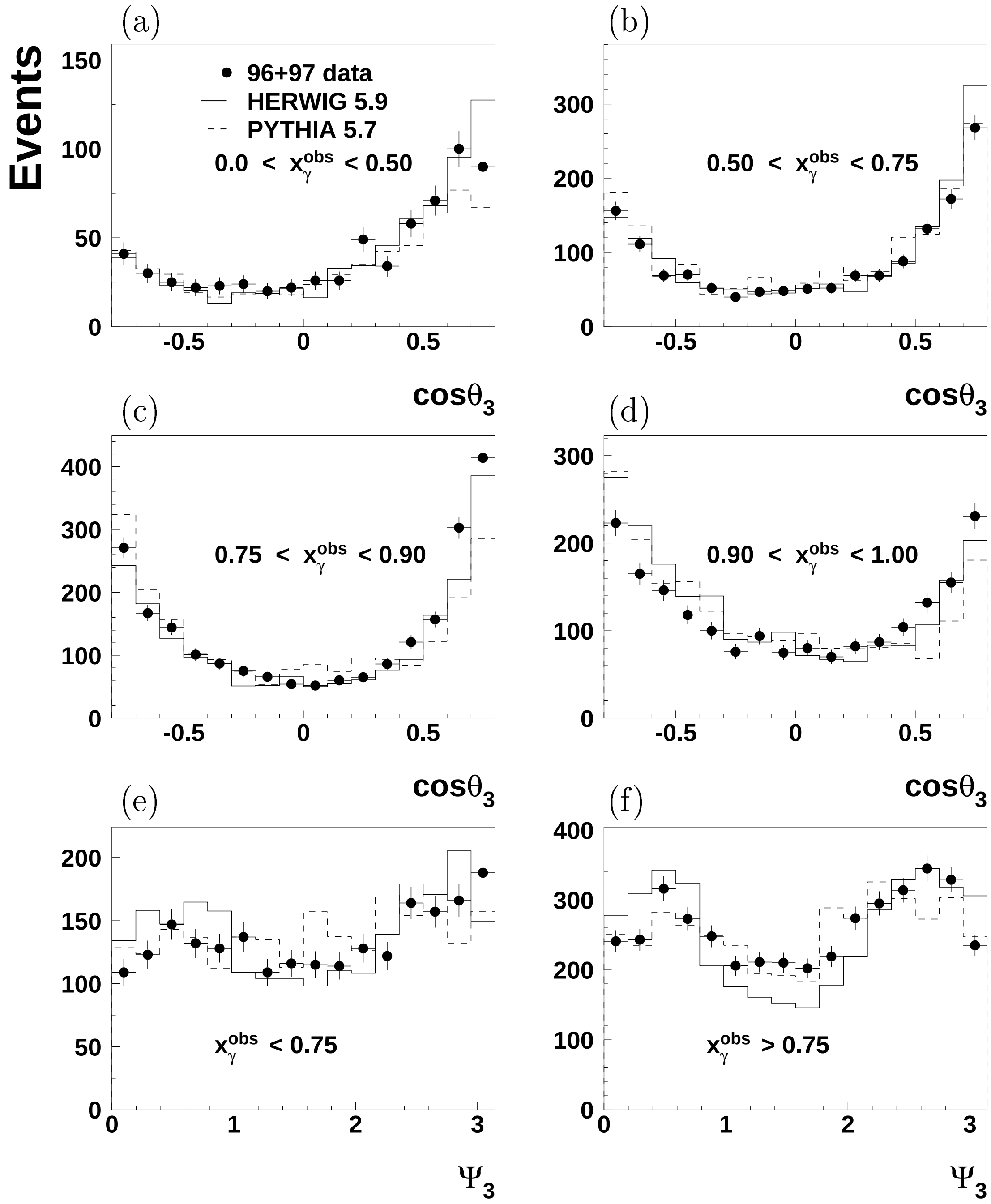

Figure 6.7: Comparison of data to HERWIG and PYTHIA predictions for three-jet quantities.

6.3 Binning the Data

A number of factors must be considered before the data bins are chosen. Good agreement between data and MC is important to be able to make an appropriate choice.

For each two- and three-jet distribution, bins are initially chosen to be at least twice the resolution, σ, of the relevant variable. This reduces the effect of migrations into and out of the bins. The resolutions for the most important two- and three-jet variables are summarised in Table 6.1, corresponding to the standard deviations of the plots in Figures 6.8 and 6.9.

The hadron-level cross-sections will be compared to parton-level pQCD calculations, so it is preferable that the difference between the cross-sections defined at these levels is not large. The size of this hadronisation effect for the two-jet $x_\gamma^{\rm obs}$ distributions has been estimated using HERWIG MC. The two bins above $x_\gamma^{\rm obs} = 0.8$ are strongly affected by hadronisation, as is shown for the $14 < E_{\rm T}^{\rm jet\,1} < 17$ GeV region in Figure 6.10. The hadronisation effect in this region is greatly reduced by combining these two bins, as is shown in Figure 6.11. No large hadronisation effects are seen in the three-jet distributions, shown in Figure 6.12.

The remaining factors to be considered are the bin efficiencies and purities, which are estimated by MC, and the number of events in each bin. The efficiency, ε_i, is defined in equation 6.4 as the fraction of events generated in bin i, g_i, (hadron level) that are also measured in that bin, m_i, (detector level).

$$\varepsilon_i = \frac{g_i \cap m_i}{g_i} \tag{6.4}$$

The bin purity is defined as the fraction of events reconstructed in a particular bin that were also generated in that bin.

$$p_i = \frac{g_i \cap m_i}{m_i} \tag{6.5}$$

The purity and efficiency of a particular bin reflect the amount of events migrating into and out-of that bin, respectively. The higher the values, the better the correspondence between measured and true bins, and the more precise the data unfolding step, as discussed in the next chapter. The efficiencies and purities for two- and three-jet distributions are shown in Appendix A. Finally, some of the bins with few events, like the lower edges of the two-jet $x_\gamma^{\rm obs}$ distributions, are combined to reduce statistical error.

Resolutions of two-jet variables			
Figure	variable	mean	σ
6.8(a)	$E_{\rm T}^{\rm jet}$	-0.014	0.09
6.8(b)	M_{2j}	-0.010	0.08
6.8(c)	y_{JB} :0.15-0.35	-0.010	0.03
6.8(d)	y_{JB} :0.75-0.90	0.025	0.05
6.8(e)	x_γ	-0.013	0.04
6.8(f)	$\cos\theta^*$	-0.001	0.03
6.8(g)	$\eta^{\rm jet}$	-0.004	0.04
6.8(h)	$\bar{\eta}^{\rm jet}$	-0.005	0.04
Resolutions of three-jet variables			
Figure	variable	mean	σ
6.9(a)	M_{3j}	-0.009	0.07
6.9(b)	$x_\gamma^{\rm obs}$	0.009	0.04
6.9(c)	$\cos\theta_3$	-0.002	0.04
6.9(d)	ψ_4	-0.002	0.07
6.9(e)	X_3	-0.001	0.02
6.9(f)	X_4	-0.001	0.04
6.9(g)	$E_{\rm T}^{\rm jet}$	-0.005	0.09
6.9(h)	$\eta^{\rm jet}$	-0.005	0.04
6.9(i)	$y_{\rm jb}$:0.15-0.35	-0.005	0.03
6.9(j)	$y_{\rm jb}$:0.75-0.90	0.023	0.05

Table 6.1: Resolutions (σ) of two- and three-jet photoproduction variables and the mean difference between quantities measured at detector and hadron level, from distributions in Figures 6.8 and 6.9.

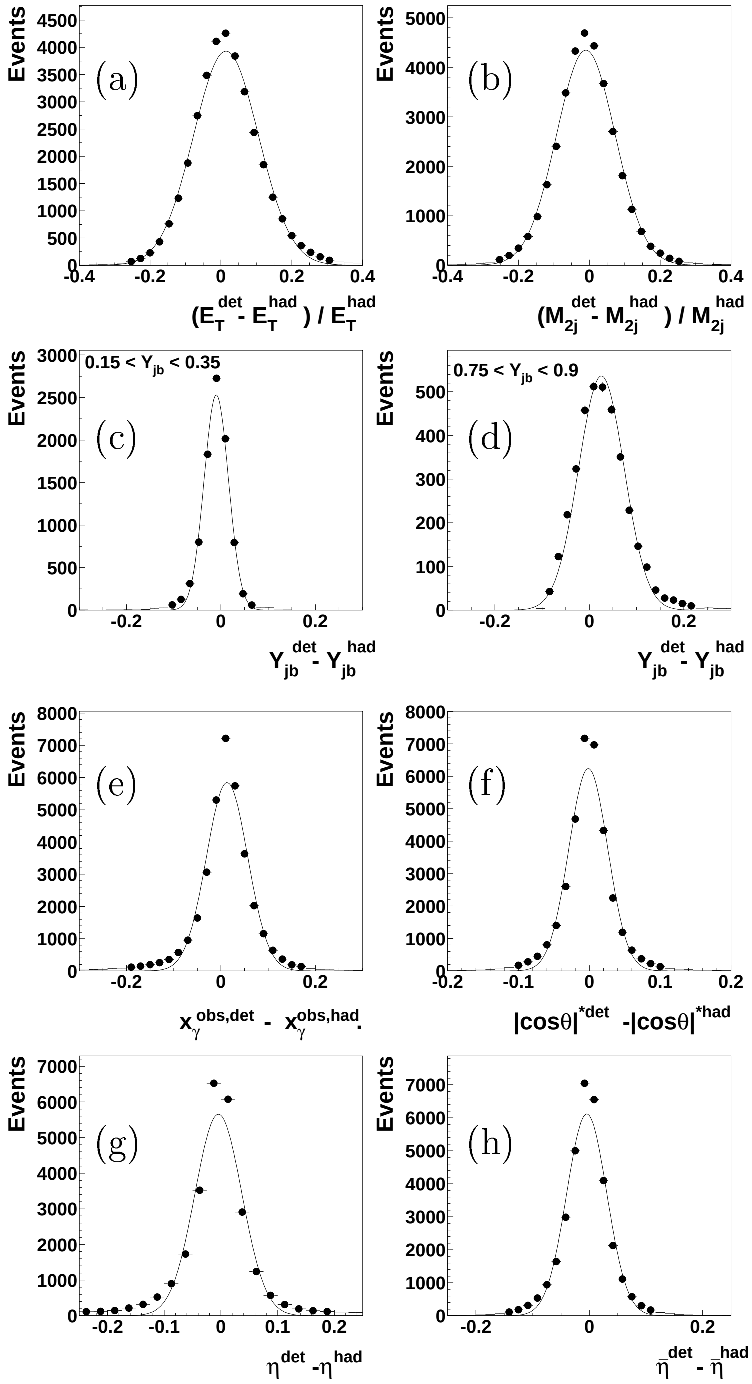

Figure 6.8: Difference between variables measured at detector and hadron level for two-jet photoproduction HERWIG 5.9 events. The distributions are fitted to a Gaussian function.

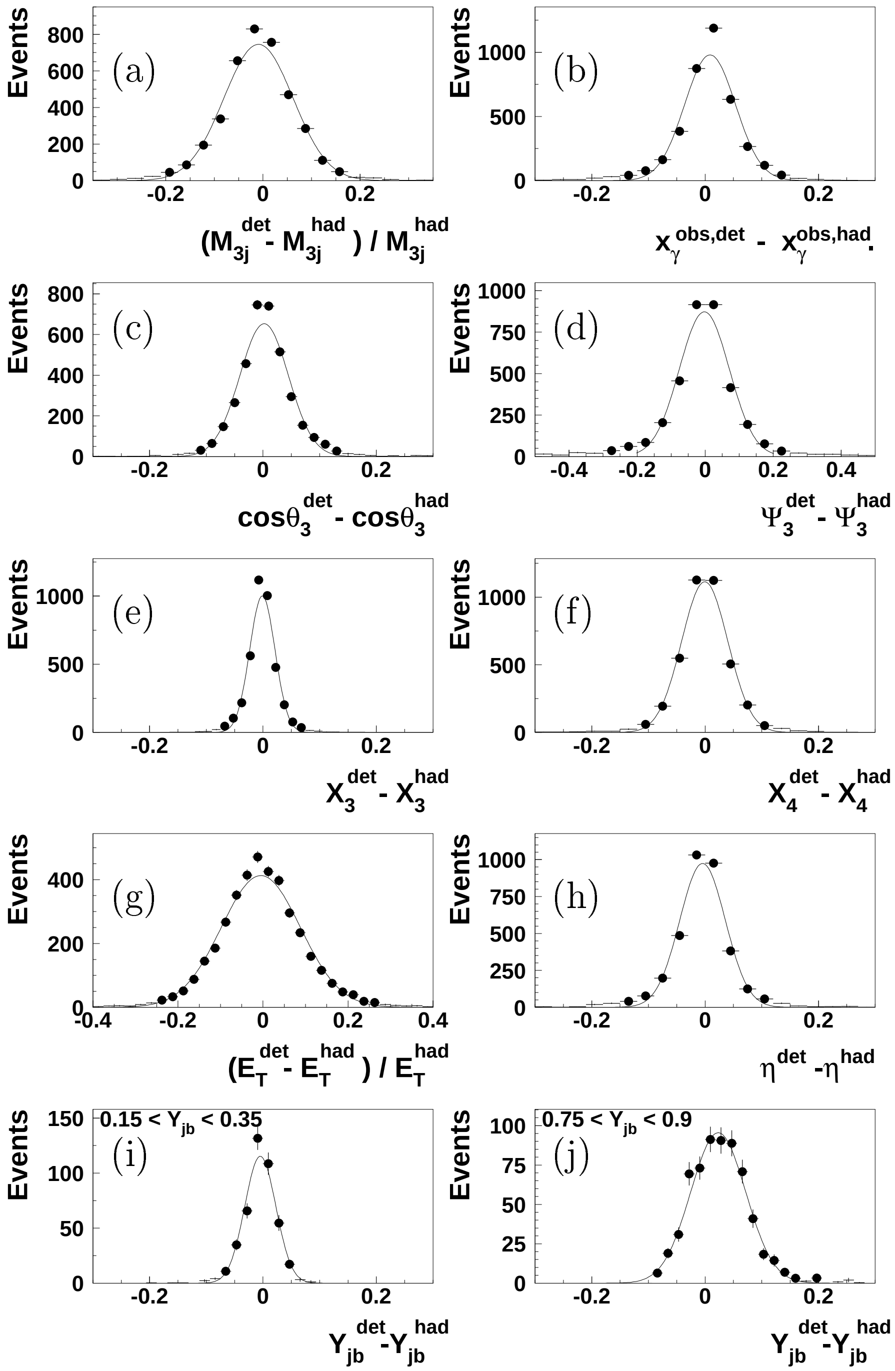

Figure 6.9: Difference between variables measured at detector and hadron level for three-jet photoproduction HERWIG 5.9 events. The distributions are fitted to a Gaussian function.

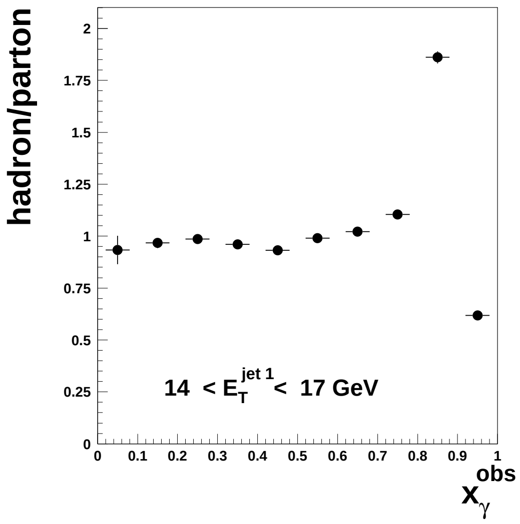

Figure 6.10: The ratio of hadron to parton level two-jet photoproduction events as estimated by HERWIG MC.

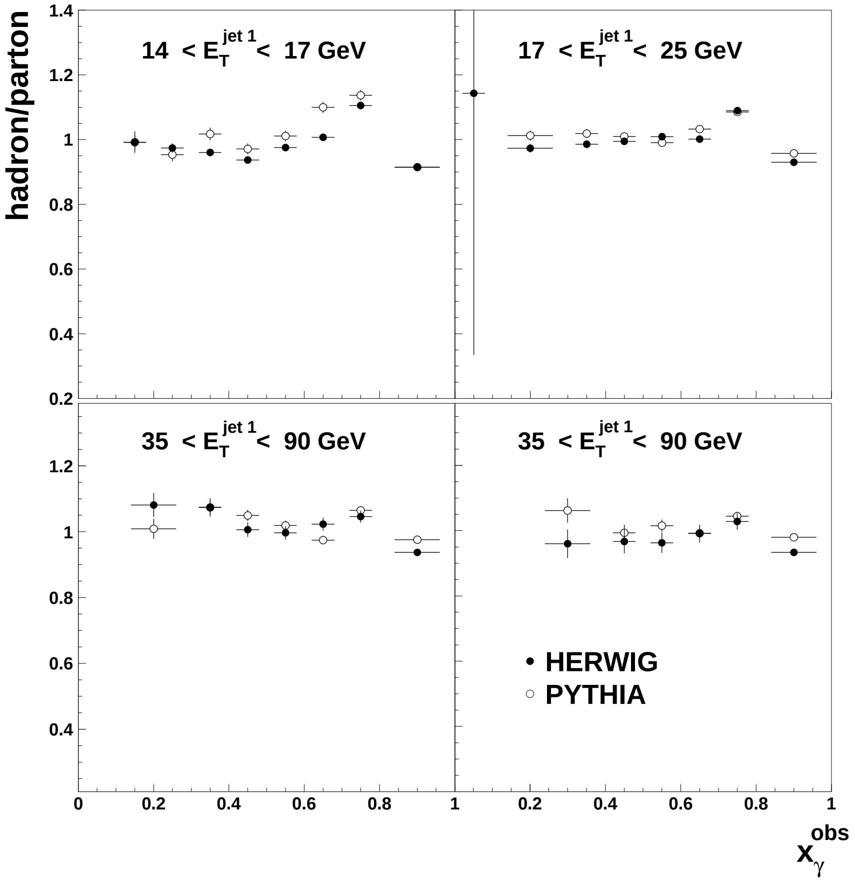

Figure 6.11: The ratio of hadron to parton level two-jet photoproduction events estimated by HERWIG (solid dots) and PYTHIA (circles).

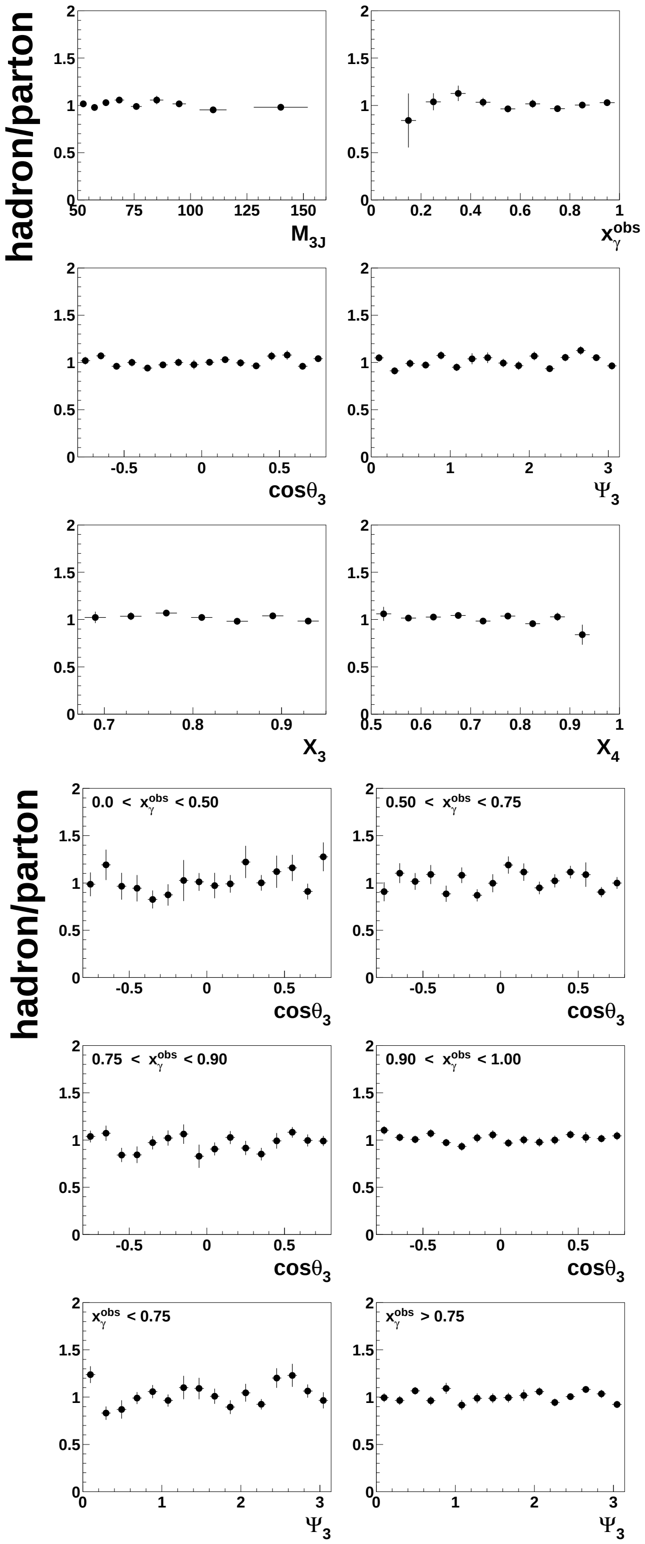

Figure 6.12: The ratio of hadron to parton level three-jet photoproduction events estimated by HERWIG (solid dots) and PYTHIA (circles)

Chapter 7

Correcting for Detector Effects

Experimentally measured distributions, obtained using an inevitably imperfect detector, differ from the corresponding 'true' distributions due to smearing and migrating of events between bins, and because acceptance and trigger efficiencies are typically less than 100%. A general expression for the relationship between measured quantities $m(x_1, x_2, ..., x_n)$ and true quantities $g(x_1, x_2, ..., x_n)$ is given by:

$$m(x_1, x_2, ..., x_n) = \int dx'_1, dx'_2 \, ... \, dx'_n \; T(x_1, x_2, ..., x_n; x'_1, x'_2, ..., x'_n) \; g(x_1, x_2, ..., x_n) \tag{7.1}$$

where $\mathbf{x}$ is a set of parameters which completely describe an event or set of events. The transfer function, $T(\mathbf{x}; \mathbf{x}')$, expresses the relationship between each measured parameter, and every true parameter. Using $T(\mathbf{x}; \mathbf{x}')$ and m to obtain a distribution corrected for detector effects is called **unfolding** the data.

To greatly simplify equation 7.1, unfolding is usually restricted to the one-dimensional case, which means ignoring the effects that other variables have on the particular variable measured in the distribution. If other variables do influence the unfolding step, the size of their effect can be estimated and included as a systematic error, as discussed in chapter 9.

Assuming one-dimensional unfolding, the number of events measured in bin j (m_j) and generated in bin i (g_i) of a particular distribution are now related by a **transfer matrix**, T_{ij}, which can be estimated using MC such that:

$$m_j^{\mathrm{MC}} = \sum_j (T_{ij}^{\mathrm{MC}})\, g_i^{\mathrm{MC}} \tag{7.2}$$

Two different methods of unfolding are now discussed.

7.1 Bin-by-bin Correction

In the bin-by-bin correction method the unfolded number of events in bin i, u_i, is given by :

$$u_i = C_i^{\mathrm{MC}} \cdot m_i \tag{7.3}$$

where C_i^{MC} is the **correction factor** for bin i calculated from MC events:

$$C_i^{\mathrm{MC}} = \frac{g_i^{\mathrm{MC}}}{m_i^{\mathrm{MC}}} = \frac{1}{T_{ij}^{\mathrm{MC}}} \tag{7.4}$$

T_{ij}^{MC} is a diagonal matrix which means that u_i is independent of m_j when $j \neq i$ and only the net migrations into and out-of each bin are considered. Correlations between adjacent bins are neglected, and so small differences between modeled and real migrations or acceptances can lead to significant inaccuracies in C_i^{MC}.

The values of C_i^{MC} can be more precisely estimated if the number of events generated and measured in the same bin are large, as can be seen from equation 7.5. This is equivalent to requiring high bin efficiencies, ε_i, and purities, p_i, which can be done by using bins that are at least twice the resolution.

$$\delta C_i^{\mathrm{MC}} = \sqrt{\frac{g_i^{\mathrm{MC}}}{(m_i^{\mathrm{MC}})^3}\,[g_i^{\mathrm{MC}} + m_i^{\mathrm{MC}} - 2 g_i^{\mathrm{MC}} \cap m_i^{\mathrm{MC}}]} \tag{7.5}$$

This method is not valid if there are significant long-range migrations or if the migrations are not well modeled by MC.

7.2 Bayesian Unfolding

In this method the number of unfolded events, u_i, is related to the number of measured events, m_i, using conditional probability:

$$u_i = \frac{1}{e_i^{\mathrm{MC}}} \sum_{j=1}^{j=n_{\mathrm{m}}} P(i|j) \cdot m_j \tag{7.6}$$

where e_i^{MC} is the fraction of events generated in bin i that are detected, as estimated by MC, and n_{m} is the number of bins in the measured distribution. $P(i|j)$ is the probability that an event originated from bin i of the true distributions given it was observed in bin j of the measured distribution. The value of $P(i|j)$ is calculated using Bayes theorem [83]:

$$P(i|j) = \frac{P(j|i) \cdot P_i}{\sum_{l=1}^{l=n_{\mathrm{g}}} P(j|l) \cdot P_l} \tag{7.7}$$

where n_{g} is the number of bins in the true or generated distribution. The probability that an event is measured in bin j given that it originated in bin i of the true distribution, $P(j|i)$, can be calculated directly from MC.

The value of $P(i|j)$ relies on knowing P_i, the probability of an event originating from bin i. Since P_i is also the distribution of interest, it appears that the formula is sterile. The way to proceed, as proposed in [84], is to use a flat P_i distribution, P_i^0, to calculated initial values for $P(i|j)$ and hence u_i. The resulting u_i^0 can be normalised to the total number of unfolded events to update the probability distribution. P_i^1 is closer to P_i than P_i^0 and can in turn be used to recalculate $P(i|j)$ and u_i. This cycle, summarised in equation 7.8, is repeated until the difference between u_i^n and u_i^{n-1} is small. Unlike bin-by-bin, the number of measured and true bins need not be equal, or cover the same range of values, and different sources of background events can be unfolded simultaneously. This method takes account of smearing and migrations in a more rigorous way than bin-by-bin unfolding, and because of the correlations between bins, the unfolded distribution is not so sensitive to differences between MC and data.

$$P_i^0; \rightarrow P^0(i|j) = \frac{P(j|i) \cdot P_i^0}{\sum_{l=1}^{l=n_{\mathrm{g}}} P(j|l) \cdot P_l^0}; \longrightarrow u_i^0 = \frac{1}{e_i^{\mathrm{MC}}} \sum_{j=1}^{j=n_{\mathrm{m}}} P^0(i|j) \cdot m_j; \longrightarrow \frac{u_i^0}{\sum_i^{n_{\mathrm{g}}} u_i^0} = P_i^1 \tag{7.8}$$

The main advantage this method has over bin-by-bin is that it can take into account any kind of smearing or migration, such that u_i is influenced by m_j for all values of j, and consequently the unfolded number of events is correlated between bins.

7.3 Comparison Between Unfolding Methods

As discussed in chapter 6, HERWIG is the MC chosen to obtain corrected cross-sections for both two- and three-jet events. In this section distributions unfolded using the bin-by-bin and Bayesian methods are compared. The difference between PYTHIA and HERWIG corrected cross-sections for a particular distribution are also compared. This gives an estimate of the amount of error in the correction procedure due to model dependency.

The bin-by-bin correction factors, estimated using HERWIG, are shown for each unfolded distribution in section B.1 of the appendix. To demonstrate that the Bayesian unfolding method works, a detector level HERWIG distribution was corrected for detector effects using the same HERWIG MC sample. The unfolded distribution corresponds closely to the known hadron level for all the distributions studied, indicating that the method does not produce results that are, for example, too smooth.

In Figure 7.1(a) this comparison is shown for the three-jet $\cos\theta_3$ distribution. In Figure 7.1(b) the same type of comparison is made, but this time the MC has been split into two independent samples. The detector level distribution in one half of the MC is corrected using the other half. The results are compared to the hadron level for the full MC sample for both unfolding methods. The results of the same two tests are shown for more two- and three- jet distributions in appendix B.2. For most three-jet distributions, the Bayes corrected cross-sections compare more closely to the real hadron level than the bin-by-bin. For two-jet events, the distributions from both methods agree better with the true hadron-level, probably due to the greater MC statistics.

In Figures 7.2, 7.3 and 7.4 the cross-sections obtained using both unfolding methods, and both MC on the data are shown. The differential cross-section in each bin is related to u_i by:

$$\frac{d\sigma}{dx} = \frac{u_i}{\mathcal{L} \times \text{ bin width}} \qquad (7.9)$$

where $\mathcal{L}$ is the integrated luminosity. The various unfolding combinations compared well for most of the distributions studied. A greater spread in results is seen in the plots with poorer statistics. Bayesian unfolded cross-sections are generally smoother than bin-by-bin for ψ_3 and $\cos\theta_3$ distributions, and the estimated model dependency is smaller in most bins.

In summary, both unfolding methods studied give consistent results. The unfolded cross-section in each bin is correlated with that in the other bins for Bayesian unfolded distributions, which makes assigning appropriate statistical errors difficult. The bin-by-bin method is therefore used to obtain corrected cross-sections.

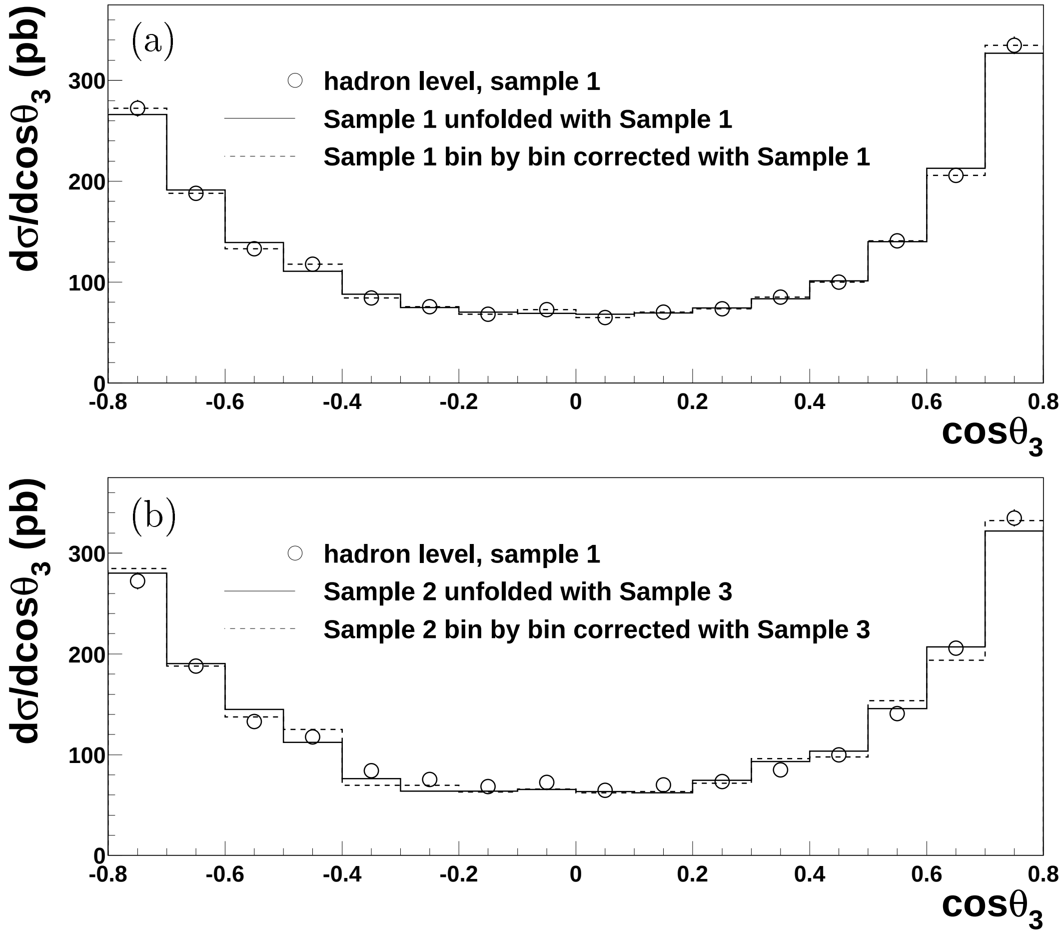

Figure 7.1: The HERWIG detector level $\cos\theta_3$ distribution corrected to hadron-level using bin-by-bin (dotted line) and Bayesian (solid line) unfolding methods. In (a) the same MC (sample 1) is used for the correction and for the measured distribution. In (b) one half of the MC (sample 2) is used to correct the other (sample 3). The hadron level for sample 1 is also shown (circle).

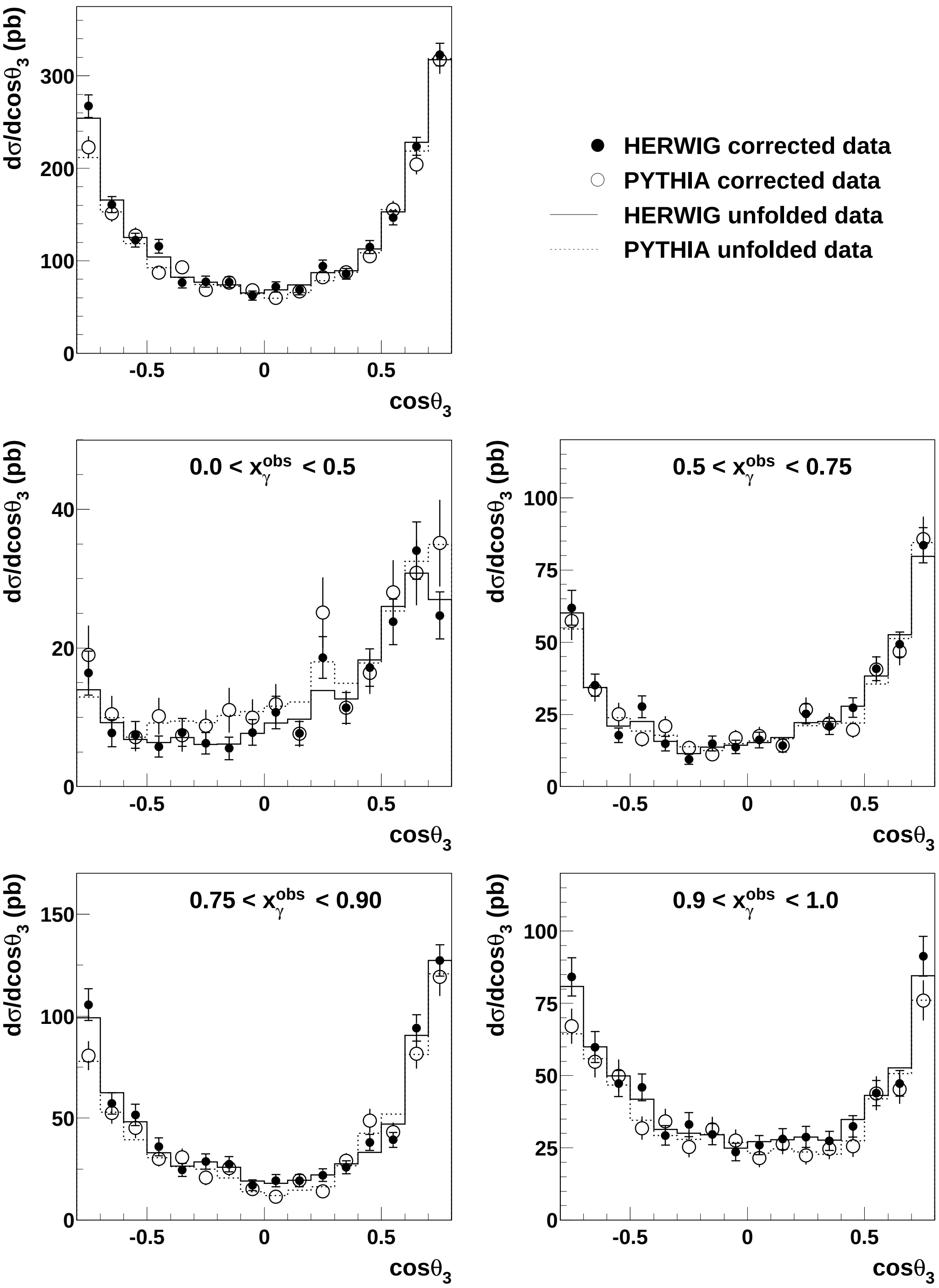

Figure 7.2: Comparison of bin-by-bin (circles) and Bayesian (lines) unfolded $\cos\theta_3$ cross-sections for 96/97 data. Statistical errors are shown.

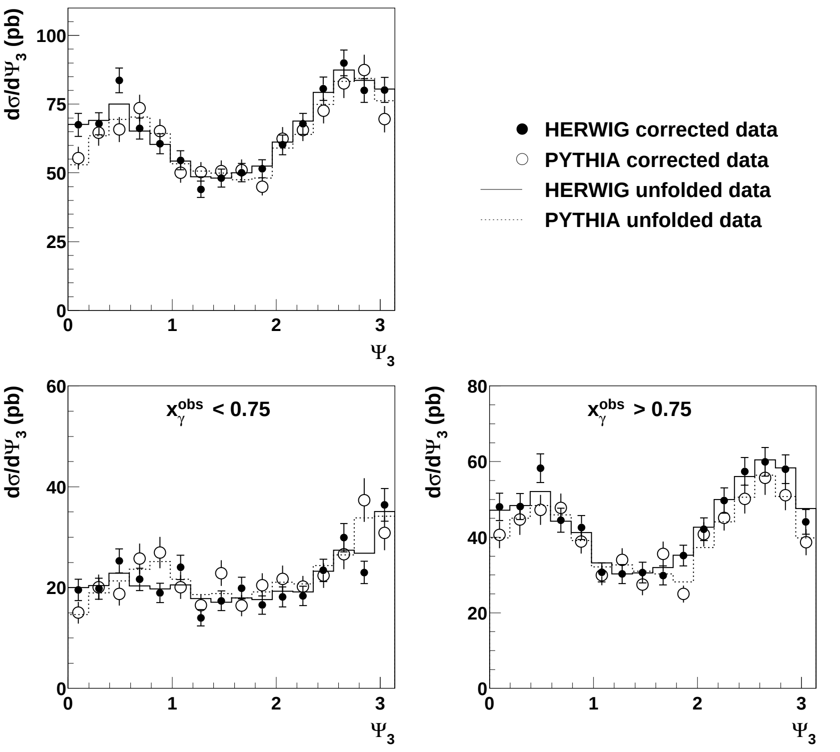

Figure 7.3: Comparison of bin-by-bin (circles) and Bayesian (lines) unfolded ψ_3 cross-sections for 96/97 data. Statistical errors are shown.

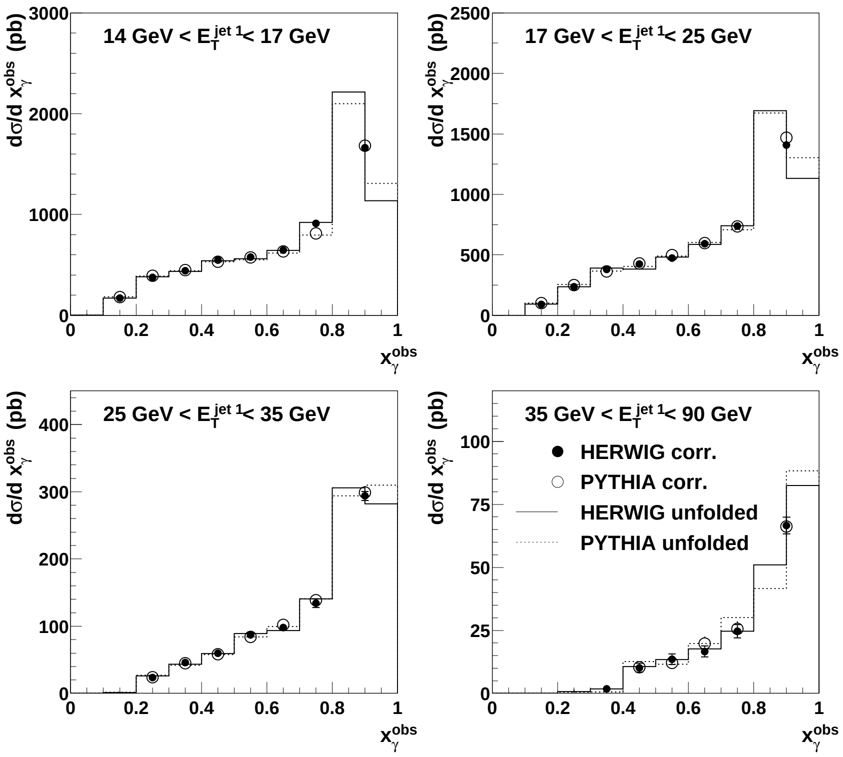

Figure 7.4: Comparison of bin-by-bin (circles) and Bayesian (lines) unfolded two-jet x_γ^{obs} cross-sections for 96/97 data. Statistical errors are shown.

Chapter 8

Systematics

There are several types of uncertainties involved in measuring two- and three-jet cross sections that need to be considered in order to evaluate their systematic effect on the results.

Firstly, the bin-by-bin unfolding method is one-dimensional. This means that a distribution is corrected for migrations within the bins of that distribution only. Any dependence the unfolding might have on other kinematic variables, or migrations in those variables is assumed to be small and so ignored. To estimate the possible error on the results due to this assumption, the unfolding for each distribution is repeated several times, with the cuts on the other kinematic variables varied in turn. The cuts are altered by $\pm 1\sigma$, on the resolution on the variable in question.

Secondly, the cleaning cuts applied to remove background events are checked in a similar way to the kinematic cuts. This time, however, the aim is to check the effect of events which are not modelled by the MC migrating into or out of the sample, and to assess the error on the modelled background level.

Thirdly, the correction procedure and background rejection should be independent of the MC used, and would be so if the MC modelled the data perfectly. To estimate the effect of model dependence, a second MC is used to obtain corrected cross sections. There is another source of systematic error resulting from the uncertainty in the energy scale as discussed in section 3.2. Therefore the values of $y_{\rm jb}$ and $E_{\rm T}^{\rm jet}$ are varied by $\pm 3\%$.

The systematic checks made are summarised in Tables 8.1 and 8.2 for the two- and three-jet cross sections respectively. The resolutions by which variables are varied correspond to those in Table 6.1 and the effects of the systematic checks on the measured cross-sections are shown in Figures 8.1 to 8.9. The systematic errors are dominated by the energy scale uncertainty, followed by the model dependency. Most other systematic errors are within statistical uncertainty.

Two-jet Systematics		
Number	Default	Systematic
1	$E_T^{jet\ 1} > 14.0$ GeV $E_T^{jet\ 2} > 11.0$ GeV	$E_T^{jet\ 1} > 15.26$ GeV $E_T^{jet\ 2} > 11.99$ GeV
2	″	$E_T^{jet\ 1} > 12.74$ GeV $E_T^{jet\ 2} > 10.01$ GeV
3	$0.2 < y_{jb} < 0.85$	$0.23 < y_{jb} < 0.90$
4	″	$0.17 < y_{jb} < 0.80$
5	$-1.0 < \eta < 2.0$	$-0.96 < \eta < 2.04$
6	″	$-1.04 < \eta < 1.96$
7	$y_e > 0.85$ (if $E_e > 5$ GeV)	$y_e > 0.9$
8	″	$y_e > 0.8$
9	$\lvert Z_{vtx}\rvert < 40.0$ cm	$\lvert Z_{vtx}\rvert < 50.0$ cm
10	″	$\lvert Z_{vtx}\rvert < 30.0$ cm
11	$\frac{\#\ vertex\ tracks}{\#\ all\ tracks} > 0.1$	> 0.2
12	″	> 0.0
13	$P_T/\sqrt{E_T} < 1.5$	$P_T/\sqrt{E_T} < 1.8$
14	″	$P_T/\sqrt{E_T} < 1.3$
15	HERWIG (detector corrections)	PYTHIA
To estimate uncertainty due to energy scale:		
16	$y_{jb} \rightarrow$ $E_T^{jet} \rightarrow$	$y_{jb} + 3\%$ $E_T^{jet} + 3\%$
17	$y_{jb} \rightarrow$ $E_T^{jet} \rightarrow$	$y_{jb} - 3\%$ $E_T^{jet} - 3\%$
The following apply only to $d\sigma/d\lvert\cos\theta^*\rvert$:		
18	$M_{2j} > 39.0$ GeV	$M_{2j} > 42.12$ GeV
19	″	$M_{2j} > 35.88$ GeV
20	$\lvert\cos\theta^*\rvert < 0.76$	$\lvert\cos\theta^*\rvert < 0.79$
21	″	$\lvert\cos\theta^*\rvert < 0.73$
22	$0.0 < \bar{\eta} < 1.0$	$0.0 < \bar{\eta} < 1.04$
23	″	$0.0 < \bar{\eta} < 0.96$

Table 8.1: Default two-jet photoproduction selection cuts and alternative cuts used to estimate systematic effects. The number in the first column corresponds to the abscissa in Figures 8.1 - 8.3.

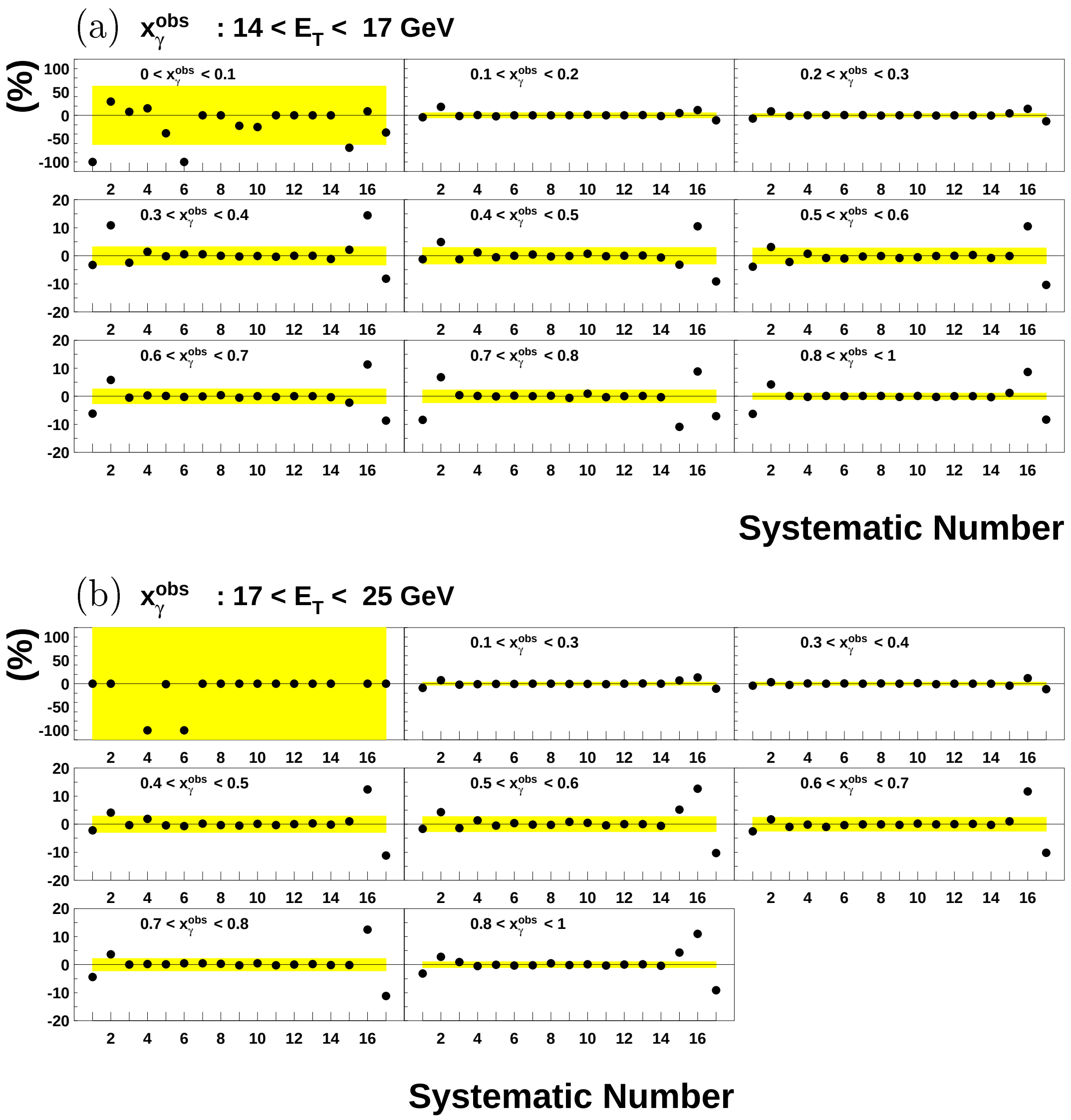

Figure 8.1: Summary of systematics uncertainties on $d\sigma/dx_\gamma^{\mathrm{obs}}$ where the transverse energy of the leading jet is in the range (a) $14 < E_T^{\mathrm{jet\,1}} < 17$ GeV and (b) $17 < E_T^{\mathrm{jet\,1}} < 25$ GeV. The percentage difference between $d\sigma/dx_\gamma^{\mathrm{obs}}$ obtained using the systematic and default cuts is shown for each systematic, which is defined and numbered as in Table 8.1. The statistical error on the nominal result is shown as a shaded band.

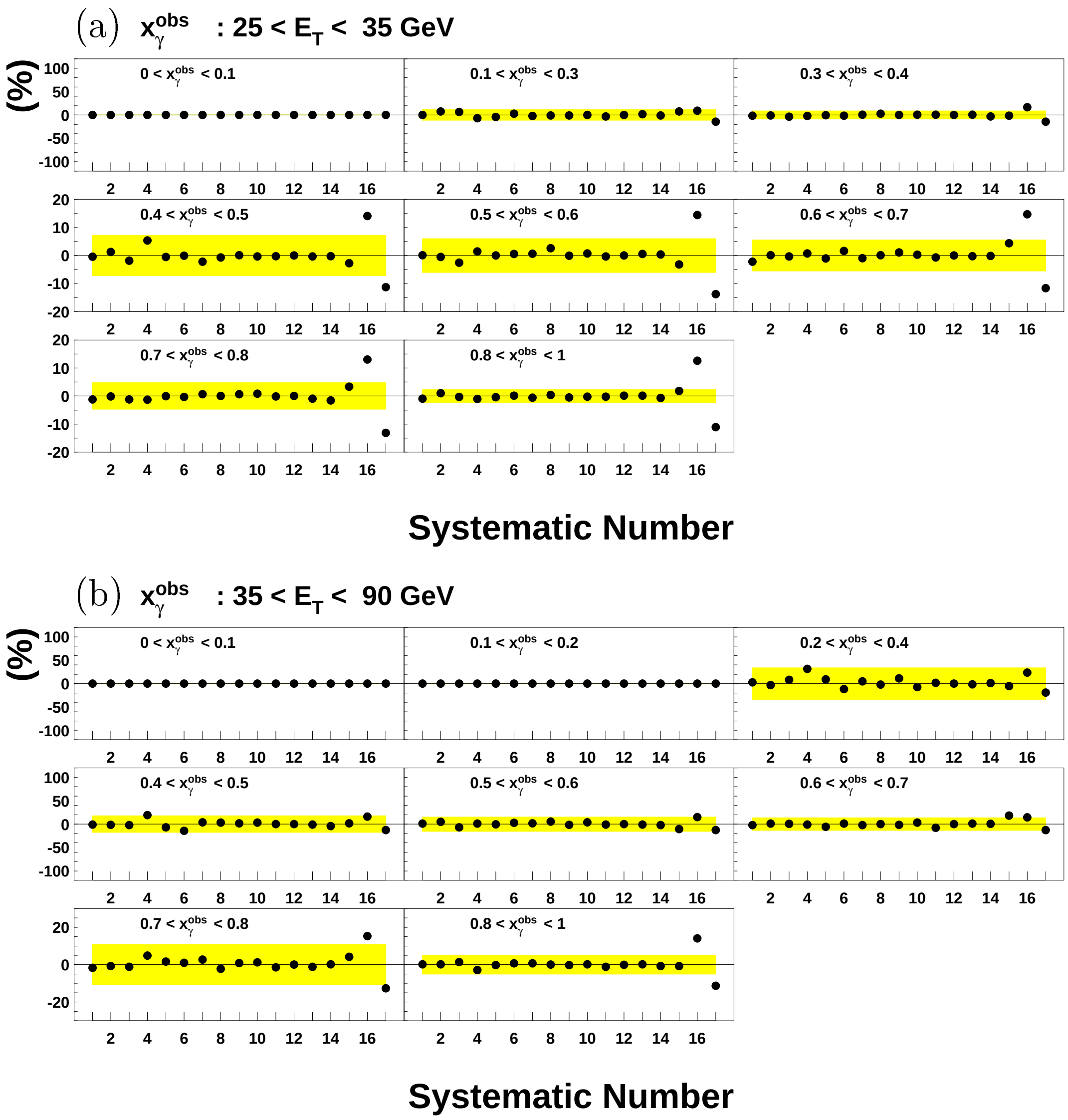

Figure 8.2: Summary of systematics uncertainties on $d\sigma/dx_\gamma^{\rm obs}$ where the transverse energy of the leading jet is in the range (a) $25 < E_T^{\rm jet\,1} < 35$ GeV and (b) $35 < E_T^{\rm jet\,1} < 90$ GeV. The percentage difference between $d\sigma/dx_\gamma^{\rm obs}$ obtained using the systematic and default cuts is shown for each systematic, which is defined and numbered as in table 8.1. The statistical error on the nominal result is shown as a shaded band. In (a) there are no data for $x_\gamma^{\rm obs} < 0.1$ and in (b) there are no data for $x_\gamma^{\rm obs} < 0.2$.

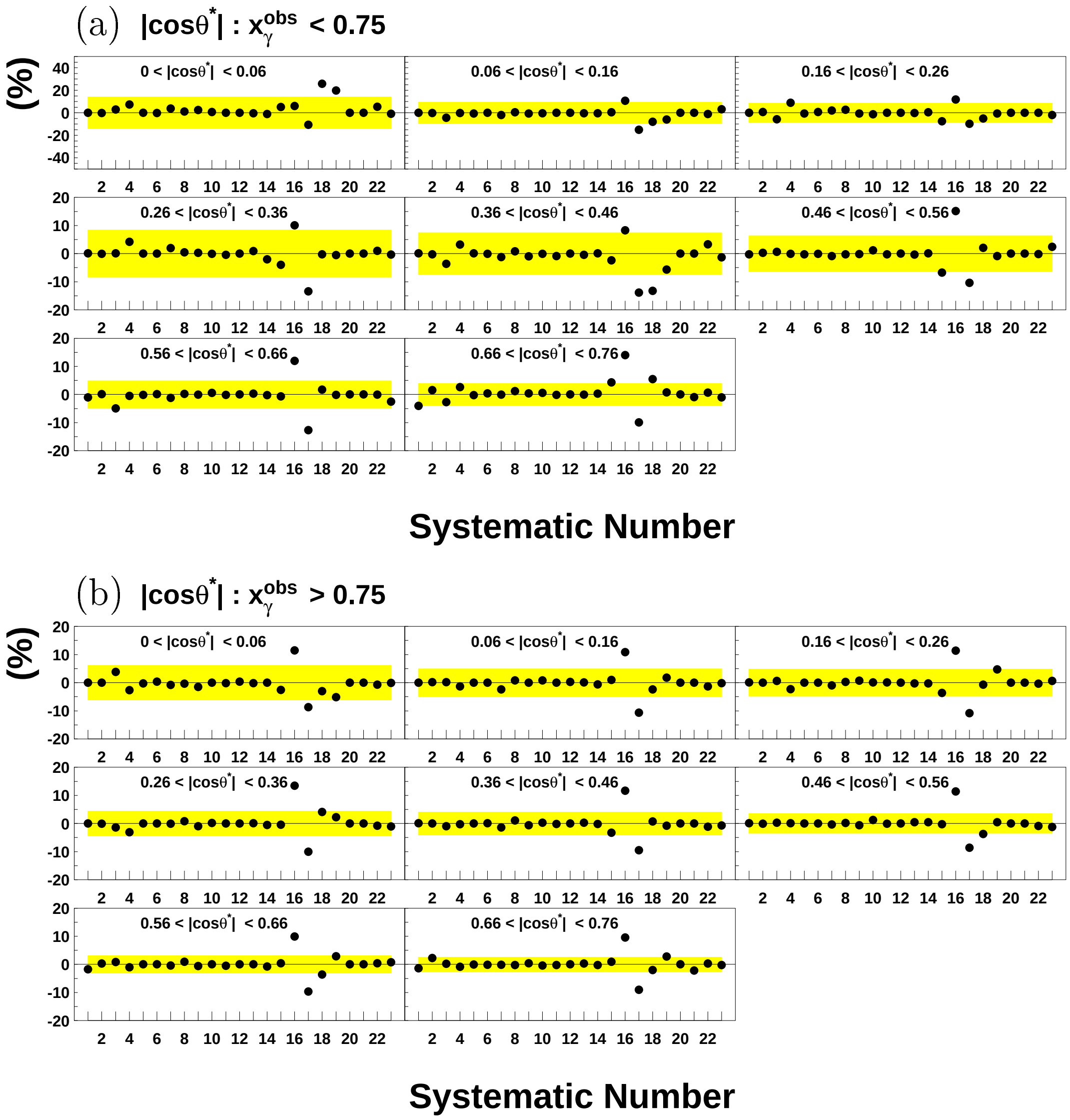

Figure 8.3: Summary of systematics uncertainties on $d\sigma/d|\cos\theta^*|$ where (a) $x_\gamma^{\rm obs} < 0.75$ and (b) $x_\gamma^{\rm obs} > 0.75$. The percentage difference between $d\sigma/d|\cos\theta^*|$ obtained using the systematic and default cuts is shown for each systematic, which is defined and numbered as in table 8.1. The statistical error on the nominal result is shown as a shaded band.

Three-jet Systematics		
Number	Default	Systematic
1	$E_T^{jet\ 1,2} > 6.0$ GeV $E_T^{jet\ 3} > 5.0$ GeV	$E_T^{jet\ 1,2} > 6.54$ GeV $E_T^{jet\ 3} > 5.45$ GeV
2	"	$E_T^{jet\ 1,2} > 5.46$ GeV $E_T^{jet\ 3} > 4.55$ GeV
3	$0.2 < y_{jb} < 0.85$	$0.23 < y_{jb} < 0.90$
4	"	$0.17 < y_{jb} < 0.80$
5	$-2.4 < \eta < 2.4$	$-2.36 < \eta < 2.44$
6	"	$-2.44 < \eta < 2.36$
7	$y_e > 0.85$ (if $E_e > 5$ GeV)	$y_e > 0.9$
8	"	$y_e > 0.8$
9	$\|Z_{vtx}\| < 40.0$ cm	$\|Z_{vtx}\| < 50.0$ cm
10	"	$\|Z_{vtx}\| < 30.0$ cm
11	$M_{3j} > 50.0$ GeV	$M_{3j} > 53.50$ GeV
12	"	$M_{3j} > 46.50$ GeV
13	$\|\cos\theta_3\| < 0.80$	$-0.76 < \cos\theta_3 < 0.84$
14	"	$-0.84 < \cos\theta_3 < 0.76$
15	$X_3 < 0.95$	$X_3 < 0.97$
16	"	$X_3 < 0.93$
17	HERWIG (detector corrections)	PYTHIA
To estimate uncertainty due to energy scale:		
18	$y_{jb} \longrightarrow$ $E_T^{jet} \longrightarrow$	$y_{jb} + 3\%$ $E_T^{jet} + 3\%$
19	$y_{jb} \longrightarrow$ $E_T^{jet} \longrightarrow$	$y_{jb} - 3\%$ $E_T^{jet} - 3\%$

Table 8.2: Default three-jet photoproduction selection cuts and alternative cuts used to estimate systematic effects. The number in the first column corresponds to the abscissa in Figures 8.4 - 8.9.

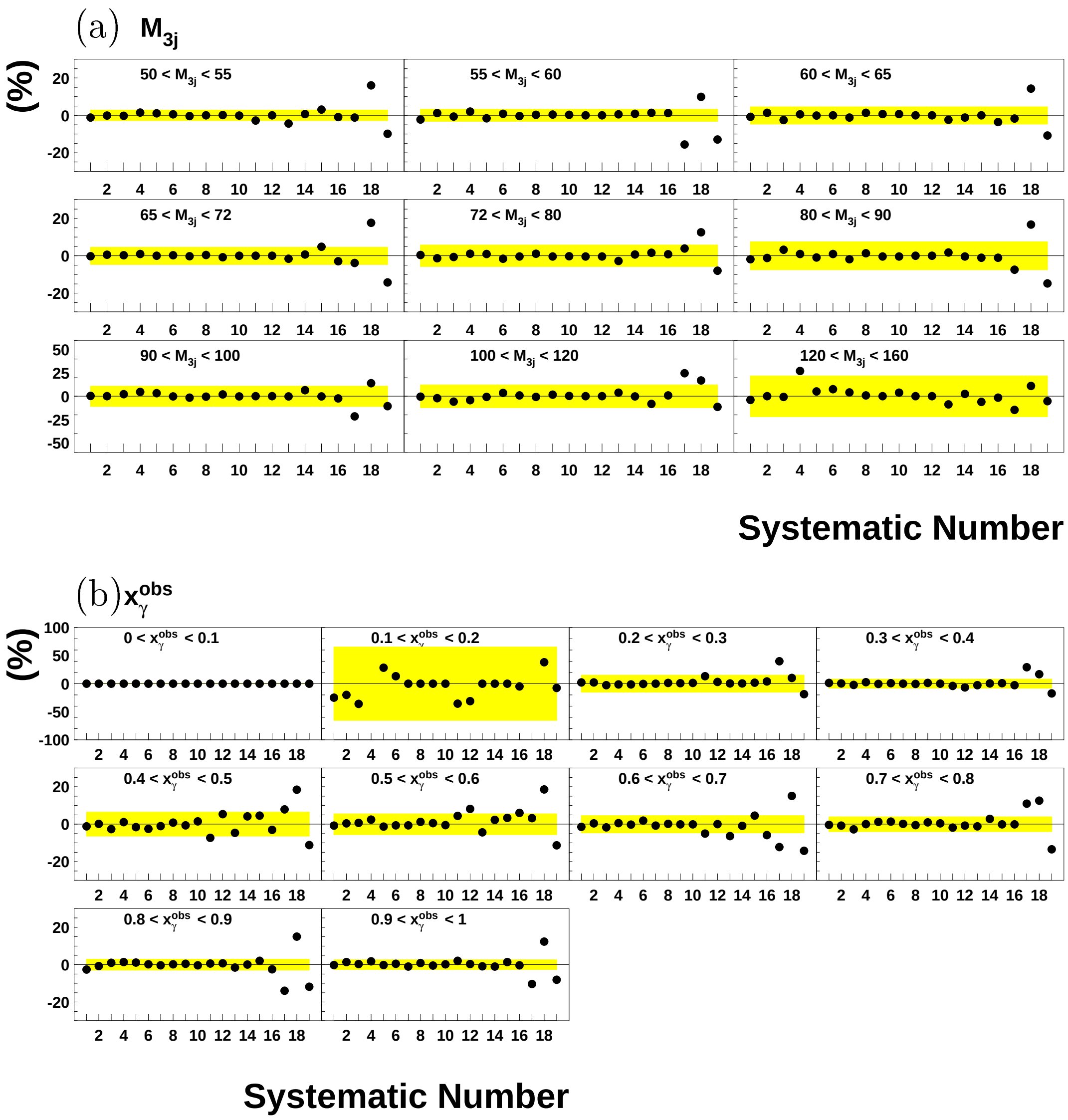

Figure 8.4: Summary of systematics uncertainties in (a) $d\sigma/dM_{3j}$ and (b) $d\sigma/dx_{\gamma}^{\rm obs}$. The percentage difference between the differential cross section obtained using the systematic and default cuts is shown for each systematic, which is defined and numbered as in table 8.2. The statistical error on the nominal result is shown as a shaded band. In (b) there are no data for $x_{\gamma}^{\rm obs} < 0.1$.

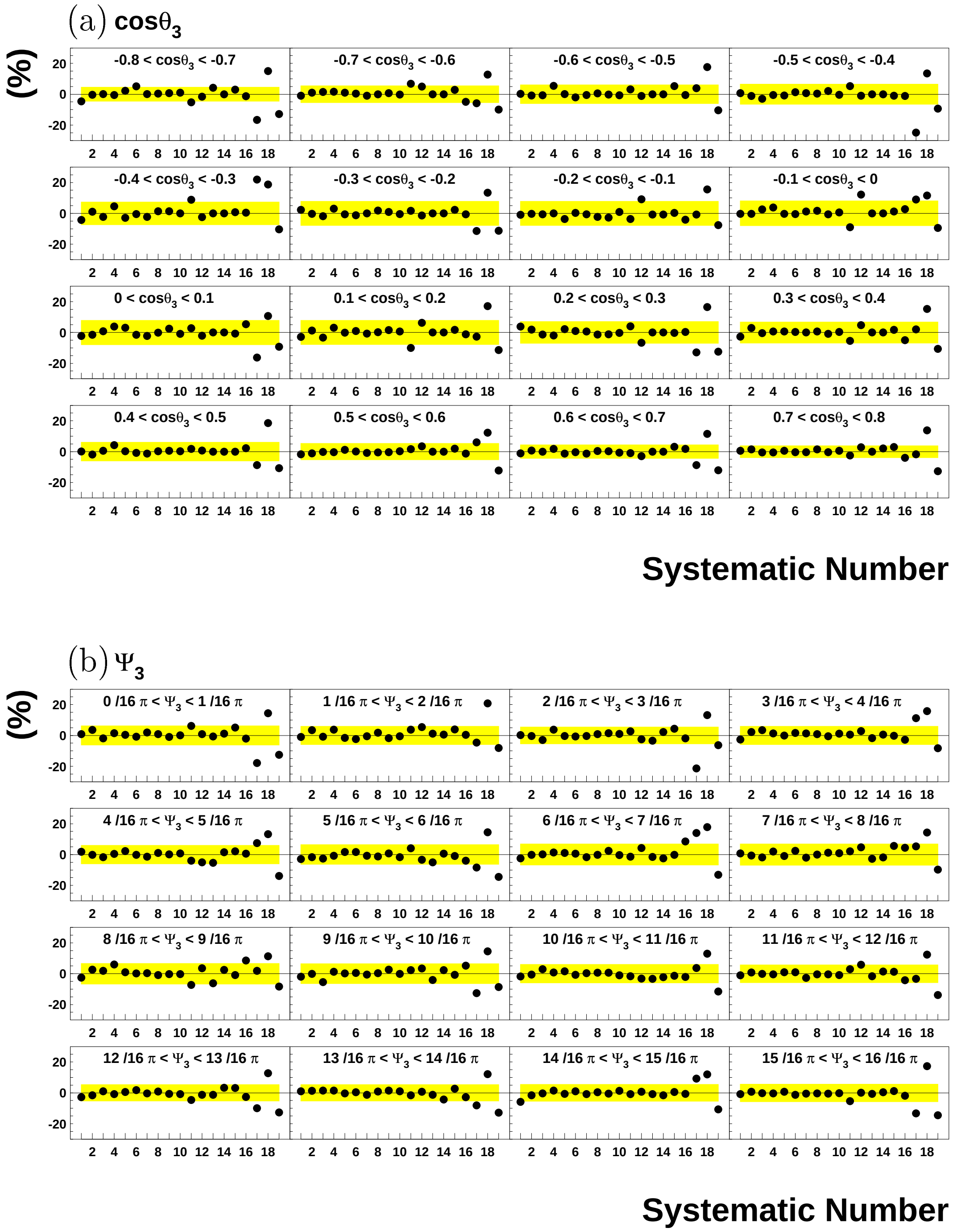

Figure 8.5: Summary of systematics uncertainties in (a) $d\sigma/d\cos\theta_3$ and (b) $d\sigma/d\psi_3$. The percentage difference between the differential cross section obtained using the systematic and default cuts is shown for each systematic, which is defined and numbered as in table 8.2. The statistical error on the nominal result is shown as a shaded band.

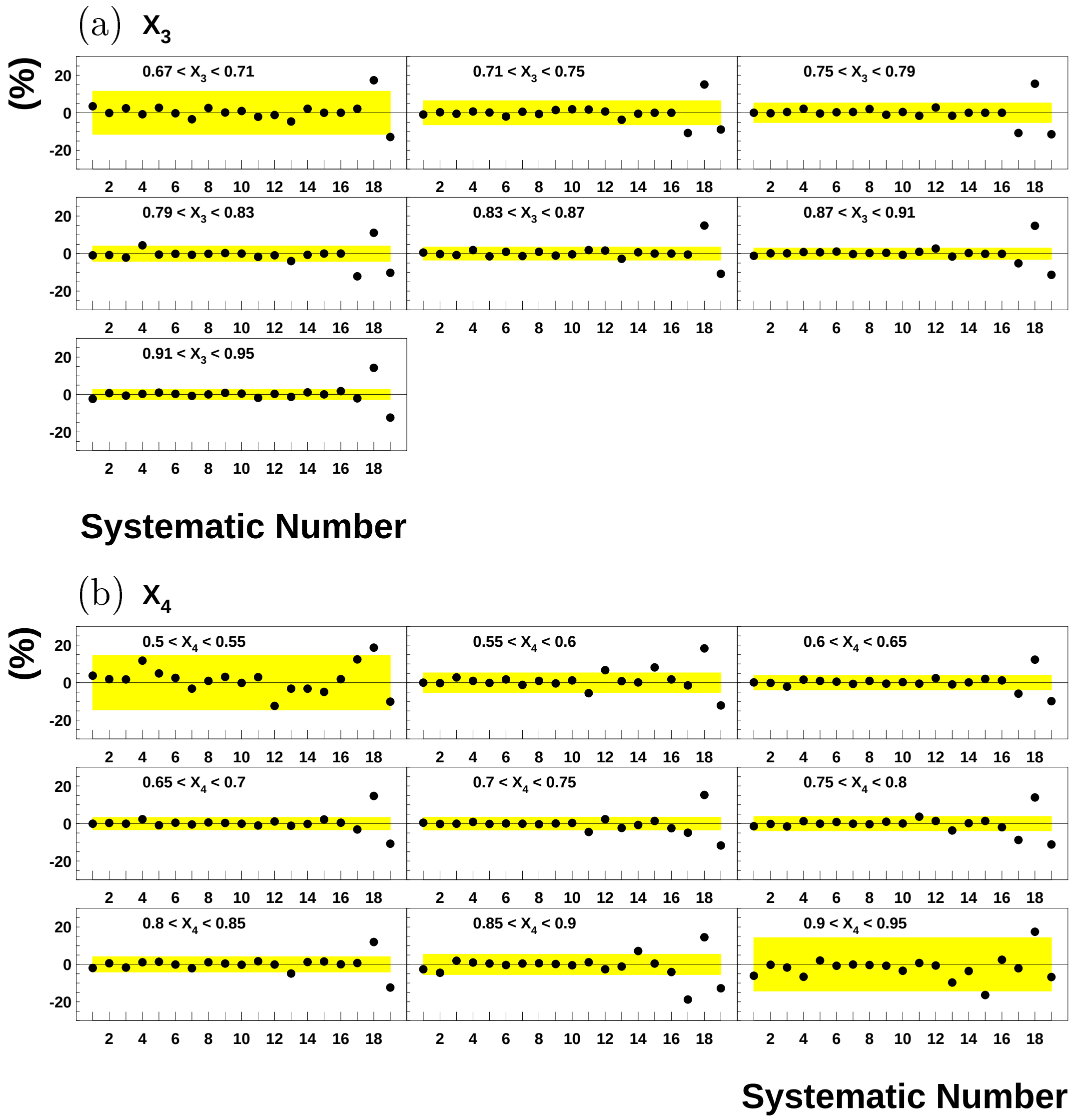

Figure 8.6: Summary of systematics uncertainties in (a) $d\sigma/dX_3$ and (b) $d\sigma/dX_4$. The percentage difference between the differential cross section obtained using the systematic and default cuts is shown for each systematic, which is defined and numbered as in table 8.2. The statistical error on the nominal result is shown as a shaded band.

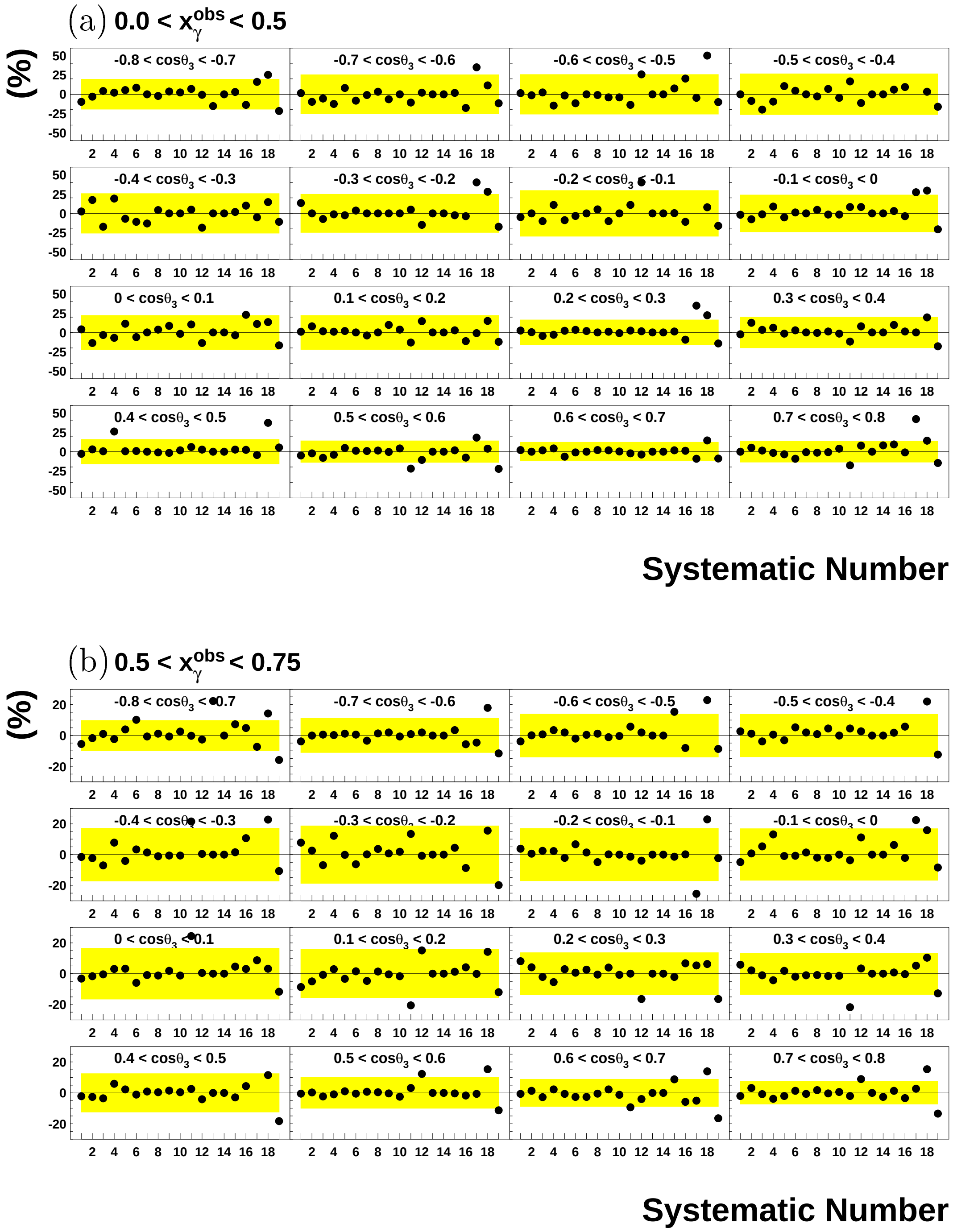

Figure 8.7: Summary of systematics uncertainties on $d\sigma/d\cos\theta_3$ where (a) $0.0 < x_\gamma^{\rm obs} < 0.5$ and (b) $0.5 < x_\gamma^{\rm obs} < 0.75$. The percentage difference between $d\sigma/d\cos\theta_3$ obtained using the systematic and default cuts is shown for each systematic, which is defined and numbered as in table 8.2. The statistical error on the nominal result is shown as a shaded band.

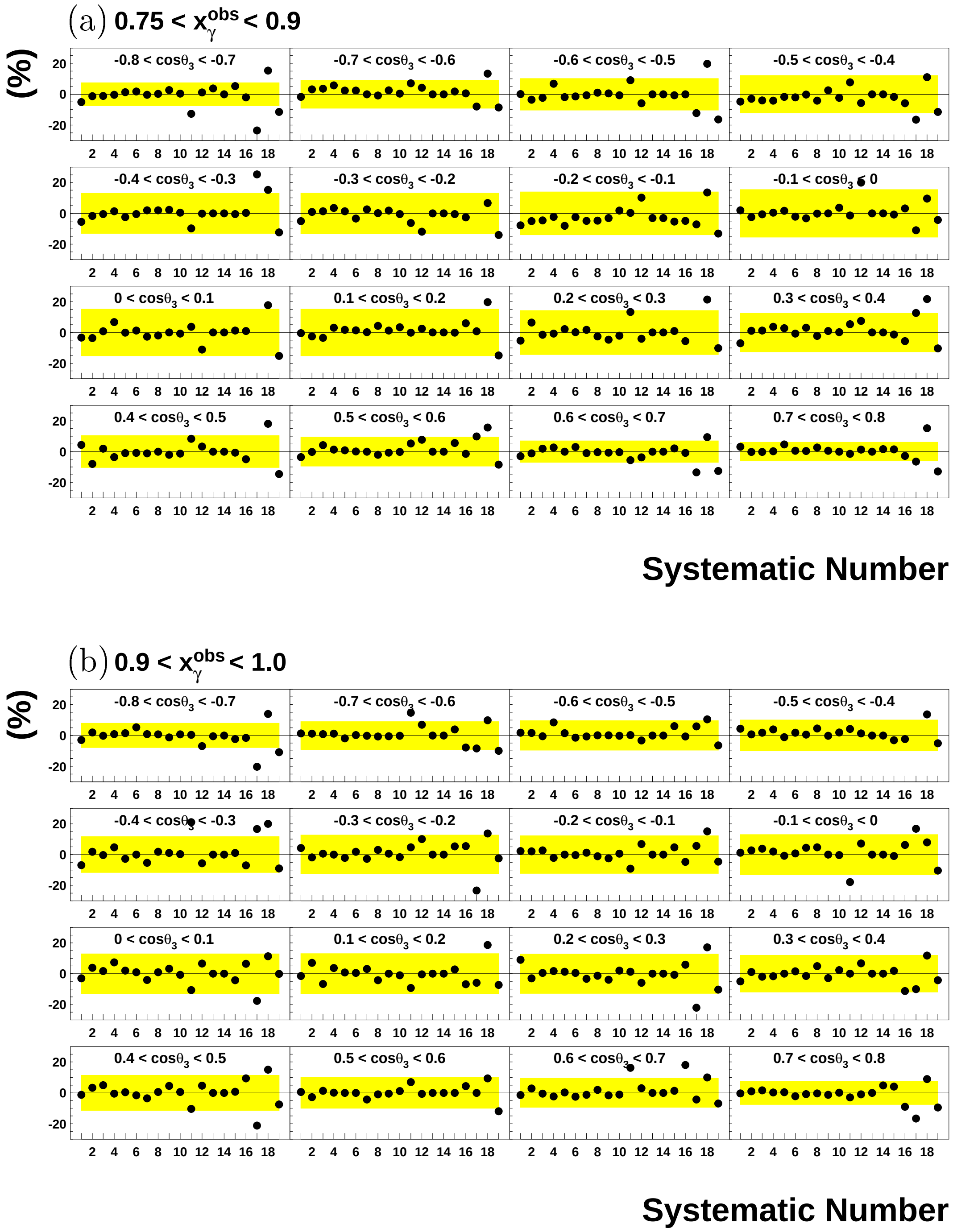

Figure 8.8: Summary of systematics uncertainties on $d\sigma/d\cos\theta_3$ where (a) $0.75 < x_\gamma^{\rm obs} < 0.9$ and (b) $0.9 < x_\gamma^{\rm obs} < 1.0$. The percentage difference between $d\sigma/d\cos\theta_3$ obtained using the systematic and default cuts is shown for each systematic, which is defined and numbered as in table 8.2. The statistical error on the nominal result is shown as a shaded band.

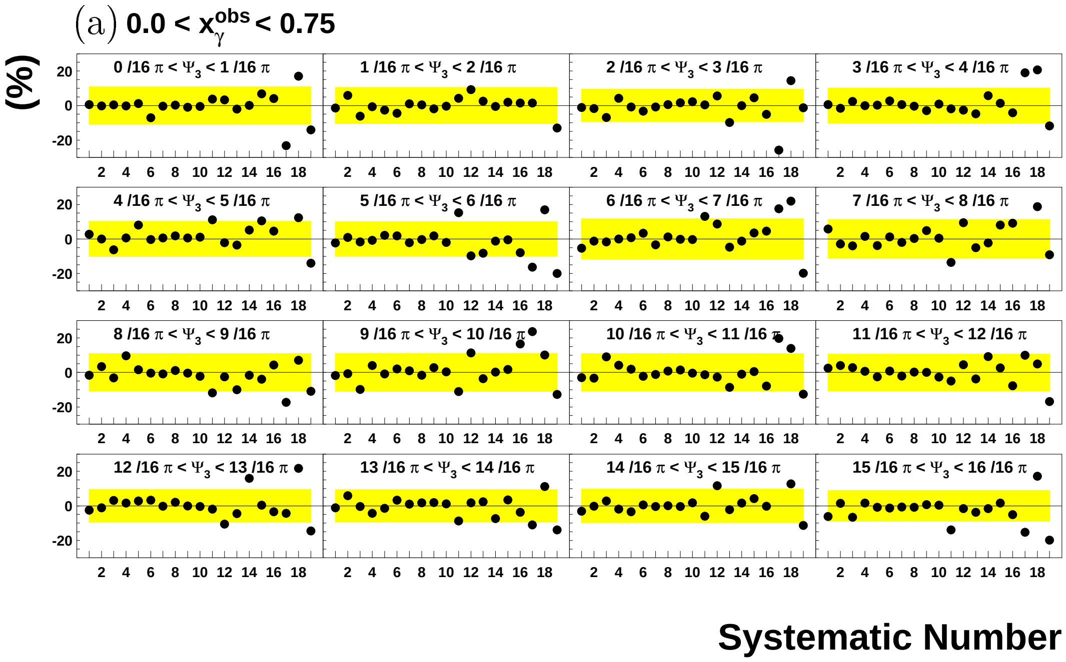

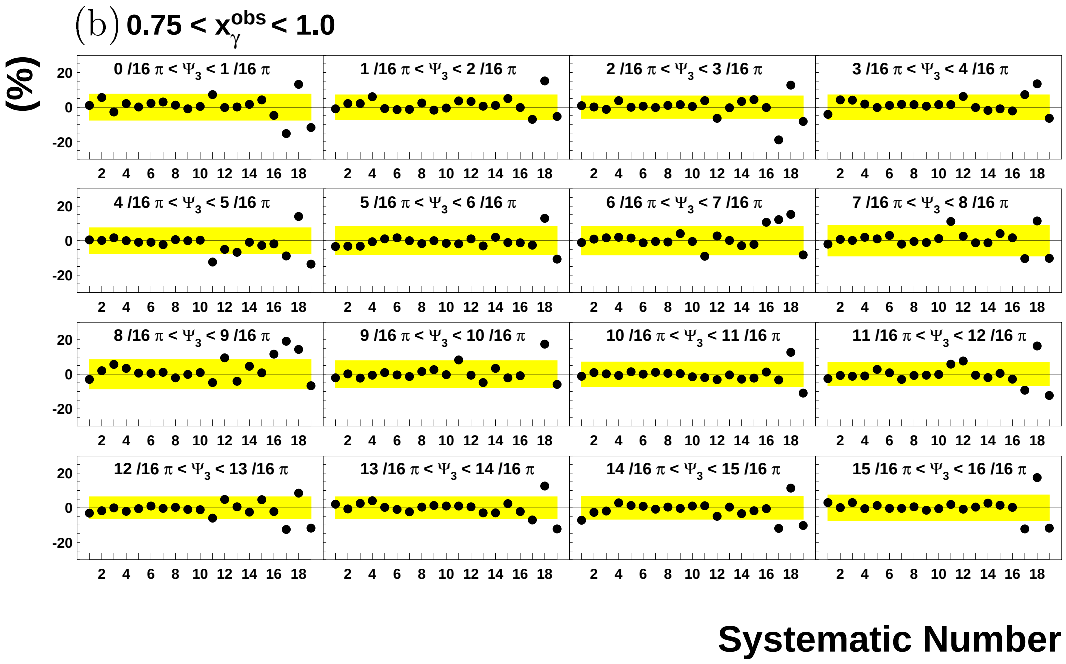

Figure 8.9: Summary of systematics uncertainties on $d\sigma/d\psi_3$ where (a) $x_\gamma^{obs} < 0.75$ and (b) $x_\gamma^{obs} > 0.75$. The percentage difference between $d\sigma/d\psi_3$ obtained using the systematic and default cuts is shown for each systematic, which is defined and numbered as in table 8.2. The statistical error on the nominal result is shown as a shaded band.

Chapter 9

Results

Differential cross sections are presented for two- and three-jet photoproduction events. The statistical errors for each point in the distributions are added in quadrature with the systematic errors for all the checks detailed in chapter 8, except for the uncertainty due to the energy scale. This is correlated between bins and so is shown separately as a shaded band.

The measured distributions are compared with $\mathcal{O}(\alpha\alpha_s^2)$ pQCD predictions (described in chapter 1) which are calculated using GRV, AFG and GS96 photon PDFs for two-jet distributions. The factorisation and renormalisation scales used in the calculation are varied by a factor of two to estimate the size of higher order corrections to the cross section.

For three-jet photoproduction, the calculation is leading order and its cross section is lower by a factor of ~ 2.1 than the data. In order to compare the shape of the measured data with theory the three-jet calculations are multiplied by the factors in Table 9.1.

Variable	$\sigma_{data}/\sigma_{nlo}$
M_{3J} ,x_γ^{obs}, $\cos\theta_3$, ψ_3, X_3, X_4	2.1
$\cos\theta_3$ $(0.0 < x_\gamma^{obs} < 0.5)$	3.9
$\cos\theta_3$ $(0.5 < x_\gamma^{obs} < 0.75)$	3.8
$\cos\theta_3$ $(0.75 < x_\gamma^{obs} < 0.9)$	7.7
$\cos\theta_3$ $(0.9 < x_\gamma^{obs} < 1.0)$	0.9
ψ_3 $(x_\gamma^{obs} < 0.75)$	3.8
ψ_3 $(x_\gamma^{obs} > 0.75)$	1.7

Table 9.1: NLO normalisation factors.

9.1 Two-jet Distributions

The two-jet cross sections and comparisons between data and theory are shown in Figures 9.1 to 9.5.

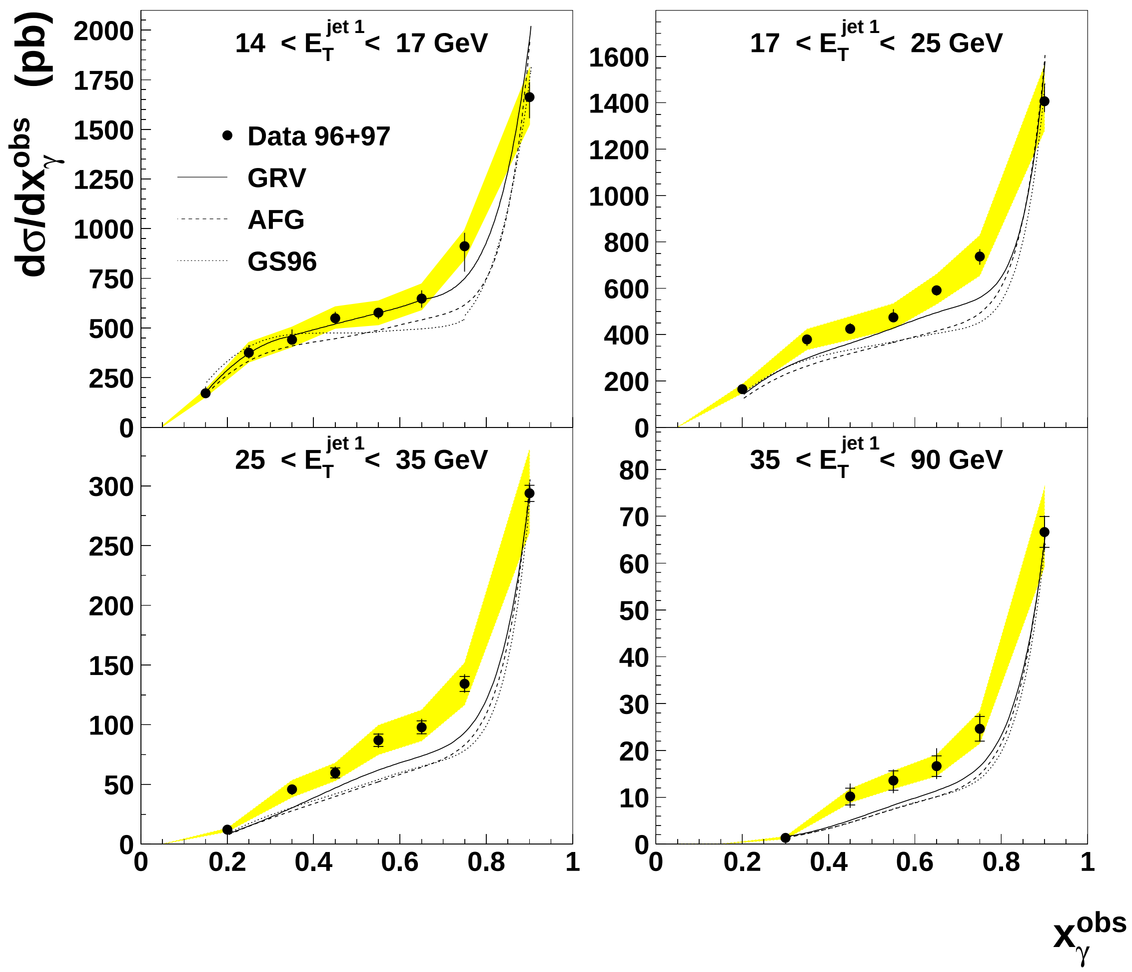

Figure 9.1: Two-jet cross section differential in x_γ^{obs} presented in four regions of $E_T^{jet\,1}$. Data points are shown with statistical errors (inner bars) and statistical and systematic errors added in quadrature (outer bars). The energy scale uncertainty is shown for each region by a shaded band. NLO predictions using GRV, AFG and GS96 for the photon PDF are also shown for each $E_T^{jet\,1}$ region.

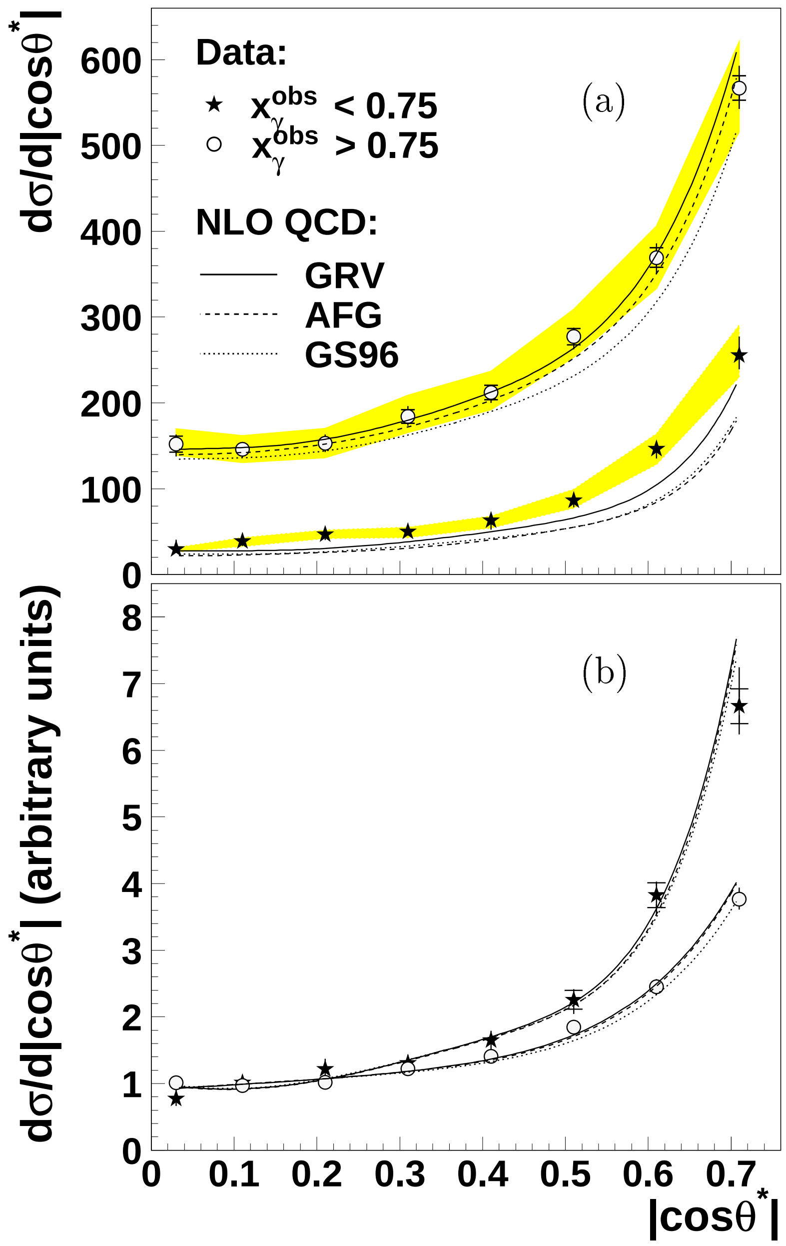

Figure 9.2: (a) Two-jet cross section differential in $|\cos\theta^*|$ shown for resolved- ($x_\gamma^{obs} < 0.75$) and direct-enhanced ($x_\gamma^{obs} > 0.75$) regions of x_γ^{obs}. Data points are shown with statistical errors (inner bars) and statistical and systematic errors added in quadrature (outer bars). The energy scale uncertainty is shown for each region by a shaded band. NLO predictions using GRV, AFG and GS96 for the photon PDF are also shown for each x_γ^{obs} region. (b) Data and theory in (a) normalised such that their integrals over the first three bins are equal.

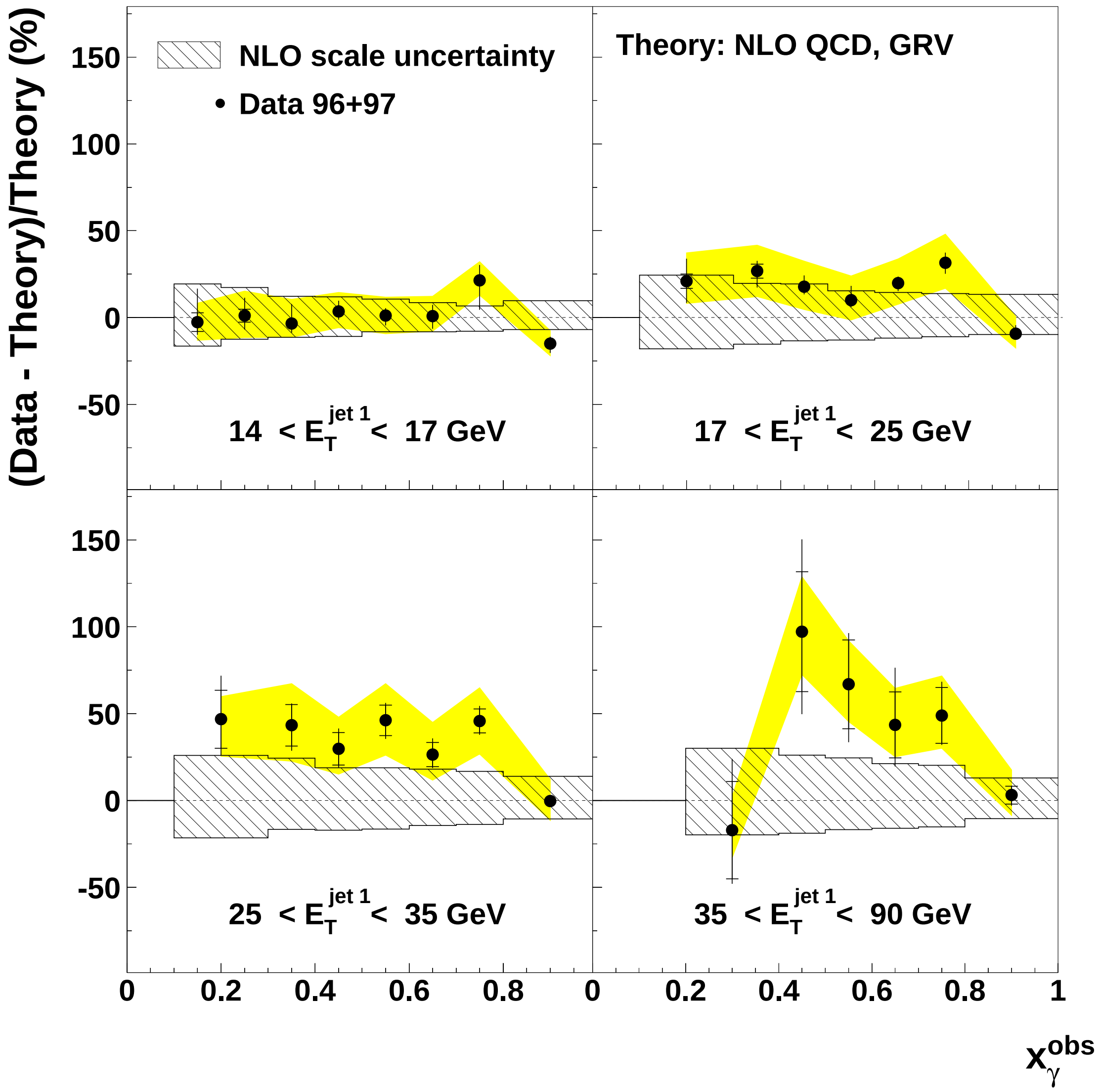

Figure 9.3: Percentage difference between data and theory for the two-jet cross section differential in x_γ^{obs} shown for four regions of $E_T^{jet\,1}$. The theory is an NLO pQCD prediction with GRV for the photon PDF. The uncertainty in this calculation due to choice of renormalisation and factorisation scale, μ, is shown by the hatched area, which is obtained by replacing μ in the calculation with $\mu \to 2\mu$ (lower limit) and $\mu \to \mu/2$ (upper limit). Data points are shown with statistical errors (inner bars) and statistical and systematic errors added in quadrature (outer bars). The energy scale uncertainty is shown for each region by a shaded band.

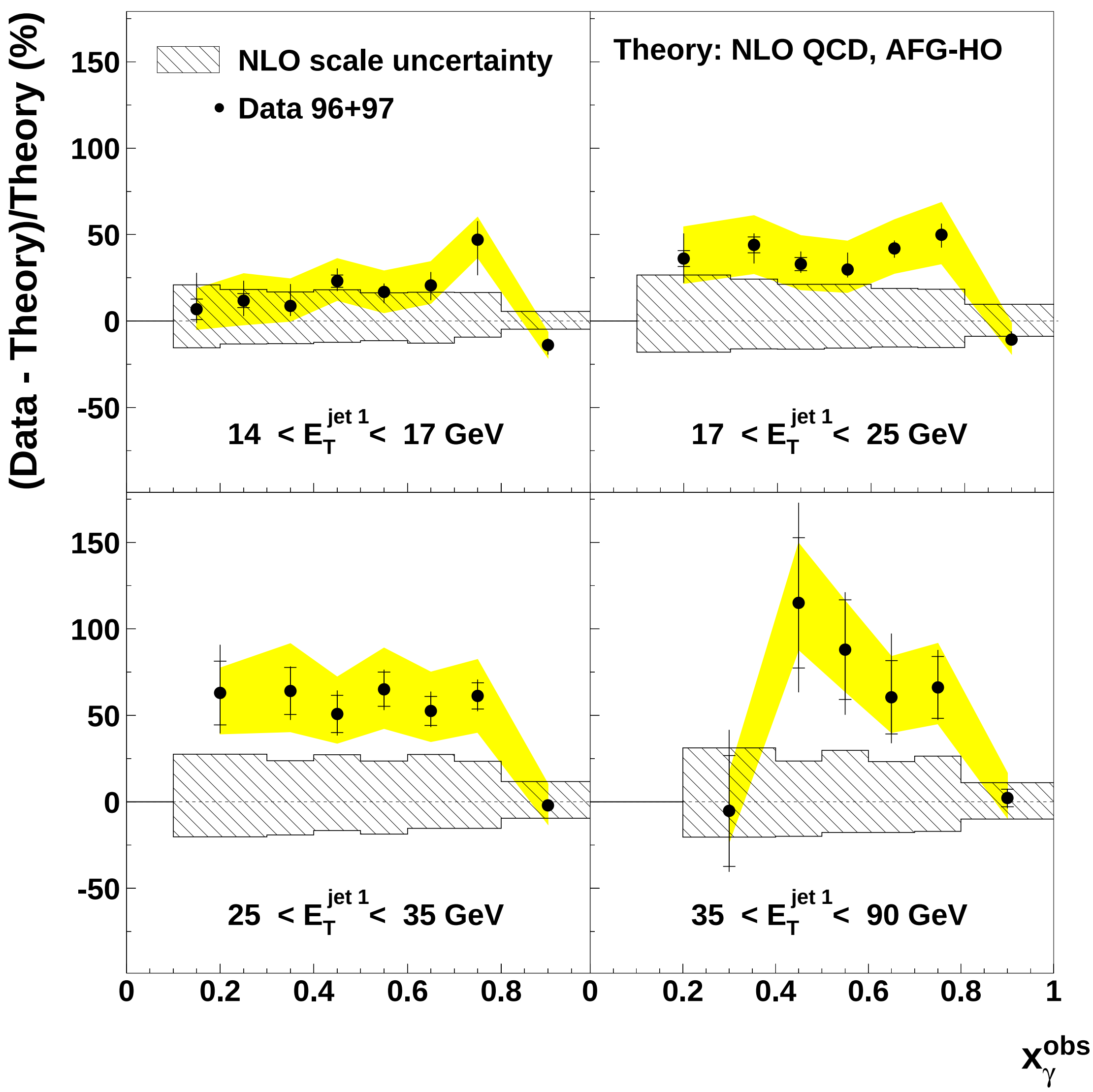

Figure 9.4: Percentage difference between data and theory for the two-jet cross section differential in x_γ^{obs} shown for four regions of $E_T^{jet\,1}$. The theory is an NLO pQCD prediction with AFG for the photon PDF. The uncertainty in this calculation due to choice of renormalisation and factorisation scale, μ, is shown by the hatched area, which is obtained by replacing μ in the calculation with $\mu \to 2\mu$ (lower limit) and $\mu \to \mu/2$ (upper limit). Data points are shown with statistical errors (inner bars) and statistical and systematic errors added in quadrature (outer bars). The energy scale uncertainty is shown for each region by a shaded band.

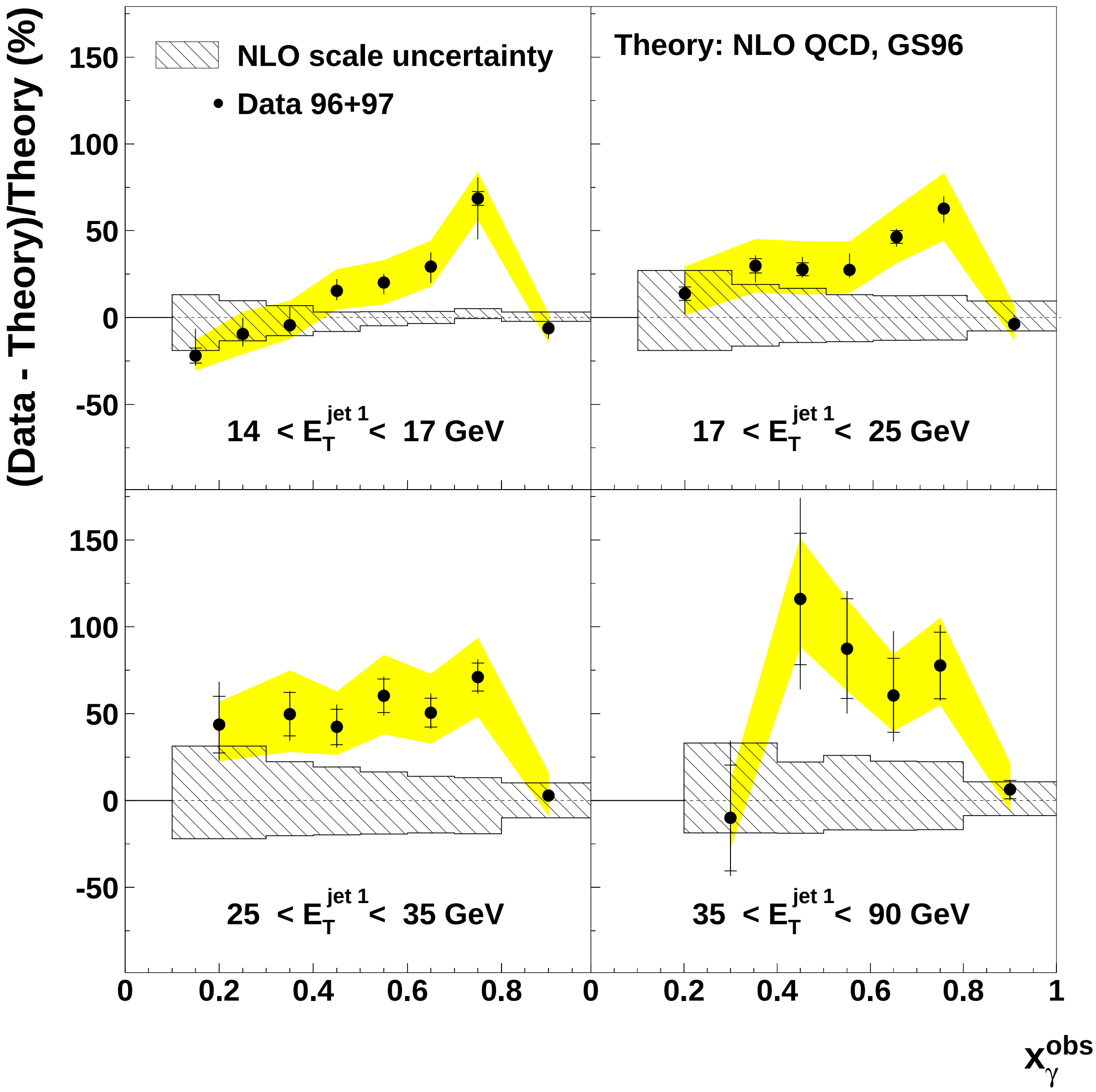

Figure 9.5: Percentage difference between data and theory for the two-jet cross section differential in x_γ^{obs} shown for four regions of $E_T^{jet\,1}$. The theory is an NLO pQCD prediction with GS96 for the photon PDF. The uncertainty in this calculation due to choice of renormalisation and factorisation scale, μ, is shown by the hatched area, which is obtained by replacing μ in the calculation with $\mu \rightarrow 2\mu$ (lower limit) and $\mu \rightarrow \mu/2$ (upper limit). Data points are shown with statistical errors (inner bars) and statistical and systematic errors added in quadrature (outer bars). The energy scale uncertainty is shown for each region by a shaded band.

9.2 Three-jet Distributions

The three-jet cross sections and comparisons between data and theory are shown in Figures 9.6 to 9.8.

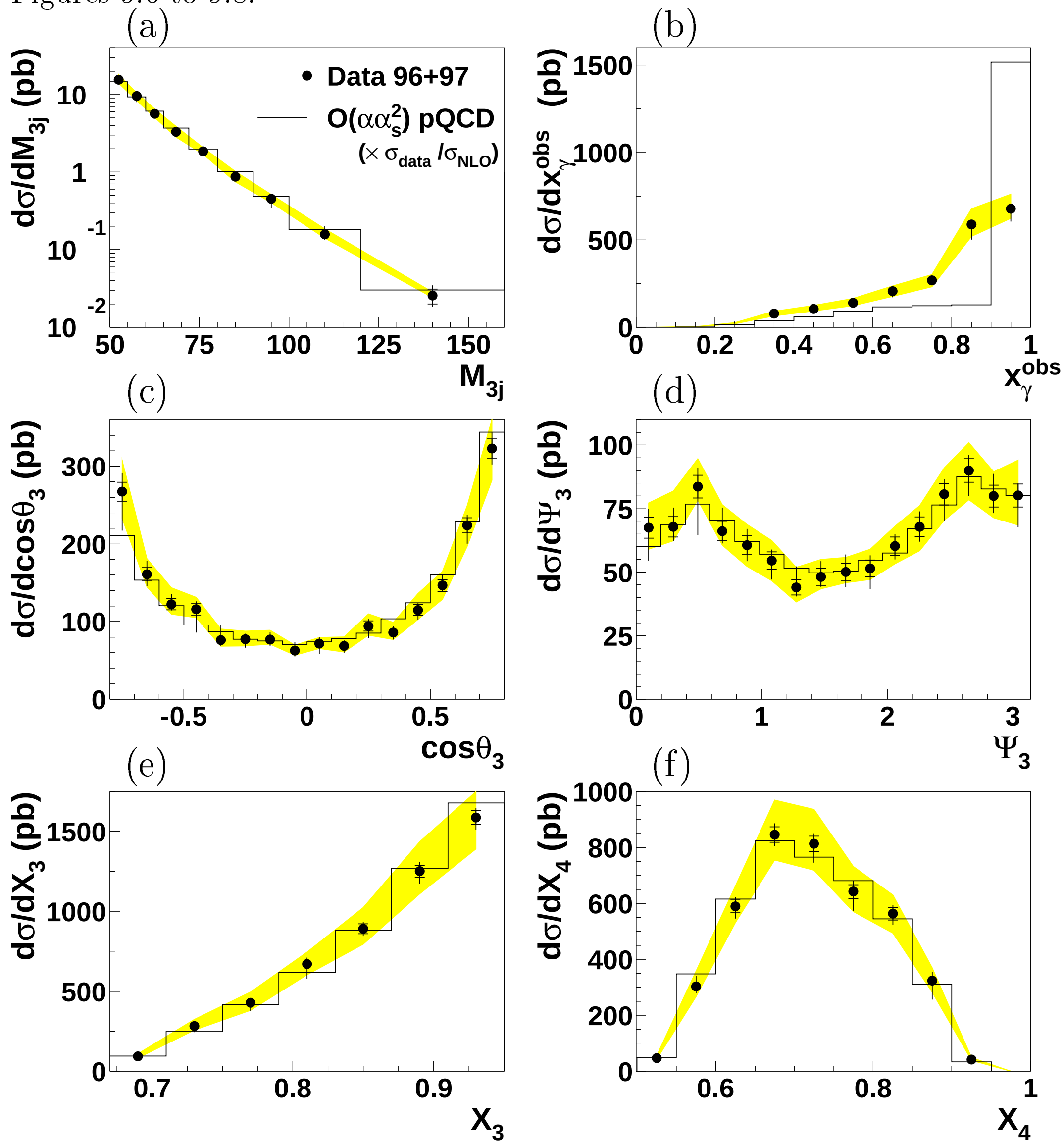

Figure 9.6: Three-jet cross section differential in (a) the three-jet invariant mass, M_{3j} (b) x_γ^{obs}, the angular vairables (c) $\cos\theta_3$ and (d) ψ_3, and the energy sharing variables (e) X_3 and (f) X_4. Data points are shown with statistical errors (inner bars) and statistical and systematic errors added in quadrature (outer bars). The energy scale uncertainty is shown for each distribution by a shaded band. A leading order pQCD calculation using GRV (photon PDF) and CTEQ 4M (proton PDF) is also shown, normalised to the data by the factors shown in Table 9.1.

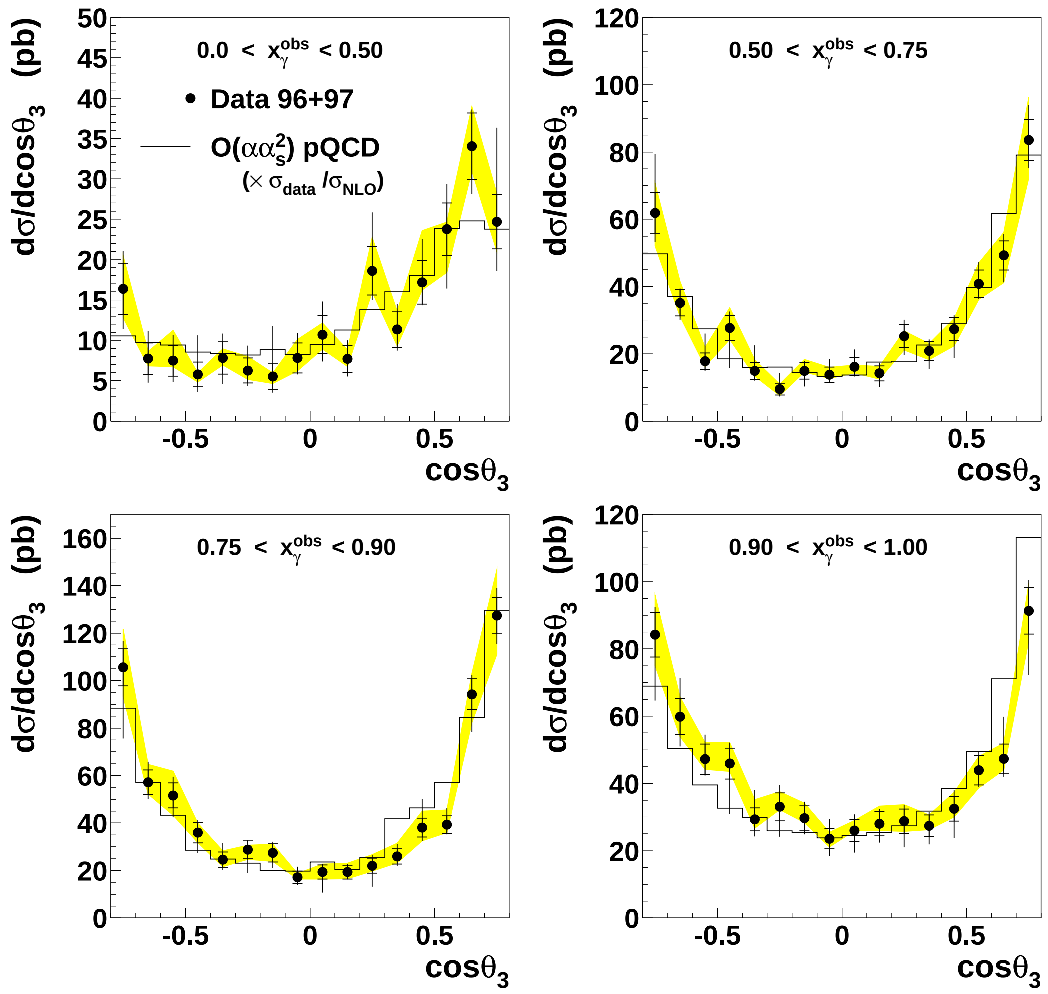

Figure 9.7: Three-jet cross section differential in $\cos\theta_3$ presented in four regions of x_γ^{obs}. Data points are shown with statistical errors (inner bars) and statistical and systematic errors added in quadrature (outer bars). The energy scale uncertainty is shown for each distribution by a shaded band. A leading order pQCD calculation using GRV (photon PDF) and CTEQ 4M (proton PDF) is also shown, normalised to the data by the factors shown in Table 9.1.

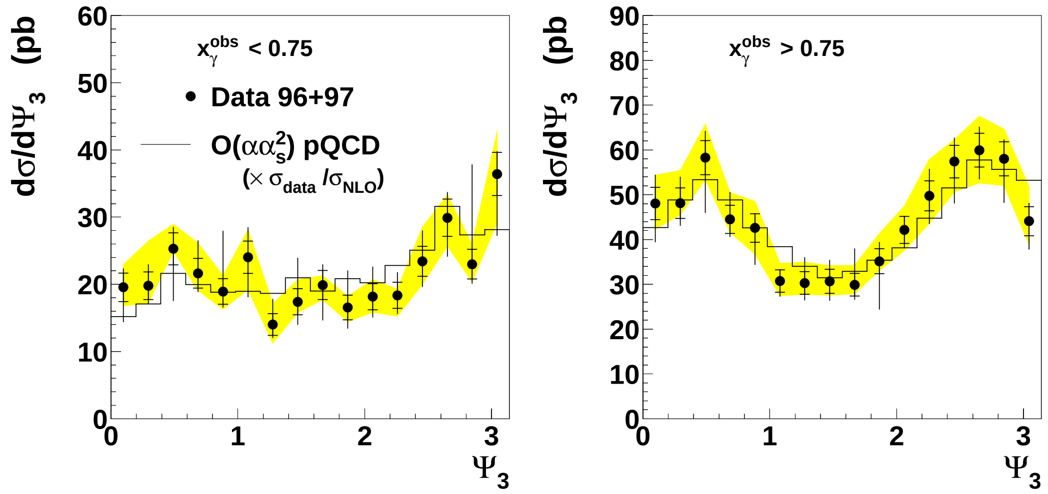

Figure 9.8: Three-jet cross section differential in ψ_3 presented for resolved- ($x_\gamma^{obs} < 0.75$) and direct-enhanced ($x_\gamma^{obs} > 0.75$) regions of x_γ^{obs}. Data points are shown with statistical errors (inner bars) and statistical and systematic errors added in quadrature (outer bars). The energy scale uncertainty is shown for each distribution by a shaded band. A leading order pQCD calculation using GRV (photon PDF) and CTEQ 4M (proton PDF) is also shown, normalised to the data by the factors shown in Table 9.1.

Chapter 10

Discussion

10.1 Two-jet Photoproduction

The two-jet photoproduction results in chapter 9 represent a six-fold increase in statistics over the previous analysis. The cross section is presented as a function of $x_{\gamma}^{\rm obs}$ and $\cos\theta^*$ to elicit information on the discrepancy between ZEUS data and theoretical predictions that was previously observed in $d\sigma/d\eta$ distributions [9].

In Figure 9.1 the measured $d\sigma/dx_{\gamma}^{\rm obs}$ distribution is compared with NLO predictions using three different photon PDFs, and in four bins of $E_{\rm T}^{jet\,1}$. The NLO underestimates the data in the region $x_{\gamma}^{\rm obs} < 0.8$ for the entire $E_{\rm T}^{jet\,1}$ range for calculations using AFG or GS96 for the photon PDF. Predictions using GRV are in good agreement with the data in the range $14 < E_{\rm T}^{jet\,1} < 17$ GeV and $x_{\gamma}^{\rm obs} < 0.8$, but also fall short of the data at higher $E_{\rm T}^{jet\,1}$.

The observed discrepancy could arise from a number of sources, such as inadequacies in the parton distribution functions or higher order corrections. In order to check that the calculations can reproduce two-jet photoproduction dynamics, the cross section differential in the jet scattering angle, θ^*, has been measured. In Figure 9.2(a) the shape and normalisation of $d\sigma/d|\cos\theta^*|$ in the region dominated by direct events $x_{\gamma}^{\rm obs} > 0.75$ is well reproduced by NLO calculations using GRV and AFG. Data in the resolved-enhanced region ($x_{\gamma}^{\rm obs} < 0.75$) however is not described well by any of the calculations, which fall short by $\sim$30% for GRV and $\sim$45% for AFG and GS96.

In Figure 9.2 (b) the data and NLO are normalised such that their integrals over the first three bins in $d\sigma/d|\cos\theta^*|$ are equal. This allows a comparison of their overall shape, and in particular, how rapidly their cross sections increase with $|\cos\theta^*|$. This is interesting because the shape of the distribution is sensitive to the spin of the propagator in the hard scatter. For spin-1 gluons $\sigma \sim (1 - |\cos\theta^*|)^{-2}$ while for spin-$\frac{1}{2}$ quark propagators $\sigma \sim (1 - |\cos\theta^*|)^{-1}$. Therefore the direct cross section, which is dominated by quark exchange, is expected to rise more slowly than the resolved cross section, which is dominated by gluon exchange. This is confirmed by the data in Figure 9.2, which is also well described by the NLO calculations for both direct and resolved events.

Both the $d\sigma/d|\cos\theta^*|$ and $d\sigma/dx_\gamma^{\rm obs}$ distributions disagree with the NLO calculations in the region which is most sensitive to the photon structure, while there is reasonable agreement in the region which is mainly sensitive to the proton structure. The percentage difference between data and theory is shown in Figures 9.3, 9.4 and 9.5 for calculations using GRV, AFG and GS96 photon PDFs respectively. An estimate of the error associated with higher order corrections to the NLO is shown by the hatched area. The shape and the size of the difference generally increases with $E_{\rm T}^{jet\,1}$ for all three NLO in bins where $x_\gamma^{\rm obs} < 0.8$. In order to estimate the significance of this discrepancy a χ^2 goodness-of-fit test has been performed for each photon PDF, where χ^2 is calculated by:

$$\chi^2 = \sum_{i=1}^{i=nbins} \frac{\left(\mathrm{NLO} \times \left(\frac{\mathrm{hadr.}}{\mathrm{part.}}\right)^{\mathrm{MC}} - u\right)_i^2}{\left(\sigma_{stat}^2 + \sigma_{sys}^2 + \sigma_{had}^2\right)_i} \tag{10.1}$$

The NLO calculation is only directly comparable to data when corrected for hadronisation. The size of the hadronisation effect in each bin, $(\frac{\mathrm{hadr.}}{\mathrm{part.}})_i^{\mathrm{MC}}$, is taken to be the average of HERWIG and PYTHIA estimates, as shown in Figure 6.11. The error on this estimate, σ_{had}, is then half the difference between the two MC models.

In Table 10.1(a) the χ^2/N values for a test including all 28 data points in the $d\sigma/dx_\gamma^{\rm obs}$ distribution in the range $14 < E_{\rm T}^{jet\,1} < 90$ GeV is shown, and then for each of the four $E_{\mathrm{T}}^{jet\,1}$ bins separately. The fit between data and theory is consistently better for GRV than AFG or GS96 in all regions of $E_{\mathrm{T}}^{jet\,1}$, although the overall χ^2/N is a very high at 5.6. The discrepancy between data and theory is most significant in the region $25 < E_{\mathrm{T}}^{jet\,1} < 35$ GeV for GRV and least significant at low $E_{\mathrm{T}}^{jet\,1}$.

(a)

Nominal Values		
PDF	factor	χ^2/N
All bins		
GRV	1.0	5.6
AFG	1.0	13.4
GS96	1.0	13.6
$14 < E_{\mathrm{T}}^{jet\,1} < 17$ GeV		
GRV	1.0	0.7
AFG	1.0	5.4
GS96	1.0	6.0
$17 < E_{\mathrm{T}}^{jet\,1} < 25$ GeV		
GRV	1.0	9.8
AFG	1.0	29.1
GS96	1.0	29.0
$25 < E_{\mathrm{T}}^{jet\,1} < 35$ GeV		
GRV	1.0	11.4
AFG	1.0	20.7
GS96	1.0	20.3
$35 < E_{\mathrm{T}}^{jet\,1} < 90$ GeV		
GRV	1.0	3.8
AFG	1.0	5.1
GS96	1.0	5.9

(b)

Minimised χ^2		
PDF	factor	χ^2/N
All bins		
GRV	1.11	3.6
AFG	1.13	8.0
GS96	1.11	8.4
$14 < E_{\mathrm{T}}^{jet\,1} < 17$ GeV		
GRV	1.00	0.9
AFG	1.12	3.5
GS96	1.09	5.1
$17 < E_{\mathrm{T}}^{jet\,1} < 25$ GeV		
GRV	1.13	4.3
AFG	1.19	14.2
GS96	1.20	11.3
$25 < E_{\mathrm{T}}^{jet\,1} < 35$ GeV		
GRV	1.18	5.9
AFG	1.24	13.6
GS96	1.23	10.5
$35 < E_{\mathrm{T}}^{jet\,1} < 90$ GeV		
GRV	1.16	2.9
AFG	1.17	4.3
GS96	1.22	4.3

(c)

Free		
PDF	factor	χ^2/N
All bins		
GRV	-	-
AFG	1.20	7.2
GS96	1.21	6.7
$14 < E_{\mathrm{T}}^{jet\,1} < 17$ GeV		
GRV	-	-
AFG	-	-
GS96	-	-
$17 < E_{\mathrm{T}}^{jet\,1} < 25$ GeV		
GRV	-	-
AFG	1.25	13.0
GS96	1.30	11.8
$25 < E_{\mathrm{T}}^{jet\,1} < 35$ GeV		
GRV	-	-
AFG	-	-
GS96	1.27	10.3
$35 < E_{\mathrm{T}}^{jet\,1} < 90$ GeV		
GRV	-	-
AFG	-	-
GS96	-	-

Table 10.1: Tables showing (a) the χ^2 per degree of freedom, N ($N = n_{\mathrm{bins}} - 1 - n_{\mathrm{parameters}}$), for a fit between data and GRV, AFG and GS96 NLO calculations (b) χ^2/N minimised by varying the normalisation of the NLO, f_{norm}, where f_{norm} is constrained by the condition in equation 10.2 (c) χ^2/N minimised by varying f_{norm} freely (values quoted only when different from those in Table (b))

The errors due to uncertainty in the absolute energy scale, σ_e, on the data and on the NLO calculations due to the scale uncertainty, σ_μ are correlated between bins and do not contribute to χ^2. This gives an artificially large value for χ^2/N. To take account for these uncertainties, χ^2 is minimised by varying the normalisation of the NLO cross section, f_{norm}. The value of f_{norm} is constrained by requiring that for every bin i :

$$\mathrm{NLO}_i - (\sigma_e + \sigma_\mu)_i < \mathrm{NLO}_i \times f_{norm} < \mathrm{NLO}_i + (\sigma_e + \sigma_\mu)_i \qquad (10.2)$$

The results of this constrained fit are shown in Table 10.1(b).

The minimised χ^2/N values are much smaller than those obtained using the nominal values in most regions, though the best overall fit, using the GRV photon PDF, is still rather poor at 3.6. The most significant difference between data and theory for GRV is still in the $25 < E_{\mathrm{T}}^{jet} < 35$ GeV region, for which χ^2 minimises when the NLO is increased by ~18%.

The GRV χ^2 function reaches its minimum within the region allowed by equation 10.2. For AFG and GS96, however, the overall χ^2 minimisation is constrained by the upper limit on f_{norm} in the $x_\gamma^{\mathrm{obs}} > 0.8$ bin and in the region $14 < E_{\mathrm{T}}^{jet\,1} < 17$ GeV. It is possible that σ_μ in this bin has been underestimated, and so the fit is repeated with no constraint on f_{norm} as a cross check. The results are quoted in Table (c) where they are different from Table (b). The AFG and GS96 NLO overall χ^2 functions minimise when the NLO is increased by ~20%, which is considerably higher than GRV at 11%. It is clear that despite removing this constraint, the fit between data and NLO remains poor, though slightly improved for AFG and GS96.

The χ^2/N values remain large, even after a free fit is performed, because the offset between the discrepancy at $x_\gamma^{\mathrm{obs}} < 0.8$ and at $x_\gamma^{\mathrm{obs}} > 0.8$ is unchanged by varying f_{norm}, and because the direct points are comparatively well measured. To check that the large χ^2 is not due entirely to the four direct points, they are removed from the fitting procedure and the χ^2 calculation. The results are shown in Table 10.2 for each PDF.

The value of χ^2/N changes little for the nominal values when the direct point is removed from the fit, and improves when minimised in a constrained fit, as shown in Tables 10.2(a) and 10.2(b) respectively. The AFG χ^2/N value reduces by over two thirds when the direct points are removed from the fit, whilst

(a)

No Fit ($x_\gamma^{\rm obs} < 0.8$)		
PDF	factor	χ^2/N
$14 < E_{\rm T}^{jet\,1} < 90$ GeV		
GRV	1.0	5.4
AFG	1.0	13.2
GS96	1.0	13.4

(b)

Constrained Fit ($x_\gamma^{\rm obs} < 0.8$)		
PDF	factor	χ^2/N
$14 < E_{\rm T}^{jet\,1} < 90$ GeV		
GRV	1.16	2.2
AFG	1.28	2.4
GS96	1.15	6.7

(c)

Free Fit ($x_\gamma^{\rm obs} < 0.8$)		
PDF	factor	χ^2/N
$14 < E_{\rm T}^{jet\,1} < 90$ GeV		
GRV	-	-
AFG	1.34	2.0
GS96	1.30	4.3

Table 10.2: Same description as Table 10.1 except the $x_\gamma^{\rm obs} > 0.8$ point in each $E_{\rm T}^{\rm jet\,1}$ region is excluded from the χ^2 calculation.

for GS96 the improvement is only slight, mostly due to its relatively small scale uncertainty in the region $14 < E_{\rm T}^{\rm jet\,1} < 17$ GeV. The NLO calculation using GRV gives the best overall fit to data, though it is interesting to note that even without the highest $x_\gamma^{\rm obs}$ point in the calculation, χ^2/N is still large at 2.2 and the discrepancy between data and theory, therefore, significant.

As before, the fit is repeated with $f_{\rm norm}$ unconstrained. The results in Table 10.2(c) show that despite ignoring the direct points and performing an unconstrained fit, the difference between data and theory is still significant for all three photon PDFs tested. To illustrate that the method used gives sensible values for χ^2, and that it minimises at a reasonable value of $f_{\rm norm}$, the percentage difference between data and theory is shown in Figure 10.1 for different values of $f_{\rm norm}$, obtained using the minimisation procedure.

In Figure 10.2 a comparison between data and theory is shown where χ^2/N has been minimised in a constrained fit, and the photon PDF used in the theory is that which has been shown to fit the data best, GRV. The χ^2/N value for this NLO is 3.6, but since all of the possible errors were not considered in the calculation, it is not sensible to quote confidence levels. Other sources of error such as the effect on χ^2 of the choice of proton PDF, and α_s need to be studied before this could be done.

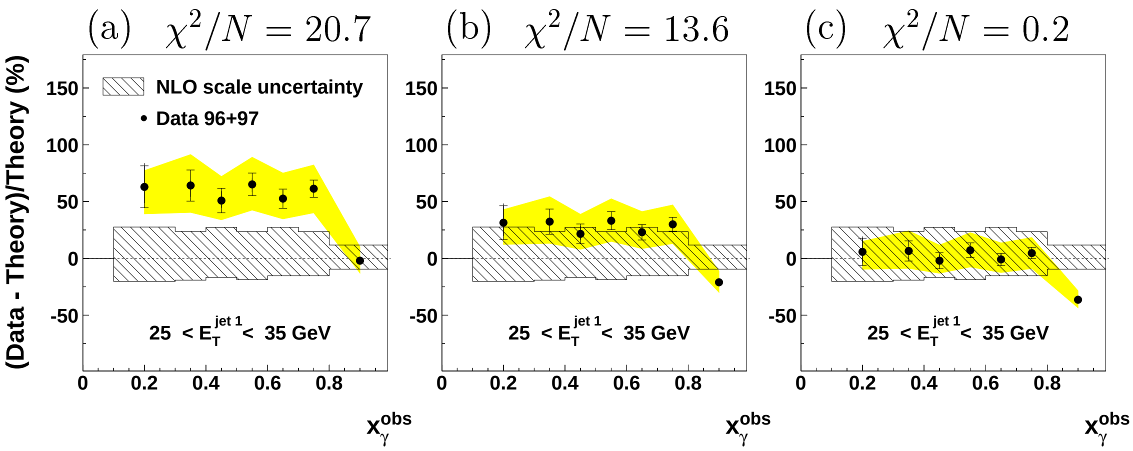

Figure 10.1: In (a) the percentage difference between data and theory is shown for NLO calculations using the AFG photon structure function. In (b) the NLO is normalised by a factor of 1.24, which gives the smallest χ^2/N when the fit is constrained by the energy and NLO scale uncertainties. In (c) the NLO is normalised by 1.54, which is the value at which χ minimises when the range in the fit is free and the point at $x_\gamma^{\rm obs} > 0.8$ is excluded from the fit.

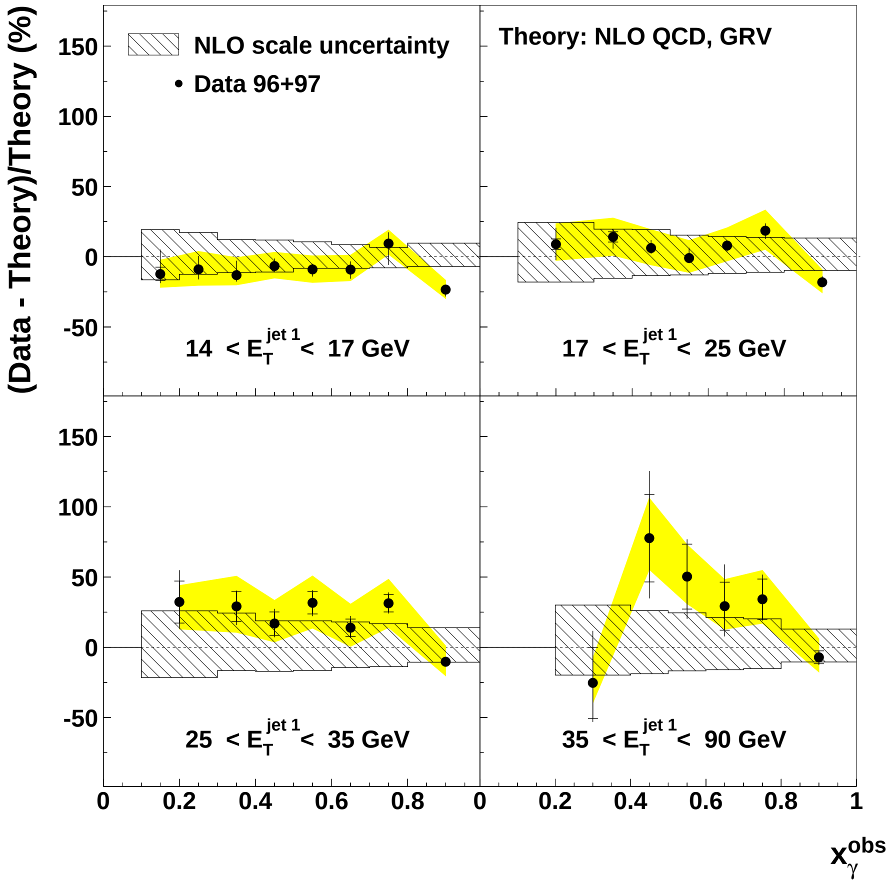

Figure 10.2: The percentage difference between data and theory is shown where the GRV photon structure function is used in the NLO calculation. The NLO is normalised by a factor of of 1.11, which is the value at which the best overall fit is found.

10.2 Three-jet Photoproduction

The three-jet photoproduction measurements presented in Chapter 9 reproduce the results of the first three-jet analysis from ZEUS [10], but with more than double the statistics, and using an improved method of reconstructing the hadronic final state (see section 3.2). In addition, the three-jet cross section differential in $x_\gamma^{\rm obs}$ is presented for the first time with HERA data, and its influence on the angular variables $\cos\theta_3$ and ψ_3 has been investigated.

The data are compared with an $\mathcal{O}(\alpha\alpha_s^2)$ pQCD calculation which has been normalised to the data. Despite being only LO for three-jet events, the calculation agrees very well in shape with the data as a function of the mass ($M_{\rm 3j}$), angular ($\cos\theta_3$ and ψ_3) and energy sharing (X_3 and X_4) variables (see Figure 9.6). The shape of $d\sigma/dx_\gamma^{\rm obs}$ in Figure 9.6 (b), however, is sensitive to the lack of higher orders in the calculation, and does not agree with the data, although its shape is consistent with LO expectations.

Unlike the two-jet case, the leading jet in the three-jet centre of mass frame is distinguishable in terms of energy and orientation from the non-leading jets. This makes it is possible to determine whether it is aligned with the incoming proton (forward) or the incoming photon (backward) and $\cos\theta_3$ is therefore shown for both positive and negative values. In Figure 9.6 (c) the $\cos\theta_3$ distribution shows a slight forward bias in both the data and LO. The development and origin of this asymmetry in $\cos\theta_3$ has been investigated further, and is shown in Figure 9.7 to vary with $x_\gamma^{\rm obs}$. At $x_\gamma^{\rm obs} < 0.5$ the highest energy jet has a tendency to be in the forward direction. As $x_\gamma^{\rm obs}$ increases, it becomes increasingly likely that the leading jet is aligned with the incoming photon.

The shape of the $\cos\theta_3$ data distribution is described well by LO in each of the $x_\gamma^{\rm obs}$ regions studied, except at $0.9 < x_\gamma^{\rm obs} < 1.0$. HERWIG gives a slightly better overall description of the data, as shown in Figure 10.3 where the direct component is shown separately for both $\cos\theta_3$ and ψ_3 distributions. There is a clear tendency for the highest energy jet to go backwards for direct events, and forwards for resolved events. However, the shape of the $\cos\theta_3$ distribution in each bin of x_γ^{obs} cannot be entirely ascribed to the ratio of direct to resolved events, as the shape in regions $x_\gamma^{\mathrm{obs}} < 0.5$ and $0.5 < x_\gamma^{\mathrm{obs}} < 0.75$ look very different despite being both overwhelming resolved bins. Nor is it immediately obvious why direct and resolved events are biased in these ways.

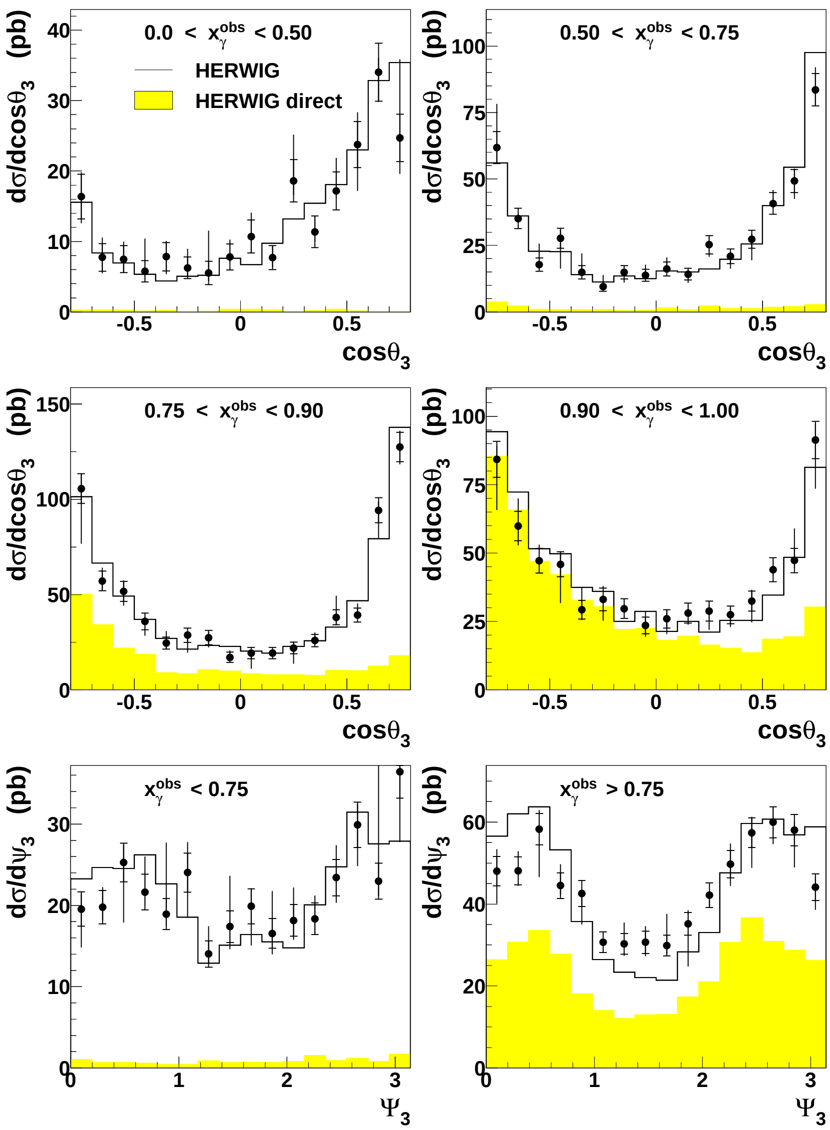

Figure 10.3: Three-jet differential cross sections compared to HERWIG MC. Direct and resolved MC events are combined according to their cross section, and then normalised to the cross section of the data.

HERWIG MC events have been used to investigate the origin of the asymmetry, which assumes that the MC describes the data well enough to be used for this purpose. The results point to three main factors which influence the shape of the $\cos\theta_3$ distributions. Firstly, the forward η cut imposed on all three jets influences the shape. This is shown in Figure 10.4 (a), where HERWIG is used to estimate $\mathrm{d}\sigma/\mathrm{d}\cos\theta_3$ when the restriction on jet η is varied. The forward η cut suppresses both forward and backward $\cos\theta_3$, though the effect on the latter is stronger. This means that though the distribution is roughly symmetric with the cut used in the actual measurement, $\eta < 2.4$, it is backward peaked for $\eta < 3.0$ and forward peaked for $\eta < 2.0$. Changing the backward η cut from $\eta < -3$ to $\eta < -2$ has no effect on the distribution in either normalisation or shape.

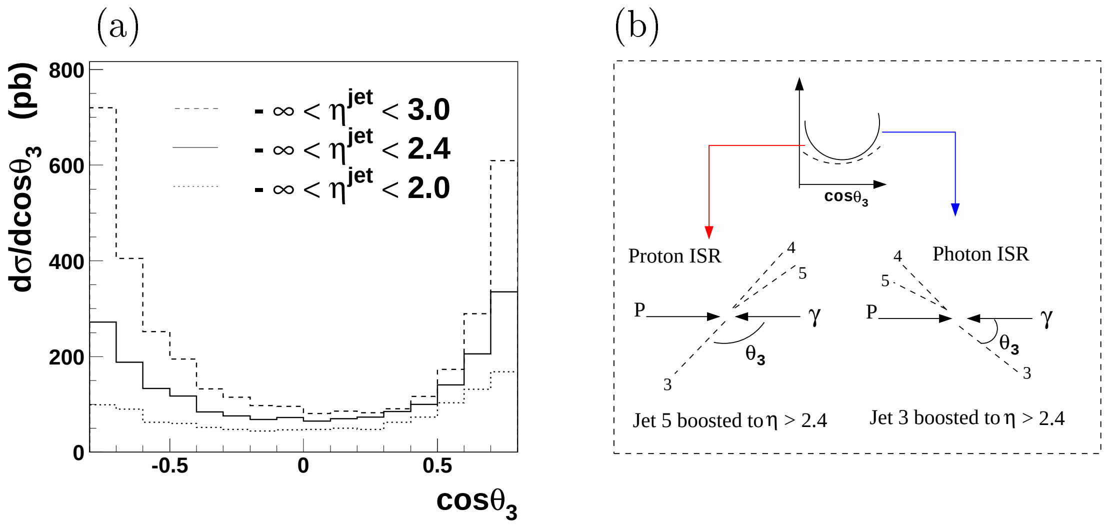

Figure 10.4: In (a) the effect of a forward η cut on the three-jet cross section differential in $\cos\theta_3$ is shown for hadron-level HERWIG MC. Diagram (b) shows how a forward η cut suppresses events where the third jet arises from either photon or proton ISR.

It has been shown in the previous analysis that the third jet arises predominantly from initial state radiation (ISR). It seems sensible, therefore, to assume that forward values of $\cos\theta_3$ occur when this third jet is radiated off a parton from the incoming photon, called here photon ISR. In this case the third jet would be in the backwards direction, and therefore the highest energy jet would most likely be going forwards. By similar reasoning it can be assumed that the backward peak in $\cos\theta_3$ is due mainly to proton ISR. Figure 10.4 (b) illustrates how both the proton and photon ISR peaks in the $\cos\theta_3$ distribution could be affected by a forward η cut. The asymmetric beam energies mean that the boost is always positive along the proton direction, and so the backward η cut does not suppress events unless $\eta_{\mathrm{cut}}^{\mathrm{backward}} > -1.5$, which is seen in both data and MC studies.

The second important factor when explaining the shape of three-jet $\cos\theta_3$ distributions, is the shape of the individual subprocess distributions in $\cos\theta_3$. In Figure 10.5 (a) the four main subprocesses which contribute to the three-jet cross section at $x_{\gamma}^{\mathrm{obs}} < 0.5$ region are shown. The distributions are shown for both $\eta < 2.4$ and $\eta < 3.0$, though the latter is less biased and therefore more useful for interpretation. The subprocesses in Figure 10.5 (a) have outgoing partons that are either of the same type and therefore indistinguishable in their rest frame, or different i.e. qg. The two subprocesses with an outgoing quark and a gluon are asymmetric in $\cos\theta_3$, while the other two are roughly symmetric. Also, the two asymmetric subprocesses have opposite behaviours with $\cos\theta_3$ such that the process $qg \to qg$ (where the incoming quark is from the photon) is backward peaked, whilst $gq \to gq$ is forward peaked.

The 2$\to$2 partonic cross section has been calculated for various ep subprocesses in [85]. Figure 10.5 (b) illustrates how an asymmetric distribution in $\cos\theta$ arises, where θ is the angle between the proton beam direction and the outgoing quark. The $\hat{t}$-channel subprocess dominates over $\hat{u}$-channel for both $qg \to qg$ and $gq \to gq$, which in the first case leads to a peak at large $\cos\theta$, and in the second to a peak at small $\cos\theta$.

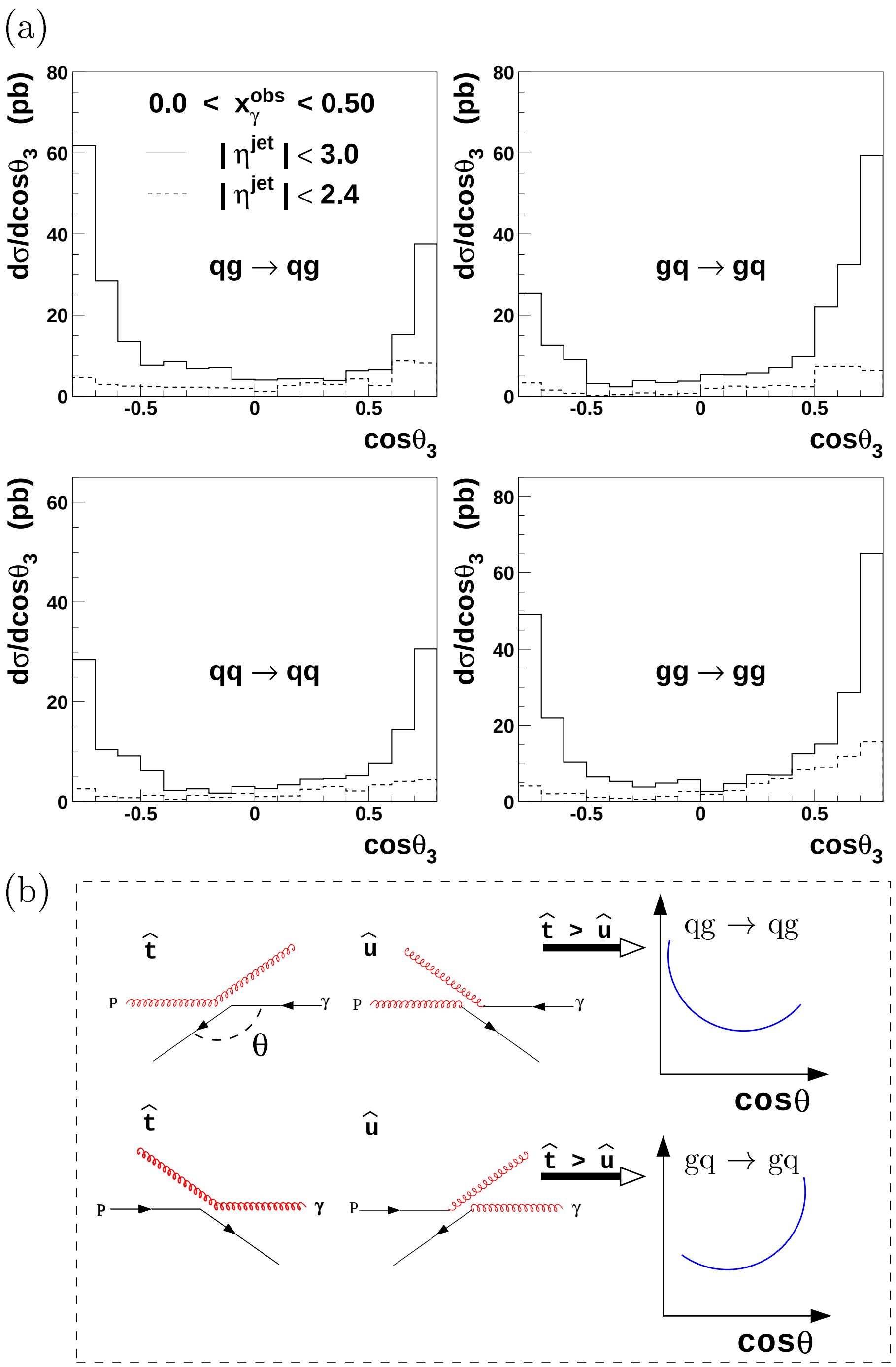

Figure 10.5: In (a) the distributions for the four main subprocesses that contribute to the three-jet cross section at $x_\gamma^{\rm obs} < 0.5$ are shown for hadron level HERWIG MC. The 2→2 parton scattering subprocesses are labelled $ab \to cd$ where a refers to the parton from the photon and b refers to the parton from the proton. Diagram (b) shows how the dominance of the $\hat{t}$-channel subprocess over $\hat{u}$-channel leads to an asymmetric distribution in the subprocess partonic cross section differential in $\cos\theta$, where θ is the angle between the proton beam direction and the outgoing quark.

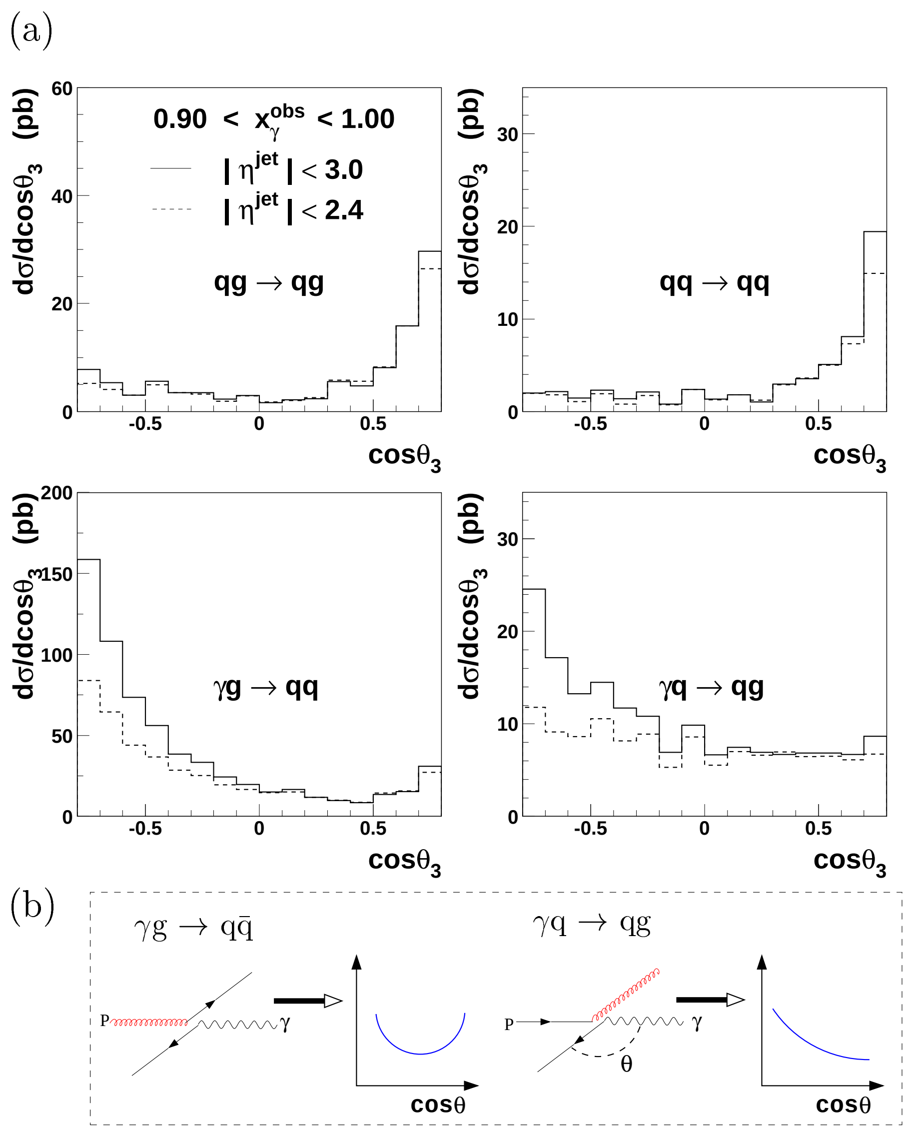

Figure 10.6: In (a) the distributions for the four main subprocesses that contribute to the three-jet cross section at $x_\gamma^{\text{obs}} > 0.9$ are shown for hadron level HERWIG MC. The 2→2 parton scattering subprocesses are labelled $ab \to cd$ where a refers to the parton from the photon and b refers to the parton from the proton. Diagram (b) shows the shape of 2→2 parton scattering $\cos\theta$ distributions involving a photon in the initial state, where θ is the angle between the proton beam direction and the outgoing quark.

The shape of three-jet $\cos\theta_3$ subprocess distributions and those obtained from 2→2 scattering where the quark jet scattering angle is plotted are very similar. This suggests that the presence of a third jet effectively tags a quark jet as the leading jet where there is a choice between a quark or gluon jet. Quark jets are more collimated and radiate less energy than gluon jets, so this is plausible. Alternatively, the orientation of the third jet, which is more likely to be radiated from an incoming gluon than a quark, could account for the peaks in the asymmetric three-jet subprocesses. It is difficult to separate the effects of these two explanations, but they both indicate that the shape of $\cos\theta_3$ distributions are influenced by the photon and proton PDFs.

Before the influence of PDFs on the $\cos\theta_3$ distribution is explored, the shape of the subprocess distributions in a region of phase space dominated by direct events is examined. In Figure 10.6 (a) $\cos\theta_3$ distributions for the two dominant resolved and two direct subprocesses are shown for $x_\gamma^{\rm obs} > 0.9$. The third jet in resolved events at very high $x_\gamma^{\rm obs}$ will, by virtue of *being* at high $x_\gamma^{\rm obs}$, arise mostly from photon rather than proton ISR. The backward peak in $qg \to qg$ seen at $x_\gamma^{\rm obs} < 0.5$ is therefore heavily suppressed at $x_\gamma^{\rm obs} > 0.9$. For direct events however, if the third jet arises from ISR it must be from proton ISR, and therefore both subprocess are backward peaked. The $\gamma g \to qq$ subprocess falls more steeply than $\gamma q \to qg$, which is also true for the 2→2 partonic subprocesses shown in Figure 10.6 (b). Figure 10.6 (a) also indicates that the effect of the η cut on the shape of the distribution is less at high $x_\gamma^{\rm obs}$.

Given that the shape of individual subprocesses are different, presumably the overall shape is sensitive to their relative mixture in the cross section. This is the third factor that has been studied using MC in order to understand the three-jet data. In Figure 10.7 (a) the fraction of resolved events which are asymmetric, that is either $qg \to qg$ or $gq \to gq$, are shown as a function of $x_\gamma^{\rm obs}$, and for both $\eta < 2.4$ and $\eta < 3.0$. More than half of all resolved events are of this type, and the fraction increases with $x_\gamma^{\rm obs}$. Of these events, the fraction with a quark in the

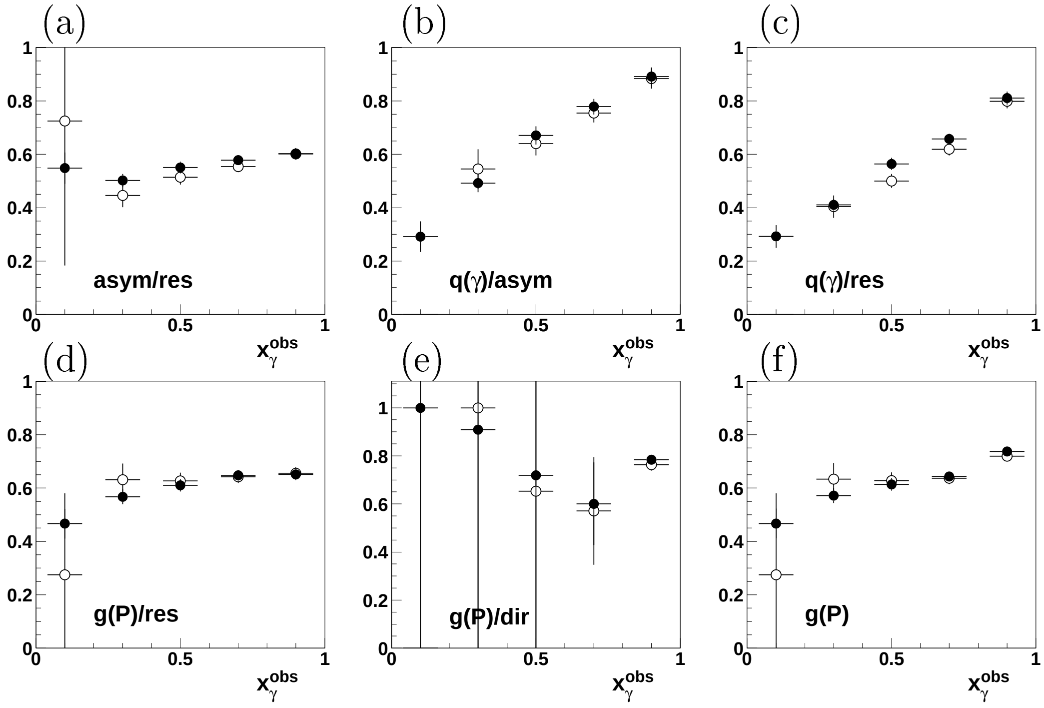

Figure 10.7: Distribution of (a) the fraction of resolved MC events where the subprocess is qg→qg (b) the fraction of qg→qg events with an incoming quark from the photon (c) the fraction of resolved events with a quark from the photon (d) the fraction of resolved events with a gluon from the incoming proton (e) the fraction of direct events with a gluon from the proton and (f) the fraction of total events with a gluon from the proton for three-jet photoproduction HERWIG MC events as a function of $x_\gamma^{\rm obs}$, shown for both $\eta < 2.4$ (circles) and $\eta < 3.0$ (dots).

photon (and hence a gluon in the proton) taking part in the hard scatter rises rapidly with $x_\gamma^{\rm obs}$, from around 30% to 90% as shown in Figure 10.7 (b). This is true also for resolved events as a whole, as shown in Figure 10.7 (c). The fraction of resolved events where a gluon from the proton is involved in the scatter rises more slowly with $x_\gamma^{\rm obs}$ as is shown in Figure 10.7 (d) and is generally greater that 50%. Figure 10.7 (d) shows that this fraction is also high for direct events. The fraction of total three-jet events with a gluon from the proton, $g(P)$, as estimated by HERWIG MC is shown in Figure 10.7 (e) to be rising slightly with $x_\gamma^{\rm obs}$. In summary, the shape of these distributions seems to be driven mostly by the increase in the quark fraction in the photon as $x_\gamma^{\rm obs}$ increases, and the difference in these ratios for cross sections with $\eta < 2.4$ and $\eta < 3.0$ is generally small.

To test the sensitivity of the $\cos\theta_3$ distribution to $g(P)$ and $q(\gamma)/res$, and by association the proton and photon PDFs, these two parameters have been maximised and minimised in HERWIG MC cross sections which are then normalised to the data. The shape of $\cos\theta_3$ shows particular sensitivity to these changes in two of the four $x_\gamma^{\rm obs}$ bins. In Figures 10.8 (a) and (b) the $\cos\theta_3$ distribution for $0.5 < x_\gamma^{\rm obs} < 0.75$ is shown with $g(P)$ and $q(\gamma)/res$ maximised and minimised. The shape is much more sensitive to changes in the photon parameter, $g(\gamma)$/res, than $g(P)$. The description of data by MC shown in Figure 10.3 can also be improved by reducing $g(\gamma)/res$ by 0.15, as is shown in Figure 10.8 (c).

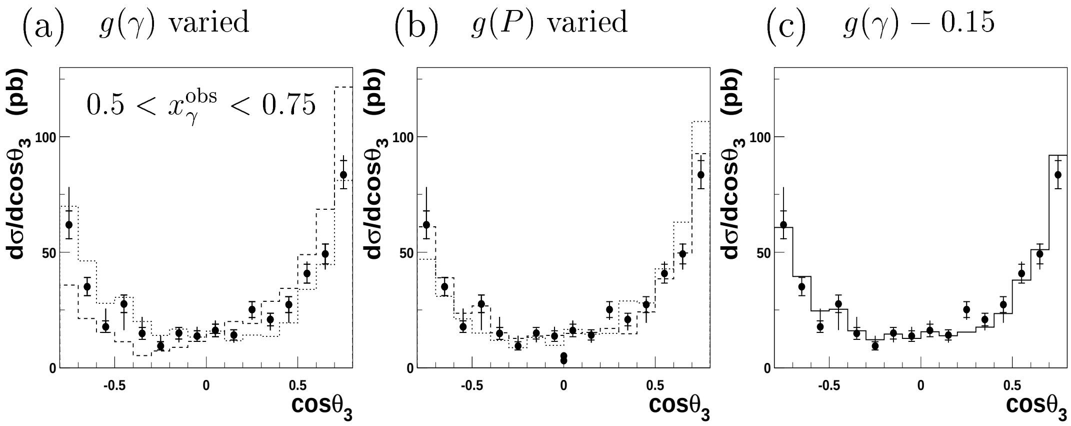

Figure 10.8: Three-jet cross section differential in $\cos\theta_3$ and with $0.5 < x_\gamma^{\rm obs} < 0.75$. The data (points) are compared to HERWIG MC (lines) which has been normalised to the data. In (a) the shape of the HERWIG distribution is shown where the fraction of photon-gluon induced events, $g(\gamma)$, is maximised (dashed line) and minimised (dotted line). In (b) MC is shown where the fraction of proton-gluon induced events, $g(P)$, is varied. In (c) $g(\gamma)$ has been decreased by 0.15 in the MC.

The shape of $\cos\theta_3$ is sensitive to changes in both $g(P)$ and $q(\gamma)/res$ at $x_\gamma^{\rm obs} > 0.9$, as shown in Figure 10.9. To get a better agreement with the data, the MC distribution in Figure 10.3 (d) needs its shape altered such that the backward peak is slightly less pronounced. This could be done by reducing $g(\gamma)/res$ drastically, or a less dramatic reduction in $g(P)$. A good fit is shown in Figure 10.9 (c), where $g(P)$ is reduced by 0.2. The effect on the ψ_3 distribution of a change in these values is shown in Figures 10.10 (a) for $x_\gamma^{\rm obs} < 0.75$ and 10.10 (b) for $x_\gamma^{\rm obs} > 0.75$. The values of these parameters are altered by the amounts that were shown to improve the $\cos\theta_3$ fit in the two sensitive regions of $x_\gamma^{\rm obs}$: $0.5 < x_\gamma^{\rm obs} < 0.75$ and $x_\gamma^{\rm obs} > 0.9$. The ψ_3 MC distribution at low $x_\gamma^{\rm obs}$ is only weakly affected by the changes. For high $x_\gamma^{\rm obs}$ however, reducing $g(P)$ by 0.2 gives an improvement in the fit of MC to data over that shown in Figure 10.10 (b), whilst reducing $g(\gamma)/res$ by 0.15 worsens it slightly.

Reducing $g(P)$ is similar to reducing the fraction of gluon in the proton, though the exact relationship between these two actions is complicated by the fact that the amplitudes of the individual subprocesses vary. However, a downward shift in $g(P)$ as recommended by this study, agrees quantitatively with the downward adjustment made in xG between the CTEQ 3M and CTEQ 4M versions of the proton PDF (see Figure 10.11) in the region of $x_{\rm proton}^{\rm obs}$ where the three-jet measurement is made ($0.04 < x_{\rm proton}^{\rm obs} < 0.4$). The LO calculation and HERWIG use the same photon PDF (GRV) whilst HERWIG uses CTEQ-3M and the LO calculation uses CTEQ-4M. The difference in xG between these two proton PDFs

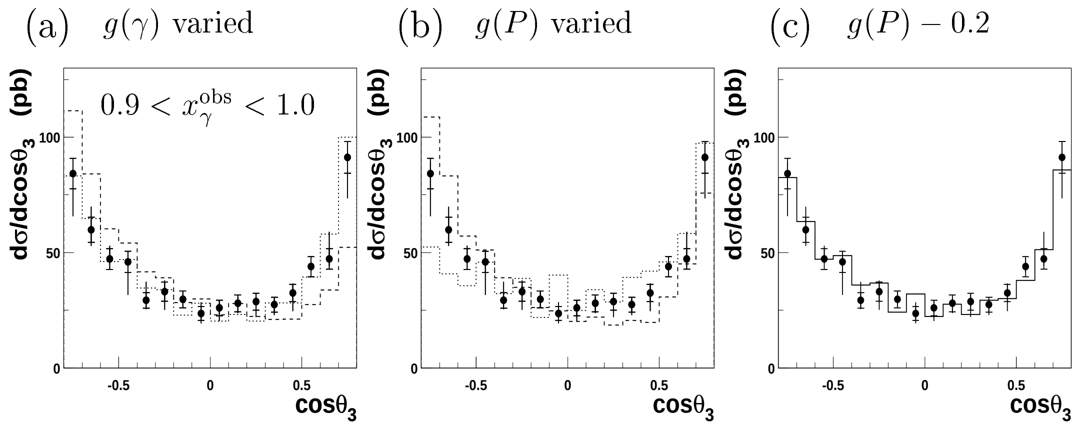

Figure 10.9: Three-jet cross section differential in $\cos\theta_3$ and with $0.9 < x_\gamma^{\rm obs} < 1.0$. The data (points) are compared to HERWIG MC (lines) which has been normalised to the data. In (a) the shape of the HERWIG distribution is shown where the fraction of photon-gluon induced events is maximised (dashed line) and minimised (dotted line). In (b) MC is shown where the fraction of gluon in the proton is varied. In (c) the fraction of proton-gluon induced events has been decreased by 0.2 in the MC.

is consistent with their different $\cos\theta_3$ shapes at highest $x_\gamma^{\rm obs}$, and is consistent with the change expected from Figure 10.9 (b). In Figure 10.12 the fit between normalised MC and data is shown for $\cos\theta_3$ and ψ_3 distributions where $g(P)$ has been reduced by 0.2 in all regions.

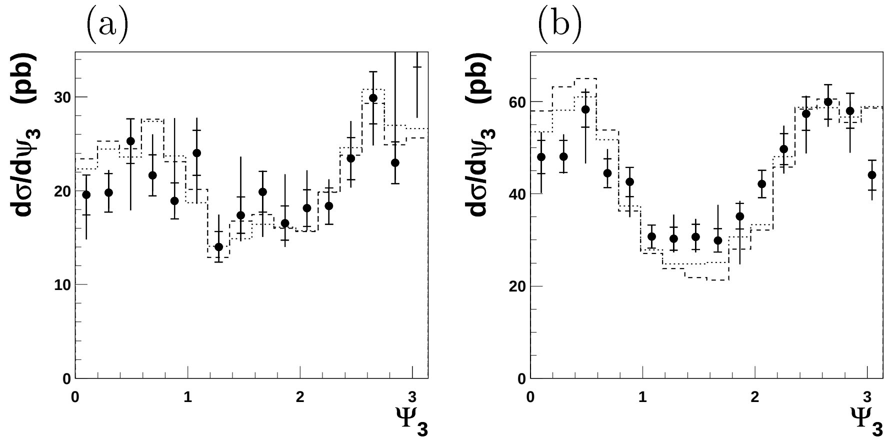

Figure 10.10: Three-jet cross section differential in ψ_3 and with (a) $x_\gamma^{\rm obs} < 0.75$ and (b) $x_\gamma^{\rm obs} > 0.75$. The data (points) are compared to HERWIG MC (lines) which has been normalised to the data. The dotted line shows the shape of the MC distribution when the gluon content of the proton is reduced by 20%. The dashed line shows the shape when the gluon content of the photon is reduced by 15%.

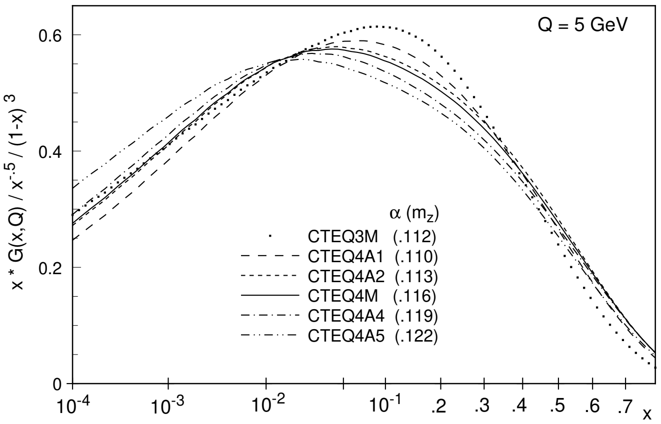

Figure 10.11: Series-CTEQ4A gluon distributions normalized by the function $x^{-1.5}\,(1-x)^3$ and compared to the CTEQ 3M gluon distribution. (Taken from [48])

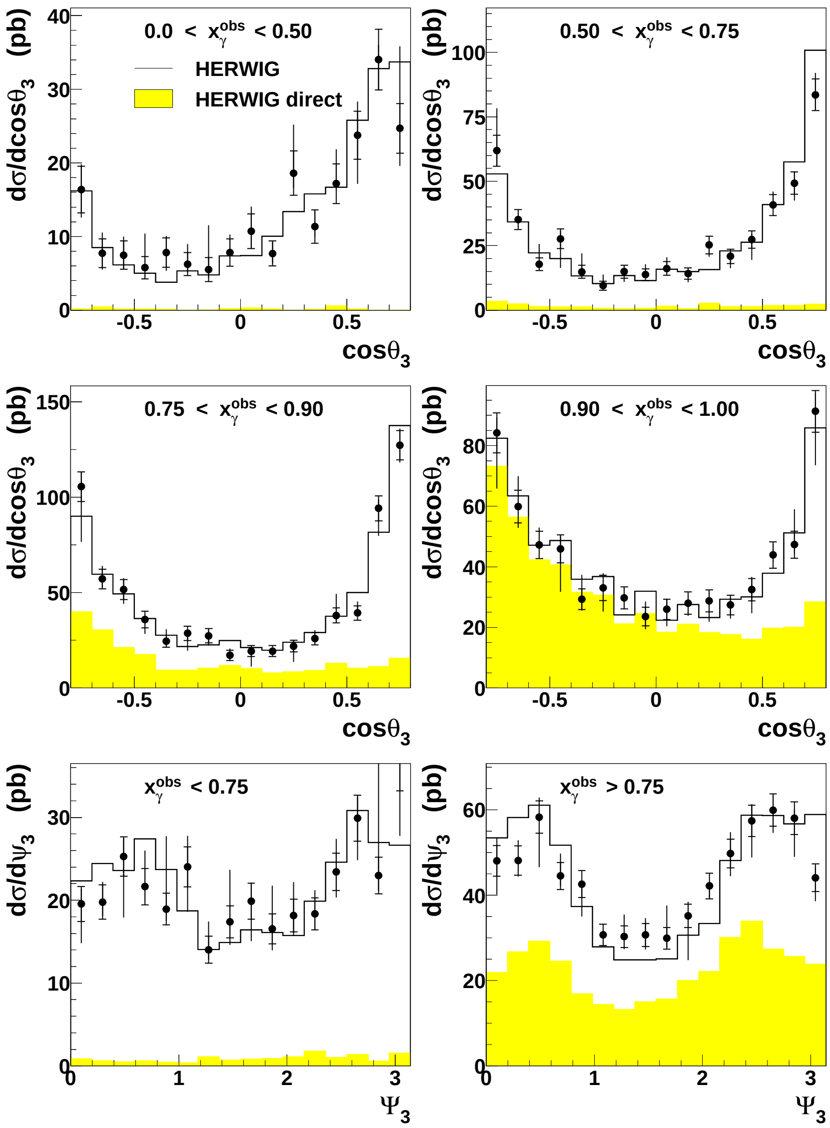

Figure 10.12: Three-jet differential cross sections compared to HERWIG MC. The fraction of proton-gluon induced events has been reduced by 0.2 in the MC, which is then normalised to the data.

10.3 Conclusions

Two-jet photoproduction cross sections have been measured for high E_{T} events as a function of x_γ^{obs} and $|\cos\theta^*|$. Large differences between data and pQCD NLO calculations are seen at low x_γ^{obs}, the kinematic region most sensitive to the photon structure. However, reasonable agreement is seen at high x_γ^{obs} and in the shape of the $|\cos\theta^*|$ distributions. In χ^2 tests, the NLO calculation using the GRV photon PDF and normalised by a factor of 1.11 was found to give a significantly better description of data than AFG or GS96, though the discrepancy remained significant.

Three-jet photoproduction events with $M_{3\mathrm{j}} > 50$ GeV have been measured. HERWIG and $\mathcal{O}(\alpha\alpha_s^2)$ pQCD calculations describe the shape of the distributions reasonably well, though they underestimate the cross section by $\sim$50%. The distribution of the angular variable, $\cos\theta_3$, has been observed to vary with x_γ^{obs}. Within the context of the parton shower model, the asymmetry that evolves can be explained in terms of the effects of the forward η cut, the shape of individual subprocesses in the cross section, and the proton and photon structures. In particular, the three-jet $\cos\theta_3$ distribution is sensitive to the photon PDF at $0.5 < x_\gamma^{\mathrm{obs}} < 0.75$ and the proton PDF at $x_\gamma^{\mathrm{obs}} > 0.9$. The agreement between the shape of the data and HERWIG can be improved by reducing $g(P)$ by 0.2.

10.4 Future Prospects

HERA is currently undergoing an upgrade, which is expected to bring the intergrated luminosity up to 1 fb^{-1} by 2005. With these data, jet photoproduction cross section measurements will clearly improve, particularly at $E_{\mathrm{T}}^{\mathrm{jet\,1}} > 25$ GeV, as indicated by the two-jet results in this thesis. Below 25 GeV the two-jet photoproduction measurements are already more precise than the theoretical predictions. To improve their interpretation, therefore, it is important that the errors associated with the pQCD calculations are reduced, and a full NLO fit to two-jet data be performed.

The next three-jet analysis should take advantage of the 1998-2000 data set, corresponding to $\sim$70 pb^{-1}, which will improve the measurement of the angular distributions. Also pQCD calculations that are NLO for these events are needed. It should then be possible to use three-jet data to discriminate between different parameterisations of the proton and photon structure, as suggested by the MC study.

Appendix A

Efficiencies and Purities

A.1 Two-jet Measurements

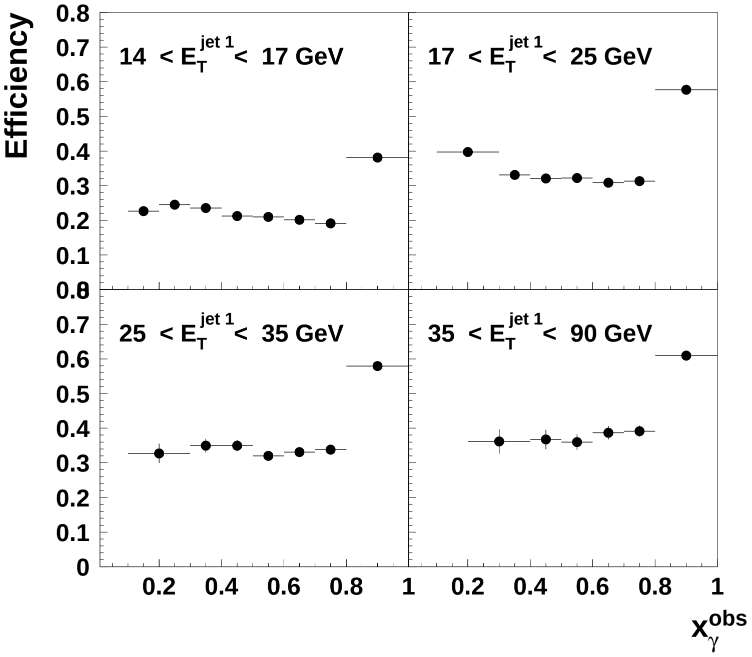

Figure A.1: Bin efficiency for HERWIG two-jet events as a function of $x_\gamma^{\rm obs}$ and $E_{\rm T}^{\rm jet\,1}$

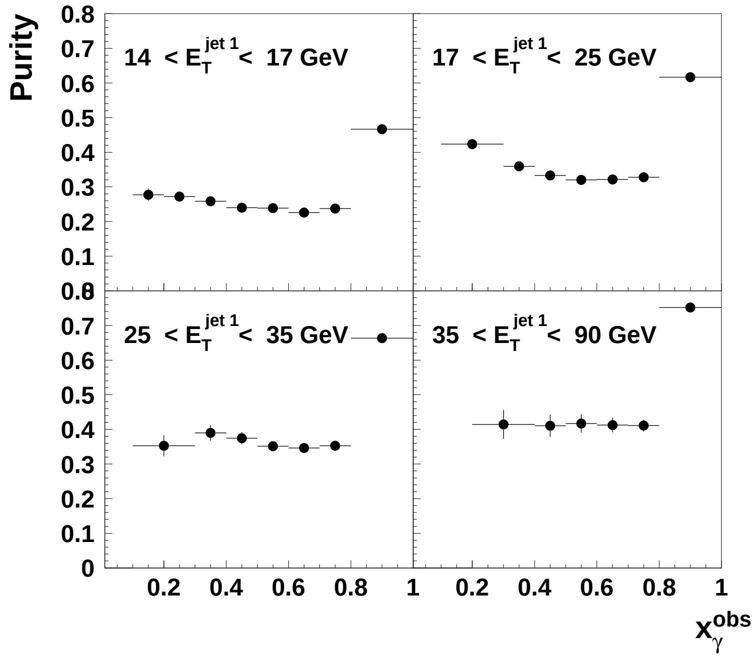

Figure A.2: Bin purity for HERWIG two-jet events as a function of $x_\gamma^{\rm obs}$ and $E_{\rm T}^{\rm jet\,1}$

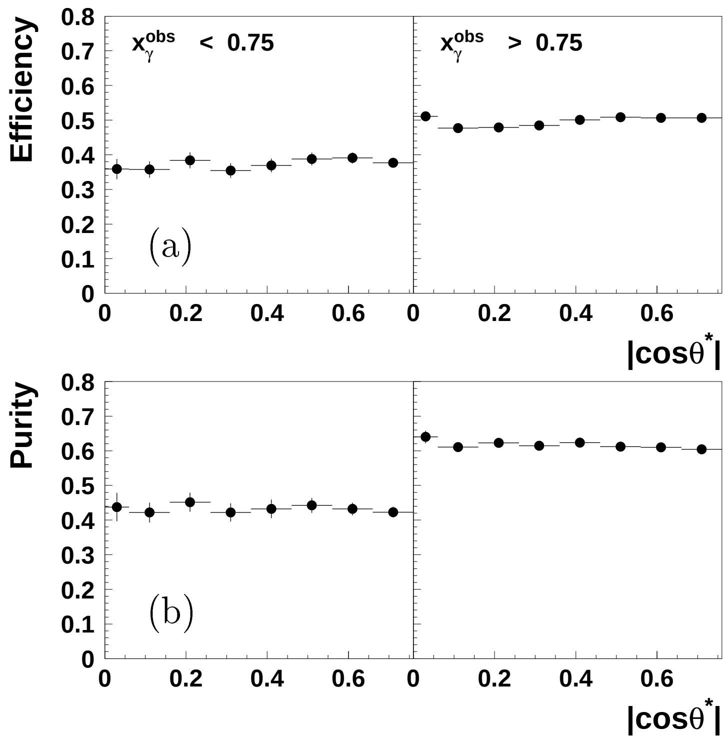

Figure A.3: Bin (a) efficiency and (b) purity for HERWIG two-jet events as a function of $|\cos\theta^*|$ and $x_\gamma^{\rm obs}$

A.2 Three-jet Measurements

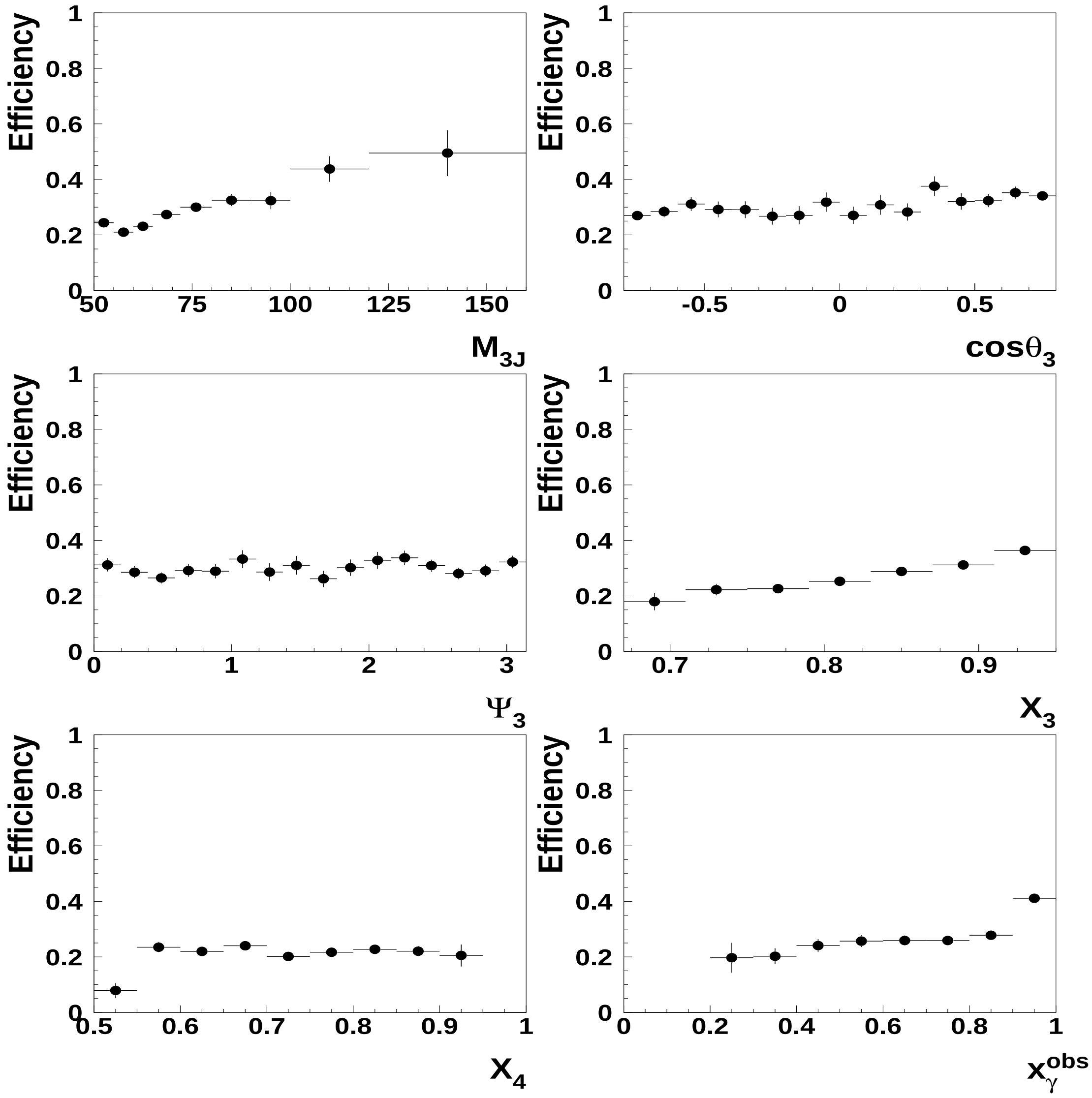

Figure A.4: Bin efficiency for HERWIG three-jet events.

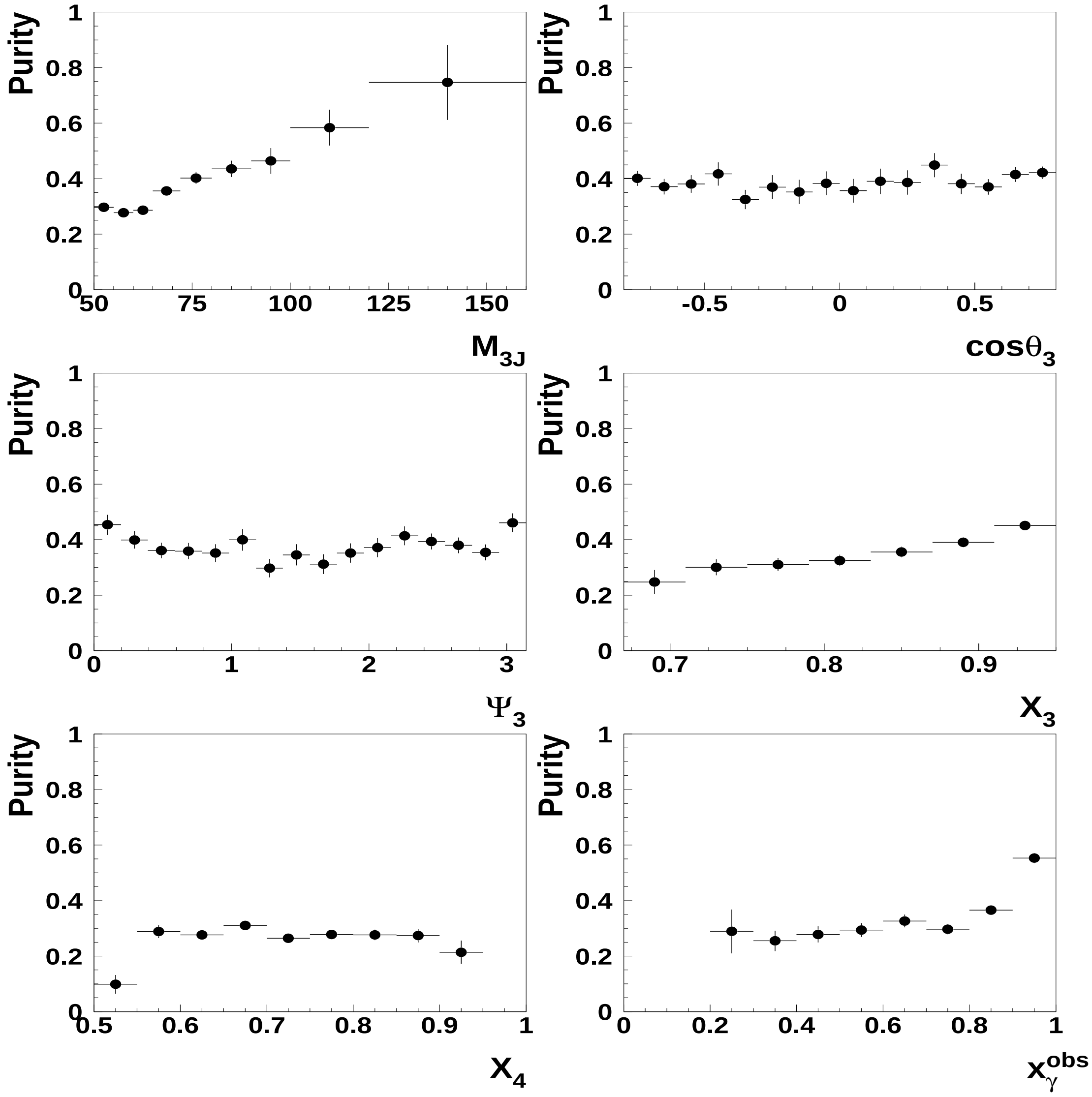

Figure A.5: Bin purity for HERWIG three-jet events.

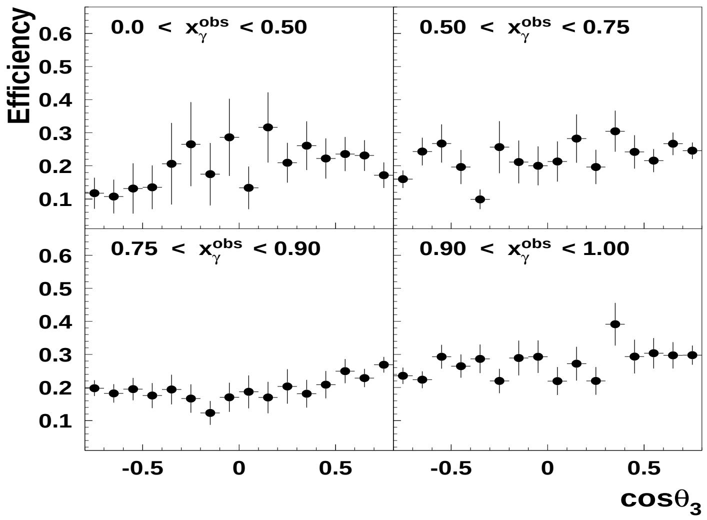

Figure A.6: Bin efficiency for HERWIG three-jet events as a function of $\cos\theta_3$ and x_γ^{obs}.

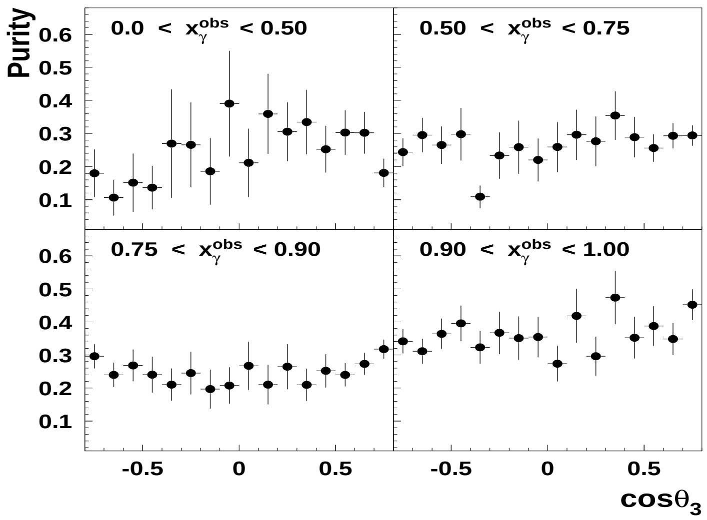

Figure A.7: Bin purity for HERWIG three-jet events as a function of $\cos\theta_3$ and x_γ^{obs}.

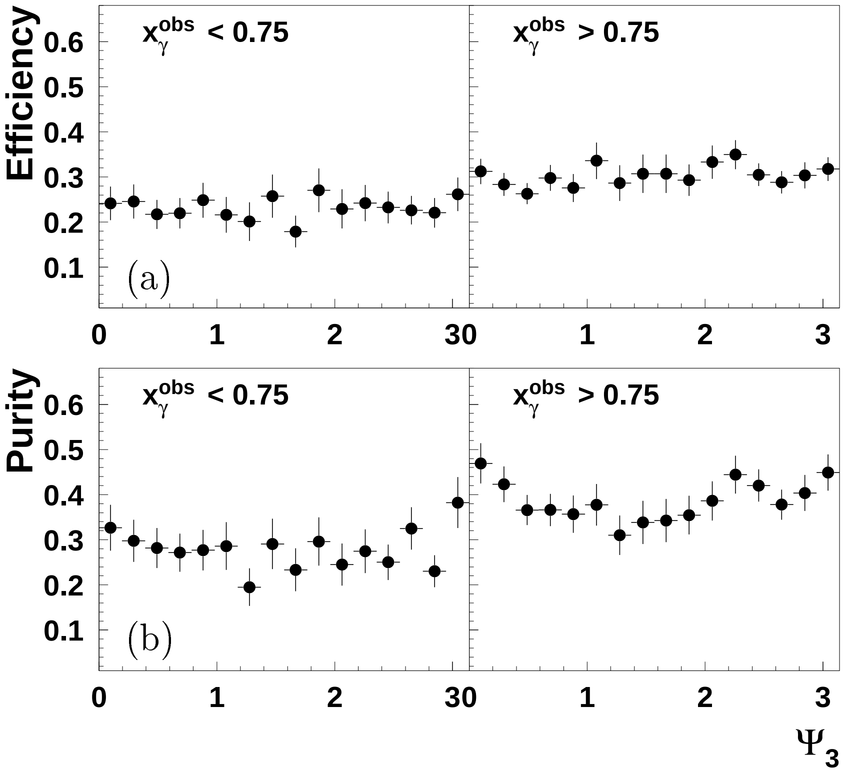

Figure A.8: Bin (a) efficiency and (b) purity for HERWIG three-jet events as a function of ψ_3 and $x_\gamma^{\rm obs}$

Appendix B

Unfolding

B.1 Correction Factors

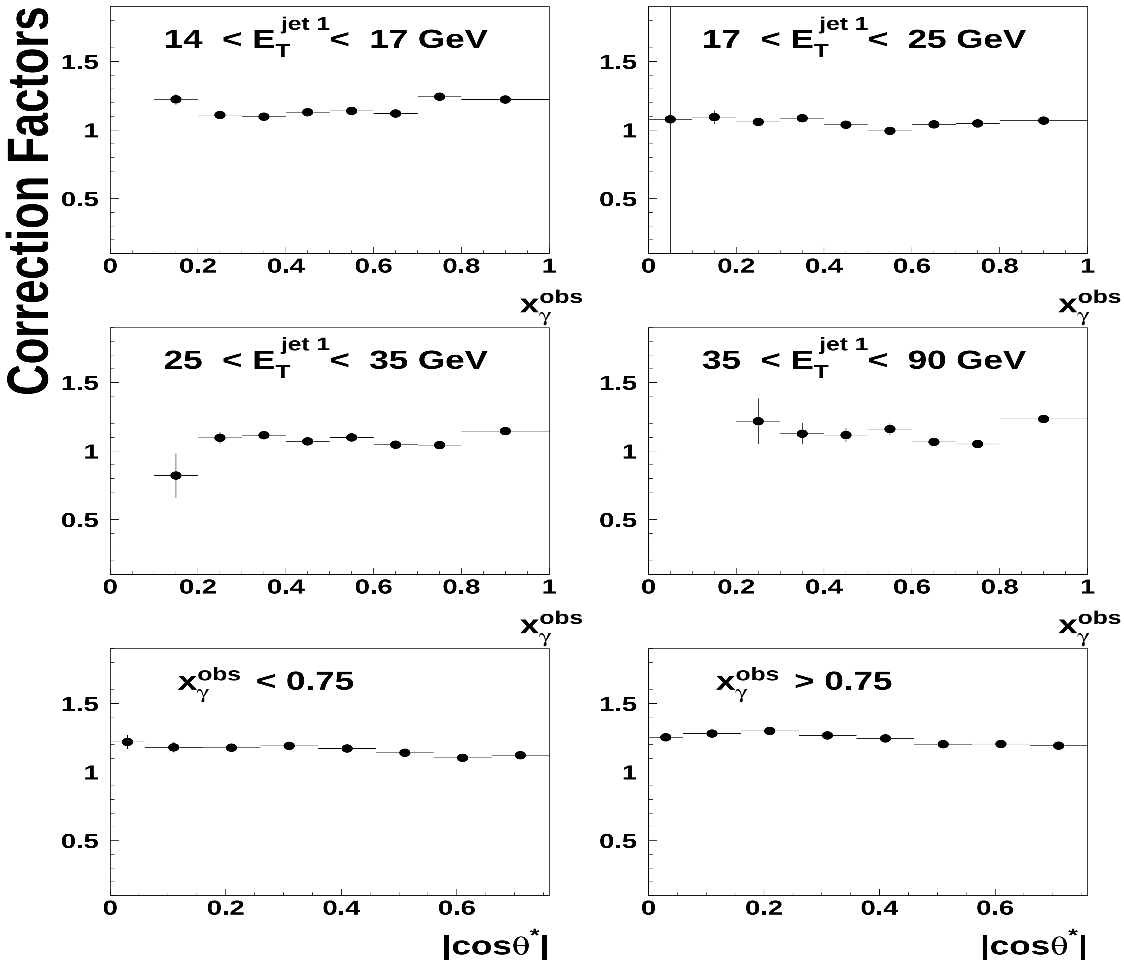

Figure B.1: Correction factors for two-jet distributions estimated using HERWIG.

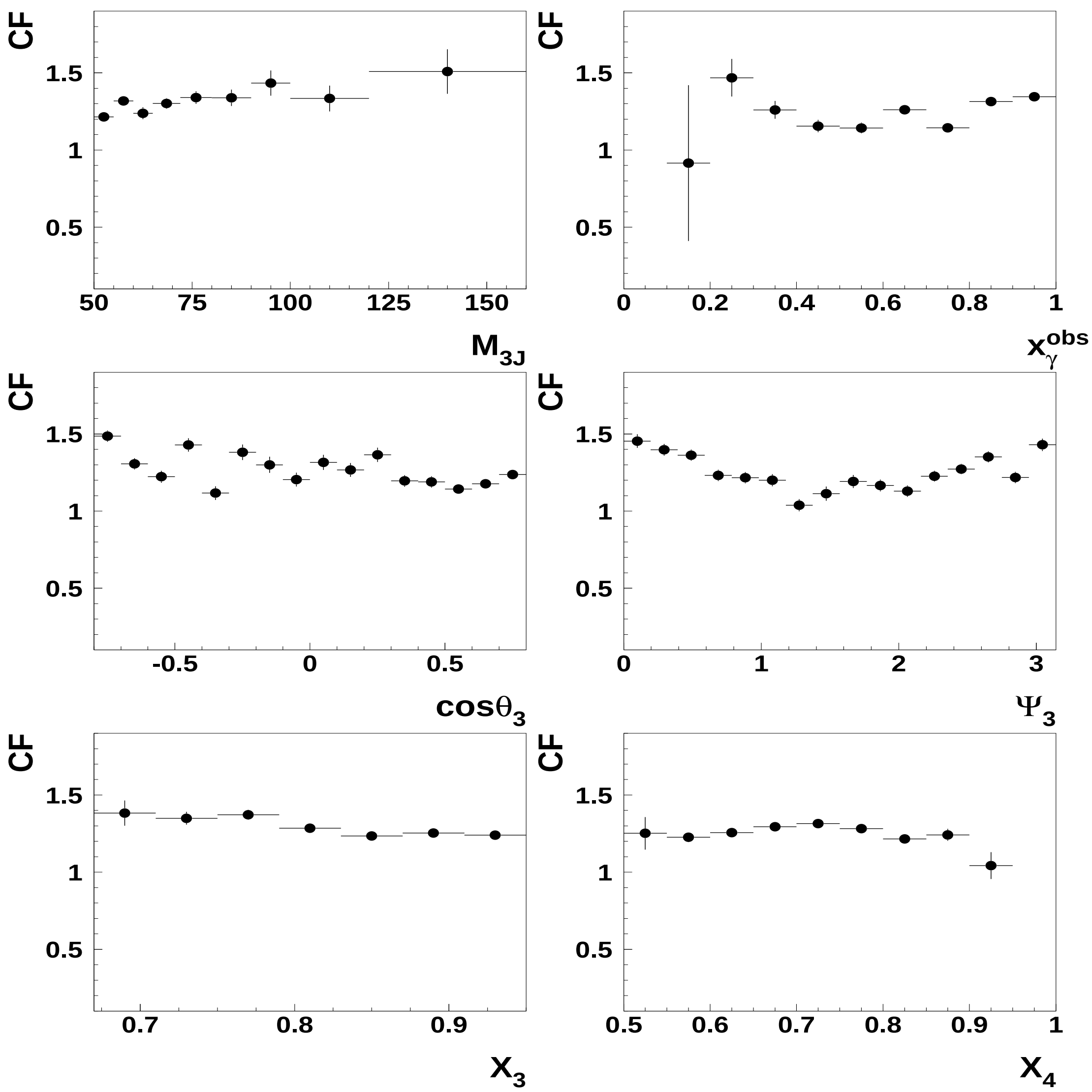

Figure B.2: Correction factors for three-jet distributions estimated using HERWIG.

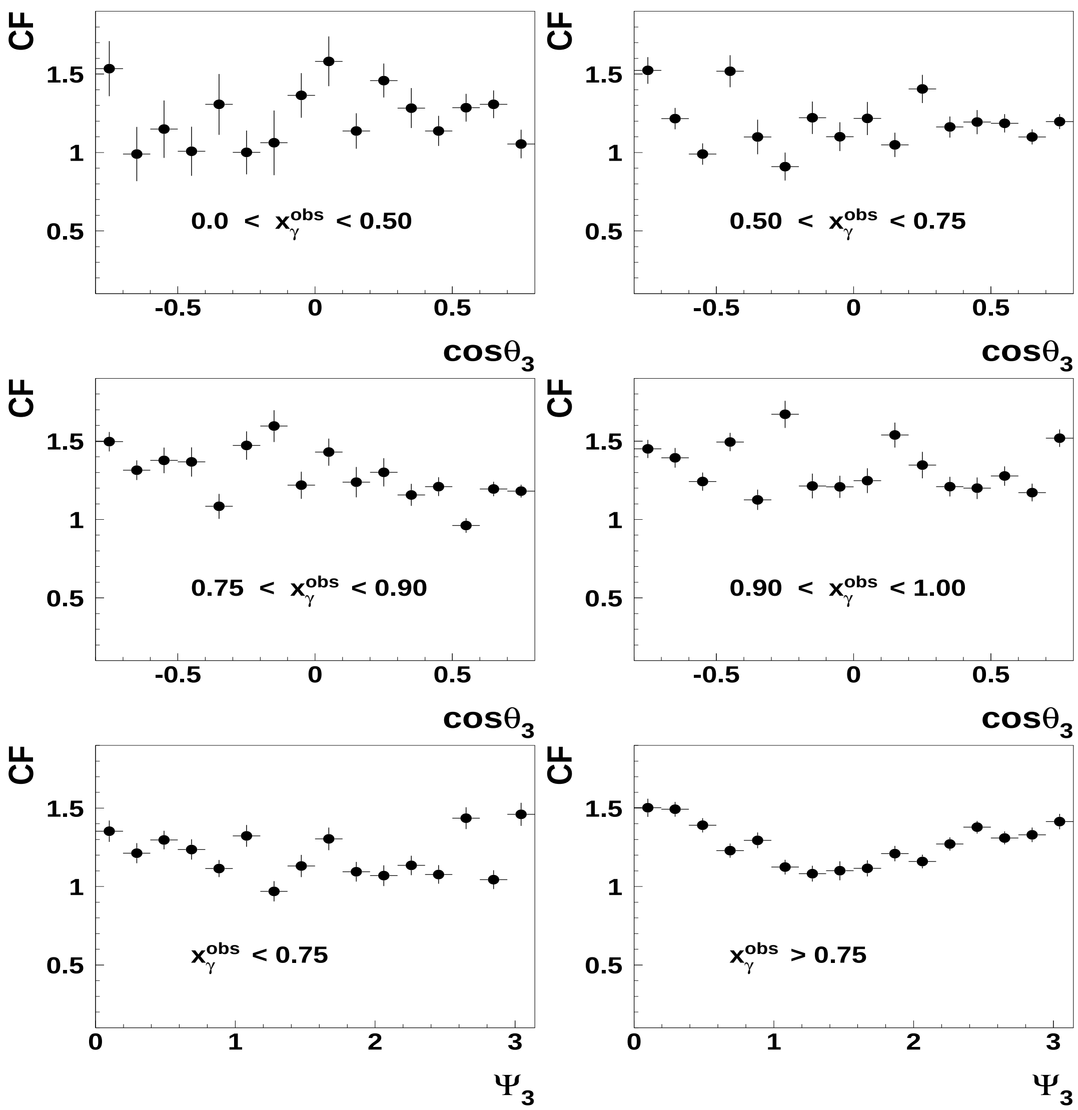

Figure B.3: Correction factors for three-jet distributions estimated using HERWIG.

B.2 Comparison of Unfolding Methods

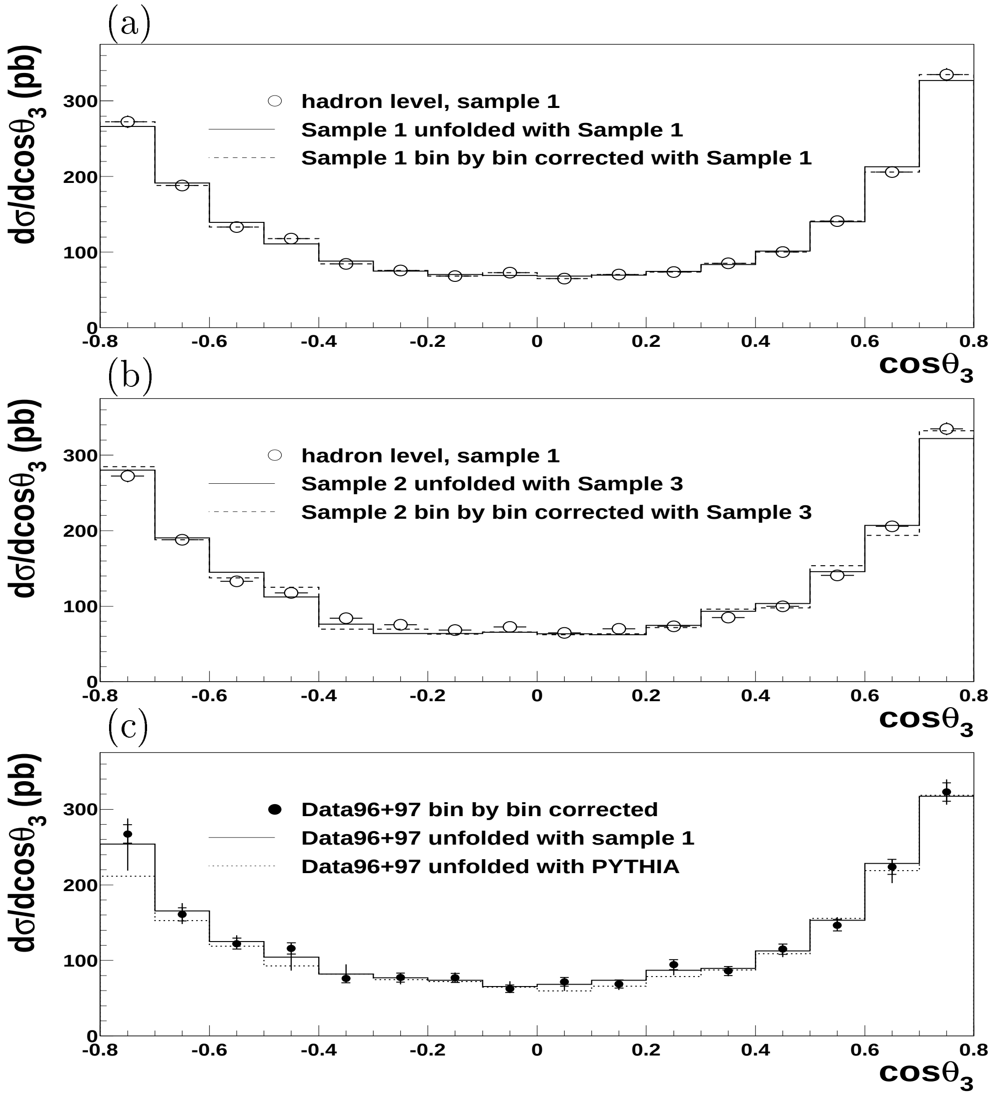

Figure B.4: The HERWIG detector level $\cos\theta_3$ distribution corrected to hadron-level using bin-by-bin (dotted line) and bayesian (solid line) unfolding methods. In (a) the same MC (sample 1) is used for the correction and for the measured distribution. In (b) one half of the MC (sample 2) is used to correct the other (sample 3). The hadron level for sample 1 is also shown (circle). In (c) data corrected using the bin-by-bin method (dots) is compared to data unfolded with HERWIG (solid line) and PYTHIA (dotted line). Data points are shown with statistical errors (inner bars) and statistical and systematic errors added in quadrature (outer bars).

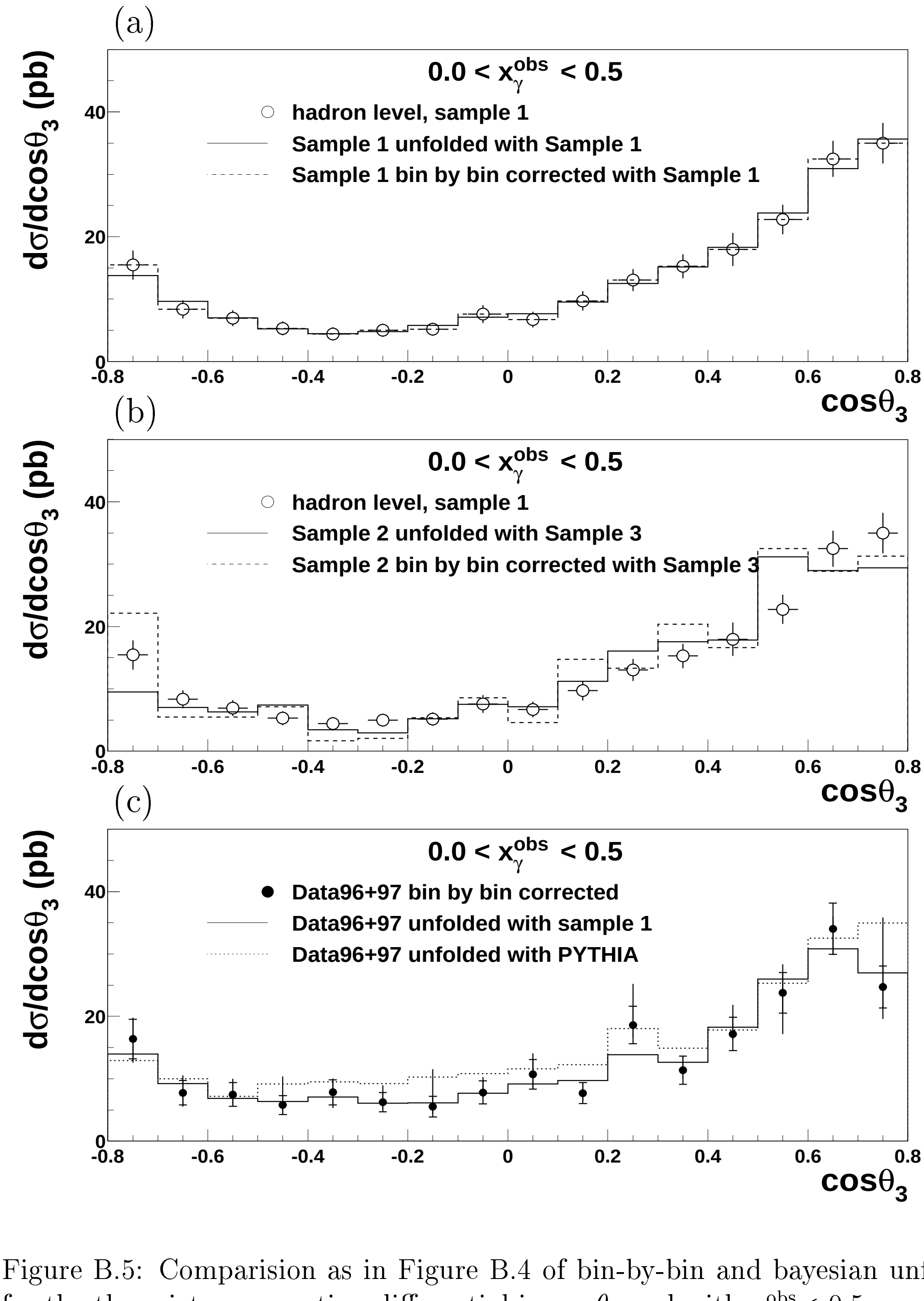

Figure B.5: Comparision as in Figure B.4 of bin-by-bin and bayesian unfolding for the three-jet cross section differential in $\cos\theta_3$ and with $x_\gamma^{\text{obs}} < 0.5$.

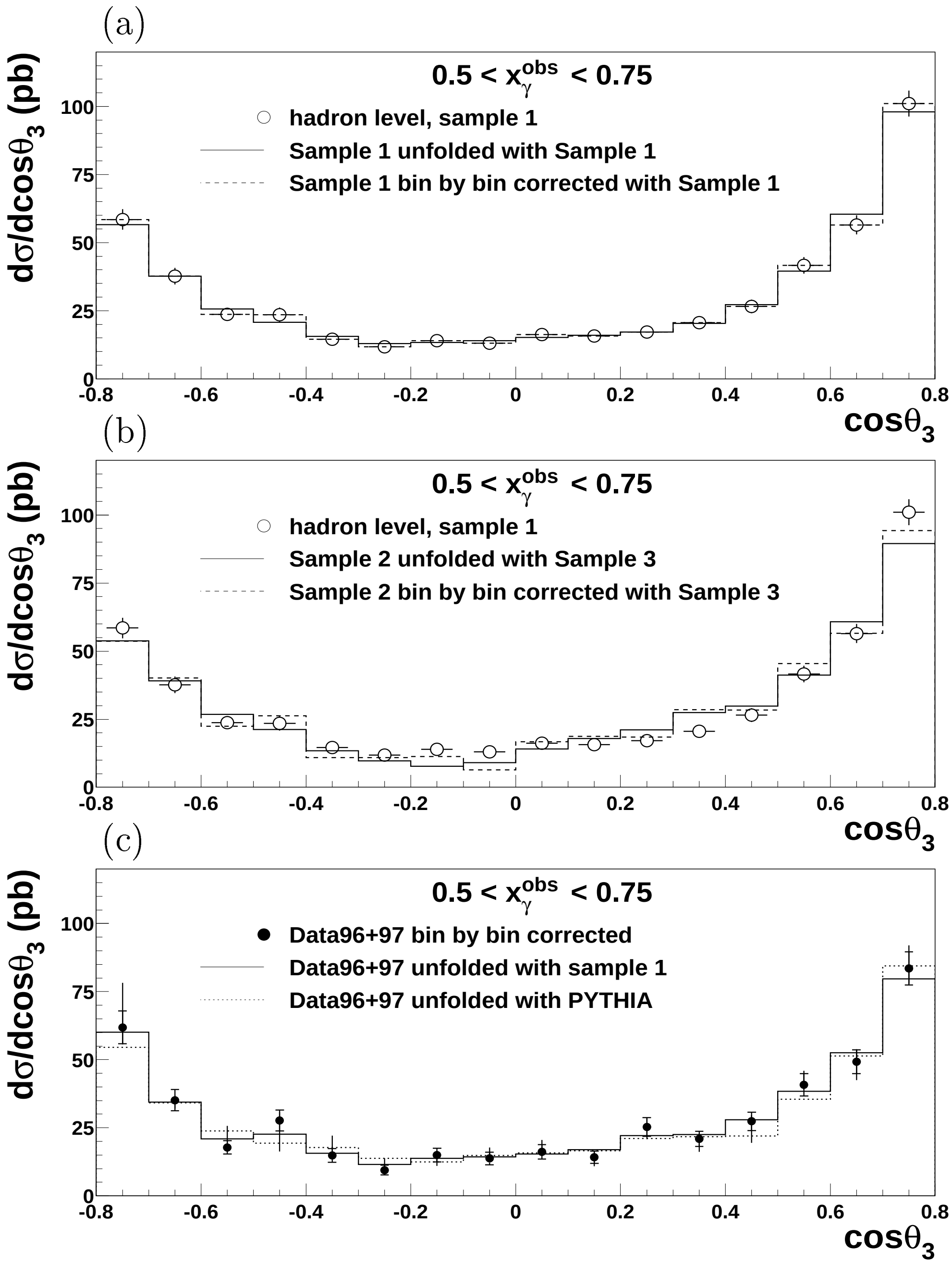

Figure B.6: Comparision as in Figure B.4 of bin-by-bin and bayesian unfolding for the three-jet cross section differential in $\cos\theta_3$ and with $0.5 < x_\gamma^{obs} < 0.75$.

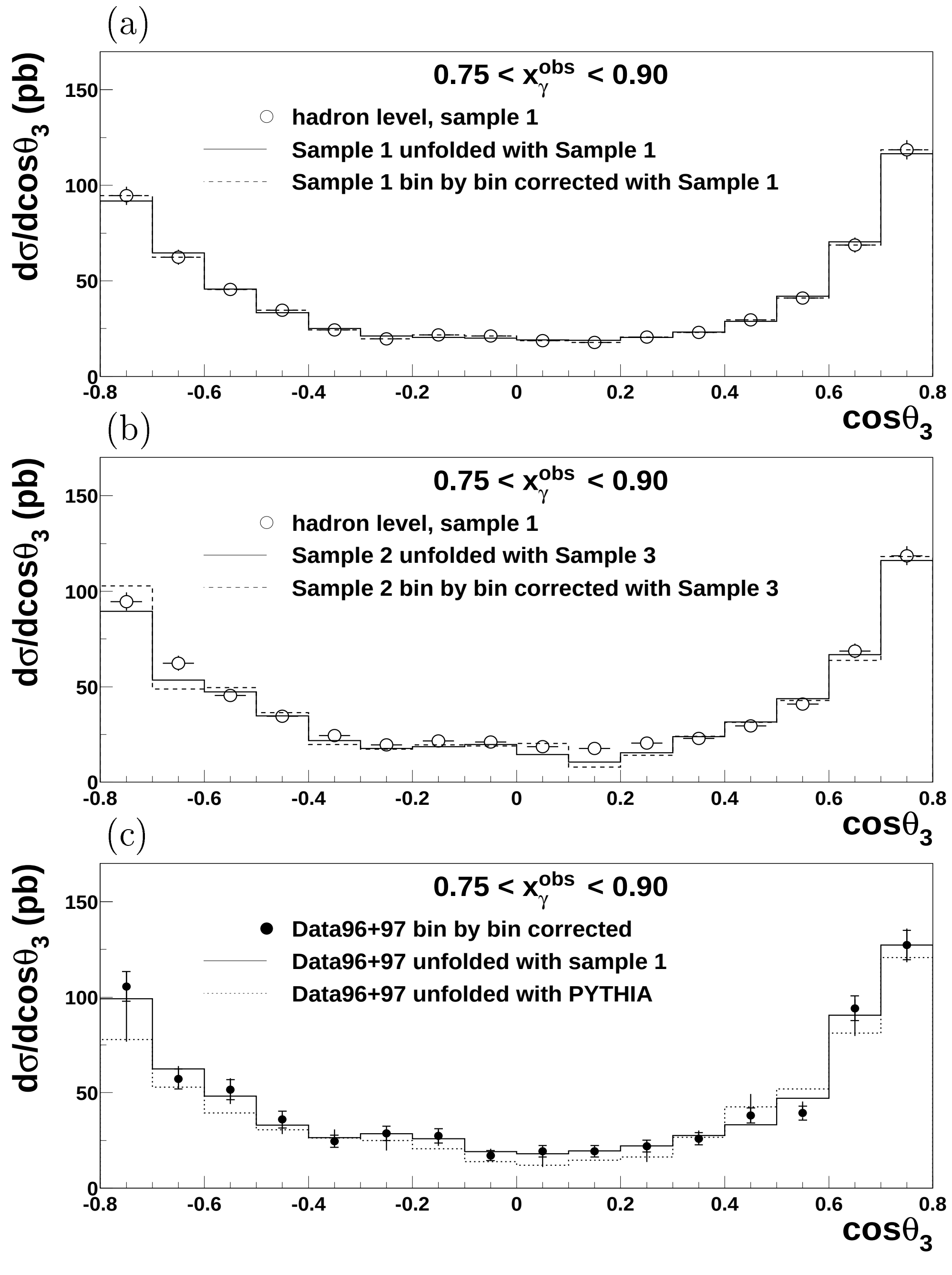

Figure B.7: Comparision as in Figure B.4 of bin-by-bin and bayesian unfolding for the three-jet cross section differential in $\cos\theta_3$ and with $0.75 < x_\gamma^{\rm obs} < 0.9$.

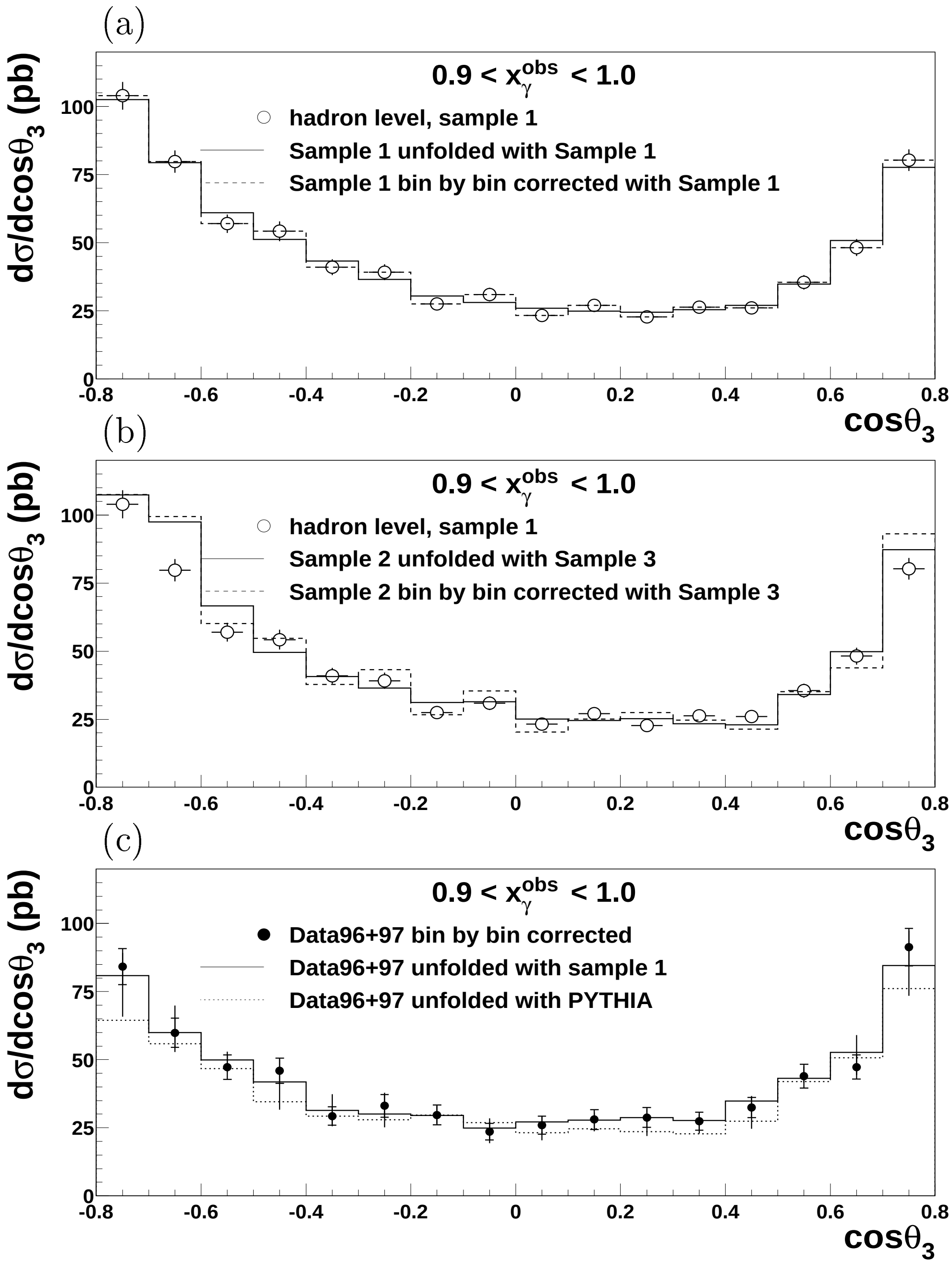

Figure B.8: Comparision as in Figure B.4 of bin-by-bin and bayesian unfolding for the three-jet cross section differential in $\cos\theta_3$ and with x_γ^{obs}> 0.9.

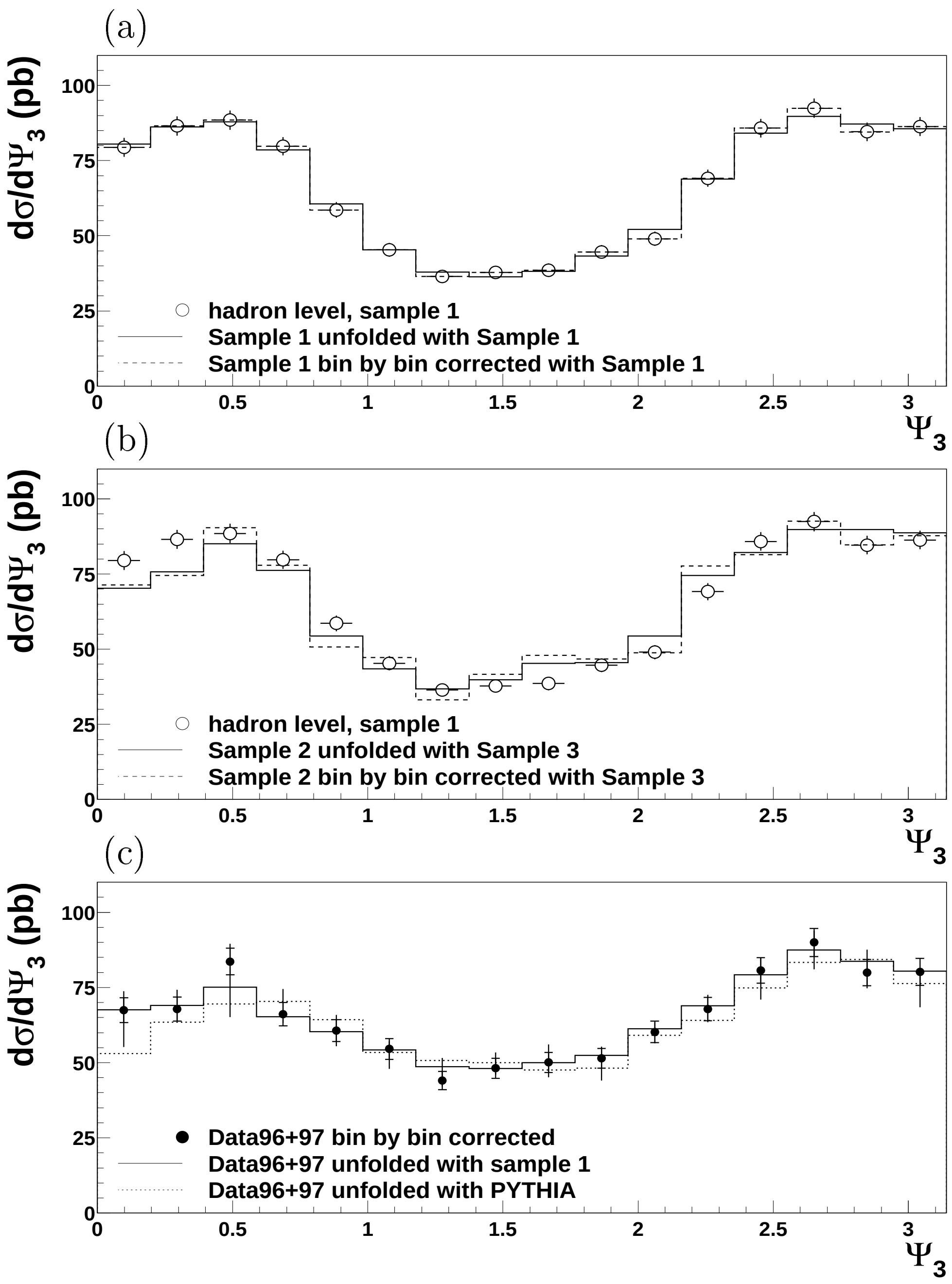

Figure B.9: Comparision as in Figure B.4 of bin-by-bin and bayesian unfolding for the three-jet cross section differential in ψ_3

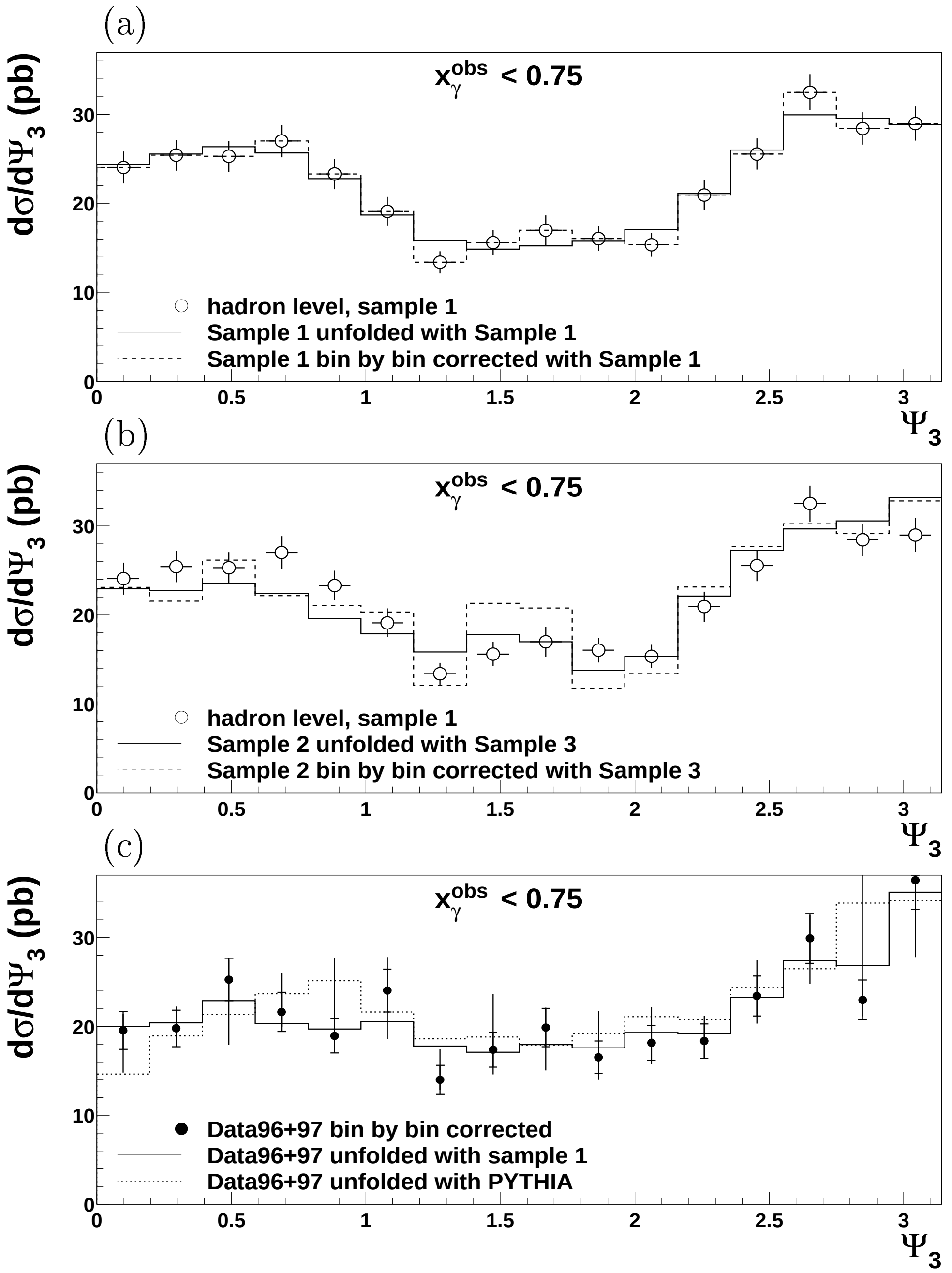

Figure B.10: Comparision as in Figure B.4 of bin-by-bin and bayesian unfolding for the three-jet cross section differential in ψ_3 and with $x_\gamma^{\rm obs}$< 0.75.

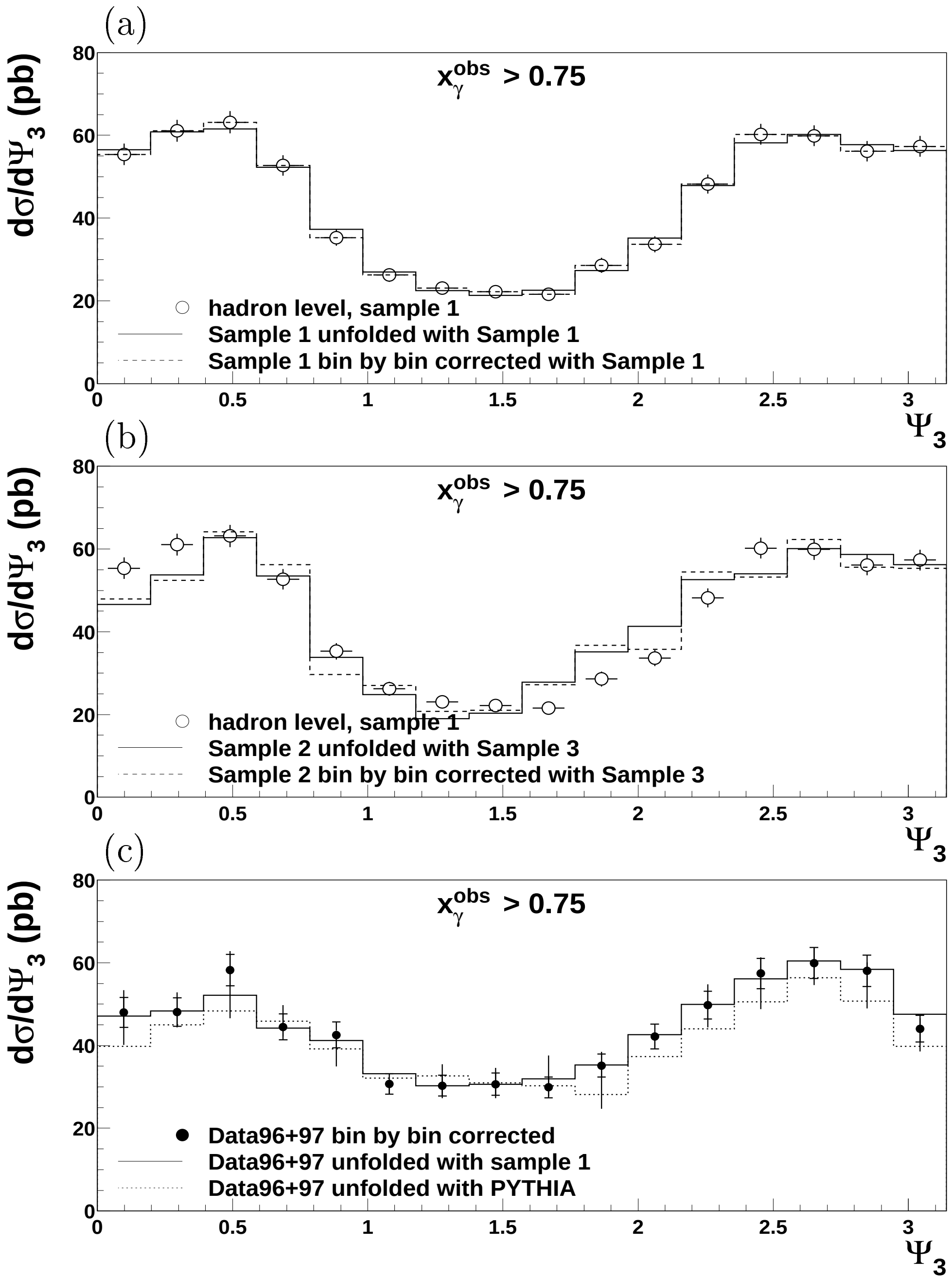

Figure B.11: Comparision as in Figure B.4 of bin-by-bin and bayesian unfolding for the three-jet cross section differential in ψ_3 and with $x_\gamma^{\mathrm{obs}} > 0.75$.

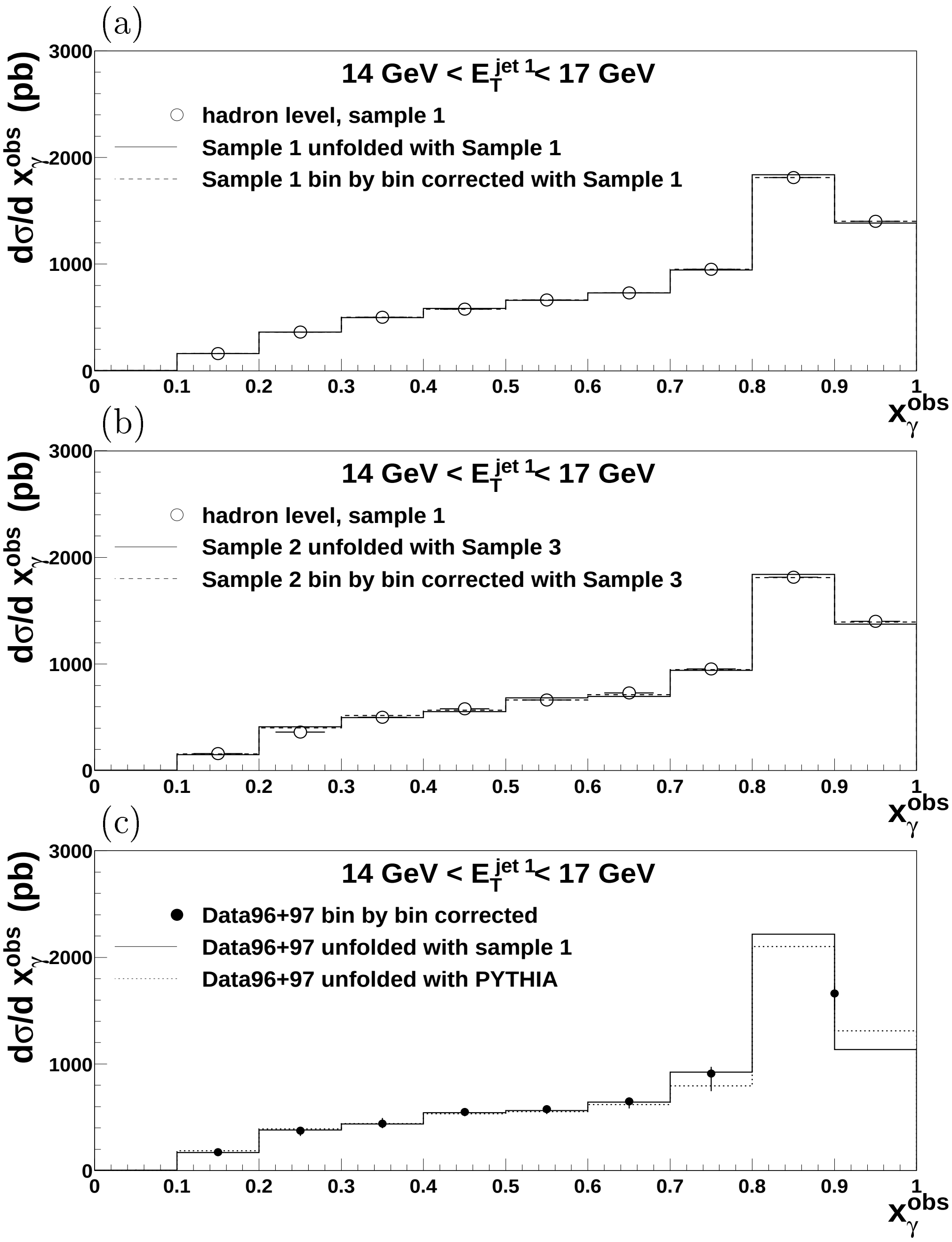

Figure B.12: Comparision as in Figure B.4 of bin-by-bin and bayesian unfolding for the two-jet cross section differential in $x_\gamma^{\rm obs}$ and with 14 $< E_{\rm T}^{\rm jet\,1} <$ 17 GeV.

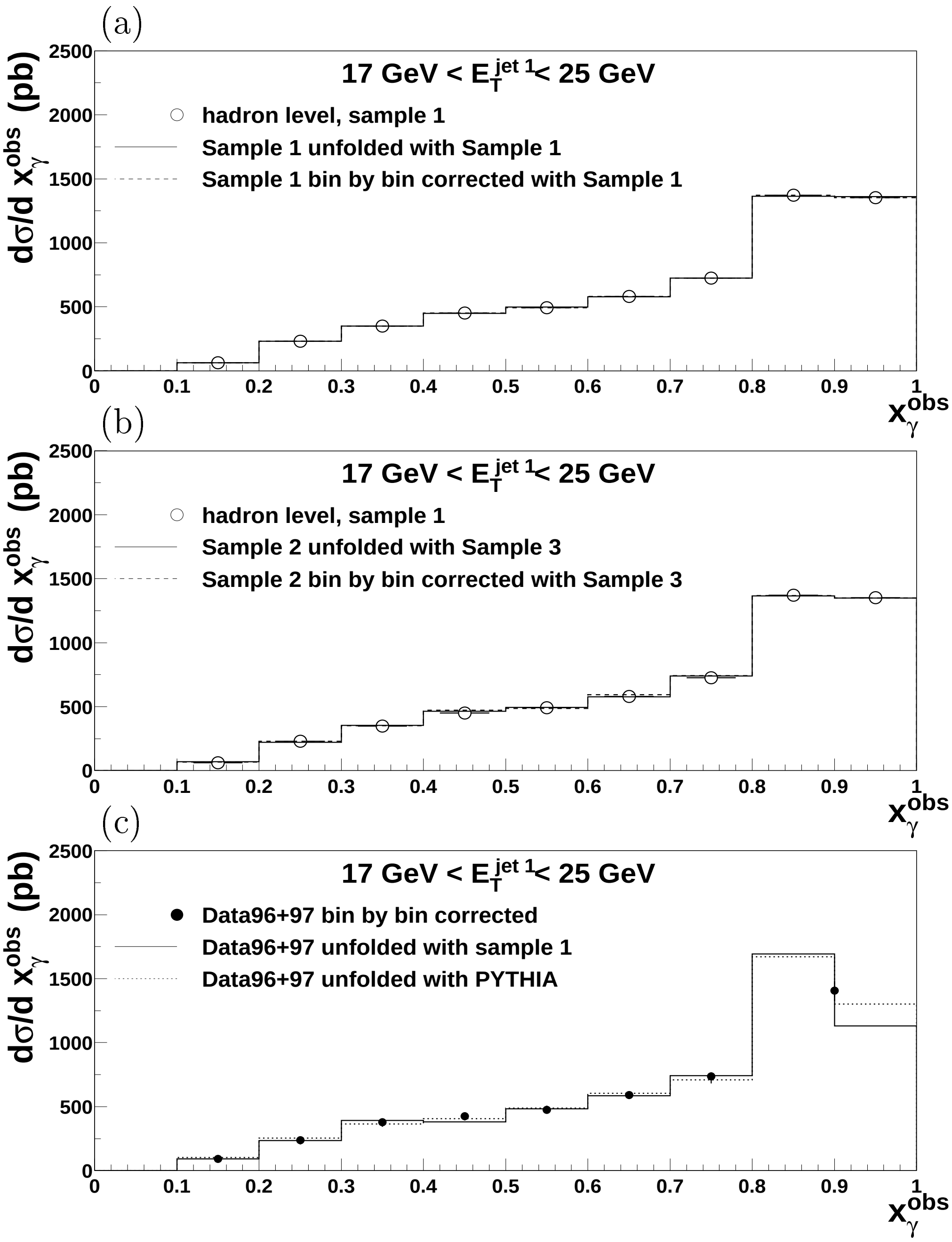

Figure B.13: Comparision as in Figure B.4 of bin-by-bin and bayesian unfolding for the two-jet cross section differential in x_γ^{obs} and with $17 < E_T^{jet\,1} < 25$ GeV.

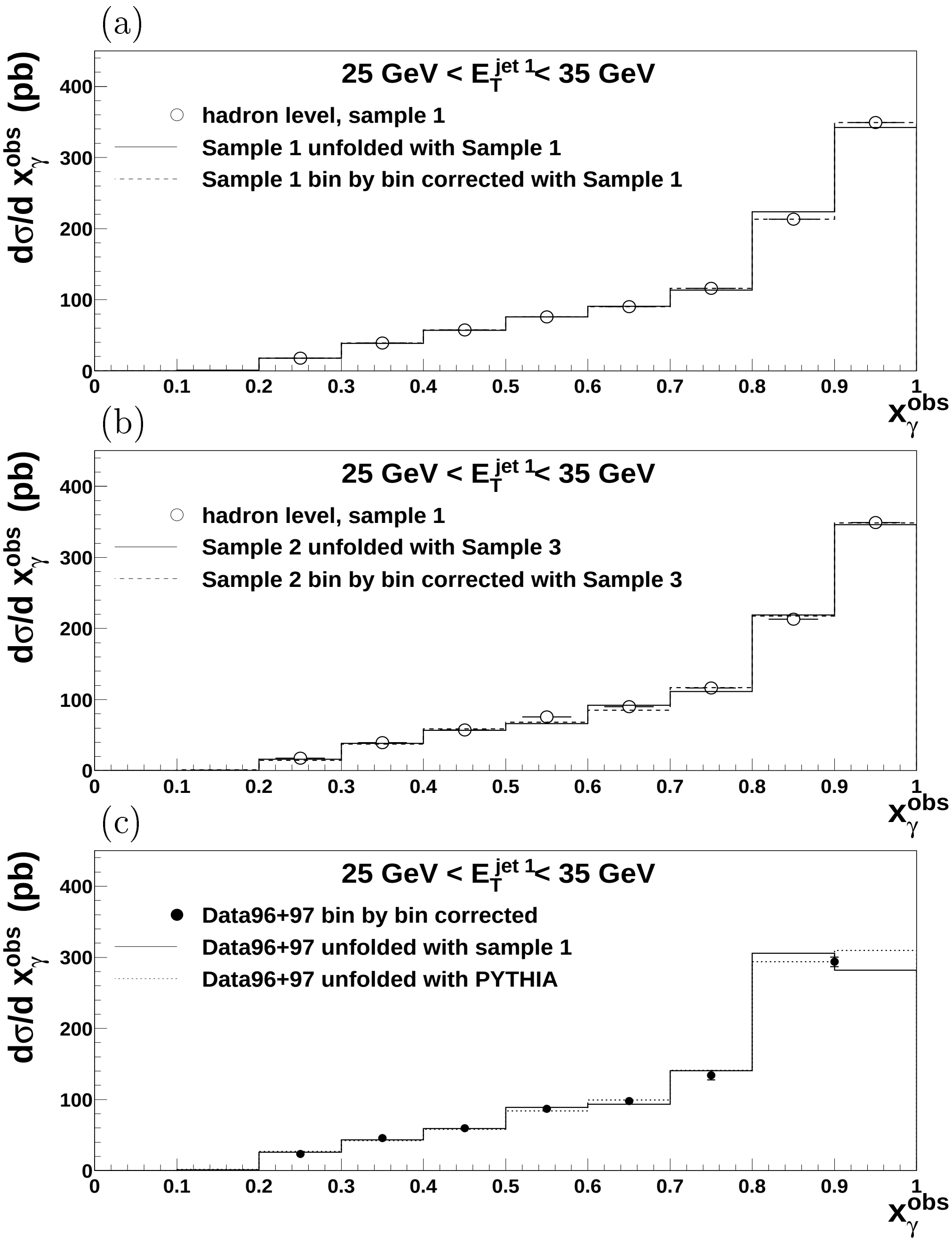

Figure B.14: Comparision as in Figure B.4 of bin-by-bin and bayesian unfolding for the two-jet cross section differential in x_γ^{obs} and with $25 < E_{\mathrm{T}}^{\mathrm{jet}\,1} < 35$ GeV.

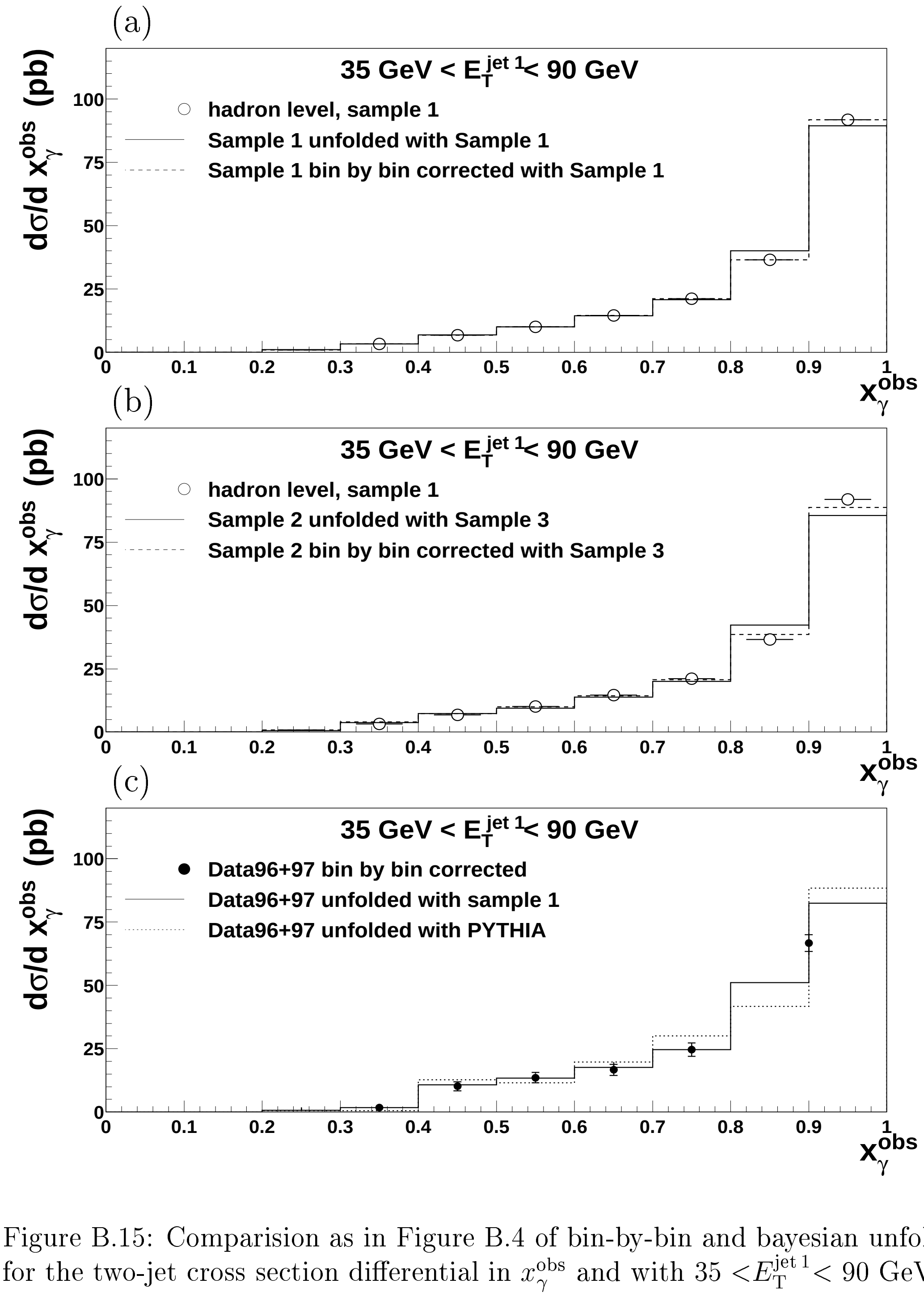

Figure B.15: Comparision as in Figure B.4 of bin-by-bin and bayesian unfolding for the two-jet cross section differential in $x_\gamma^{\rm obs}$ and with 35 $<E_{\rm T}^{\rm jet\,1}<$ 90 GeV.

Appendix C

Tables of Data

C.1 Two-jet Measurements

$x_\gamma^{\rm obs}$	$\mathrm{d}\sigma/\mathrm{d}x_\gamma^{\rm obs} \pm \Delta_{\rm stat}$ (pb)	$+\Delta_{\rm sys}$ / $-\Delta_{\rm sys}$ (pb)	$+\Delta_E$ / $-\Delta_E$ (pb)
$14 < E_T^{\rm jet\,1} < 17$ GeV			
0.00 .. 0.10	6.7 ± 4.2	2.2 / -11.0	0.6 / -2.4
0.10 .. 0.20	171.8 ± 9.5	32.6 / -8.7	19.3 / -18.6
0.20 .. 0.30	375.6 ± 13.7	36.2 / -26.3	52.4 / -47.0
0.30 .. 0.40	441.2 ± 14.2	49.6 / -19.0	63.5 / -35.9
0.40 .. 0.50	548.6 ± 16.0	28.3 / -20.3	57.9 / -49.9
0.50 .. 0.60	576.4 ± 16.1	18.4 / -27.6	60.4 / -59.7
0.60 .. 0.70	648.2 ± 16.9	38.2 / -43.2	73.6 / -56.2
0.70 .. 0.80	911.2 ± 21.0	62.7 / -125.8	80.5 / -64.2
0.80 .. 1.00	1662.3 ± 18.0	72.9 / -105.0	143.6 / -138.4
$17 < E_T^{\rm jet\,1} < 25$ GeV			
0.00 .. 0.10	0.3 ± 0.5	1.6 / -0.4	0.0 / -0.0
0.10 .. 0.30	164.1 ± 5.6	16.6 / -16.0	22.2 / -17.4
0.30 .. 0.40	378.8 ± 12.0	12.7 / -25.4	44.5 / -43.8
0.40 .. 0.50	424.9 ± 12.3	19.8 / -10.6	52.7 / -47.6
0.50 .. 0.60	473.7 ± 12.7	32.9 / -11.2	60.0 / -48.9
0.60 .. 0.70	591.1 ± 14.5	11.9 / -17.5	69.0 / -60.1
0.70 .. 0.80	736.8 ± 16.1	27.8 / -32.3	91.8 / -82.6
0.80 .. 1.00	1407.1 ± 14.8	73.7 / -45.4	154.2 / -127.7

Table C.1: The two-jet $\mathrm{d}\sigma/\mathrm{d}x_\gamma^{\rm obs}$ measurements in the regions $14 < E_T^{\rm jet\,1} < 17$ GeV and $17 < E_T^{\rm jet\,1} < 25$ GeV, with statistical ($\Delta_{\rm stat}$), systematic ($\Delta_{\rm sys}$) and energy scale (Δ_E) uncertainties.

$x_\gamma^{\rm obs}$	$\mathrm{d}\sigma/\mathrm{d}x_\gamma^{\rm obs} \pm \Delta_{\rm stat}$ (pb)	$+\Delta_{\rm sys}$ / $-\Delta_{\rm sys}$ (pb)	$+\Delta_E$ / $-\Delta_E$ (pb)
	$25 < E_T^{\rm jet\,1} < 35$ GeV		
0.00 .. 0.10	0.0 ± 0.0	0.0 / -0.0	0.0 / -0.0
0.10 .. 0.30	12.2 ± 1.4	1.6 / -1.1	1.1 / -1.8
0.30 .. 0.40	45.9 ± 3.8	1.2 / -2.8	7.6 / -6.6
0.40 .. 0.50	59.7 ± 4.3	3.3 / -2.5	8.4 / -6.7
0.50 .. 0.60	87.0 ± 5.2	2.8 / -3.6	12.6 / -11.9
0.60 .. 0.70	97.8 ± 5.4	4.8 / -2.7	14.4 / -11.4
0.70 .. 0.80	134.2 ± 6.3	4.8 / -3.8	17.5 / -17.6
0.80 .. 1.00	293.7 ± 6.7	6.3 / -5.3	36.9 / -32.6
	$35 < E_T^{\rm jet\,1} < 90$ GeV		
0.00 .. 0.10	0.0 ± 0.0	0.0 / -0.0	0.0 / -0.0
0.10 .. 0.20	0.0 ± 0.0	0.0 / -0.0	0.0 / -0.0
0.20 .. 0.40	1.3 ± 0.5	0.5 / -0.2	0.3 / -0.3
0.40 .. 0.50	10.2 ± 1.8	2.1 / -1.7	1.6 / -1.3
0.50 .. 0.60	13.6 ± 2.1	1.2 / -1.7	2.0 / -1.8
0.60 .. 0.70	16.7 ± 2.2	3.1 / -1.7	2.4 / -2.1
0.70 .. 0.80	24.6 ± 2.7	1.8 / -0.9	3.8 / -3.1
0.80 .. 1.00	66.7 ± 3.3	1.2 / -2.2	9.4 / -7.5

Table C.2: The two-jet $\mathrm{d}\sigma/\mathrm{d}x_\gamma^{\rm obs}$ measurements in the regions $25 < E_T^{\rm jet\,1} < 35$ GeV and $35 < E_T^{\rm jet\,1} < 90$ GeV, with statistical ($\Delta_{\rm stat}$), systematic ($\Delta_{\rm sys}$) and energy scale (Δ_E) uncertainties.

$\lvert\cos\theta^*\rvert$	$\mathrm{d}\sigma/\mathrm{d}\lvert\cos\theta^*\rvert \pm \Delta_{\mathrm{stat}}$ (pb)	$+\Delta_{\mathrm{sys}}$ / $-\Delta_{\mathrm{sys}}$ (pb)	$+\Delta_E$ / $-\Delta_E$ (pb)
$x_\gamma^{\mathrm{obs}} < 0.75$			
0.0 .. 0.06	29.6 ± 4.2	10.2 / -0.4	1.8 / -3.2
0.06 .. 0.16	38.7 ± 3.7	1.2 / -4.3	4.1 / -5.8
0.16 .. 0.26	46.6 ± 4.0	4.4 / -5.2	5.5 / -4.6
0.26 .. 0.36	49.9 ± 4.2	2.4 / -2.3	5.0 / -6.7
0.36 .. 0.46	63.1 ± 4.7	3.0 / -9.6	5.3 / -8.7
0.46 .. 0.56	86.4 ± 5.4	3.0 / -6.0	13.1 / -9.0
0.56 .. 0.66	146.7 ± 7.2	2.7 / -8.6	17.5 / -18.6
0.66 .. 0.76	255.3 ± 10.0	19.9 / -12.9	35.7 / -25.2
$x_\gamma^{\mathrm{obs}} > 0.75$			
0.00 .. 0.06	152.3 ± 9.3	5.9 / -11.1	17.4 / -13.3
0.06 .. 0.16	146.0 ± 7.1	3.5 / -5.7	15.8 / -15.6
0.16 .. 0.26	153.0 ± 7.4	7.4 / -6.9	17.5 / -16.5
0.26 .. 0.36	184.2 ± 8.0	8.8 / -7.0	24.7 / -18.4
0.36 .. 0.46	212.1 ± 8.5	2.8 / -8.6	24.7 / -20.1
0.46 .. 0.56	277.3 ± 9.7	4.3 / -11.2	31.6 / -23.9
0.56 .. 0.66	369.3 ± 11.3	12.3 / -15.9	36.5 / -35.8
0.66 .. 0.76	566.9 ± 14.2	21.5 / -19.6	54.0 / -51.0

Table C.3: The two-jet $\mathrm{d}\sigma/\mathrm{d}\lvert\cos\theta^*\rvert$ measurements in the regions $x_\gamma^{\mathrm{obs}} < 0.75$ and $x_\gamma^{\mathrm{obs}} > 0.75$, with statistical ($\Delta_{\mathrm{stat}}$), systematic ($\Delta_{\mathrm{sys}}$) and energy scale ($\Delta_E$) uncertainties.

C.2 Three-jet Measurements

M_{3j}	$\mathrm{d}\sigma/\mathrm{d}M_{3j} \pm \Delta_{\text{stat}}$ (pb)	$+\Delta_{\text{sys}}$ / $-\Delta_{\text{sys}}$ (pb)	$+\Delta_E$ / $-\Delta_E$ (pb)
50.00 .. 55.00	15.5 ± 0.4	0.6 / -0.9	2.5 / -1.5
55.00 .. 60.00	9.5 ± 0.3	0.3 / -1.5	0.9 / -1.2
60.00 .. 65.00	5.6 ± 0.3	0.1 / -0.3	0.8 / -0.6
65.00 .. 72.00	3.3 ± 0.2	0.2 / -0.2	0.6 / -0.5
72.00 .. 80.00	1.8 ± 0.1	0.1 / -0.1	0.2 / -0.1
80.00 .. 90.00	0.9 ± 0.1	0.0 / -0.1	0.1 / -0.1
90.00 .. 100.00	0.5 ± 0.0	0.0 / -0.1	0.1 / -0.0
100.00 .. 120.00	0.2 ± 0.0	0.0 / -0.0	0.0 / -0.0
120.00 .. 160.00	0.0 ± 0.0	0.0 / -0.0	0.0 / -0.0

Table C.4: The three-jet $\mathrm{d}\sigma/\mathrm{d}M_{3j}$ measurements, with statistical (Δ_{stat}), systematic (Δ_{sys}) and energy scale (Δ_E) uncertainties.

x_γ^{obs}	$\mathrm{d}\sigma/\mathrm{d}x_\gamma^{\text{obs}} \pm \Delta_{\text{stat}}$ (pb)	$+\Delta_{\text{sys}}$ / $-\Delta_{\text{sys}}$ (pb)	$+\Delta_E$ / $-\Delta_E$ (pb)
0.00 .. 0.10	0.0 ± 0.0	0.0 / -0.0	0.0 / -0.0
0.10 .. 0.20	1.9 ± 1.2	2.8 / -1.3	0.7 / -0.1
0.20 .. 0.30	24.5 ± 3.7	10.5 / -0.8	2.5 / -4.6
0.30 .. 0.40	78.8 ± 6.2	23.2 / -7.1	13.3 / -13.8
0.40 .. 0.50	105.0 ± 6.7	12.1 / -10.6	19.3 / -11.7
0.50 .. 0.60	139.6 ± 7.7	17.6 / -6.6	25.9 / -15.7
0.60 .. 0.70	205.9 ± 9.4	10.2 / -32.9	31.2 / -29.3
0.70 .. 0.80	267.9 ± 10.6	31.0 / -10.0	33.8 / -35.8
0.80 .. 0.90	589.1 ± 16.8	18.4 / -85.3	88.5 / -69.2
0.90 .. 1.00	678.6 ± 17.6	24.5 / -71.3	83.6 / -54.5

Table C.5: The three-jet $\mathrm{d}\sigma/\mathrm{d}x_\gamma^{\text{obs}}$ measurements, with statistical (Δ_{stat}), systematic (Δ_{sys}) and energy scale (Δ_E) uncertainties.

$\cos\theta_3$	$d\sigma/d\cos\theta_3 \pm \Delta_{\text{stat}}$ (pb)	$+\Delta_{\text{sys}}$ / $-\Delta_{\text{sys}}$ (pb)	$+\Delta_E$ / $-\Delta_E$ (pb)
-0.80 .. -0.70	267.4 ± 12.2	20.6 / -48.6	40.3 / --34.3
-0.70 .. -0.60	160.8 ± 8.7	15.0 / -12.6	20.5 / -16.1
-0.60 .. -0.50	122.2 ± 7.3	11.1 / -3.3	21.5 / -12.7
-0.50 .. -0.40	115.7 ± 7.5	6.8 / -29.1	15.6 / -10.7
-0.40 .. -0.30	76.2 ± 5.6	18.4 / -5.0	14.2 / -7.9
-0.30 .. -0.20	77.3 ± 6.0	3.9 / -9.1	10.4 / -8.8
-0.20 .. -0.10	76.8 ± 6.0	7.0 / -5.9	11.9 / -5.9
-0.10 .. 0.00	62.4 ± 5.0	10.1 / -5.6	7.3 / --5.9
0.00 .. 0.10	71.6 ± 5.6	5.9 / -12.1	7.7 / -6.6
0.10 .. 0.20	68.6 ± 5.3	5.2 / -7.7	11.7 / -7.8
0.20 .. 0.30	94.2 ± 6.6	6.1 / -13.9	15.5 / -11.7
0.30 .. 0.40	85.9 ± 5.8	5.4 / -6.8	13.2 / -9.1
0.40 .. 0.50	114.9 ± 6.9	5.9 / -10.5	21.3 / -12.3
0.50 .. 0.60	146.5 ± 7.6	10.9 / -3.9	17.9 / -18.0
0.60 .. 0.70	223.8 ± 9.8	9.3 / -21.4	25.7 / -27.0
0.70 .. 0.80	322.9 ± 12.3	16.6 / -16.7	44.6 / -40.9

Table C.6: The three-jet $d\sigma/d\cos\theta_3$ measurements, with statistical (Δ_{stat}), systematic (Δ_{sys}) and energy scale (Δ_E) uncertainties.

ψ_3	$\mathrm{d}\sigma/\mathrm{d}\psi_3 \pm \Delta_{\mathrm{stat}}$ (pb)	$+\Delta_{\mathrm{sys}}$ / $-\Delta_{\mathrm{sys}}$ (pb)	$+\Delta_E$ / $-\Delta_E$ (pb)
$0 \;..\; \frac{1}{16}\pi$	67.5 ± 4.2	6.3 / -12.3	9.7 / -8.5
$\frac{1}{16}\pi \;..\; \frac{2}{16}\pi$	67.9 ± 4.0	6.4 / -4.0	14.1 / -5.5
$\frac{2}{16}\pi \;..\; \frac{3}{16}\pi$	83.6 ± 4.5	5.9 / -18.5	11.1 / -5.3
$\frac{3}{16}\pi \;..\; \frac{4}{16}\pi$	66.1 ± 3.8	8.4 / -2.9	10.4 / -5.5
$\frac{4}{16}\pi \;..\; \frac{5}{16}\pi$	60.7 ± 3.6	5.2 / -5.2	8.0 / -8.4
$\frac{5}{16}\pi \;..\; \frac{6}{16}\pi$	54.6 ± 3.4	2.6 / -6.6	7.9 / -7.9
$\frac{6}{16}\pi \;..\; \frac{7}{16}\pi$	44.1 ± 3.0	7.6 / -1.9	7.8 / -5.8
$\frac{7}{16}\pi \;..\; \frac{8}{16}\pi$	48.1 ± 3.3	5.2 / -2.1	6.9 / -4.7
$\frac{8}{16}\pi \;..\; \frac{9}{16}\pi$	50.1 ± 3.3	6.0 / -5.0	5.7 / -4.2
$\frac{9}{16}\pi \;..\; \frac{10}{16}\pi$	51.5 ± 3.3	3.9 / -7.5	7.5 / -4.5
$\frac{10}{16}\pi \;..\; \frac{11}{16}\pi$	60.2 ± 3.6	3.1 / -3.8	7.8 / -6.9
$\frac{11}{16}\pi \;..\; \frac{12}{16}\pi$	67.8 ± 3.9	4.7 / -4.3	8.4 / -9.3
$\frac{12}{16}\pi \;..\; \frac{13}{16}\pi$	80.7 ± 4.2	4.1 / -9.6	10.3 / -10.3
$\frac{13}{16}\pi \;..\; \frac{14}{16}\pi$	90.0 ± 4.7	3.9 / -9.0	11.0 / -11.5
$\frac{14}{16}\pi \;..\; \frac{15}{16}\pi$	80.0 ± 4.3	7.6 / -5.2	9.5 / -8.6
$\frac{15}{16}\pi \;..\; \frac{16}{16}\pi$	80.2 ± 4.5	1.2 / -11.7	13.9 / -11.7

Table C.7: The three-jet $\mathrm{d}\sigma/\mathrm{d}\psi_3$ measurements, with statistical (Δ_{stat}), systematic (Δ_{sys}) and energy scale (Δ_E) uncertainties.

X_3	$\mathrm{d}\sigma/\mathrm{d}X_3 \pm \Delta_{\mathrm{stat}}$ (pb)	$+\Delta_{\mathrm{sys}}$ / $-\Delta_{\mathrm{sys}}$ (pb)	$+\Delta_E$ / $-\Delta_E$ (pb)
0.67 .. 0.71	92.7 ± 10.7	6.0 / -5.9	16.1 / -12.0
0.71 .. 0.75	282.0 ± 18.0	9.0 / -32.9	42.7 / -25.3
0.75 .. 0.79	428.8 ± 22.1	17.5 / -47.6	66.2 / -48.9
0.79 .. 0.83	670.9 ± 27.5	29.9 / -88.4	74.4 / -68.7
0.83 .. 0.87	890.6 ± 31.1	31.6 / -32.8	133.5 / -95.5
0.87 .. 0.91	1251.4 ± 37.6	42.3 / -70.0	185.1 / -140.8
0.91 .. 0.95	1588.2 ± 42.7	42.9 / -63.5	224.7 / -196.9

Table C.8: The three-jet $\mathrm{d}\sigma/\mathrm{d}X_3$ measurements, with statistical (Δ_{stat}), systematic (Δ_{sys}) and energy scale (Δ_E) uncertainties.

X_4	$\mathrm{d}\sigma/\mathrm{d}X_4 \pm \Delta_{\mathrm{stat}}$ (pb)	$+\Delta_{\mathrm{sys}}$ / $-\Delta_{\mathrm{sys}}$ (pb)	$+\Delta_E$ / $-\Delta_E$ (pb)
0.50 .. 0.55	46.9 ± 6.8	9.0 / -6.7	8.8 / -4.7
0.55 .. 0.60	302.8 ± 15.9	34.1 / -17.8	55.2 / -36.7
0.60 .. 0.65	589.6 ± 22.7	23.6 / -37.3	72.6 / -58.3
0.65 .. 0.70	846.1 ± 27.6	28.9 / -31.5	123.9 / -91.3
0.70 .. 0.75	813.2 ± 27.4	23.1 / -61.8	123.7 / -94.8
0.75 .. 0.80	642.4 ± 24.2	29.2 / -63.7	89.4 / -71.9
0.80 .. 0.85	563.0 ± 22.8	19.9 / -33.2	67.1 / -69.7
0.85 .. 0.90	323.3 ± 17.6	24.7 / -65.0	46.8 / -41.1
0.90 .. 0.95	41.3 ± 5.9	1.4 / -9.0	7.2 / -2.8

Table C.9: The three-jet $\mathrm{d}\sigma/\mathrm{d}X_4$ measurements, with statistical (Δ_{stat}), systematic (Δ_{sys}) and energy scale (Δ_E) uncertainties.

$\cos\theta_3$	$d\sigma/d\cos\theta_3 \pm \Delta_{\rm stat}$ (pb)	$+\Delta_{\rm sys}$ / $-\Delta_{\rm sys}$ (pb)	$+\Delta_E$ / $-\Delta_E$ (pb)
$0.0 < x_\gamma^{\rm obs} < 0.5$			
-0.80 .. -0.70	16.4 ± 3.2	3.4 / -3.8	4.1 / -3.6
-0.70 .. -0.60	7.7 ± 2.0	2.8 / -2.2	0.9 / -0.9
-0.60 .. -0.50	7.5 ± 1.9	2.5 / -1.8	3.7 / -0.8
-0.50 .. -0.40	5.8 ± 1.5	4.6 / -1.5	0.2 / -0.9
-0.40 .. -0.30	7.8 ± 2.0	2.2 / -2.5	1.1 / -0.9
-0.30 .. -0.20	6.3 ± 1.5	2.7 / -1.1	1.8 / -1.1
-0.20 .. -0.10	5.5 ± 1.6	6.0 / -1.2	0.4 / -0.9
-0.10 .. 0.00	7.8 ± 1.9	2.5 / -0.8	2.3 / --1.6
0.00 .. 0.10	10.7 ± 2.4	3.4 / -2.4	1.5 / -1.8
0.10 .. 0.20	7.7 ± 1.7	1.6 / -1.4	1.2 / -0.9
0.20 .. 0.30	18.6 ± 3.0	6.6 / -2.0	4.1 / -2.6
0.30 .. 0.40	11.4 ± 2.3	2.2 / -1.4	2.2 / -2.0
0.40 .. 0.50	17.2 ± 2.7	4.7 / -1.0	6.4 / -0.9
0.50 .. 0.60	23.8 ± 3.3	4.6 / -6.6	0.9 / -5.3
0.60 .. 0.70	34.0 ± 4.1	2.0 / -4.2	4.9 / -3.0
0.70 .. 0.80	24.7 ± 3.4	11.2 / -5.1	3.5 / -3.7
$0.5 < x_\gamma^{\rm obs} < 0.75$			
-0.80 .. -0.70	61.9 ± 6.0	16.4 / -6.2	8.9 / -9.8
-0.70 .. -0.60	35.1 ± 3.9	1.7 / -3.1	6.3 / -4.1
-0.60 .. -0.50	17.8 ± 2.5	7.8 / -1.7	4.1 / -1.6
-0.50 .. -0.40	27.7 ± 3.8	3.1 / -11.3	6.1 / -3.4
-0.40 .. -0.30	14.9 ± 2.5	7.2 / -1.3	3.4 / -1.6
-0.30 .. -0.20	9.5 ± 1.8	4.4 / -1.2	1.5 / -1.9
-0.20 .. -0.10	14.9 ± 2.5	1.3 / -3.9	3.4 / -0.4
-0.10 .. 0.00	13.8 ± 2.3	4.0 / -1.0	2.2 / -1.2
0.00 .. 0.10	16.2 ± 2.7	4.3 / -1.2	0.5 / -1.9
0.10 .. 0.20	14.2 ± 2.2	2.3 / -3.3	2.0 / -1.7
0.20 .. 0.30	25.3 ± 3.4	3.5 / -4.4	1.6 / -4.1
0.30 .. 0.40	20.9 ± 2.8	1.9 / -4.7	2.2 / -2.7
0.40 .. 0.50	27.4 ± 3.4	2.3 / -7.9	3.2 / -5.0
0.50 .. 0.60	40.8 ± 4.1	5.2 / -1.7	6.2 / -4.6
0.60 .. 0.70	49.2 ± 4.3	4.6 / -6.8	6.8 / -8.1
0.70 .. 0.80	83.5 ± 6.1	8.5 / -5.8	12.8 / -11.3

Table C.10: The three-jet $d\sigma/d\cos\theta_3$ measurements in the regions $x_\gamma^{\rm obs} < 0.5$ and $0.5 < x_\gamma^{\rm obs} < 0.75$, with statistical ($\Delta_{\rm stat}$), systematic ($\Delta_{\rm sys}$) and energy scale ($\Delta_E$) uncertainties.

$\cos\theta_3$	$d\sigma/d\cos\theta_3 \pm \Delta_{\rm stat}$ (pb)	$+\Delta_{\rm sys}$ / $-\Delta_{\rm sys}$ (pb)	$+\Delta_E$ / $-\Delta_E$ (pb)
$0.75 < x_\gamma^{\rm obs} < 0.9$			
-0.80 .. -0.70	105.6 ± 7.8	7.8 / -28.9	16.2 / -12.2
-0.70 .. -0.60	57.2 ± 5.2	6.9 / -4.7	7.6 / -4.9
-0.60 .. -0.50	51.6 ± 5.3	5.9 / -7.5	10.2 / -8.4
-0.50 .. -0.40	35.9 ± 4.3	2.9 / -7.5	4.0 / -4.2
-0.40 .. -0.30	24.6 ± 3.2	6.3 / -2.8	3.7 / -3.0
-0.30 .. -0.20	28.7 ± 3.8	1.5 / -9.1	1.9 / -4.0
-0.20 .. -0.10	27.4 ± 3.8	2.8 / -5.2	3.7 / -3.6
-0.10 .. 0.00	17.1 ± 2.6	3.5 / -2.1	1.6 / -0.7
0.00 .. 0.10	19.4 ± 2.9	1.6 / -8.2	3.4 / -3.0
0.10 .. 0.20	19.3 ± 2.9	1.8 / -0.8	3.8 / -2.9
0.20 .. 0.30	22.0 ± 3.1	3.3 / -8.3	4.7 / -2.2
0.30 .. 0.40	25.9 ± 3.2	4.3 / -2.4	5.6 / -2.7
0.40 .. 0.50	38.1 ± 3.9	11.3 / -4.0	6.9 / -5.6
0.50 .. 0.60	39.3 ± 3.7	6.0 / -1.8	6.2 / -3.3
0.60 .. 0.70	94.2 ± 6.5	4.6 / -14.5	8.8 / -11.9
0.70 .. 0.80	127.4 ± 7.7	8.6 / -9.1	19.4 / -16.3
$0.9 < x_\gamma^{\rm obs} < 1.0$			
-0.80 .. -0.70	84.2 ± 6.6	5.1 / -18.4	11.7 / -9.1
-0.70 .. -0.60	59.9 ± 5.4	10.1 / -7.0	5.9 / -5.9
-0.60 .. -0.50	47.2 ± 4.5	5.8 / -1.8	5.0 / -3.0
-0.50 .. -0.40	45.9 ± 4.6	4.2 / -14.2	6.2 / -2.3
-0.40 .. -0.30	29.3 ± 3.4	8.0 / -3.8	5.8 / -2.6
-0.30 .. -0.20	33.1 ± 4.2	4.8 / -7.8	4.5 / -0.8
-0.20 .. -0.10	29.7 ± 3.6	3.2 / -3.2	4.5 / -1.4
-0.10 .. 0.00	23.6 ± 3.1	4.9 / -4.2	1.9 / -2.4
0.00 .. 0.10	26.0 ± 3.3	3.4 / -5.6	2.9 / -0.0
0.10 .. 0.20	28.0 ± 3.7	2.5 / -4.3	5.2 / -2.1
0.20 .. 0.30	28.8 ± 3.6	3.2 / -6.8	4.9 / -3.0
0.30 .. 0.40	27.4 ± 3.3	2.5 / -4.5	3.2 / -1.2
0.40 .. 0.50	32.5 ± 3.7	4.2 / -7.8	4.9 / -2.5
0.50 .. 0.60	43.9 ± 4.4	3.6 / -2.3	4.1 / -5.3
0.60 .. 0.70	47.3 ± 4.4	11.7 / -3.0	4.7 / -3.3
0.70 .. 0.80	91.3 ± 6.9	6.0 / -17.8	8.1 / -8.7

Table C.11: The three-jet $d\sigma/d\cos\theta_3$ measurements in the regions $0.75 < x_\gamma^{\rm obs} < 0.9$ and $0.9 < x_\gamma^{\rm obs} < 1.0$, with statistical ($\Delta_{\rm stat}$), systematic ($\Delta_{\rm sys}$) and energy scale ($\Delta_E$) uncertainties.

ψ_3	$\mathrm{d}\sigma/\mathrm{d}\psi_3 \pm \Delta_{\mathrm{stat}}$ (pb)	$+\Delta_{\mathrm{sys}}$ / $-\Delta_{\mathrm{sys}}$ (pb)	$+\Delta_E$ / $-\Delta_E$ (pb)
$x_\gamma^{\mathrm{obs}} < 0.75$			
$0 \,..\, \frac{1}{16}\pi$	19.6 ± 2.1	1.9 / -4.8	3.3 / -2.8
$\frac{1}{16}\pi \,..\, \frac{2}{16}\pi$	19.8 ± 2.1	2.5 / -1.7	6.6 / -2.6
$\frac{2}{16}\pi \,..\, \frac{3}{16}\pi$	25.3 ± 2.4	2.2 / -7.4	3.6 / -0.3
$\frac{3}{16}\pi \,..\, \frac{4}{16}\pi$	21.6 ± 2.2	4.4 / -1.7	4.5 / -2.5
$\frac{4}{16}\pi \,..\, \frac{5}{16}\pi$	18.9 ± 1.9	8.8 / -1.4	2.3 / -2.7
$\frac{5}{16}\pi \,..\, \frac{6}{16}\pi$	24.0 ± 2.4	3.8 / -5.4	4.0 / -4.8
$\frac{6}{16}\pi \,..\, \frac{7}{16}\pi$	14.0 ± 1.6	3.4 / -1.2	3.1 / -2.8
$\frac{7}{16}\pi \,..\, \frac{8}{16}\pi$	17.4 ± 1.9	6.3 / -2.8	3.3 / -1.6
$\frac{8}{16}\pi \,..\, \frac{9}{16}\pi$	19.9 ± 2.2	2.2 / -4.8	1.4 / -2.2
$\frac{9}{16}\pi \,..\, \frac{10}{16}\pi$	16.5 ± 1.8	5.2 / -2.6	1.7 / -2.1
$\frac{10}{16}\pi \,..\, \frac{11}{16}\pi$	18.2 ± 2.0	4.0 / -2.4	2.5 / -2.3
$\frac{11}{16}\pi \,..\, \frac{12}{16}\pi$	18.4 ± 1.9	2.8 / -2.0	0.9 / -3.1
$\frac{12}{16}\pi \,..\, \frac{13}{16}\pi$	23.4 ± 2.2	4.0 / -3.1	5.1 / -3.4
$\frac{13}{16}\pi \,..\, \frac{14}{16}\pi$	29.9 ± 2.8	2.6 / -5.1	3.4 / -4.2
$\frac{14}{16}\pi \,..\, \frac{15}{16}\pi$	23.0 ± 2.2	14.7 / -1.9	2.9 / -2.6
$\frac{15}{16}\pi \,..\, \frac{16}{16}\pi$	36.4 ± 3.2	1.0 / -8.6	6.2 / -7.2
$x_\gamma^{\mathrm{obs}} > 0.75$			
$0 \,..\, \frac{1}{16}\pi$	48.0 ± 3.6	5.4 / -7.9	6.3 / -5.7
$\frac{1}{16}\pi \,..\, \frac{2}{16}\pi$	48.1 ± 3.4	4.8 / -3.7	7.3 / -2.6
$\frac{2}{16}\pi \,..\, \frac{3}{16}\pi$	58.3 ± 3.8	4.6 / -11.7	7.4 / -4.9
$\frac{3}{16}\pi \,..\, \frac{4}{16}\pi$	44.5 ± 3.1	5.3 / -2.3	6.0 / -2.9
$\frac{4}{16}\pi \,..\, \frac{5}{16}\pi$	42.6 ± 3.2	0.8 / -7.6	5.9 / -5.8
$\frac{5}{16}\pi \,..\, \frac{6}{16}\pi$	30.7 ± 2.5	0.9 / -2.4	4.0 / -3.3
$\frac{6}{16}\pi \,..\, \frac{7}{16}\pi$	30.3 ± 2.5	5.2 / -3.0	4.6 / -2.5
$\frac{7}{16}\pi \,..\, \frac{8}{16}\pi$	30.7 ± 2.7	3.9 / -3.4	3.5 / -3.1
$\frac{8}{16}\pi \,..\, \frac{9}{16}\pi$	29.9 ± 2.5	7.7 / -2.2	4.3 / -2.0
$\frac{9}{16}\pi \,..\, \frac{10}{16}\pi$	35.2 ± 2.8	3.3 / -10.4	6.1 / -2.1
$\frac{10}{16}\pi \,..\, \frac{11}{16}\pi$	42.1 ± 3.0	1.0 / -2.8	5.3 / -4.6
$\frac{11}{16}\pi \,..\, \frac{12}{16}\pi$	49.7 ± 3.3	5.0 / -5.3	8.1 / -6.1
$\frac{12}{16}\pi \,..\, \frac{13}{16}\pi$	57.4 ± 3.6	3.9 / -8.6	4.9 / -6.8
$\frac{13}{16}\pi \,..\, \frac{14}{16}\pi$	59.9 ± 3.8	3.6 / -5.4	7.6 / -7.3
$\frac{14}{16}\pi \,..\, \frac{15}{16}\pi$	58.0 ± 3.8	2.1 / -9.1	6.6 / -6.0
$\frac{15}{16}\pi \,..\, \frac{16}{16}\pi$	44.1 ± 3.3	2.5 / -5.5	7.7 / -5.2

Table C.12: The three-jet $\mathrm{d}\sigma/\mathrm{d}\psi_3$ measurements in the regions $x_\gamma^{\mathrm{obs}} < 0.75$ and $x_\gamma^{\mathrm{obs}} > 0.75$, with statistical ($\Delta_{\mathrm{stat}}$), systematic ($\Delta_{\mathrm{sys}}$) and energy scale ($\Delta_E$) uncertainties.

Bibliography

[1] E. Auge et al., *Phys. Lett.* B **168**, 163 (1986)

[2] AMY Collaboration, R. Tanaka et al., *Phys. Lett.* B **277**, 215 (1992)

[3] H1 Collaboration, T. Ahmed et al., *Phys. Lett.* B **297**, 205 (1992)

[4] ZEUS Collaboration, M. Derrick et al., *Phys. Lett.* B **297**, 404 (1992)

[5] ZEUS Collaboration, M. Derrick et al., *Phys. Lett.* B **322**, 287 (1994)

[6] ZEUS Collaboration, M. Derrick et al., *Phys. Lett.* B **384**, 401 (1996)

[7] H1 Collaboration, C. Adloff et al., *Eur. Phys. J.* C **1**, 97 (1998)

[8] ZEUS Collaboration, J. Breitweg et al., *Eur. Phys. J.* C **1**, 109 (1998)

[9] ZEUS Collaboration, J. Breitweg et al., *Eur. Phys. J.* C **11**, 35 (1999)

[10] ZEUS Collaboration, J. Breitweg et al., *Phys. Lett.* B **443**, 394 (1998)

[11] The original papers are collected in M. Gell-Mann and Y. Ne'eman, *"The Eightfold Way"*, (New York: Benjamin, 1964).

[12] V. E. Barnes et al., *Phys. Rev. Lett.* **12**, 204 (1964)

[13] M. Gell-Mann, *Phys. Lett.* **8**, 214 (1964)

[14] G. Zweig, CERN-TH 401 and CERN-TH 412 (1964)

[15] O. W. Greenberg, *Phys. Rev. Lett.* **13**, 598 (1964)

[16] H. Fritzsch, M. Gell-Mann and H. Leutwyler, *Phys. Lett.* B **47**, 365 (1973)

[17] E. D. Bloom et al., *Phys. Rev. Lett.* **23**, 930 (1969);
M. Breidenbach et al., *Phys. Rev. Lett.* **23**, 935 (1969)

[18] PDG, D. E. Groom et al., *Eur. Phys. J.* C **15**, 1 (2000)

[19] J. D. Bjorken, *Phys. Rev. Lett.* **179**, 1547 (1969)

[20] R. P. Feynman, *Phys. Rev. Lett.* **23**, 1415 (1969)

[21] C. Callan and D. Gross, *Phys. Rev. Lett.* **22**, 156 (1969)

[22] ZEUS Collaboration, S. Chekanov et al., *Eur. Phys. J.* C **21**, 443 (2001)

[23] T. Eichten et al., *Phys. Lett.* B **46**, 274 (1973)

[24] H1 Collaboration, I. Abe et al., *Nucl. Phys.* B **407**, 515 (1993),
ZEUS Collaboration, M. Derrick et al., *Phys. Lett.* B **316**, 412 (1993)

[25] C. F. von Weizsäcker, *Z. Phys.* **88**, 612 (1934);
E. J. Williams, *Phys. Rev.* **45**, 729 (1934);
S. Frixione, M.L. Mangano, P. Nason and G. Ridolfi, *Phys. Lett.* B **319**, 339 (1993)

[26] G. Alterellei and G. Parisi, *Nucl. Phys.* B **126**, 298 (1977);
Y. L. Dokshitzer, *Sov. Phys. JETP* **46**, 641 (1977);
L. N. Lipatov, *Sov. J. Nucl. Phys.* **20**, 94 (1975);
V. N. Gribov and L.N. Lipatov, *Sov. J. Nucl. Phys.* **15**, 675 (1972)

[27] S. Söldner-Rembold and M. Krämer, *"Summary of Photon 2000"*, to be published in the AIP Conference Proceedings Series (2001).

[28] R. Nisius, *Phys. Rept.* **332**, 165 (2000)

[29] PLUTO Collaboration, C. Berger et al., *Phys. Lett.* B **142**, 111 (1984) and *Nucl. Phys.* B **281**, 365 (1987)

[30] JADE Collaboration, W. Bartel et al., *Phys. Lett.* B **121**, 203 (1983) and *Z. Phys.* C **24**, 231 (1984)

[31] TASSO Collaboration, M. Althoff et al., *Z. Phys.* C **31**, 527 (1986)

[32] TPC/2γ Collaboration, H. Aihara et al., *Phys. Rev. Lett.* **58**, 97 (1987) and *Z. Phys.* C **34**, 1 (1987)

[33] AMY Collaboration, T. Sasaki et al., *Phys. Lett.* B **252**, 491 (1990);
S. K. Sahu et al., *Phys. Lett.* B **346**, 208 (1995);
T. Kojima et al., *Phys. Lett.* B **400**, 395 (1997)

[34] TOPAZ Collaboration, K. Muramatsu et al., *Phys. Lett.* B **332**, 477 (1994)

[35] OPAL Collaboration, R. Akers, *Z. Phys.* C **61**, 199 (1994);
K. Ackerstaff et al., *Z. Phys.* C **74**, 33 (1997)

[36] DELPHI Collaboration, P. Abreu et al., *Z. Phys.* C **69**, 223 (1996)

[37] M. Glück, E. Reya and A. Vogt, *Phys. Rev.* D **45**, 3986 (1992)

[38] M. Glück, E. Reya and A. Vogt, *Phys. Rev.* D **46**, 1973 (1992)

[39] P. Aurenche, J. Guillet and M. Fontannaz, *Z. Phys.* C **64**, 621 (1994)

[40] W. A. Bardeen, A. J. Buras, D. W. Duke and T. Muta, *Phys. Rev.* D **18**, 3998 (1978)

[41] L. E. Gordon and J. K. Storow, *Nucl. Phys.* B **489**, 405 (1997)

[42] DELPHI Collaboration, CERN-PPE/95-164

[43] L3 Collaboration, M. Acciarri et al., *Phys. Lett.* B **345**, 74 (1995)

[44] OPAL Collaboration, CERN-PPE/95-83

[45] G. Marchesini, B. R. Webber, G. Abbiendi, I. G. Knowles, M. H. Seymour and L. Stanco, *Comput. Phys. Common.* **67**, 465 (1992)

[46] T. Sjostrand, *Comput. Phys. Commun.* **82** , 74 (1994)

[47] S. Frixione and G. Ridolfi, *Nucl. Phys.* B **507**, 315 (1997);
S. Frixione, *Nucl. Phys.* B **507**, 295 (1997)

[48] CTEQ Collaboration, H. L. Lai et al., *Phys. Rev.* D **55**, 1280 (1997)

[49] M. Klasen and G. Kramer, *Z. Phys.* C **76**, 67 (1997);
M. Klasen, T. Kleinwort and G. Kramer, *Eur. Phys. J. Direct*, **C1**, 1 (1998)

[50] B. W. Harris and J. F. Owens, *Phys. Rev.* D **56**, 4007 (1997) and *Phys. Rev.* D **57**, 5555 (1998)

[51] B. W. Harris, M. Klasen and J. Vossebeld, hep-ph/9905348

[52] HERA, *"A proposal for a Large Electron-Proton Colliding Beam Facility at DESY"*, DESY HERA Report 81-10;
G.A. Voss and B.H. Wiik, *Ann. Rev. Nucl. Part. Sci.* **44**, 413 (1994)

[53] HERMES Collaboration, *"The HERMES Spectrometer"*, DESY Note 98-057

[54] HERA-B Collaboration, *"HERA-B: An Experiment to study CP violation in the B system using an Internal Target at the HERA Proton Ring"*, Design Report, DESY-PRC 95/01 (1995)

[55] H1 Collaboration, I. Abt et al., *Nucl. Instrum. Methods* A **386**, 310 (1997)

[56] E. Hilger, *"Zeus coordinate System"*, ZEUS Note 86-17

[57] B. Foster et al., *Nucl. Instrum. Methods* A **338**, 254 (1994)

[58] ZEUS Collaboration, *"A detector for HERA"*, PRC 87-02
ZEUS Collaboration; *"The ZEUS Detector"*, Status Report (1993)

[59] R. Hall-Wilton, N. McCubbin, P. Nylander, M. Sutton and M. Wing, ZEUS Note 99-24

[60] http://giroz.desy.de/physics/lumi/lumi96/lumi.html

[61] http://giroz.desy.de/physics/lumi/lumi97/lumi.html

[62] For example, the three-jet photoproduction paper [10] and all two-jet photoproduction papers before 1999 [6, 8, 76].

[63] J. Vossebeld, Ph.D. Thesis, NIKHEF (1999)

[64] P. de Jong, *"Status of the Uranium Calorimeter Reconstruction Software"*, ZEUS Note 92-19

M. De Kamps, *"Gluon Momentum Fraction Measurements in the ZEUS Detector"*, ZEUS Note 94-14

[65] G. Briskin and A. Caldwell, *"Comparison of CAL Energy for Electrons with CTD"*, ZEUS Note 95-35;

M. Vreeswijk, Ph. D. Thesis, University of Amsterdam (1996)

[66] R. Saunders, Ph. D Thesis, UCL (1997)

[67] G. M. Briskin, Ph. D. Thesis, Tel Aviv University (1998)

[68] F. Sciulli, B. Straub and L. Wai, ZEUS Note 95-140

[69] S. Bentvelsen, J. Engelen and P. Kooijman, *"Proceeding of the Workshop on Physics at HERA, DESY"*, 23 (1992)

[70] CERN Application Software Group, CERN Program Library Long Writeup D506

[71] P. J. Bussey, EUCELL, ZEUS PHANTOM Users Library

[72] S. Catani, Y. L. Dokshitzer and B. R. Webber, *Phys. Lett.* B **285**, 291 (1992);

S. Catani, Y. L. Dokshitzer, M. H. Seymour and B. R. Webber, *Nucl. Phys.* B **406**, 187 (1993)

[73] S. D. Ellis and D. E. Soper, *Phys. Rev.* D **48**, 3160 (1993)

[74] J. Huth et al., Proceedings of the 1990 DPF Summer Study on High Energy Physics, Snowmass, Colorado, edited by E. L. Berger (World Scientific Singapore, p134) (1992)

[75] F. Jacquet and A. Blondel, *"Proceedings of the study of an ep facility for Europe"*, DESY Note 79-048, 391 (1979)

[76] ZEUS Collaboration, M. Derrick et al., *Phys. Lett.* B **348**, 665 (1995)

[77] E. Strickland, Ph.D. Thesis, University of Glasgow (1998)

[78] L. Lönnblad, *Comp. Phys. Comm.***71**, 15 (1992)

[79] ICHEP 2000, Paper 417, Abstract 888, *"A measurement of the dijet production cross section in neutral current deep inelastic scattering at HERA"*

[80] CTEQ Collaboration, H. L. Lai et al., *Phys. Rev.* D **51**, 4763 (1995)

[81] M. Glück, E. Reya and A. Vogt, *Z. Phys.* C **53**, 127 (1992)

[82] G. Schuler and T. Sjöstrand, *Z. Phys.* C **68**, 607 (1995)

[83] Rev. T. Bayes, *"An Essay Toward Solving a Problem in the Doctrine of Chances"*, *Philos. Trans. R. Soc. London* **53**, 370 (1763)

[84] G. D'Agostini *Nucl. Instrum. Meth* A**362**, 487 (1995)

[85] T. Tymieniecka and A. F. Zarnecki, *"Formulae and Figures for Basic Two-Body QCD Processes in ep Interaction"*, DESY Note 92-137